UNIVERSITÀ DI TRENTO

FONDAZIONE EDMUND MACH

Doctoral School in

Agrifood and Environmental Sciences

Matteo Tonezzer

Gas nanosensors for quality assessment of food products

Economic devices that can be integrated into the production and distribution chain

Supervisors

prof. Flavia Gasperi, dr. Franco Biasioli

Tutor

prof. Flavia Gasperi

XXXV Cycle, 2023

TABLE OF CONTENTS

LIST OF TABLES

LIST OF FIGURES

LIST OF SYMBOLS AND ABBREVIATIONS

cfu	Colony Forming Unit
CVD	Chemical Vapor Deposition
DMA	Dimethylamine
DMF	Dimethylformamide
GC	Gas Chromatography
LDA	Linear Discriminant Analysis
LoD	Limit of Detection
MO	Metal Oxide
MS	Mass Spectrometry
NW	Nanowire
PCA	Principal Component Analysis
PID	Photoionization detectors
ppbv	parts per billion
ppmv	parts per million
PTR	Proton Transfer Reaction
QMB	Quartz Micro Balance
RMSE	Root Mean Square Error
sccm	standard cubic centimeters per minute
SEM	Secondary Electron Microscopy
SnO_2	Tin oxide
SVM	Support Vector Machine
TEM	Transmission Electron Microscopy
ToF	Time of Flight

TVB-N	Total Volatile Basic Nitrogen
TVC	Total Viable count
TMA	Trimethylamine
UPGMA	Unweighted Pair Group Method with Arithmetic mean
VLS	Vapor-Liquid-Solid mechanism
V_2O_5	Vanadium oxide
VOC	Volatile Organic Compound
XRD	X-Ray Diffraction
ZnO	Zinc oxide

ABSTRACT

This PhD project arises from the growing awareness of food quality and safety on the part of citizens and institutions. The increase in the population to feed, the lengthening of the production and distribution chains and the socio-economic risks of a poor diet make it crucial to monitor the quality of food from the producer to the consumer. Traditional methods (sensory panels and laboratory analytical techniques) are too expensive and above all slow to evaluate the quality of fresh foods that deteriorate over the course of a few hours. In this context, it is crucial to develop monitoring devices that are cheap, rapid and non-invasive, in order to be able to evaluate the quality of food products extensively and constantly.

Solid-state gas sensors are an ideal candidate, as they are inherently non-invasive and inexpensive. In this context, the project focused on chemoresistive sensors based on semiconductor metal oxides, which are among the simplest and most performing, and have the advantage of being sensitive to almost all gases and VOCs. Initially, nanostructures of different materials (n- and p-type semiconductors) and of different morphologies (nanowires and nanosheets) were studied in order to investigate the performance of individual sensors. In this way, some devices have been optimized with respect to the detection of possible biomarkers of the degradation of specific foods. The sensors have demonstrated a rapid response (from a few seconds to a minute), an intense response and above all a very low detection limit (less than 1ppmv, in some cases a few tens of ppbv), important for agri-food applications.

This approach is the simplest since it requires a single sensor that is selective towards a certain molecule (ammonia, ethylene...) which can be considered the only important information parameter in a certain application.

In most cases, however, the gaseous emission of a food is composed of a large quantity of volatile compounds, and the low selectivity of resistive sensors makes it difficult to discriminate the molecules most informative regarding the degradation process. For this reason, in the second part of the PhD we used the sensors developed up to then to create electronic noses. Exploiting the dimensions of nanostructures, we have developed a new concept of thermal electronic nose, i.e. with sensors of the same material, but within a thermal gradient. In this way, by exploiting multivariate statistical analysis and machine learning techniques, the devices acquired a greater ability to discriminate and quantify the different gases. The electronic noses have shown that they can perfectly recognize the different gases tested (100%) and estimate their concentration with an error of a few ppmv.

Measurements in the laboratory are very useful for testing the performance parameters of sensors and electronic noses, as they make it possible to evaluate the correctness of the classification and the error in estimating the concentration of any gas. On the other hand, measuring the emissions of fresh food is different, as the concentrations are not known, and therefore a different approach is needed.

The final stage of the project involved using electronic noses to assess the freshness of certain agri-food products. As the developed sensors were particularly sensitive to ammonia, it was decided to study the degradation of meat and fish, where this gas is an important marker. The electronic noses have been able to accurately recognize the meat from the fish (> 95%), and evaluate the state of degradation by giving a very accurate estimate of the microbial count (>95%), responding in a very short time (tens of seconds).

The miniaturized electronic noses developed during this PhD project have therefore successfully demonstrated to be a rapid and non-invasive cross-sectional tool for assessing the freshness of agri-food products.

CHAPTER 1. INTRODUCTION

1.1 Analytical chemistry for food quality

Evaluating the freshness of agri-food products is a growing problem as traditional methods keep pace with production. In the past, panels of human experts smelled and tasted the products [1], recently joined by non-invasive analytical techniques such as gas chromatography, spectrometry and mass spectrometry [2].

These techniques can separate gas mixtures by distinguishing their individual components and quantifying them in a precise manner. Their high sensitivity and specificity make them a precious objective aid to the human experience of the panelists. Unfortunately, all these techniques share the same problems of sensory analysis: they are expensive in terms of personnel (expert personnel are needed), money (they are expensive laboratory instruments) and above all in terms of time (the analysis of a sample takes long).

1.2 Gas sensors

In parallel to traditional analytical techniques, gas sensors have experienced remarkable growth, driven by innovations in materials science and nanotechnology. Among these, metal oxide nanowires have garnered significant attention. These nanomaterials exhibit remarkable sensitivity to various gases and offer a platform for the development of chemoresistive gas sensors. Chemical gas sensors operate on the principle that the electrical resistance of a sensing material changes in response to gas adsorption. This change in resistance depends on the type and concentration of the gas and is very fast, thus enabling real-time gas detection. Furthermore, the miniaturization and possible integration of these sensors in portable devices would allow their use on a large scale,

measuring the headspace of agri-food products one by one and not just randomly [3]. Gas sensors have some advantages over laboratory analytical techniques:

1. Real-time monitoring: One of the paramount advantages of chemical gas sensors is their ability to provide real-time, continuous monitoring of gas concentrations. Unlike traditional analytical techniques such as gas chromatography, which involve sample collection and subsequent analysis, chemical gas sensors offer immediate feedback. This measurement speed is very important in the analysis of fresh food products such as vegetables, fruit and even more meat and fish, as their quality degrades quickly.

2. Portability and miniaturization: Metal oxide nanowires have played a pivotal role in the advancement of miniaturization of gas sensors. Their small size and low power consumption make them suitable for integration into production and distribution chains, portable devices and even wearable technologies. This portability would allow for on-site measurements on production farms, warehouses, shops and even by the customer with his smartphone.

3. Cost-effectiveness: Chemical gas sensors cost thousands of times less than traditional analytical instruments. Their simplicity in design and low cost of production and operation make them accessible for mass production and therefore extensive use, so as to analyze all products and not just a few samples.

While gas chromatography and mass spectrometry are powerful analytical methods for gas analysis, they are relatively complex, require skilled operators, and are less suitable for real-time monitoring. Gas sensors, on the other hand, offer a simpler, faster and cheaper approach. However, it is essential to recognize that gas sensors do not achieve the same level of sensitivity and specificity as advanced analytical techniques.

The synergy between analytical techniques and gas sensors could foster a comprehensive approach to gas analysis, where sensors act as rapid screening tools, directing complex samples to analytical instruments for detailed characterization.

Unfortunately, the performance of gas sensors is not only "worse" than that of analytical techniques, but they lack selectivity almost completely. In fact, chemoresistors are sensitive to almost any gas and volatile organic compound. In simple contexts, in which it is necessary to detect a gas in the absence of interferents or in the presence of few interferents, choosing the right material can solve the issue, but in most cases the situation is more complex and cannot be solved with a single sensor. In these cases, several gas sensors are combined into an array that works together and is called an electronic nose, as it simulates the functioning of the mammalian olfactory system.

1.3 Electronic noses

An electronic nose consists of a series of chemical sensors, each with a different selectivity to gases or volatile organic compounds (VOCs). When used for a measurement, these sensors produce a pattern of distinct electrical responses that is characteristic of the gas, VOC or mixture being sensed by the electronic nose. This pattern is then analyzed using multivariate statistical analysis techniques and machine learning algorithms, allowing the electronic nose to identify and quantify the gas or mixture it is detecting. This process follows the way our sense of smell interprets the world (receptors with different sensitivities, then processed together by the brain), albeit with the precision and speed of modern technology [4].

Although electronic noses are not able to understand which molecules they are detecting, they are able to work very efficiently by comparing the measurement in progress with a database of measurements, in order to recognize the aroma that they are measuring as a whole. In this way, not

leaving out a "calibration" phase that requires the use of established analytical techniques, the electronic nose could then be able to evaluate the freshness and quality of food products quickly and efficiently [5]. Unfortunately, the development of electronic noses is still being studied, and the prototypes made and marketed so far are still quite bulky and expensive. This PhD course on miniaturized electronic noses for the agri-food sector is located in this context.

CHAPTER 2. AIM OF THE THESIS AND SPECIFIC OBJECTIVES

Current electronic noses are devices with great potential, but still limited by both performance and size and above all by cost. Simplifying the device at a technological level would make it possible to significantly reduce both parameters, making electronic noses more affordable in many applications, including the agri-food sector. From this point of view, the present PhD project aimed to develop a new type of electronic noses, based on chemoresistive gas sensors, which were cheap, tiny and therefore integrable in an extensive way in the agro-food sector chain.

2.1 Gas sensors

The most suitable chemiresistive gas sensors for this purpose are those based on metal oxides, since the gas molecules absorbed on the surface withdraw or release electrons inside the material (depending on whether the gases are oxidizing or reducing) and thus modify the resistance creating a sensor signal in a very simple way. The use of nanostructured materials greatly improves the performance of the sensors as it leads to a huge increase of the surface/volume ratio and because the surface effect influences the resistance of the sensor more importantly. In fact, the morphology of the nanostructures and the possible functionalization with other materials (organic molecules or metallic nanoparticles) allows to substantially optimize the sensor performance. Therefore, during the PhD it was planned to study sensors based on nanowires and nanosheets of different metal oxides, possibly functionalized on the surface in order to improve their sensitivity and selectivity towards specific volatile organic compounds. Optimizing individual sensors towards the detection of agri-food biomarkers is in fact the first step, necessary to create the elements that make up the arrays for electronic noses.

2.1.1 Specific objectives

Within this first phase, the specific objectives to evaluate the progress of the doctoral project were:

- realization of nanowires (1D) and nanosheets (2D) of metal oxides;
- possible functionalization with metal nanoparticles or organic molecules;
- morphological, compositional and structural characterization of nanomaterials;
- fabrication of chemoresistive sensors and testing of their detection performance with single gases.

2.2 Electronic noses

Based on tiny sensors composed of metal oxide nanostructures, the PhD project aimed to develop innovative electronic noses, which work on the basis of different working temperatures rather than different materials. In this way, the entire device could be miniaturized by exploiting a temperature gradient in which a series of identical sensors based on metal oxide nanowires operate. The general aim was therefore to manufacture electronic noses with microelectronic techniques, so as to be able to integrate the different sensors together with an asymmetric heater, reducing the size of the entire device to a few millimeters.

However, this approach is technologically difficult, and therefore a proof-of-concept was also implemented in parallel by realizing single nanowire sensors in which the thermal gradient was not spatial but temporal (the same sensor measured sequentially at different temperatures). The idea was to exploit both architectures in order to test different sensors and evaluate their performance against specific food products. In fact, even if the discrimination of an electronic nose is "artificial" (it derives from the different response of the sensors which creates a unique pattern for a certain

bouquet of odours), the detection performance of the sensors that compose it greatly influences its operation.

2.2.1 Specific objectives

Within this second phase, the specific objectives to evaluate the progress of the doctoral project were:

- measurements with natural thermal gradient and simulation of thermal electronic nose;
- integration of sensors and asymmetric heater and creation of a miniaturized electronic nose;
- multivariate statistical analysis of electronic nose responses and performance evaluation;
- feedback from machine learning algorithms regarding the effectiveness of the single sensors used.

2.3 Measurements of food products

The ultimate goal of the project was to develop a new non-invasive tool for assessing the quality and freshness of agri-food products. As already mentioned, the electronic nose is an instrument which, unlike analytical techniques, does not recognize the molecules it detects. For this reason, the measurement of real food must be accompanied, at least in the first phase, by a standard technique that allows its "calibration".

Furthermore, measurements with real foods are very different from those made in the laboratory with single gases, as they measure dynamic headspaces instead of a constant flow. Therefore, the measurement procedure itself also had to be reviewed and adapted, and this was only possible by using them simultaneously with a sensitive, selective and rapid technique such as proton transfer reaction mass spectrometry (PTR-MS).

Of course, the ultimate goal was that electronic noses would later be able to function on their own, quickly, efficiently and accurately.

2.3.1 Specific objectives

Within this last phase, the specific objectives aimed at evaluating the progress of the doctoral project were:

- headspace measurement test and comparison with flowmeter measurements;
- measurement with PTR-MS and electronic noses to analyze and optimize the functioning of the sensors;
- measuring foods with single nanowire electronic noses and standard calibration technologies;
- field measurement of foods with integrated electronic nose prototype.

CHAPTER 3. ULTRASENSITIVE NO_2 GAS SENSING PERFORMANCE OF TWO DIMENSIONAL ZNO NANOMATERIALS: NANOSHEETS AND NANOPLATES

This chapter is based on the scientific paper [6]:

"Ultrasensitive NO_2 gas sensing performance of two dimensional ZnO nanomaterials: Nanosheets and nanoplates", Ceramics International, 47 (2021) 28811–28820. Doi: 10.1016/j.ceramint.2021.07.042

3.1 Abstract

Highly sensitive NO_2 gas sensors with low detection limit are vital for practical application in air pollution monitoring. Here, the NO_2 gas sensing performance of porous ZnO nanosheets and nanoplates were investigated, with different shape and thickness. It was found that ultra-thin ZnO nanoplates had a higher sensitivity than coral-like ZnO nanosheets. The results were attributed to the high specific surface and very small thickness of the ultrathin nanoplates. The nanoplates have indeed a thickness of 15 nm compared to that of the nanosheets which is 100 nm, and a BET surface area of 75 m²/g, while that of the nanosheets is 6 m²/g. The chemosensor based on ultra-thin ZnO nanoplates shows a response of 156 to 0.5 ppmv of NO_2 at 200°C, with a theoretical detection limit of 3 parts per trillion and a selectivity higher than 760. The specific surface and the small thickness of the ultra-thin nanoplates contribute to its highly improved sensing performance, making it ideal for NO_2 gas sensing.

3.2 Introduction

According to the World Health Organization (WHO), more than 90% of the world's population lives in areas that exceed air pollution limits, nearly 98% of cities in low-income countries do not meet air quality standards, and about 3 million people lose their lives each year due to pollution-related disorders [7]. One of the most toxic gases present in the atmosphere is nitrogen dioxide (NO_2), a reddish-brown gas with a characteristic sharp odor [8]. There is a lot of interest in monitoring this gas and reducing its concentration, due to its harmful effects on human health and the environment [9]. Nitrogen dioxide is mainly produced from the industrial exhaust gas, power plants, petrochemical plants, vehicles and laboratories [10]. It can produce photochemical pollution and acid rain, as well as irritation to the eyes and lungs, respiratory diseases, weakening of the immune system and even death [9,11].

According to the WHO and the European Commission for Air Quality Standards, the NO_2 hourly mean value may not exceed 0.1 parts per million in volume (ppmv) more than 18 times in a year, while the NO_2 annual mean value may not exceed 0.02 ppmv [12]. In the environment, the NO_2 concentration is on the order of ppbv, making it difficult to detect [9]. For these reasons, different types of devices have been studied recently, trying to obtain NO_2 sensors that are very sensitive, reliable and selective. NO_2 chemical gas sensors based on semiconductor metal oxides (SMOs) are very promising due to their advantages such as low manufacturing cost, simple operation, low power consumption, high sensitivity and stability, and good compatibility with silicon technology [13,14,15].

Among the various sensing technologies, solid state chemoresistors are among the most used for NO_2 detection, and among the most used materials several SMOs are found: SnO_2, ZnO, In_2O_3, WO_3 and TiO_2 [16,17,18]. Recently, heterostructures based on combinations of these semiconductors or on the surface decoration with metallic nanoparticles such as Pt, Au and Ag have

been deeply studied [19]. Zinc oxide is one of the most studied SMOs for its properties, and it has been used widely to realize different types of devices, namely gas sensors [20,21], electrochemical sensors and biosensors [22,23] but also supercapacitors [21] and environmental tools for pollution degradation [22].

Furthermore, ZnO proved to have some natural selectivity towards NO_2 [23,24,25]. For instance, Wang et al. [26] incorporated ZnO nanowires and black phosphorus nanosheets for the detection of NO_2 gas with enhanced response value. Zhou et al. [27] used nanowire-network sensor for the detection of NO_2 gas under UV illumination, where they studied the effect of carrier gas on the sensing performance. Such sensors could detect NO_2 at ppbv level at room temperature, but the sensors required long response and recovery time. Recently, improvements in nanotechnology allow for better control of ZnO nanostructures in terms of crystal structure, size and dimensionality, porosity and microstructure on the mesoscale [28,29,30]. The geometry and size of the ZnO nanostructures are particularly important in the case of gas sensors due to the great influence that morphology has on gas detection performance. Wang et al. developed a sensor based on ZnO nanospheres that exhibits a response of 29.4 to 5 ppmv of NO_2 at room temperature when illuminated with ultraviolet (UV) light [23]. Due to their larger surface area and the small diameter of the nanoparticles that compose them, the nanospheres showed a better response than nanorods and nanoflowers. The response of all ZnO nanostructures was very low for all other gases tested (NO, CO, NH_3, C_6H_6, H_2, ethanol and acetone), indicating excellent shape-independent selectivity. Kusumam et al. have shown that very thin nanosheets (thickness of 30 nm) give a much greater response than nanoparticles with a diameter of 100 nm: a response of 260% to 5 ppmv of NO_2 and a sensitivity of 21%/ppmv [29].

In this work, porous coral-like nanosheets and ultra-thin ZnO nanoplates were grown by

hydrothermal technique followed by thermal annealing. The sensor based on the ultra-thin nanoplates exhibits superior NO_2 sensing performance compared to the coral-like nanosheets counterpart. It can detect very low NO_2 concentrations with a detection limit of 3 parts per trillion at the optimal working temperature of 200°C. The response of the ultra-thin ZnO nanoplates was 76 to 0.5 ppmv NO_2, twice that of the porous coral-like ZnO nanosheets. The selectivity of the sensor with respect to interferents (acetone, ethanol, isopropyl alcohol, triethylamine, SO_2 and CO) is higher than 760. This excellent performance, combined with the advantages of chemoresistors based on metal oxide nanostructures (reduced size and cost, simplicity of fabrication and measurement), make the ultra-thin ZnO nanoplates an ideal material for NO_2 sensors.

3.3 Experimental

The chemicals used in this work ($ZnSO_4 \cdot 7H_2O$, urea (CH_4N_2O) and $Zn(NO_3)_2 \cdot 6H_2O$) were bought from Sigma-Aldrich. All reagents were analytic grade and used as received without further purification. Both porous ZnO nanostructures were synthesized by hydrothermal method (Fig. 3.1), using deionized water as solvent.

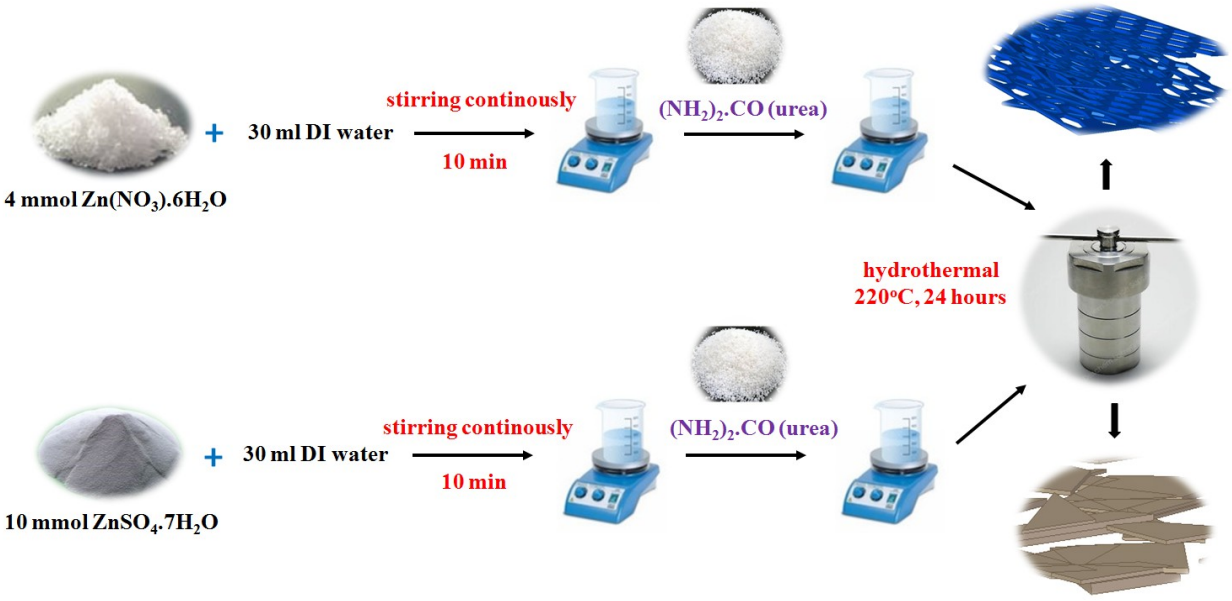

Figure 3.1 - Hydrothermal synthesis procedure of ZnO nanosheets and nanoplates.

In a typical process to grow ZnO nanosheets, zinc nitrate hexahydrate [$Zn(NO_3)_2 \cdot 6H_2O$] (4 mmol) was dissolved in 30 mL deionized water under continuously stirring for 15 min. Then 20 ml urea (CH_4N_2O) solution (8 mmol) was added with further stirring for 15 min to obtain pH 5. The resulting solution was transferred into a 100 ml Teflon-lined stainless-steel autoclave, where it was maintained at 220°C for 24 h for the hydrothermal growth. After being naturally cooled to room temperature, the precipitate on the bottom was centrifuged, washed several times with deionized water, then with ethanol solution, and finally collected by centrifugation at 4000 rpm. The obtained white powder was dried in an oven at 60°C for 24 h, and then calcined at 600°C [31].

The ultra-thin ZnO nanoplates were grown following a very similar procedure (Fig. 3.1). Zinc sulfate heptahydrate [$ZnSO_4 \cdot 7H_2O$] (10 mmol) was dissolved in 30 mL deionized water. After continuously stirring for 15 min, 20 mL urea solution (20 mmol) was added with further stirring for 15 min to adjust the pH to 5. The resulting solution was then transferred into a Teflon-lined stainless-steel autoclave and the hydrothermal process was maintained for 24 h at 220°C. The

washing and collecting process of the nanomaterial was the same as that for the porous ZnO nanosheets [32].

The synthesized materials were characterized by field-emission scanning electron microscopy (SEM, JEOL 7600F), powder x-ray diffraction (XRD, Advance D8, Bruker), and high-resolution transmission electron microscopy (HRTEM, JEOL 2100F). The specific surface area of the nanomaterials was determined using Brunauer–Emmett–Teller nitrogen adsorption/desorption isotherms (Micromeritics Gemini VII). The sensing properties of the synthesized coral-like ZnO nanosheets and ultra-thin ZnO nanoplates were then characterized by using a laboratory-made system. Prior to the gas sensing measurements, the sensor was preheated at 600°C for 2 h in order to improve the adhesion between Pt electrodes and materials and to stabilize the sensor output. This also eliminate the effect of heat treatment condition on the gas sensing performance of the fabricated sensors for comparison. Sensor resistance was measured continuously using a source meter (Keithley 2602) while the chamber was flowed with different concentrations of gas, intersperse with dry air. Schematic diagram of the gas sensing measurement system was reported in Ref. [33]. The sensing measurement setup consists of a heater, a temperature controller, gas inlet and outlet valves, and probes connecting the sensor to Keithley 2602 source meter. Target gases (NO_2, SO_2, and VOCs) of different concentrations were prepared by mixing standard gases with dry air as reference and dilution using a series of mass flow controllers. Details about the calculation of target gas concentration can be found in our recent publication [34]. The response (S) was calculated as the ratio R_a/R_g (for reducing gases) or R_g/R_a (for oxidizing gases), where R_a and R_g were the resistances of the sensor in dry air and tested gas, respectively. The response and recovery times (τ_{resp}, τ_{recov}) were defined as the time taken by the sensor to reach 90% of its saturated response after exposure to NO_2 and air, respectively [30].

3.4 Results and discussion

Typical SEM images of coral-like ZnO nanosheets and ultra-thin ZnO nanoplates are shown in Figure 3.2(A,B) and Fig. 3.2(C,D), respectively. Both materials show a high homogeneity, with two-dimensional nanostructures about one micron wide, randomly oriented. The nanosheets in Fig. 3.2A,B have very large size, with an average thickness of about 100 nm and show a marked porosity (pores of about 90 nm in diameter). The nanoplates in Fig. 3.2C,D look smooth and have an average thickness of 15 nm. Herein, homogenous coral-like ZnO nanosheets and ultra-thin ZnO nanoplates were obtained without using any surfactant, thus reducing the usage of chemicals.

The mechanism of formation of coral-like ZnO nanosheets and ultra-thin ZnO nanoplates can be explained as follows: zinc sulphate heptahydrate, and zinc nitrate hexahydrate are used as precursor of Zn^{2+}, while urea is used as a means to control the pH of the solutions. During the hydrothermal process, urea is easily broken down into NH_3 and HNCO [35], and CH_4N_2O decomposes into NH_4OH and HNCO [36]. Therefore, the $(OH)^-$ group reacts with Zn^{2+} ions to form $Zn(OH)_2$ flakes. The morphology and thickness of the ZnO nanostructures were attributed to the use of precursor salts.

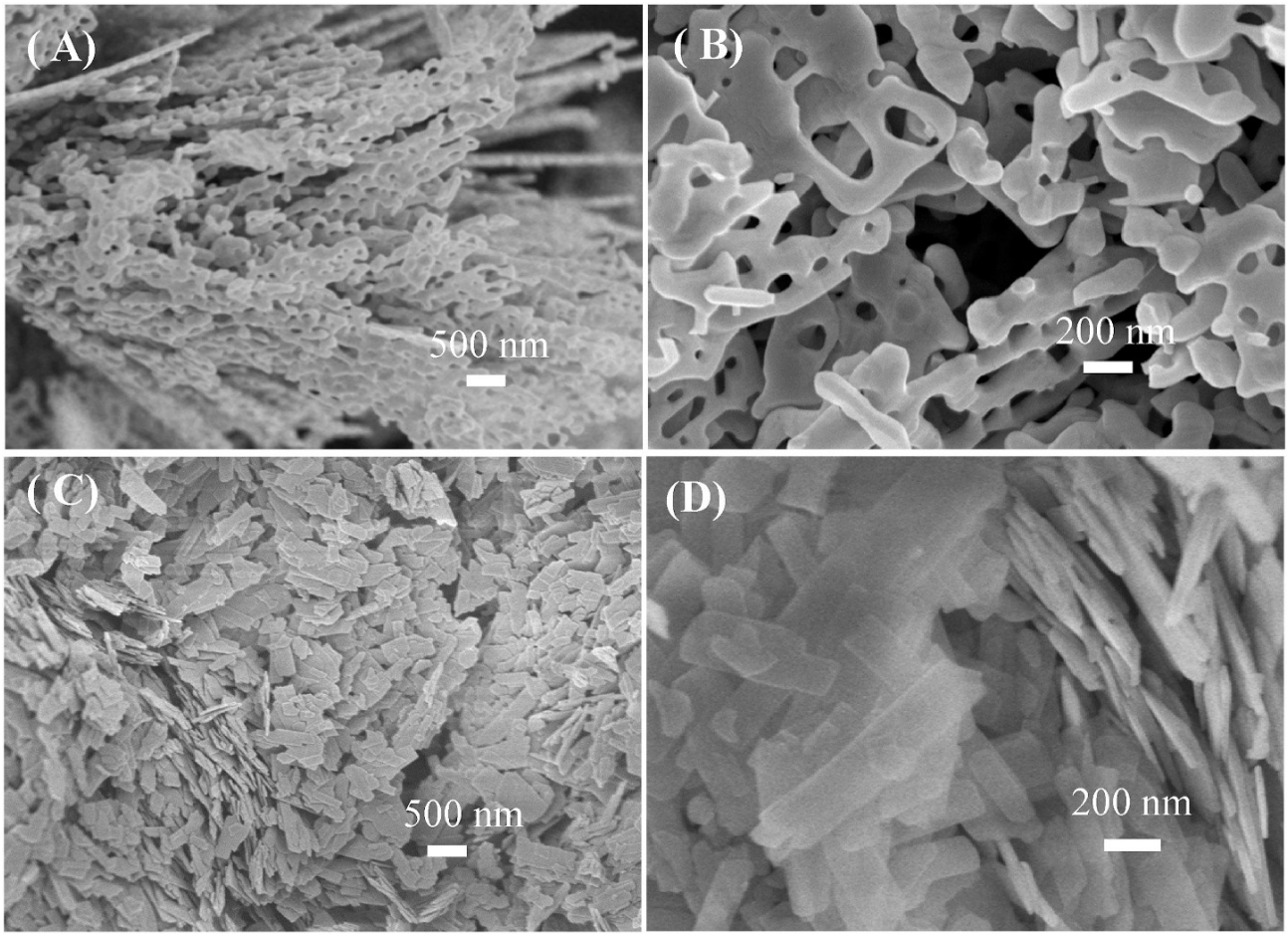

Figure 3.2 - SEM images of the synthesized ZnO nanostructures: (A, B) coral-like nanosheets and (C,D) ultra-thin nanoplates.

The lattice structure of the ZnO nanosheets and nanoplates was analyzed by means of XRD, the patterns of which are shown in the upper panel of Fig. 3.3A. The experimental patterns for coral-like nanosheets (in blue) and ultra-thin nanoplates (in red) show the same peaks, which match well with those of the wurtzite crystal structure (JCPDS card No. 36-1451), shown in the lower panel. The intense and sharp peaks indicate a good crystallinity of the nanostructures composing both sensors. No peaks due to other phases or amorphous contributions are visible in Fig. 3.3B, confirming the good crystallinity and single phase of the nanomaterials [37]. The crystallite size was calculated using Scherrer formula, resulting in 21.2 nm for coral-like nanosheets and 19.6 nm for ultra-thin nanoplates. The specific surface of the coral-like ZnO nanosheets and ultrathin nanoplates

was tested with nitrogen adsorption/desorption isotherm measurements, the results of which are shown in Fig. 3.3B.

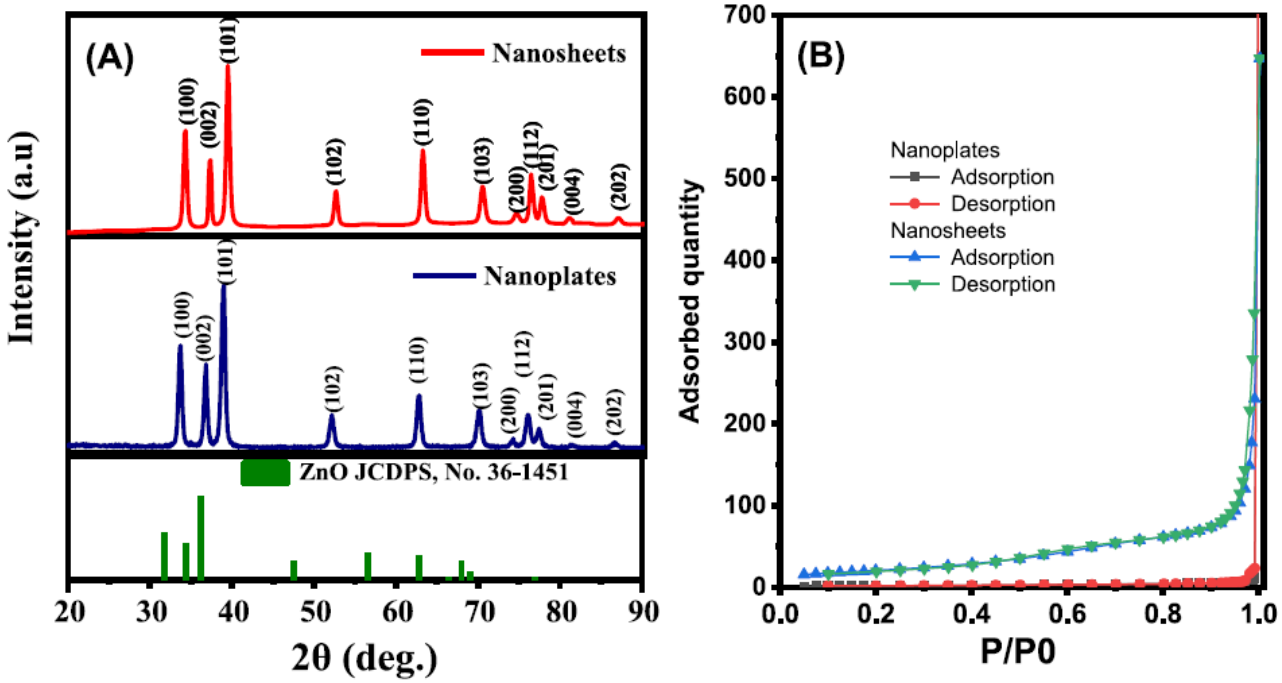

Figure 3.3 - (A) XRD patterns, (B,C) Nitrogen adsorption desorption of the synthesized ZnO nanosheets and ZnO nanoplates.

Despite their marked porosity, coral-like nanosheets have a BET surface area of 6 m^2/g (Fig. 3.3B), while ultra-thin nanoplates have a much larger BET surface area of 75 m^2/g (Fig. 3.3C). The large surface area, together with the tiny thickness of the nanoplates are two important factors why the nanoplates are expected to have better sensing performance than the coral-like nanosheets [38].

Typical TEM images of the coral-like ZnO nanosheets and ultra-thin ZnO nanoplates are shown in Fig. 3.4. Fig. 3.4A and C shows low magnification TEM images confirming the morphologies of porous nanosheets, and ultra-thin nanoplates, respectively. The size of ZnO nanosheets is very large of micrometers with many nanopores. The nanoplate are smaller with a size of about 100 nm. The HRTEM images in Fig. 3.4B and D clearly show the lattice fringes confirming the good crystallinity of both nanostructures. The interplanar spacing was found to be 0.25 and 0.50 nm in coral-like

nanosheets and ultrathin nanoplates, respectively. The interspacing between two adjacent planes 0.25 and 0.50 nm are in good agreement with the expected values for (101), and (001) of the hexagonal ZnO.

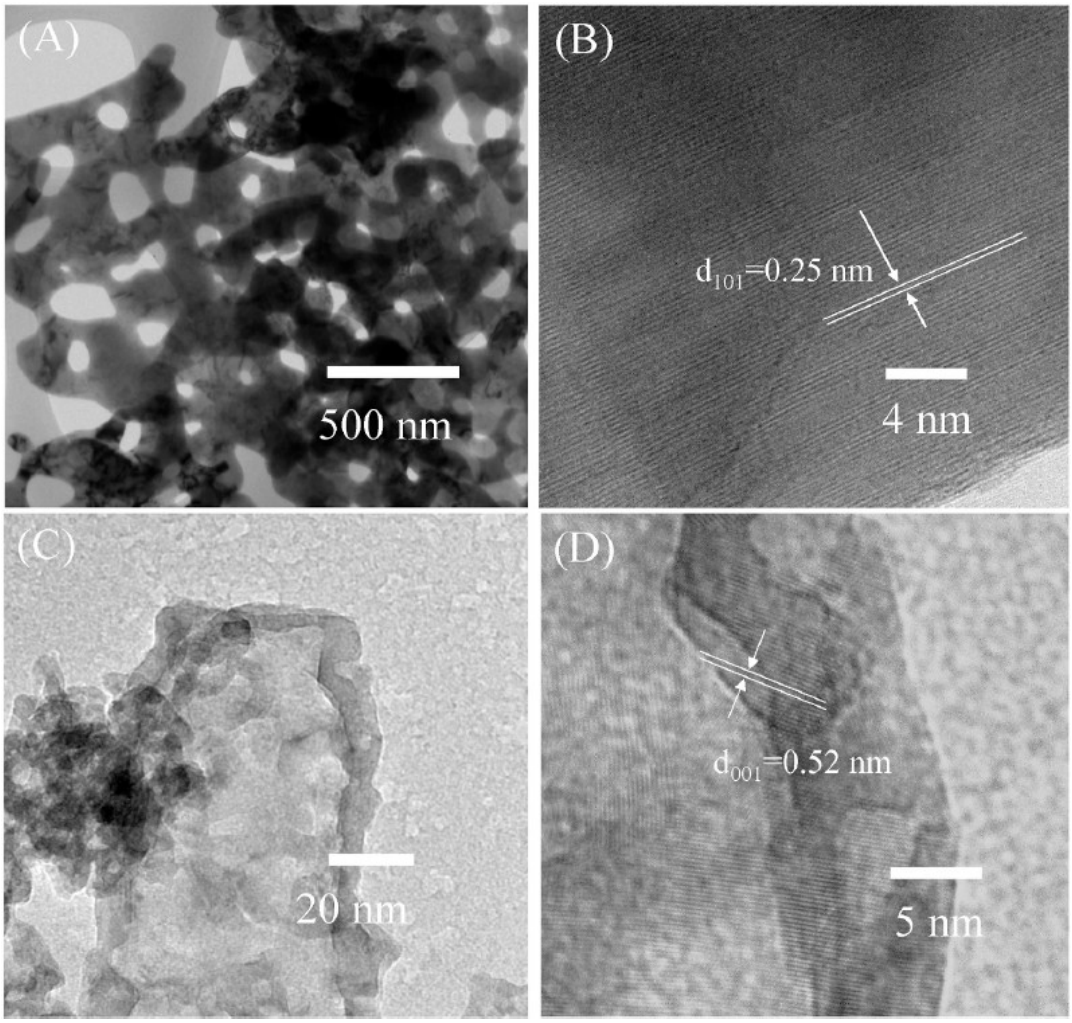

Figure 3.4 - TEM images of (A-B) the coral-like ZnO nanosheet and (C-D) ultrathin porous ZnO nanoplates.

The I-V curves of the sensors based on the two individual nanomaterials in air are shown in figures 3.5A and C. A voltage range from −5 V to +5 V was applied to the sensors. Both sensors of showed linear I-V characteristics, demonstrating good ohmic contact between the ZnO nanostructures and the electrodes. Figure 3.5B and D show the resistance of the coral-like ZnO nanosheets and ultra-thin ZnO nanoplates in air at different working temperatures. The coral-like

ZnO nanosheet sensor showed the maximum resistance at 300 °C, whereas the ZnO nanoplate device exhibited the maximum resistance at 250 °C. The results are very interesting, because it is agreed that the resistance of a semiconductor decreases with an increase of temperature. However, here, the resistance of sensors increased with an increase of temperature from 200 to 250°C for the ZnO nanoplate sensor and to 300°C for the ZnO nanosheet sensor. Such behaviors could be explained by the competition between the decrease of resistance due to the thermal excitation of electron from valent band to conduction band, and the increase of resistance caused by the surface adsorption of oxygen species. With temperature increasement from 200 to 250, and 300 °C the oxygen adsorption dominates the change in resistance, thus the sensor resistance increased, and archived the maximum values. To clarify this point, we tested the I–V curves of the nanosheet sensor in N_2 at high temperatures, and the sensor showed linear I–V curves at all measured temperatures. In addition, the sensor resistance decreases with an increase of temperature from 150 to 350 °C. No peak of resistance was detected at 300 °C as obverted when testing in air. Such results confirm that the oxygen adsorption play an important role in determination the change in based resistance of sensor with temperature.

Figures 3.6A and 3.7A show the dynamic resistance of the coral-like ZnO nanosheets and ultra-thin ZnO nanoplates when different concentrations of NO_2 were injected at different temperatures. The ZnO nanostructures were tested with 10, 5, 2.5, 1, and 0.5 ppmv of NO_2, in a temperature range of 150-350°C. The sensor resistance rapidly increases when exposed to NO_2 gas, and returns to its base value when NO_2 flow is stopped and replaced with air.

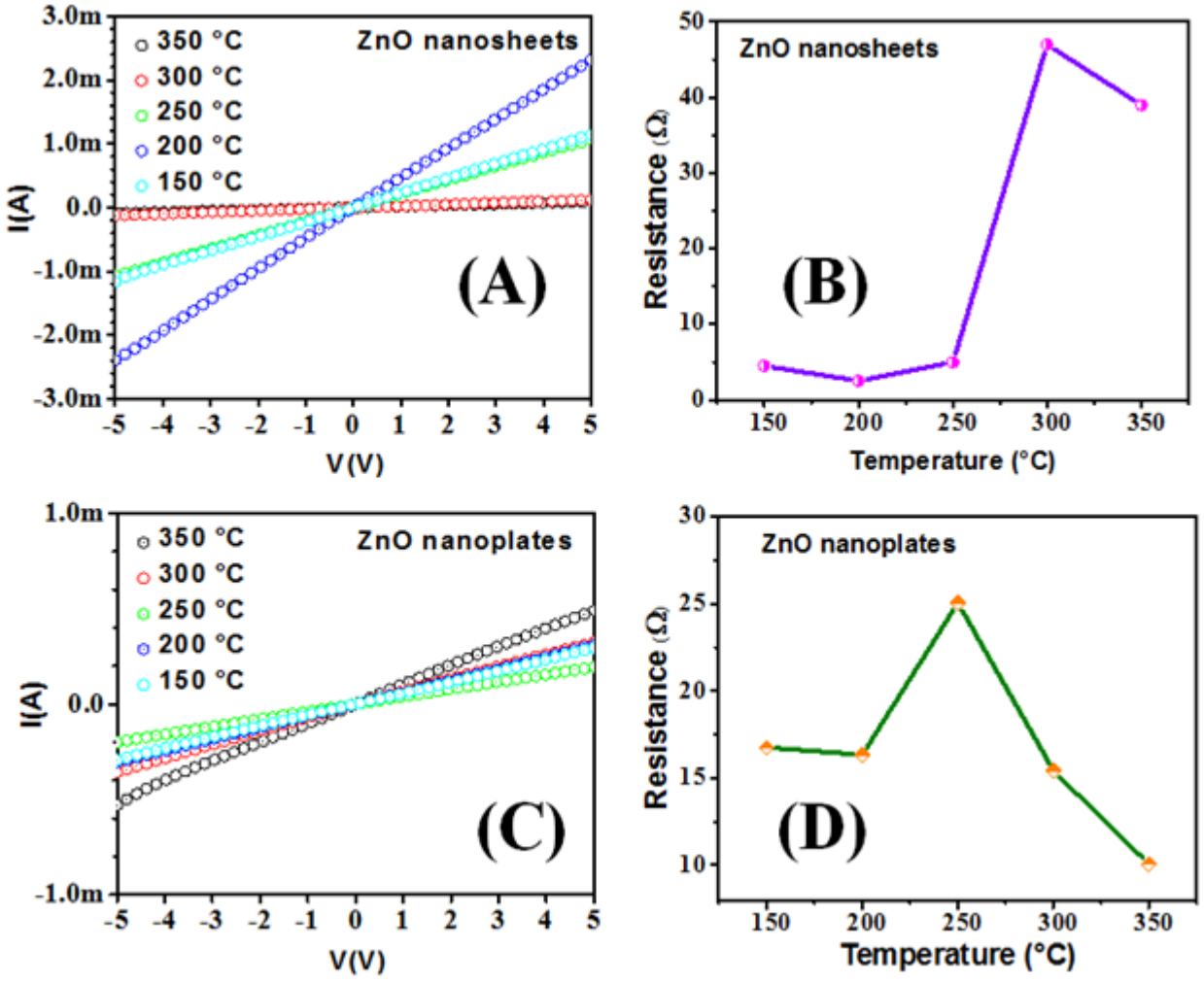

Figure 3.5 - I–V curve of the ZnO nanosheets (A) and ZnO nanoplates (B) sensor measured in air at 150 - 350°C; calculated resistance at different working temperatures for (B) ZnO nanosheets and (D) ultra-thin nanoplates.

This effect is expected for an n-type semiconductor reacting to an oxidizing gas, which withdraws electrons from the nanostructures. The response values calculated from Fig. 3.6A and 3.7A for coral-like ZnO nanosheets and ultra-thin ZnO nanoplates, are shown in Fig. 3.6B and 3.7B, respectively. While the response of nanosheets is linear throughout the concentration range, that of nanoplates tends to saturate beyond 2 ppmv. For both nanostructures, the optimal temperature (at which the response is maximum) is 200°C. The response of ultra-thin nanoplates is significantly higher than that of coral-like nanosheets, especially at lower concentrations: at 200°C the response

of nanoplates to 1 ppmv of NO_2 is 156, which is more than 2 times that of nanosheets. Fig. 3.6C and fig. 3.7C show the response and recovery time of the coral-like ZnO nanosheets and the ultra-thin ZnO nanoplates sensors, calculated at 200°C to different concentrations of NO_2. Response times are in the order of tens of seconds, while recovery times are in the order of minutes. The ultra-thin nanoplates respond and recover faster than the coral-like nanosheets, probably due to their thinness and larger surface.

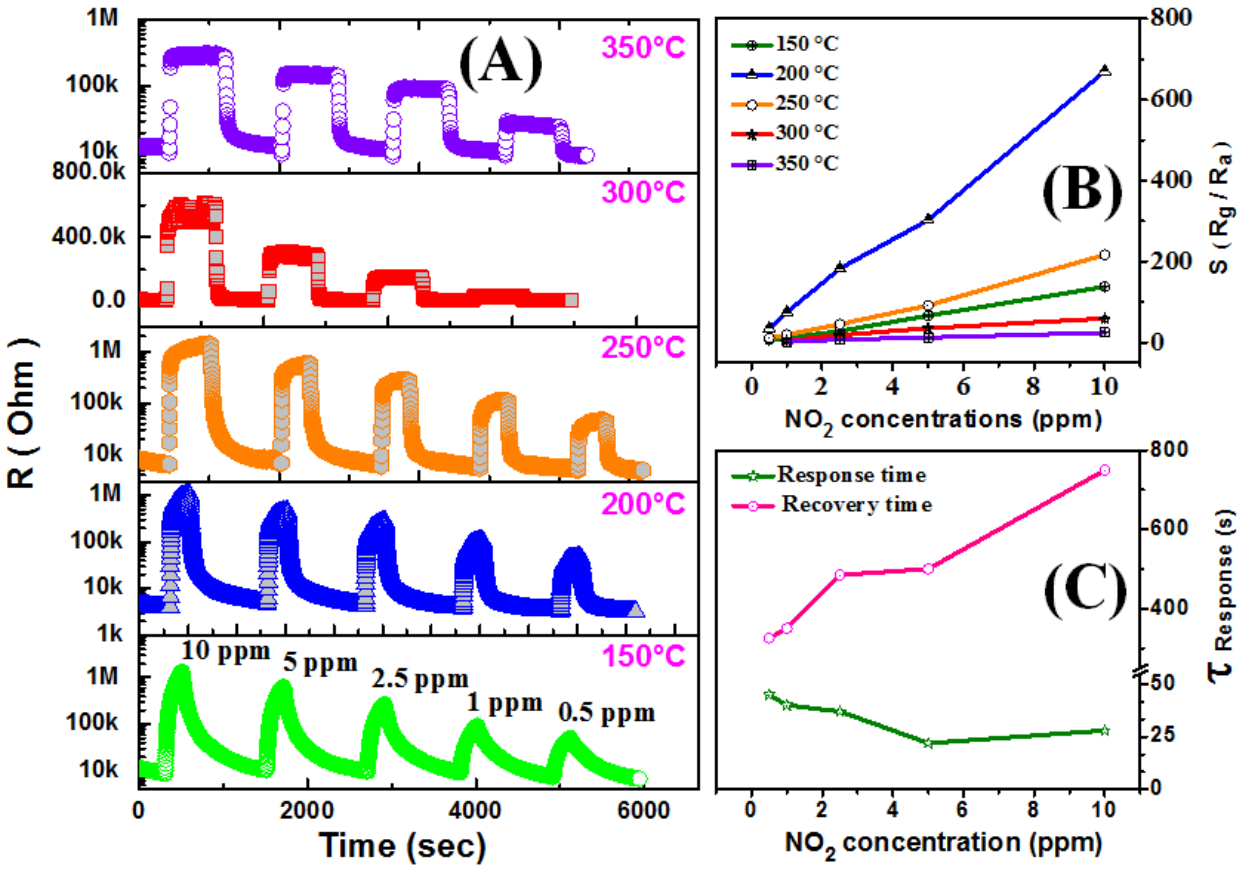

Figure 3.6 - NO_2 sensing performance of the coral-like ZnO nanosheets: (A) dynamic resistance upon exposure to different concentrations of NO_2 measured at different temperatures; (B) sensor response as a function of NO2 concentration; (C) response and recovery time as a function of the NO_2 concentration.

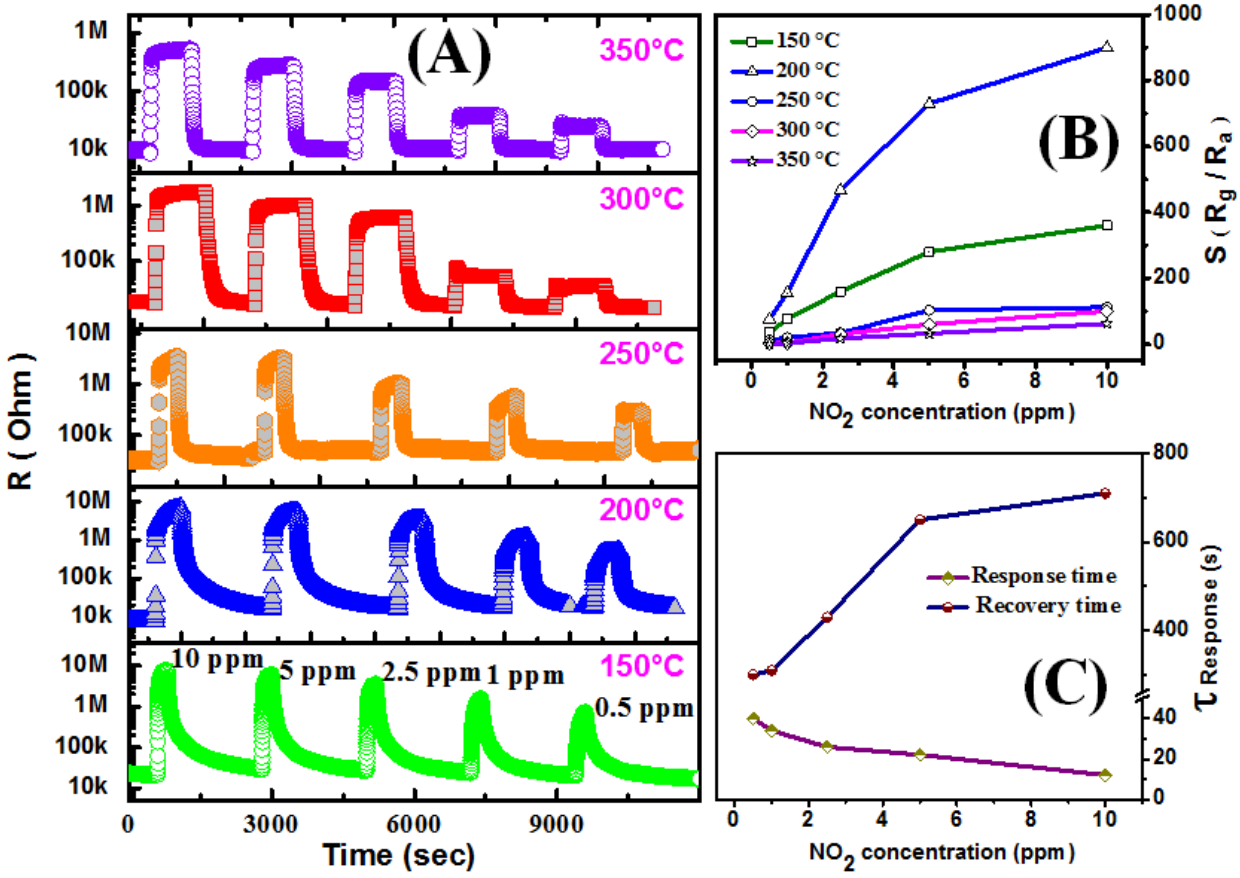

Figure 3.7 - NO_2 sensing performance of the porous ZnO nanoplates: (A) dynamic resistance upon exposure to different concentrations of NO_2 measured at different temperatures; (B) sensor response as a function of NO_2 concentration; (C) response and recovery time as a function of the NO_2 concentration.

The NO_2 detection limit (DL) of the sensors based on the coral-like ZnO nanosheets and ultra-thin ZnO nanoplates, was calculated at their optimal operating temperature of 200°C. Although the lowest gas concentration investigated in this study is of 0.5 ppmv, the sensor theoretical detection limit can be determined by the formula: $DL = SD_{noise}/Sensitivity$, which is the IUPAC definition with k = 3 [39]. In the formula SD_{noise} is the standard deviation of the sensor noise measured in air, while *Sensitivity* is the derivative of its response as a function of NO_2 concentration, calculated at the minimum concentrations. Details on the calculation method of detection limit can be found

elsewhere [34]. At 200°C the ultra-thin ZnO nanoplates sensor has a detection limit of 3 ppt, which is lower than that of the coral-like ZnO nanosheets sensor, which is 25 ppt.

Table 1 shows NO_2 sensing performance of ZnO nanostructures in scientific literature. As can be seen, the response of ultra-thin nanoplates is very high, while the detection limit is orders of magnitude lower than the others reported. Such low detection limit is advantageous in practical application in monitoring of ultralow concentration of NO_2 gas in air pollution monitoring.

Table 3.1 - NO_2 sensing performance of ZnO nanostructures in scientific literature.

Morphology	**Size (nm)**	**NO_2 concentration (ppmv)**	**Temperature (^oC)**	**Response (R/R_0)**	**Detection limit***	**Ref**
Nanorods	Ø 150-200	1	300°C	1.8 (1 ppmv)	<1 ppmv	[40]
Nanorods	Ø 30	0.2-5	250°C	200 (5 ppmv)	0.2 ppmv	[41]
Nanotubes	Ø 200	1-20	150°C	1.31 (1 ppmv)	1 ppmv	[42]
Nanorods	Ø 60	0.1-1	200°C	1.3 (100 ppbv)	100 ppbv	[30]
Nanopetals	Thickness 70	20	RT	119 (20 ppmv)	20 ppmv	[43]
Nanorods	Ø 260	1-100	200°C	1.41 (1 ppmv)	1 ppmv	[31]
Nanowires	Ø 80-90	1-30	250°C	1.3 (1 ppmv)	1 ppmv	[44]
Rose-like hierarchical structures	Flowers: Ø 200 Sheet: thickness 10	5-80	300°C	49 (10 ppmv)	5 ppmv	[45]
Nanorods	Ø 50-300	0.1-5	25°C + UV	1.6 (0.5 ppmv)	100 ppbv	[46]
Flowers	Sheet thickness: 30			2.0 (0.5 ppmv)		
Sphere	NPs Ø 20-30			2.2 (0.5 ppmv)		
Nanoplates	Thickness 15	0.5-10	200°C	156 (1 ppmv)	3 ppt	This work

To evaluate the short-term stability of the coral-like ZnO nanosheets and ultra-thin ZnO nanoplates sensors, we investigated 8 recovery-response cycles to 1 ppmv NO_2 at 200 °C. The results are shown in Fig. 3.8 and indicate that both sensors are very stable and repeatable.

Selectivity is considered an important parameter for practical applications. The ultra-thin ZnO sensor was tested to various concentrations of interfering gases such as 0.5 ppmv NO_2, 500 ppmv acetone, 500 ppmv ethanol, 500 ppmv isopropyl alcohol, 500 ppmv triethylamine, 5 ppmv SO_2, and 200 ppmv CO at a working temperature of 200 ◦C, as shown in Fig. 3.9. The sensor exhibits the highest response to NO_2, followed by CO, SO_2, acetone, triethylamine, isopropyl alcohol, and ethanol. The sensor response to NO_2 is much higher than that to all the interfering gases tested, although the NO_2 concentration was much lower than those of the other gases (in most cases by a thousand times). Note that the sensor is highly selective to even oxidant SO_2 gas, where the response value is about 1.58 for 5 ppmv SO_2. This suggests the potential application of the ultra-thin ZnO nanoplates sensor for selective detection of NO_2 in air quality monitoring.

It is clearly that the ZnO nanoplates based sensor is suitable for application in detection of NO_2 gas in air. However, for practical application in air pollution monitoring, the effect of humidity and long- term stability is also important [26]. Thus, we tested the response to 0.5 ppmv NO_2 at 200 °C in ambient air with different relative humidity vales of 30–90 %RH, and the data are shown in Fig. 3.10A and B. As shown in Fig. 3.10A, the based resistance of the sensor decreases from 14.6 kΩ to 8.2 kΩ with an increase of relative humidity from 30% RH to 90% RH. The decrease of based resistance was ascribed to the adsorption of water molecules, which induces free electrons to the conduction band of ultra-thin porous ZnO nanoplates. In addition, the response value to 0.5 ppmv NO_2 was also slightly decreased from 78 to 46 with an increase of relative humidity from 30% RH to 90% RH (Fig. 3.10B). However, the NO_2 response of the sensor was not influenced at low

relative humidity of less than 40% RH. The influence of ambient humidity on NO_2 response can be explained by the occupation of physically absorbed water on the active sites of the ZnO nanoplates, which prevent the adsorption of NO_2 molecules and results in a decrease of sensor response.

Repeatability and long-term stability of the ZnO nanoplates based sensor at 200 °C were also studied for the detection of 1 ppmv NO_2. As shown in Fig. 3.10C, the sensor maintained its performance after ten consecutive cycles measurement with NO_2 gas confirming the good repeatability. After storage of 3 months in air, and a week of testing at 200 °C, the sensor still maintained its response values (Fig. 3.10D). Such results indicate that the porous ZnO nanoplates based sensor had good repeatability and long-term stability, proving its suitability in practical applications [27].

Because NO_2 is highly toxic pollutant, thus for air quality monitoring, we tested the response of the porous ZnO nanoplates based sensor to ppbv level NO_2 concentration, as shown in Fig. 3.10E. It is clearly that the sensor could detect NO_2 gas down to ppbv level with significant response values of 3.5–10 for the NO_2 concentration in the range of 5–50 ppbv (Fig. 3.10F).

Furthermore, the response of the ZnO nanoplates based sensor to oxidation gas (SO_2), was also studied, and the response of the sensor is relatively low of about 1.26–1.58 for SO_2 concentrations in the range of 1–5 ppmv, confirming the high selectivity of the sensor over the contamination of SO_2 gas. Such results document the possibility of using the porous ZnO nanoplates based sensor to monitor NO_2 at ppbv level for application in air pollution monitoring.

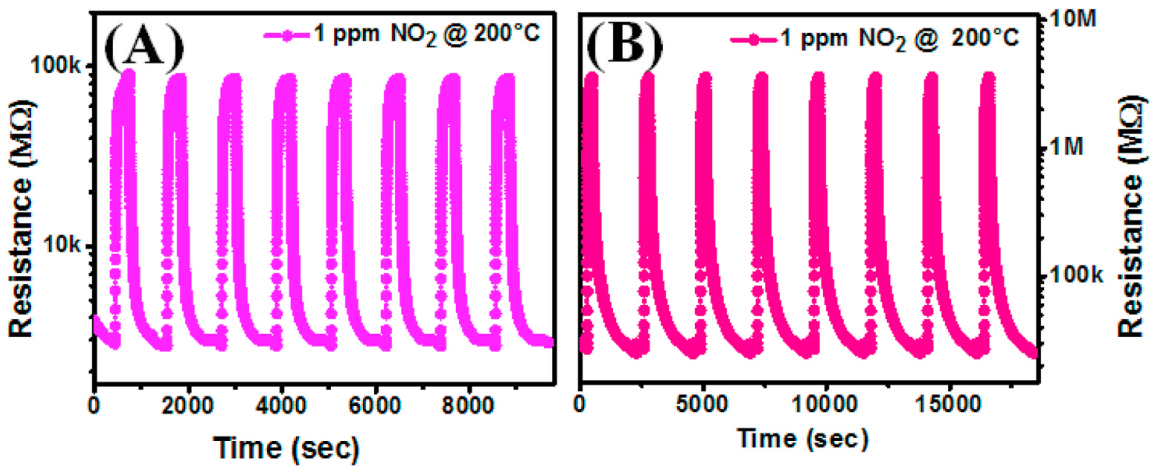

Figure 3.8 – Short-term stability of (A) ZnO nanosheets and (B) ZnO nanoplates sensor to NO_2.

The sensing properties of metal oxide-based sensors rely on the change in electrical resistance that occurs when the gas molecules interact with the surface of the semiconductor [47,48]. Basically, when the ZnO nanoplates and nanosheets are exposed to air, oxygen is absorbed on their surface forming oxygen anions such as O^{2-}, O^- and O_2^- and thus forming a thin depletion layer (top configuration in Fig. 3.11).

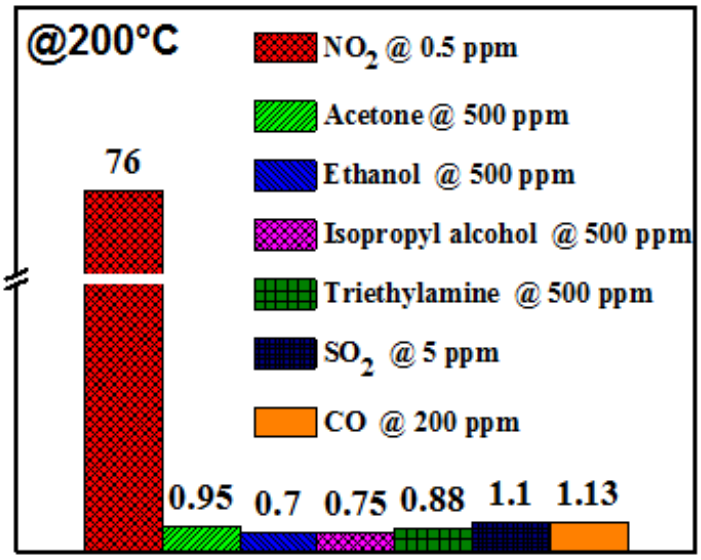

Figure 3.9 - Selectivity of the ZnO nanoplates sensor: response values to different gases.

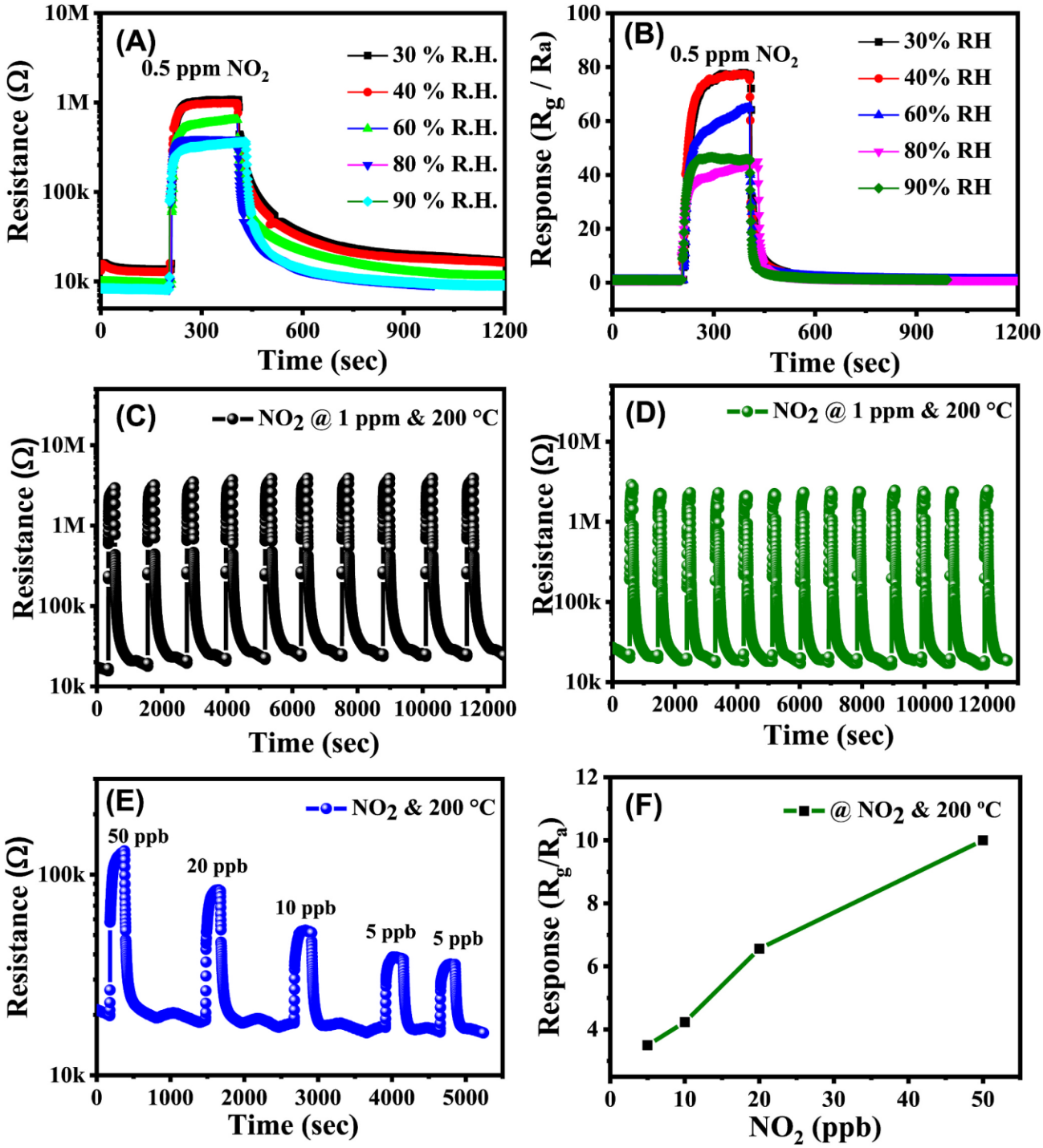

Figure 3.10- (A) transient resistance, and (B) response to 0.5 ppmv NO_2 of the ZnO nanoplate sensor in different relative humidity values; (C) short-term, and (D) long-term stability of the sensor after storage of 3 months in air and a week of testing at 200 °C; (E) transient resistance, and (F) response of the sensor to ppbv level NO_2 at 200 °C.

Although the effect is one and acts on the interface between the gas and the semiconductor creating a zone depleted of electrons, it works in two distinct ways. Along the path of the current, the depletion zones are found at the edges between different crystalline nanostructures, and create potential barriers that the electrons must overcome. When NO_2 reacts on the surface of the ZnO nanostructures withdrawing electrons, these barriers rise and the current decreases, as fewer electrons are able to pass them.

$$NO_{2\ (gas)} + e^- \leftrightarrow NO_2^-{}_{(ads)} \tag{3.1}$$

$$NO_{2\ (ads)} + O_2^-{}_{(ads)} + 2e^- \leftrightarrow NO_2^-{}_{(ads)} + 2O^-{}_{(ads)} \tag{3.2}$$

Perpendicularly to the current flow, the absorption of electrons does not create potential barriers, but only a large depletion layer. The reaction of NO_2 on the surface of the ZnO increases the thickness of this depleted area (bottom case in Fig. 3.11), reducing the number of electrons available for conduction. Both of these mechanisms work in the same direction: a higher concentration of NO_2 increases the thickness of the depletion layers, raising the potential barriers and decreasing the number of electrons available, and therefore increasing the resistance of the sensor.

Since the width of the nanosheets and nanoplates are comparable, the higher response of the ultra-thin nanoplates is attributed to two other factors: the larger surface area [32,38] and the thinner thickness [40,49]. As seen in Fig. 3.11, the depth of the depletion layer is the same in the two nanostructures (indicated between the two black arrows in each case), but since the nanoplates are thinner, the relative depletion is much larger. Considering that the sensor response is the ratio between its resistance in the two conditions, it is explained why it is much higher for the ultra-thin

nanoplates. The comparison between figures 3.6B and 3.7B also confirms this mechanism: the nanoplates are so thin that even very low concentrations of NO_2 heavily deplete the nanostructure, approaching response saturation.

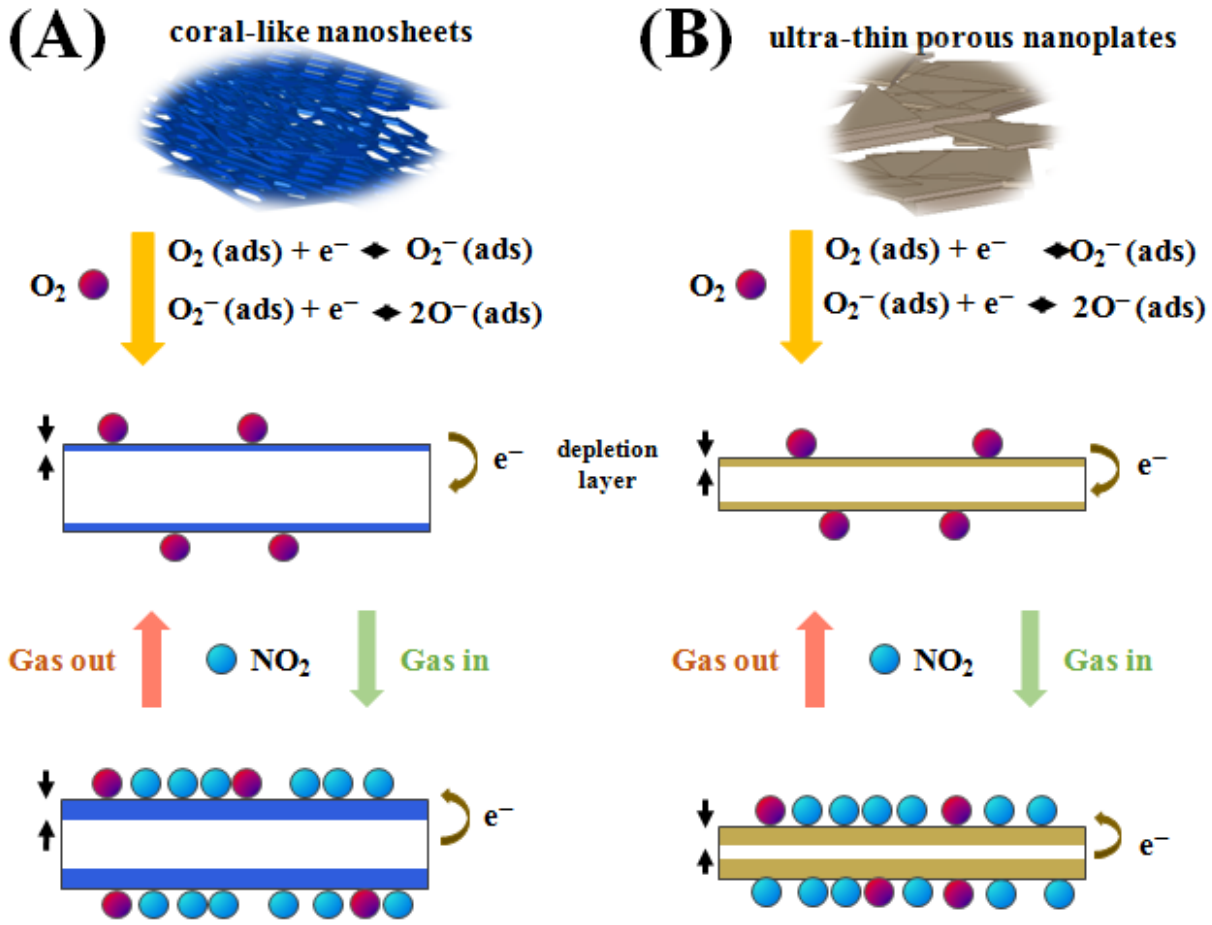

Figure 3.11 - Schematic diagram of the NO_2 gas-sensing mechanism of the ZnO coral-like nanosheets (A) and ultra-thin nanoplates (B).

3.5 Conclusion

Morphology and thickness of ZnO nanostructures were optimized for gas detection by changing only the precursor salt in a simple one-step hydrothermal process. The sensing

performance of coral-like nanosheets and ultra-thin nanoplates were compared. Thanks to their large surface and above all to their very thin thickness (15 nm), the ultra-thin nanoplates show sensing characteristics superior to those of coral-like nanosheets, with an excellent response of 76 to 0.5 ppmv of NO_2 at 200°C. The sensor also shows very low detection limit (3 ppt) and excellent selectivity (>760), showing promise for practical applications in environmental monitoring.

CHAPTER 4. ROOM TEMPERATURE AMMONIA GAS SENSOR BASED ON P-TYPE V_2O_5 NANOSHEETS TOWARDS FOOD SPOILAGE MONITORING

This chapter is based on the scientific paper [50]:

"Room Temperature Ammonia Gas Sensor Based on p-Type-like V_2O_5 Nanosheets towards Food Spoilage Monitoring", Nanomaterials, 13 (2023) 146. Doi: 10.3390/nano13010146

4.1 Abstract

Gas sensors play an important role in many areas of human life, including the monitoring of production processes, occupational safety, food quality assessment, and air pollution monitoring. Therefore, the need for gas sensors to monitor hazardous gases, such as ammonia, at low operating temperatures has become increasingly important in many fields. Sensitivity, selectivity, low cost, and ease of production are crucial characteristics for creating a capillary network of sensors for the protection of the environment and human health. However, developing gas sensors that are not only efficient but also small and inexpensive and therefore integrable into everyday life is a difficult challenge. In this paper, we report on a resistive sensor for ammonia detection based on thin V_2O_5 nanosheets operating at room temperature. The small thickness and porosity of the V_2O_5 nanosheets give the sensors good performance for sensing ammonia at room temperature (RT), with a relative change of resistance of 9.4% to 5 ppmv ammonia (NH_3) and an estimated detection limit of 0.4 ppmv. The sensor is selective with respect to the seven interferents tested; it is repeatable and stable over the long term (four months). Although V_2O_5 is generally an n-type semiconductor, in this case the nanosheets show a p-type semiconductor behavior, a tentative explanation of the sensing

mechanism is proposed. The device's performance, along with its size, low cost, and low power consumption, makes it a good candidate for monitoring freshness and spoilage along the food supply chain.

4.2 Introduction

Ammonia sensors are widely requested in different application areas, such as automobile, environmental monitoring, industrial processes, medicine, agriculture (fertilizer dosage), and food processing [51,52]. Ammonia is not a greenhouse gas, but it can indirectly contribute to greenhouse gas emissions, and cause serious health problems. According to the American Conference of Governmental Industrial Hygienists (ACGIH), the US Occupational Safety and the Health Administration (OSHA), the threshold limit values (TLVs) for NH_3 exposure are 25 ppmv [53,54].

Ammonia can be found in human breath as a result of the protein metabolism and the production of the intestinal bacteria [55]. For these reasons, it is indicated as a biomarker indicating specific diseases and health conditions such as renal failure [56], halitosis [57], hepatic encephalopathy [58], and *Helicobacter pylori* [59]. In exhaled breath, the concentration of NH_3 reaches 15 and 1.5 ppmv for end-stage renal disease patients and kidney patients, respectively, whereas its concentration is approximately 0.8 ppmv in healthy individuals [60].

Ammonia is also among the main indicators of bacterial degradation of protein-rich food (fish, poultry, and meat) [61]. For instance, NH_3 concentration produced during the de-composition of pork meat ranges from 10 to 50 ppmv [62]. The detection and monitoring of NH_3 emissions in foods enables to monitor food spoilage and to establish safe consumption. As a result, the development of sensors to detection NH_3 with high sensitivity, selectivity, rapid reaction, low detection limit at room temperature (RT) is crucial [63,64,65,66].

Resistive sensors are among the most common gas sensors. They are simple, cheap, fast, sensitive and stable, and are therefore also widely investigated for food analysis [67,68]. Nanostructured semiconducting metal oxides (SMOs) have gained great attention because of their capability to achieve the above-mentioned properties. Nanostructures of metals oxides such as SnO_2, ZnO, TiO_2, In_2O_3, Fe_2O_3, WO_3, CuO, NiO, MoO_3, and V_2O_5 with different morphologies have been prepared by different methods and used as gas sensors [69,70]. Among them, vanadium oxide draws considerable attention because of its multivalent phases and layered structure. Vanadium pentoxide (V_2O_5) is an n-type semiconductor with a bandgap in the range 2.04-2.8 eV. It shows high stability, variable oxidation states, high specific capacity, high energy density, resistivity and excellent electrical properties [71,72]. Different morphologies of V_2O_5 such as nanoparticles, nanowires, thin films, nanospheres, nanorods, nanofibers, and others have been tested as sensors for many gases such as hydrogen (H_2), ethanol (C_2H_5OH), NOx, and ammonia.

Nanomaterials with a porous structure can be easily prepared using inexpensive hydro-thermal methods with environment-friendly reagents. In particular, V_2O_5 nanostructures are characterized by a large porosity and surface-to-volume ratio that promote the diffusion of gas molecules within the sensor material improving the utilization rate of the sensor and its gas sensitivity [73].

Mounasamy et al. [74] proposed a non-invasive healthcare monitoring wearable device based on V_2O_5 nanosheets for ammonia (NH_3) detection. Surface modified poly-l-lactic acid (PLLA) substrates were used to improve the sensing performance of V_2O_5 film. The sensing mechanism of the PLLA/V_2O_5 film was related to the large specific surface formed by the molding process. The adsorption properties of V_2O_5 were exploited to develop a nanogravimetric ammonia sensors made of V_2O_5 nanoplatelets deposited onto a QCM piezoelectric transducer [75]. The physical adsorption mechanism and the V_2O_5 material's peculiar porous structure are used to explain the approach for

detecting ammonia (NH_3) using V_2O_5 platelets/QCM sensors. The rough and hydrophilic surface of the V_2O_5 thin film promotes the synthesis of additional adsorbed species, increasing the production of ammonium hydroxide (NH_4OH) and hence the sensitivity of the sensor.

In this paper, we further investigated the ammonia sensitivity of V_2O_5 being nanosheets in a resistive gas sensor obtained by hydrothermal technique followed by calcination treatment. Besides to being sensitive, the sensor also shows a good selectivity respect to a number of possible intereferents. In spite of the known n-type character of V_2O_5, the response to ammonia (an electron donor) is compatible with a p-type behaviour. It is known that a p-type material can emerge under particular growth conditions such as in hydrated amorphous V_2O_5 [76]. Here, the inversion of conductivity character is compatible with the formation of a surface inversion layer induced by molecular surface adsorption.

4.3 Materials and Methods

NH_4VO_3, Pluronic P-123, and $H_2C_2O_4$ were of analytic grade and used as received without further purification. Deionized water was used as a solvent to prepare the solution. The V_2O_5 nanosheets were synthesized by the hydrothermal method. In a typical procedure, Ammonium metavanadate (NH_4VO_3) (10 mmol) were dissolved in 30 mL of DI water and 30 mL of Ethylene glycol with stirring for 15 min. Then, Pluronic P-123 was added and stirred for 30 min. Next, add oxalic acid ($C_2H_2O_4$) (10 mmol) and continue stirring for another 15 minutes to obtain a pH of 4. The solution obtained above was transferred to a 100 ml Teflon-lined stainless-steel autoclave for the hydrothermal process, which was maintained at 200 °C for 24 h. After being gradually cooled to room temperature, the precipitate at the bottom was centrifuged and washed several times with deionized water. It was then washed twice with ethanol and collected by centrifugation at 4000 rpm. The obtained product was dried in an oven at 60 °C for 24 h and finally calcined at 500 °C for 2 h.

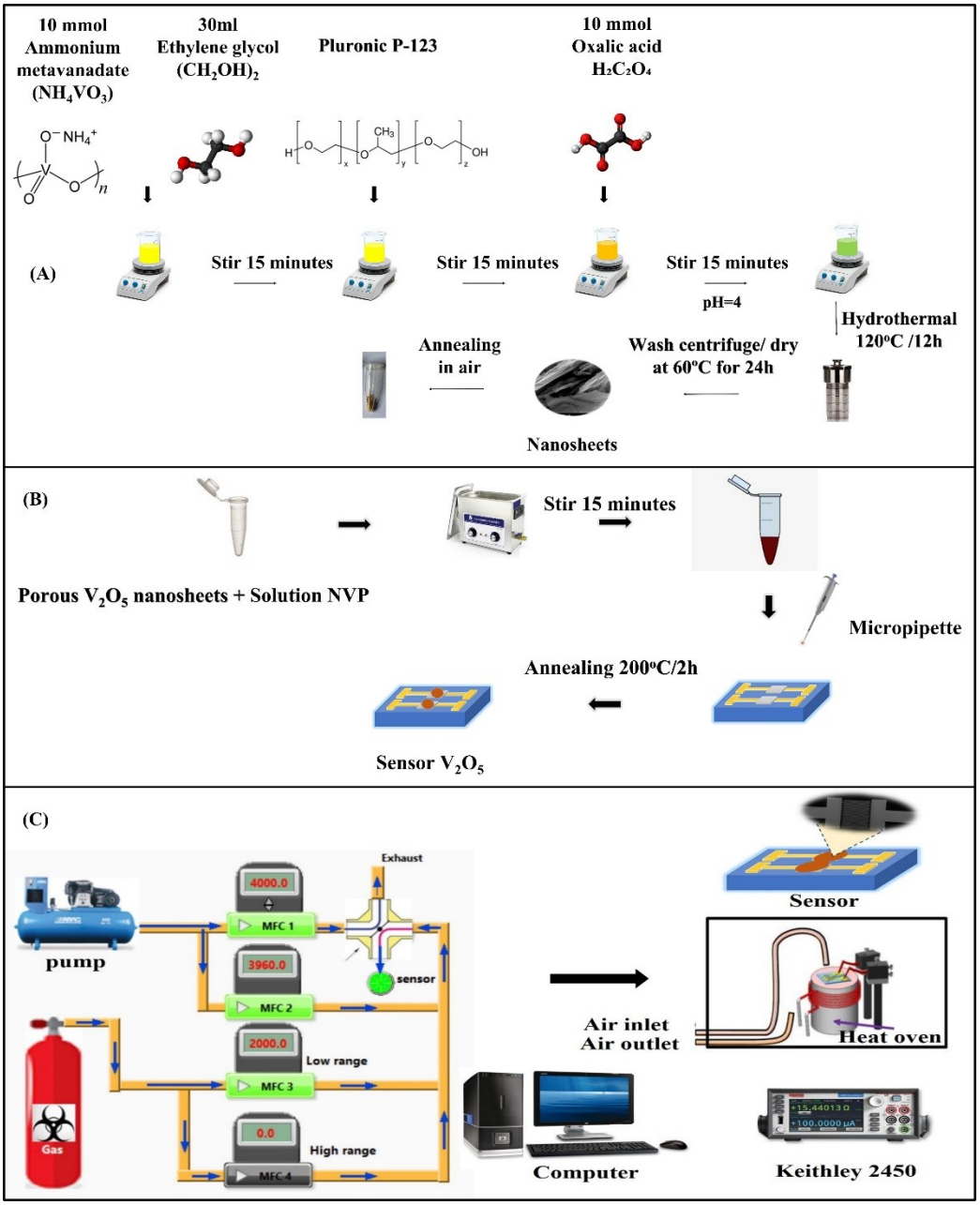

Figure 4.1 - Scheme of the deposition process of the V_2O_5 nanostructures: (A) the hydrothermal synthesis of V_2O_5 nanosheets, (B) the drop coating process of V_2O_5-based gas sensor, (C) diagram of the home-made gas measurement system.

The structure, morphology and composition of the synthesized material were characterized by field-emission scanning electron microscopy (FESEM, JEOL JSM7600F), high-resolution transmission electron microscopy (HRTEM, JSM 2100F), X-ray diffraction (XRD, D8 Advance, Bruker Corporation, Germany) with a Cu-Kα source in a 2θ range from 10° to 80°, energy-

dispersive X-ray spectroscopy (EDS)),), Raman spectroscopy (Renishaw, InVia confocal micro-Raman), thermogravimetric analysis (TGA), specific surface area are estimate with BET analysis (Micromeritics Gemini VII). The oxidation levels of the materials were investigated using X-ray photoelectron spectroscopy (XPS).

Gas sensors were prepared, as shown in Figure 4.1, by drop-casting and following literature methods [6]. V_2O_5 nanosheets were dispersed in N-vinylpyrrolidone to form a colloidal solution and then deposited on a substrate made by a silicon oxide layer of about 250 nm, on silicon. The substrate was endowed with a pair of comb-shaped interdigitated Pt electrodes fabricated by conventional UV photolithography

The sensing properties were tested using a homemade gas test station. Prior to the measurements, sensors were preheated at 500°C for 2 h to stabilize the resistance and enhance the contact between Pt electrodes and vanadium pentoxide. The sensor resistance was recorded with a source meter (Keithley 2602) as the atmosphere in the measuring chamber changed from air to analyte gas and vice versa. The limit of detection was calculated using the estimated sensitivity at the origin and the signal to noise ratio of the cur-rent signal [77].

4.4 Results and discussion

4.4.1 Morphological, compositional and structural characterization

Thermogravimetric (TGA) and differential thermal experiments (DTA) were performed in N_2 atmospheres at temperatures ranging from 20 to 950 °C to determine both the precursor breakdown temperature and the more suitable calcination temperature required to generate the V_2O_5 phase. Results are shown in Figure 4.2 where two distinct phases are identified.

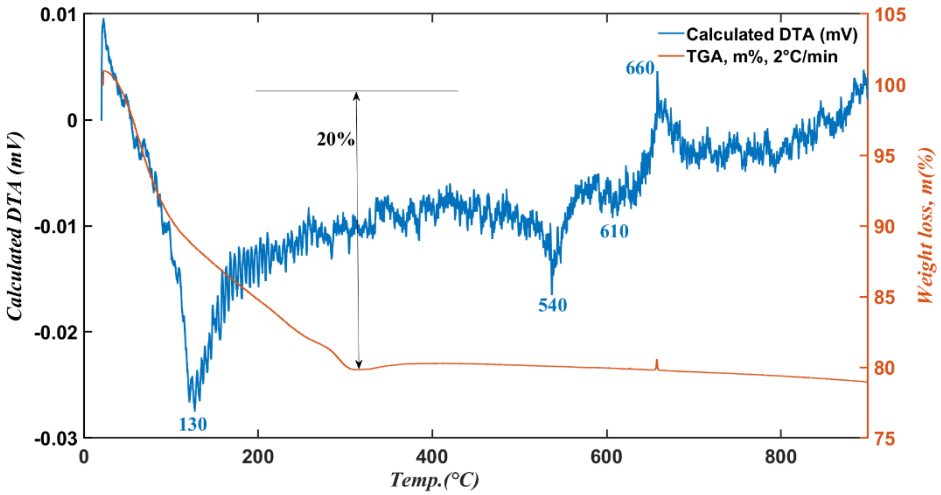

Figure 4.2 - TGA – DTG curves of V_2O_5 nanosheets.

The modest weight loss likely resulted from moisture evaporation. At the temperature of 320 °C, the TGA curve shows a large weight loss of 20 %, which is corresponding to the sharp-small endothermal peak at 130°C in the DTA curve. The endothermic peak and the related weight loss are consistent with the burning of the organic polymer component (Pluronic P123). Formation of V-O bonds was reported to happen at temperatures above 330 °C [78]. The V-O bonds are supposed to act as crystallization centers of different crystalline vanadium oxides. At temperatures above 550 °C, no additional weight loss was found since all organic material was yet destroyed at this temperature. The following increase of mass to 660 °C was most likely caused by the emergence of orthorhombic V_2O_5 [79].

The morphology of the growth material was investigated by scanning electron microscopy (SEM). SEM images, shown in Figure 4.3, were taken at low-, medium-, and high magnification. SEM images illustrate the uniform presence of wide and thin nanosheets tightly stacked parallel on top of each other. The high magnification image (Figure 4.3D) shows an average thickness of approximately 50 - 60 nm. The large surface area and the small thickness are attributed to the difference in growth rate along the different crystal orientations. The formation of stacked thin V_2O_5

nanosheets during the hydrothermal process can be described by the following reactions:

$$NH_4VO_3 \leftrightarrow NH_4^+ + VO_3^- \quad (4.1)$$

$$2VO_3 + 2H_2 \leftrightarrow V_2O_5 + H_2O \quad (4.2)$$

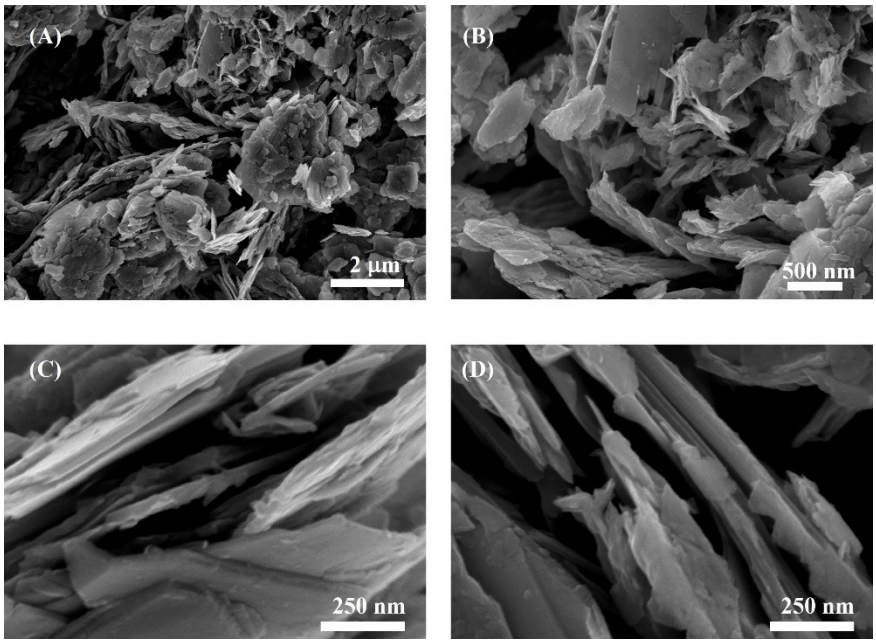

Figure 4.3 - SEM images of the grown nanostructures. A) low magnification, B) medium magnification, C, D) high magnification.

In detail, in deionized water NH_4VO_3, the precursor of vanadium, tends to dissociate into NH_4^+ and VO_3^- ions [80]. During synthesis, the production of oxalic acid increases the concentration of H^+ ions that, reacting with VO_3^- species, lead to the formation of V_2O_5. The addition of the surfactant P123 and the control of the pH value at 5 allow to optimize the formation of thin nanosheets. The resulting nanostructures are characterized by numerous active surface sites that can accelerate the adsorption of target gases.

The structure, purity, and crystalline phase of the nanostructures were investigated by X-ray diffraction analysis. The XRD diffraction patterns of the V_2O_5 nanomaterial, unannealed and

annealed at 500 °C, are shown in Figure 4.4A.

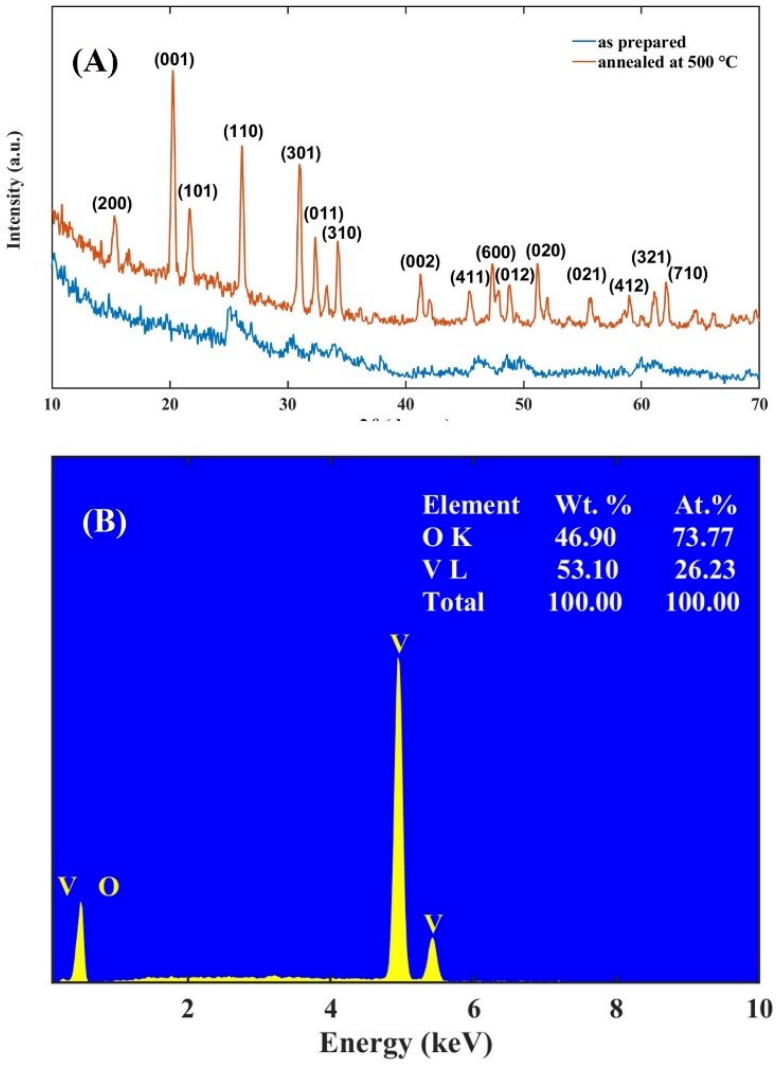

Figure 4.4 - (A) XRD spectra of as-prepared (green) and annealed at 500 °C (red) V_2O_5 nanosheets. (B) EDS spectrum and (C) EDS elemental map of annealed V_2O_5.

Before thermal treatment, the material does not show evident peaks, demonstrating that hydrothermal growth itself produces amorphous nanosheets. Interestingly, the spectrum of the nanosheets after calcination at 500 °C (red line in Figure 4.4A) shows peaks at 2θ=15.41°, 20.11°, 21.78°, 26.02°, 30.98°, 34.28°, that correspond, respectively, to the lattice planes (200), (001), (101), (110), (301), and (310) of the orthorhombic structure of V_2O_5. The diffraction peaks are in

good agreement with reference data (JCPDS 41-1426) [81,82,83]. The lack of additional peaks indicates neither contaminants nor amorphous phases affect the purity of the material [84]. XRD analysis confirms that calcinations at 500 °C is crucial to transform the hydrothermally grown material into crystalline V_2O_5 nanosheets. The crystallite size of V_2O_5 was determined by the Debye-Scherrer equation:

$$D = \frac{k \cdot \lambda}{\beta \cdot \cos \vartheta} \tag{4.3}$$

where D is the crystallite size, k is the Scherrer constant (approximately 0.89), λ is the wavelength of the incident copper radiation, β is the FWHM of the peak and ϑ is the Bragg diffraction angle (ϑ =10°-90°). From the above equation, the average crystallite size in the annealed V_2O_5 sample is 32.7 nm.

The elemental composition of the material was characterized by EDS whose results are shown in Figure 4.4B. EDS spectrum confirms that the nanosheets are composed only by V and O at weight percentages of 46.90 wt.% and 53.10 wt.%, respectively. EDS does not show additional peaks due to either impurities or contaminants. The atomic ratio between V and O is approximately 2:5, a value compatible with literature values [85]

HRTEM images of the pristine V_2O_5 nanosheets at different magnifications are shown in Figures 4.5A, B, and C. Single-crystal lattice fringes are visible in Figure 4.5C, indicating that the pristine V_2O_5 nanosheets have good crystallinity. The lattice edges of 0.34 nm can be attributed to the (110) plane of the pristine V_2O_5 crystalline orthorhombic [86,87].

Figure 4.5D shows the area selected for the electron diffraction (SAED) pattern analysis. SAED shows a uniform and well visible array of diffraction traces, indicating that the calcined nanosheets are well-crystallized. The V_2O_5 crystals in the formed nanosheets are oriented

differently, but the dissolution-recrystallization process can keep the single crystal structure intact. The observed diffraction points in the crystal correspond to the orthogonal V_2O_5 planes (101), (001), (200), (201), and (002) [88]. The elemental composition mapped in Figure 4.5E, F and G shows a homogeneous distribution of the elements V and O.

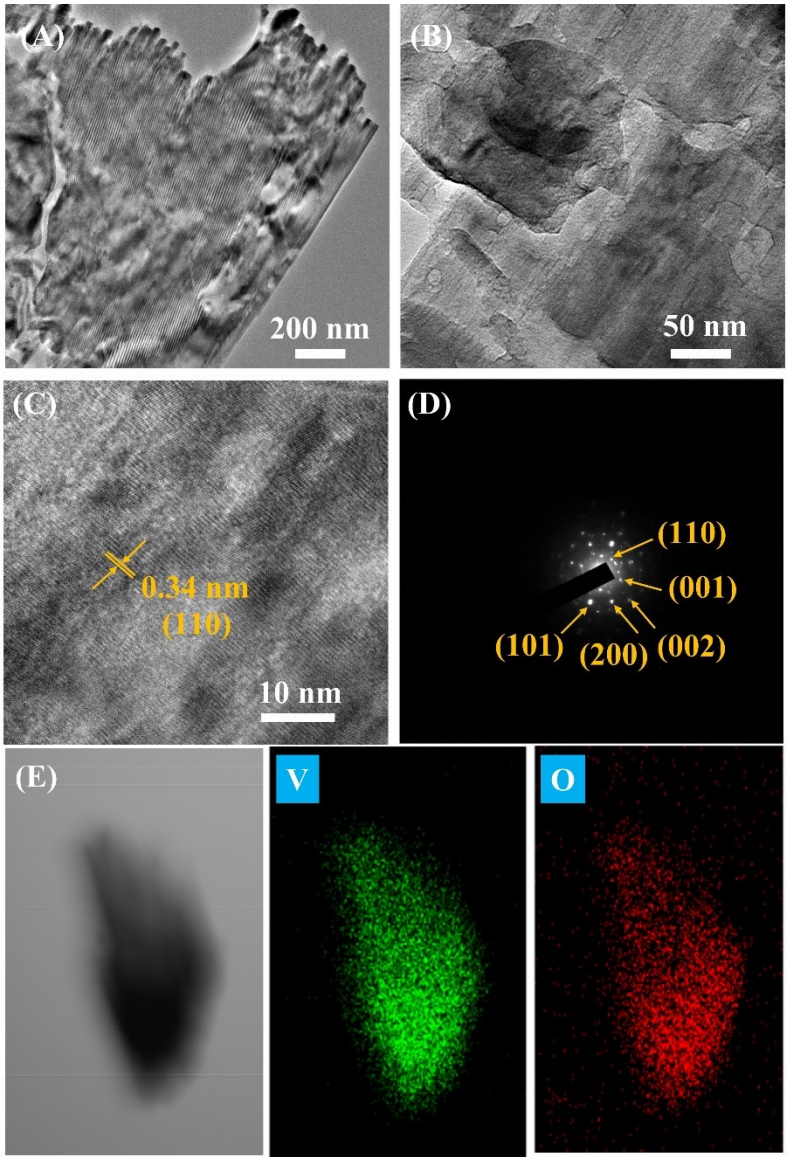

Figure 4.5 - (A-C) TEM images, (D) SEAD, and (E–G) EDS elemental mapping of annealed V_2O_5 material.

The Raman spectrum of the annealed nanomaterial is shown in Figure 4.6A. The annealed sample shows the typical crystalline peaks at 143, 196, 283, 406, 479, 526, 698, and 994 cm^{-1} [89].

The most intense peak at 143 cm^{-1} corresponds to the vibration of the V-O-V bonds. This peak is evidence of the layered structure of the V_2O_5 phase. The peaks at 283 and 406 cm^{-1} manifest the bending vibrations of the V=O bonds [90]. The peak at 479 cm^{-1} is attributed to the bending vibrations of the V-O-V bonds, whereas the peaks at 526 and 698 cm^{-1} are relative to the phonons band V_3-O. Finally, the peak at 994 cm^{-1} indicates the terminal oxygen V=O stretching mode, and confirms the crystal quality of the V_2O_5 nanosheets [91].

Figure 4.6B shows the nitrogen adsorption/desorption isotherm measured. The porous structure of the V_2O_5 nanosheets is characterized by a specific surface area S_{BET} = 4.4362 m^2/g. The material's slit distribution in the 20 - 1000 nm range exhibits a peak centered about 1000 nm compatible with the presence of multiple nano-gaps. Because the pore size has a direct influence on the diffusion rate of the gas molecules into the sensor layer. The diffusion rate may be estimated from Knudsen diffusion model:

$$D_k = 4\frac{r}{3}\sqrt{2\frac{RT}{\pi M}} \tag{4.4}$$

where D_k is the diffusion rate or constant, r is the pore size, T is the operating temperature, M is the molecular weight of the diffusing gas, and R is the universal gas constant. The diffusion rate is proportional to the slit size, thus abundances of voids and/or gap size increase are expected to enhance the gas sensitivity [92].

To understand chemical states and composition, the prepared V_2O_5 nanosheets were analyzed by XPS. Results are shown in Figure 4.7. The binding energy spectrum of V_2O_5 are depicted in Figure 4.7A where the main peaks related to vanadium and oxygen as well as sub-peak of carbon at 283 eV are visible. The Gaussian is applied to fit the XPS core levels. The core level V_{2p} and O_{1s} of XPS spectrum are shown in Figures 4.7B and C, respectively.

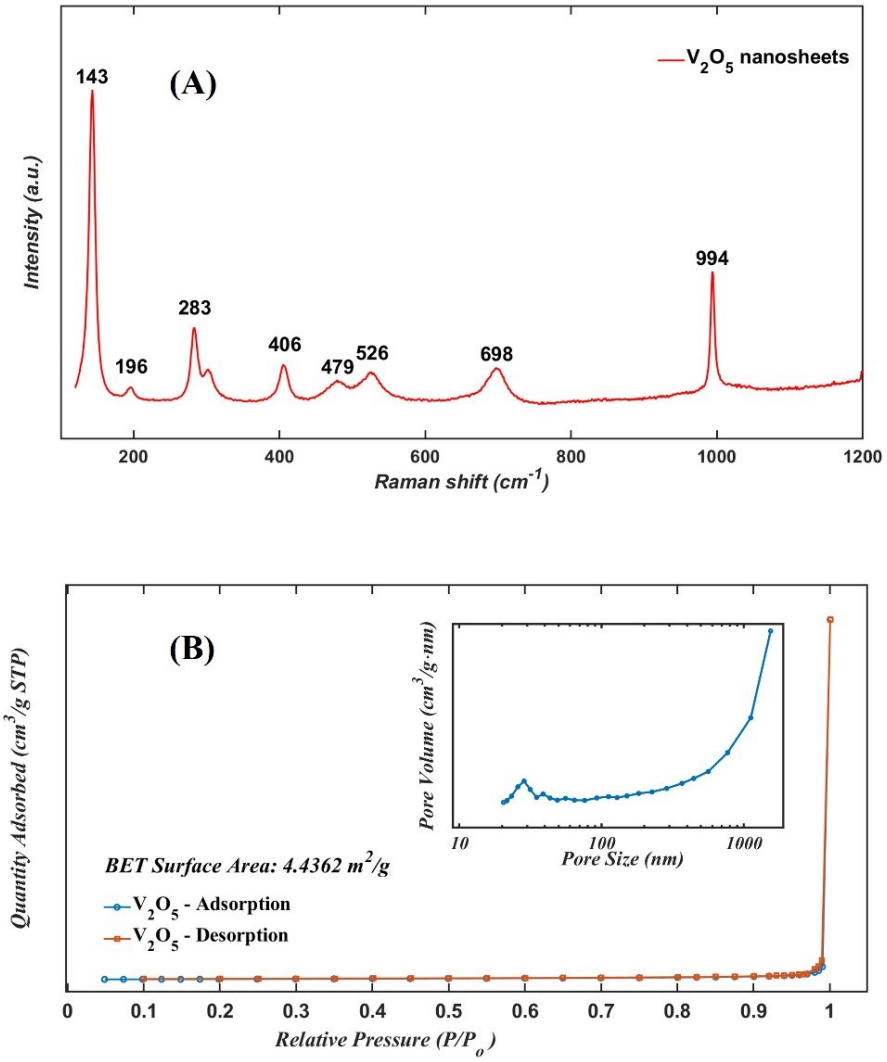

Figure 4.6 - Raman scattering and (B) BET curve of the annealed V_2O_5 nanosheets at 500 °C.

Here, there are two broad peaks centered at 516.5 eV and 523.3 eV which are associated to $V_{2p3/2}$ and $V_{2p1/2}$ doublets and corroborate to the V^{5+} oxidation state [93]. The binding energy difference of approximately 7.8 eV between $V_{2p3/2}$ and $V_{2p1/2}$ confirms the formation of orthorhombic structure. The core level of O_{1s} spectrum splits into two peaks located at 529.73 and 531.13 eV, which are attributed to O^{2-} adsorbed oxygen species at the surface of the sensing material. In particular, the peak at 529.73 eV corresponds to the bonding of O and V elements.

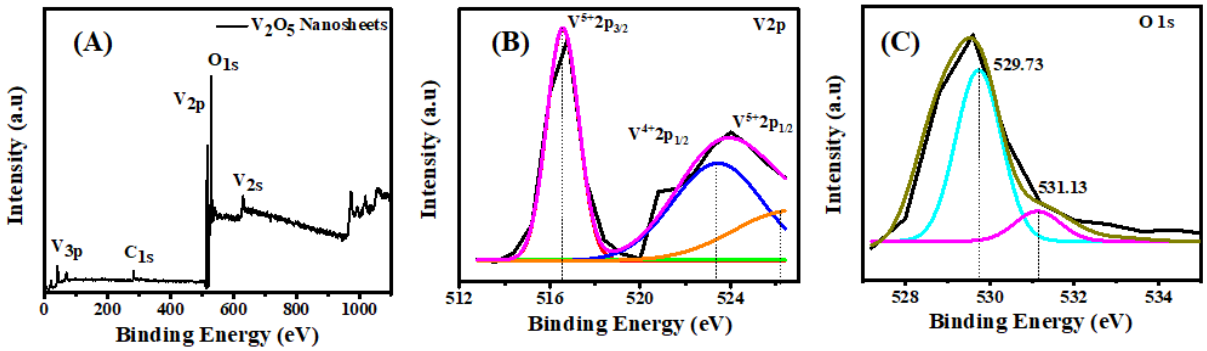

Figure 4.7 - (A) Wide bonding energy, (B) Core level V_{2p}, and (C) Core level O_{1s} of XPS spectrums of V_2O_5 nanosheets.

4.4.2 Electrical and gas sensing characteristics

The electrical properties of the sensor were analyzed, measuring the I-V curve in the range from -2 V to 2. Figure 4.8A shows the I-V curves in nitrogen and at different temperatures, from room temperature to 300°C. The linear I-V curve indicates the ohmic contact between V_2O_5 and Pt electrodes. The material shows the typical negative temperature coefficient of semiconductors. Figure 4.8B shows the corresponding Arrhenius plot of the conductance. The relationship between conductance and temperature is defined by an activation energy (E_a), i.e. the minimum energy required to promote the charge carriers [94].

$$\ln(G) = -\frac{E_a}{k_B} \cdot \frac{1}{T} + ln(G_0) \qquad (4.5)$$

where G is the conductance, k_B is the Boltzmann constant and T is the temperature. Fitting the plot in figure 4.8B returns an estimated activation energy of 0.26 ± 0.01 eV compatible with the literature values of the band gap [72].

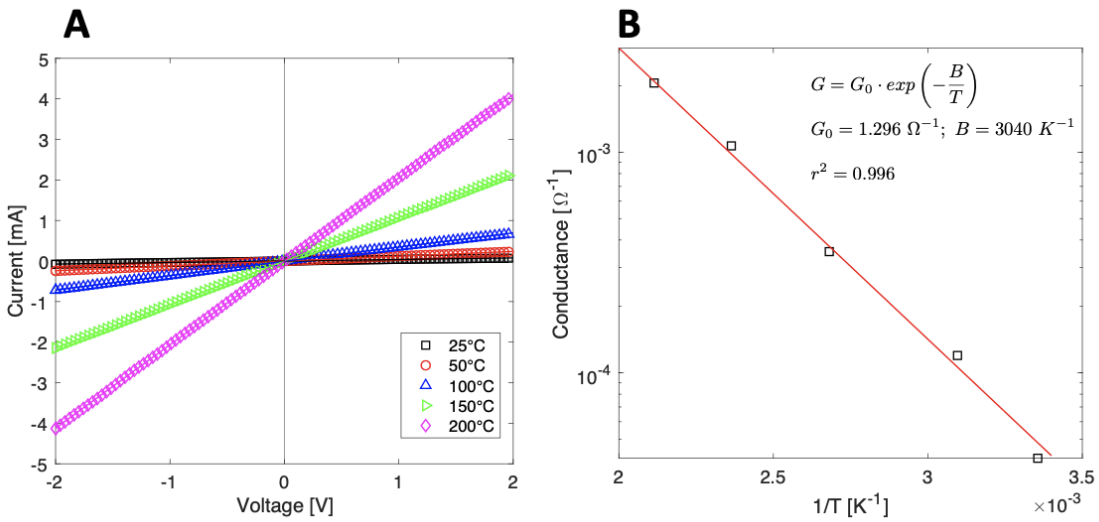

Figure 4.8 - (A) I–V curves at V_2O_5 nanosheets measured at different working temperatures, (B) Arrhenius plot: conductance vs. the inverse of temperature fitted by an exponential function.

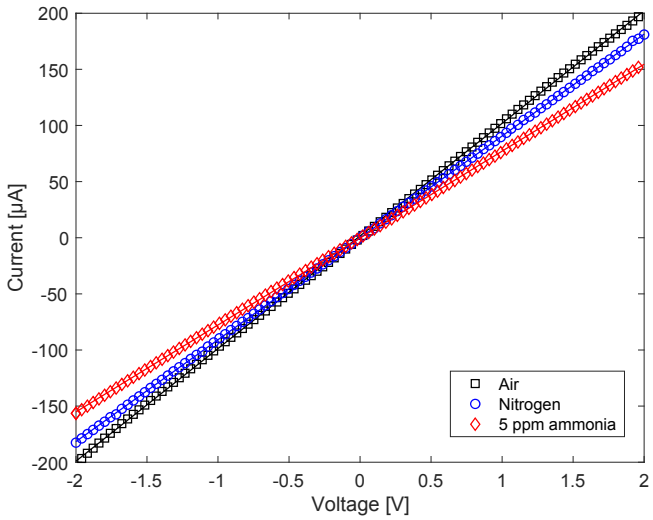

Figure 4.9 - I–V curves of the V_2O_5 nanosheets in air, in pure nitrogen, and 5 ppmv of ammonia in air.

The effects of gas have been studied measuring, at room temperature, the. I-V curve exposing to air, nitrogen, and 5 ppmv of ammonia in nitrogen. Tre three curves are shown in Figure 4.9, the I-V curve reveals that the conductivity decreases from air to nitrogen and further decreases adding ammonia to air. Considering the electron acceptor character of oxygen and water, and electron donor character of ammonia, this behaviour is compatible with a p-type semiconductor. This result

is surprising because V_2O_5 is known to be an n-type semiconductor. Change of conductivity character have been previously found in hydrated amorphous materials [76] but in this case it seems to be induced by the adsorption of gases. A full explanation of the change of character is out of the scope of this paper, and it will require deeper experimental and theoretical studies. Here, we may surmise that it might be elicited by the surface depletion of electrons. In detail, when the sensor is exposed to air the adsorbed oxygen and water molecules are expected to act as electron acceptors. Thus, the adsorption of oxygen and water should produce an upward band bending at the surface corresponding to a region depleted by electrons but at the same time enriched of holes. The conductivity, respect to nitrogen, increases, as expected in a p-type semiconductor. Such a phenomenon is emphasized in a nanometric material where the surface dominates over the bulk.

When the sensor operates at low temperatures, the oxygen species generate dominantly on the surface of V_2O_5 nanosheets is O_2^- instead of O^- ion. The p-type behavior was again observed by the exposure to NH_3, a reducing gas. The sensing mechanism is suggested as in Fig. 4.10. The initial n-type V_2O_5 adsorbs oxygen molecules forming negative ions and radicals on the surface. This layer will repel the electrons and attract the holes to form a hole accumulation region (Fig. 4.10B). At a certain condition, this hole accumulation layer would mainly contribute to the material conduction and make it behave as a p-type semiconductor. With the injection of NH_3 molecules, it possibly occurs a reaction between NH_3 and O_2^- on material surface and releases back electrons to the material leading to the descent of hole concentration via the electrons-holes recombination:

$$4\ NH_3 + 3\ O_2^- \leftrightarrow 2\ N_2 + 6\ H_2O + 3\ e^- \qquad (4.6)$$

Thus, the density of absorbed O_2^- decreases and downwards the energy band bending as in Fig. 4.10(C). As a result, the sensor resistance increases with the injection of NH_3 gas.

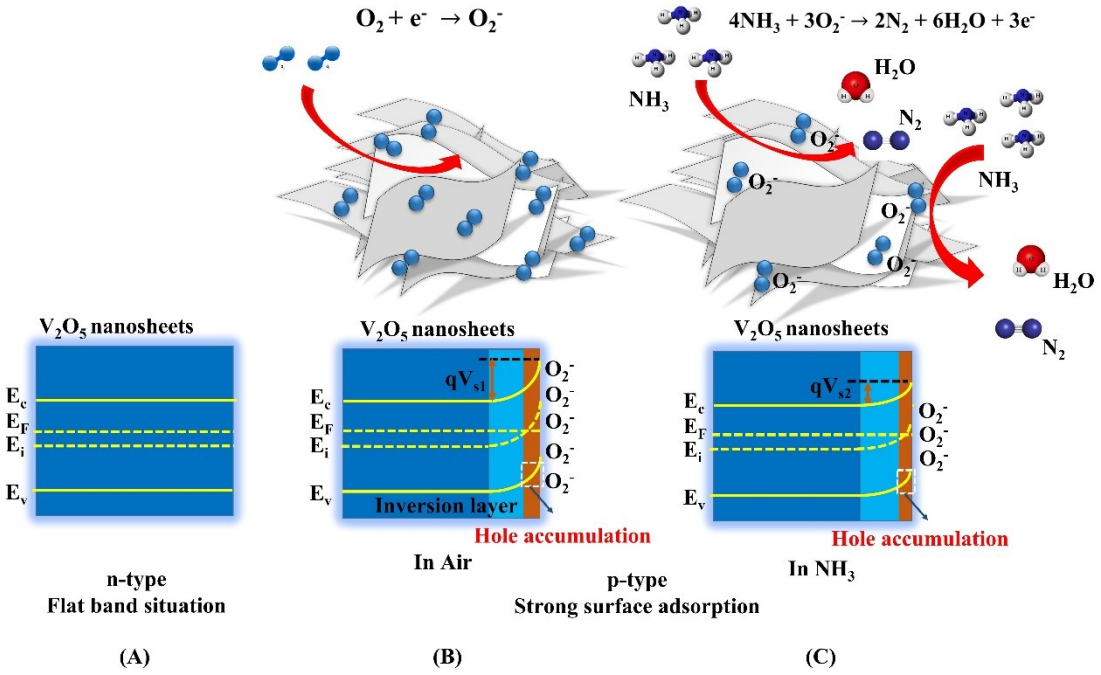

Figure 4.10 - The schematic energy band diagrams of V_2O_5 nanosheets in pure state (A); strong oxygen surface adsorption in air (B); and in ammonia gas injection (C).

In most metal oxide semiconductor gas sensors, the sensitivity is activated at high temperature, with the obvious drawback of excessive power consumption and the necessity to maintain stable the sensor temperature. Respect to this general trend, V_2O_5 nanosheets are sensitive at room temperature. The sensor sensitivity to ammonia has been tested at room temperature and at 45% of relative humidity. The sensor was exposed to pulses of concentrations of ammonia in the range 5 – 500 ppmv in air. Each pulse of ammonia lasted for 200 s and it was followed by an exposure to air for 800 s to recover the initial baseline.

The dynamics of the resistance of the sensor to the sequence of concentration pulses is shown in Figure 4.11A. As previously mentioned, the resistance increases with the concentration of ammonia. Figure 4.11B shows the response of the sensor versus the ammonia concentration. The sensor response is calculated as the relative change of the resistance:

$$\frac{R_g - R_a}{R_a} 100\% \qquad (4.7)$$

where R_a and R_g are measured before and at the end of the exposure to ammonia respectively.

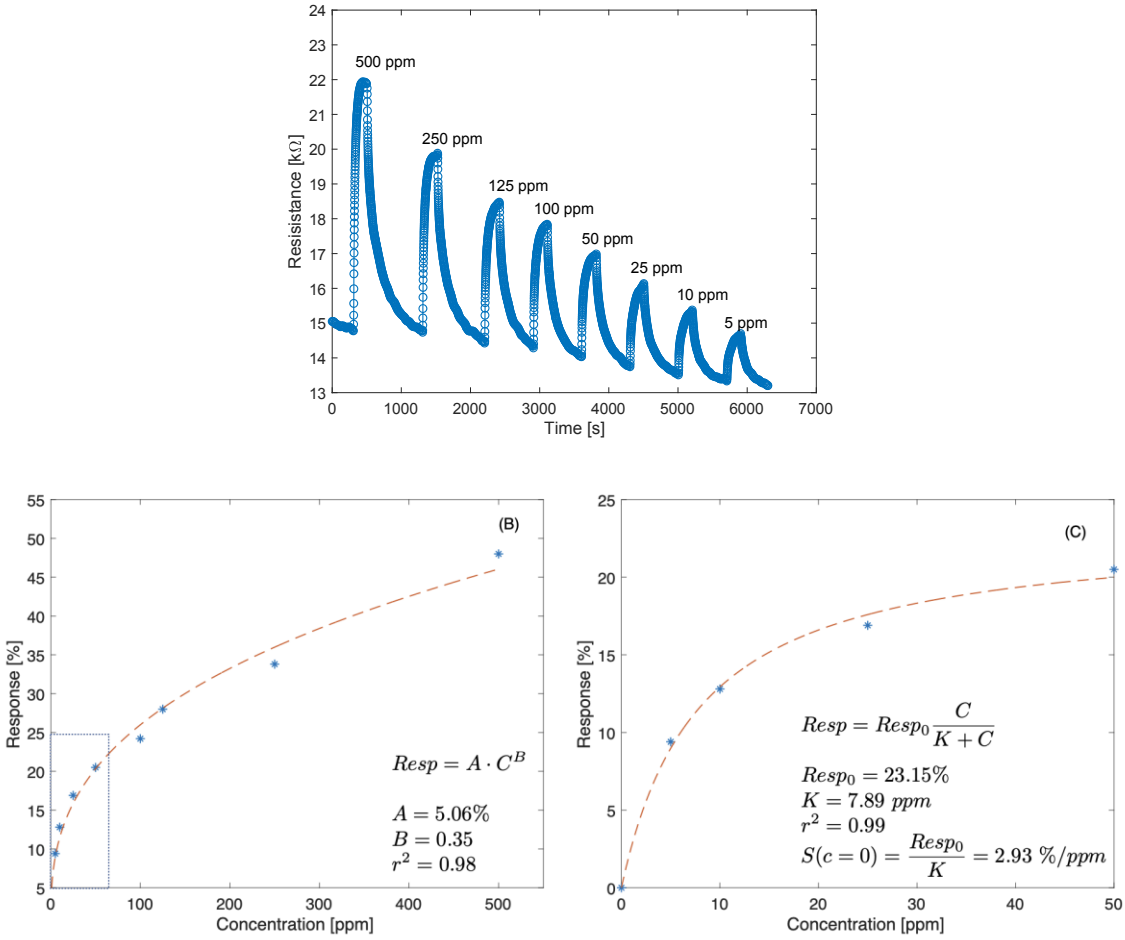

Figure 4.11 - (A) Dynamic behaviour of the resistance of the sensor at room temperature and 45% of relative humidity towards different NH_3 concentrations, (B) sensor response curve as a function of the ammonia concentration. Freundlich isotherm fit is also shown. (C) Sensor response in the range 0 -50 ppmv of ammonia fitted by a Langmuir isotherm function. The sensitivity at the origin is calculated as the derivative of the Langmuir function in c=0 ppmv.

The response curve is fitted by the Freundlich power-law isotherm. Freundlich isotherm accounts for the response in the whole range of concentrations. However, since the slope (the sensitivity) of the Freundlich isotherm at the origin is infinite, it is not adequate to represent the

sensor behavior in the low concentration range. The response at concentrations smaller than 50 ppmv is better fitted by Langmuir isotherm (see Fig 4.10C). The deviation at high concentration from the Langmuir behaviour suggests the presence of a low density of high affinity adsorption sites.

The limit of detection for ammonia was calculated as the ratio between the inverse of the signal to noise ratio and the sensitivity in the origin. The sensitivity at the origin, estimated from the Langmuir function, is about 2.9 %/ppmv. The signal to noise ratio is calculated in steady-state condition as the ratio of the mean of the current divided by three times its standard deviation. The measured signal to noise ratio is of the order of 50. Thus, the estimated limit of detection is of the order to 0.4 ppmv. Such a value is sufficient for most of medical and food quality monitoring applications.

In terms of practical applications (for example in the detection of spoilage of meats or fishes), selectivity plays a fundamental role in correctly interpreting the sensor signals. To investigate the selectivity, the sensor was exposed to 500 ppmv of NH_3, and at 500 ppmv of the following interferent compounds: trimethylamine, toluene, isopropyl alcohol, acetone, ethanol, methanol, and ethylene. The comparison of the sensor responses to the different gases is shown in Figure 4.12. The relative resistance variation to NH_3 is three times larger with respect to ethylene, and between 5- and 7-times larger with respect to the other volatile compounds. It is worth mentioning that in most applications the concentration of ethylene is much smaller than 500 ppmv. The selectivity behavior suggests the high affinity between the ammonia and the active V_2O_5 sites [95].

An additional interferent to be considered is the humidity whose presence is ubiquitous in particular in foods and breath. The effect of humidity has been tested measuring the response to 500 ppmv of ammonia and variable relative humidity in the range 45% - 95% (Fig. 4.13A).

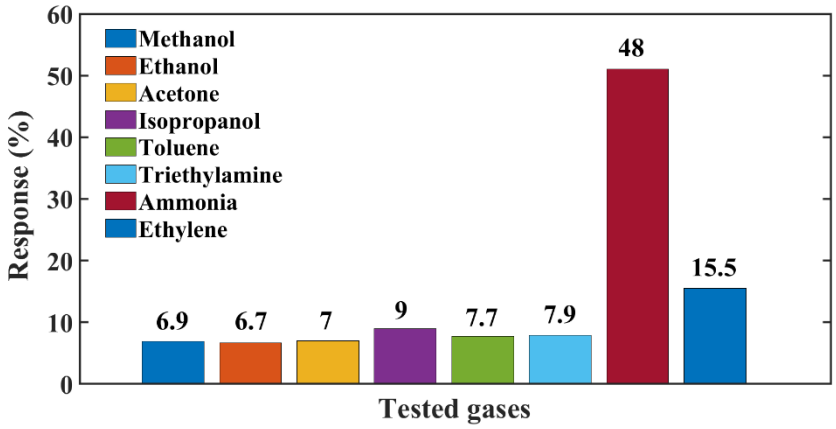

Figure 4.12 - Comparison of the responses of the sensor to the various gases.

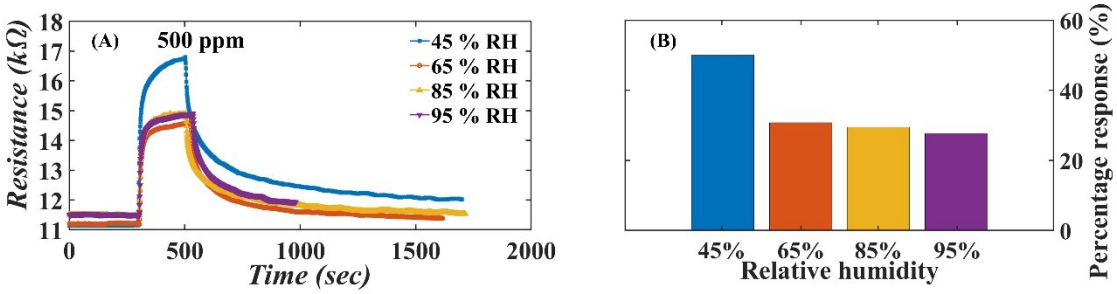

Figure 4.13 - (A) Dynamic resistance of the sensor under different humidity conditions, (B) response of the sensor to varying relative humidity.

As shown in Fig. 4.13B, the response to ammonia is larger at the smaller tested humidity while at RH larger than 65% the response to ammonia drops from 50% to 30% but it be-comes almost insensitive to further increase of humidity. The decrease of response in presence of humidity suggests that the adsorbed water molecules compete with ammonia in occupying the adsorption sites.

Other important parameters to ensure the accuracy of the sensor in real-time monitoring are the repeatability and the stability of the sensor response. The repeatability and stability were

evaluated by measuring at distance of four months the response of the same sensor to repeated cycles of 100 ppmv of ammonia in 45% of relative humidity. Results are shown in Figures 4.14A and B. In spite of the drift of resistance baseline, the relative response of the sensors is still comparable. Figure 4.14C shows the distributions of the repeated responses at four months of distance. The stability of sensor response can be appreciated calculating the ANOVA of the two distributions. Results indicate that the response to the same stimulus remain statistically undistinguishable (p-value=0.22).

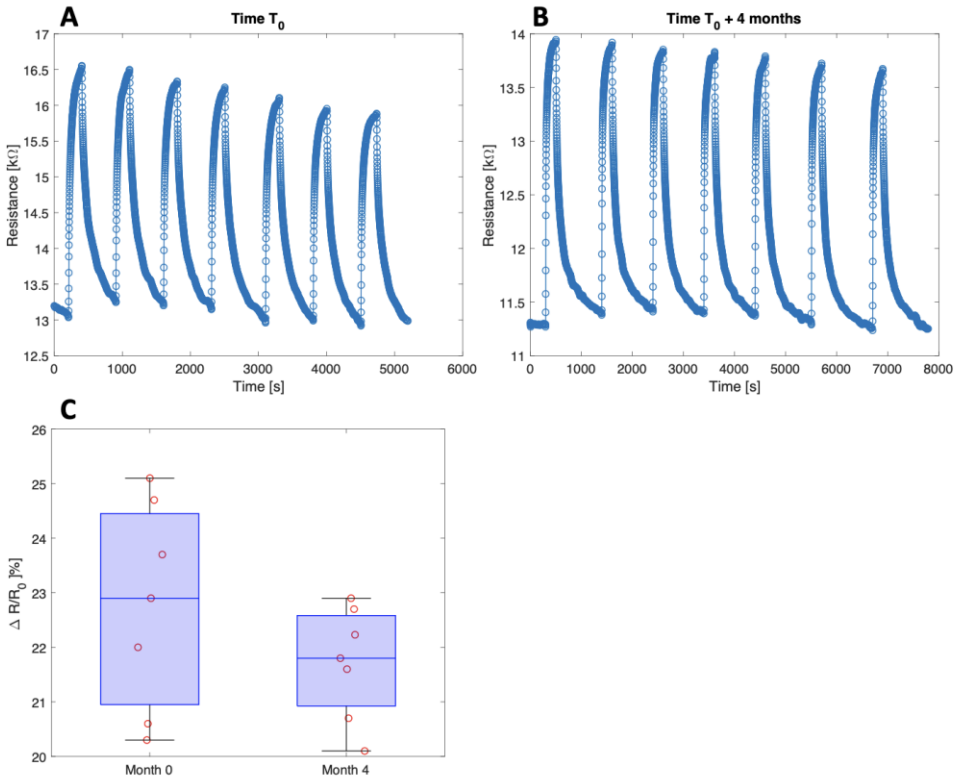

Figure 4.14 - Repeatability and stability tests. (A) Sensor resistance under consecutive exposures to 100 ppmv of ammonia and 45% of relative humidity, (B) same measurement repeated four months later. (C) Comparison of sensor responses.

A comparison with recent results reported in the scientific literature with chemoresistive sensors based on pristine and composite V_2O_5 nanostructures is summarized in Table 1. V_2O_5-based resistive sensors, grown by different methods and with different morphologies, have been tested to

detect various gases such as NO_2, xylene, ethanol, butylamine, acetone, trimethylamine (TMA), and ammonia. Table 1 indicates that vanadium pentoxide-based sensors are mostly used at high temperatures, in the range 200°C - 300°C.

Table 4.1 - Performance comparison of V_2O_5 nanostructures as gas sensors in recent scientific literature.

Material	Method	Gases	Conc. (ppmv)	Response	Temp. (°C)	Ref.
SnO_2@ V_2O_5	ALD	NO_2	100	2.5 [a]	250	[96]
V_2O_5 Flower-like	Hydrothermal	Xylene	100	2.2 [b]	300	[93]
V_2O_5 nanosphere	Solvothermal	Xylene	100	2.757 [b]	290	[97]
V_2O_5 nanorods	Hydrothermal	C_2H_5OH	3000	13.3 % [c]	100	[98]
V_2O_5 thin film	Chemical spray	NO_2	100	20.3 % [d]	200	[99]
V_2O_5 nanofibers	Spray pyrolysis	Xylene	100	27 [b]	RT	[100]
V_2O_5@TiO_2 core-shell	Sol-gel	NH_3	100	8 [b]	365	[101]
V_2O_5 hierarchical	Hydrothermal	1-butylamine	100	2.6 [b]	140	[102]
MoO_3-V_2O_5	Spray pyrolysis	NO_2	100	80 % [d]	200	[103]
V_2O_5 flower-like	Hydrothermal	TMA	5	2.25 [b]	200	[81]
3.5% Au/V_2O_5 microflowers	in-situ reduction and thermal oxidization	1-butylamine	100	7.3 [b]	240	[104]
V_2O_5/CuO nanostructures	Electrospinning	Acetone	500	8.8 [b]	440	[105]
2 wt% Sn doped V_2O_5		NH_3	50	77.84%[c]	RT	[72]
V_2O_5/PVP	Electrospinning	NH_3	0.6	6%[e]	260	[106]
V_2O_5 Fibers	Sol–gel	NH_3	2.1	11%[e]	200	[107]
V_2O_5 Films	RF sputtering	NH_3	75	17[b]		[74]
V_2O_5 nanosheets	Hydrothermal	NH_3	100	24.2%[d]	RT	This work

[a] Response defined as R_g/R_a; [b] Response defined as R_a/R_g; [c] Response defined as $(I_{gas} - I_{air})/I_{air}$ x 100%; [d] Response defined as $(R_{gas} - R_{air})/R_{air}$ x100%.

4.5 Conclusions

Nanostructured V_2O_5 was prepared with an ecologically compatible hydrothermal meth-od followed by a heat treatment at 500°C in air. Thanks to the morphology of very thin nanosheets stacked parallel, the material has a high surface/volume ratio. The V_2O_5 nanosheets show p-type semiconductor character, probably due to the growth process and to the peculiar morphology. The

resistive sensor based on the V_2O_5 nanosheets works at room temperature showing high sensitivity and a low limit of detection towards ammonia, a typical gas generated, for instance, by the bacterial spoilage of food products. The sensor also exhibits high selectivity with respect to interfering gases such as methanol, ethanol, acetone, isopropanol, toluene, trimethylamine, good repeatability and good long-term stability. The performance of the chemosensor, together with its simplicity and cost-effectiveness, make it a candidate for real-time monitoring of ammonia for instance in breath and in food along the production and distribution chain.

CHAPTER 5. ELECTRONIC NOSES BASED ON METAL OXIDE NANOWIRES: A REVIEW

This chapter is based on the scientific paper [108]:

"Electronic noses based on metal oxide nanowires: A review", Nanotechnology Reviews, 11 (2022) 897–925. Doi: 10.1515/ntrev-2022-0056

5.1 Abstract.

Metal oxides are ideal for the fabrication of gas sensors: they are sensitive to many gases while allowing the device to be simple, tiny and inexpensive. Nonetheless, their lack of selectivity remains a limitation. In order to achieve good selectivity in applications with many possible interfering gases, the sensors are inserted into an *electronic nose* that combines the signals from non-selective sensors and analyzes them with multivariate statistical algorithms in order to obtain selectivity.

This review analyzes the scientific articles published in the last decade regarding electronic noses based on metal oxide nanowires. After a general introduction, section 2 discussed the issues related to poor intrinsic selectivity. Section 3 briefly reviews the main algorithms that have hitherto been used and the results they can provide. Section 4 classifies recent literature into fundamental research, agrifood, health, security. In section 5 the literature is analyzed regarding the metal oxides, the surface decoration nanoparticles, the features that differentiate the sensors in a given array, the application for which the device was developed, the algorithm used and what type of information was obtained. Section 6 concludes by discussing the present state and points out the requirements

for their use in real world applications.

5.2 1. Introduction

Recently, gas sensors are increasingly needed in many areas of human life, from monitoring indoor and outdoor air quality, industrial processes, food quality and even to carry out non-invasive diagnostic screening. The importance of the gaseous component in human life is confirmed by the scientific interest, which has increased a lot over the years from the beginning of the 70s to today. A search for "gas sensors" in Scopus (Fig. 5.1a) shows that the first article on this topic was published in 1969, while 12,420 were published last year. The plot shows that the growth is remarkable and constant [109]. Interest gradually increased from the 1970s to the mid-2000s, and then escalated more rapidly. The advent of nanotubes and nanowires, with the concurrent increase in performance, could be the driving force of this growing attention. In fact, the scientific articles that study nanowire-based gas sensors are more than a quarter of the total, and as can be seen in Fig. 5.1b they too are constantly growing [109].

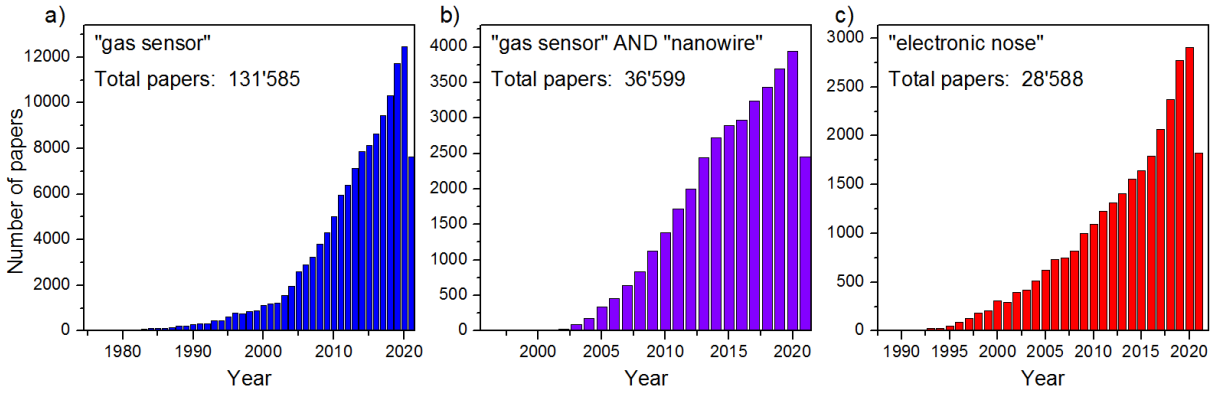

Figure 5.1 – Fig. 1: Trend in the number of scientific articles per year found searching for a) "gas sensor", b) "gas sensor AND nanowire", and c) "electronic nose" on Scopus [109].

This review focuses on electronic noses based on metal oxide nanowires, since metal oxide semiconductors are the most used materials for solid state gas sensors and nanowires, with their very high surface/volume ratio reach unthinkable performance for previous generations (thick and thin

films). Resistive sensors based on metal oxide nanowires are indeed ideal in many respects, as they are tiny and light, cheap to manufacture and operate, and sensitive to most gases and volatiles. The latter property is double-edged, since sensitivity to almost any gas means at the same time a lack of selectivity. Overcoming the lack of selectivity of semiconductor chemoresistors, inherent in any device with a one-dimensional output signal, is the main challenge to make these devices ideal for widespread use in many fields of application. In practice, any sensor that has a single value as its output (usually a ratio between a physical quantity in the presence and absence of the target gas) is inherently non-selective. In the case of resistive sensors, the response is usually defined as the ratio between the resistance of the sensor in the presence of the target gas (R_G) and its resistance in air (R_A): R_G / R_A.

The selectivity of these sensors is limited to distinguishing the two large families of gases: oxidizing and reducing gases, since in one case the resistance increases and in the other it decreases, and therefore the response will be higher or lower than 1.

For this reason, the most common approach to obtain selective devices is to combine different resistive sensors in an array and study their responses together, in order to recognize the typical trends of the various gases. These instruments have taken the name of *electronic noses* because they replicate the pattern of operation inside the nose of mammals. Also in the case of animals, the responses of non-selective or partially selective receptors are combined and processed in order to associate typical patterns to different volatile compounds. In a similar fashion, an electronic nose achieves a certain capability to recognize different gases and estimate their concentration (usually after a calibration or "training" phase) combining the response of sensors with a much poorer selectivity). As can be seen in Fig. 5.1c, the interest in electronic noses started in the 90s and continues to grow, almost exponentially [109]. Although the interest is extensive, both scientific and

economic, these devices still have limited applications, and the advancement of machine learning will certainly support their success.

Despite the strong interest in both nanowire-based gas sensors and electronic noses, scientific papers studying nanowire-based electronic noses are still very few. This can be explained by the fact that nanowires have better performance than previous generations (thin films) but also lower stability and reliability over time, and are therefore less mature for practical applications. Alternatively, the reason can be the multidisciplinarity necessary for this type of tool, which combines the latest developments in nanoscience and nanotechnology and machine learning. This requires strong collaboration between groups with very different expertise and can initially slow down the growth of the sector.

In this review we analyze the recent relevant scientific literature, trying to understand how mature the field is and what are the bottlenecks that limit its development. The analysis of the published articles shows that the development obtained by nanosciences in controlling the structural, morphological and compositional properties of nanomaterials is not matched by the computer processing counterpart. For this reason, the review focuses on the "brains" used so far for electronic noses based on metal oxide nanowires, and on the type of information obtained from them. In fact, the "brain" of the electronic noses, or rather the approach to data mining or data visualization, is the key component that determines its performance.

As will become clear in the following sections, case studies from the literature use very different approaches to the evaluation of sensor performances, from simple visual inspection of the data to advanced data mining methods, with their merits and drawbacks. A critical review of these studies with a focus on misconception and real application needs, seems important to support a better comparison of the reported performances and a more efficient a development of electronic

noses based on nanowires. We think that such an analysis can support groups working on chemosensors on their way for the realization of successful electronic noses by indicating possible strategies and achievable results.

5.3 Intrinsic selectivity

Metal oxides have been shown to be excellent gas detection materials since the 1960s [110]. Technological development has made it possible to move from thick films to thin films and then to nanostructured materials. Nanostructures, including nanowires, are characterized by having an enormous surface/volume ratio, and therefore the effect of the depletion that occurs at the surface is much more intense. Unfortunately, together with many advantages, these materials also carry two major defects: high working temperature and low selectivity. Working temperature is a minor problem that was initially solved with integrated microheaters and recently addressed with surface decoration. The surface of the MOs nanostructures is decorated with metal nanoparticles or other MOs, in order to exploit the spillover effect, the catalysis and the additional junctions created at the interfaces between the two materials. Surface decoration is commonly used to increase the response and lower the working temperature of sensors [111]. The increase in the response and the lowering of the working temperature are reproducible effects, but the influence on the other performance parameters, including selectivity, is still not yet clear because the contradictory indications of the literature that make it difficult to identify clear trends [112]. Tshabalala et al. investigated how the sensing mechanisms change with temperature [113] by photoluminescence and X-ray photoelectron spectroscopy. They were able to demonstrate that the selective response of the TiO_2 nanowire-based sensor to C_7H_{10} at 23°C is defect-dependent, while the selective response to C_8H_{10} at 150°C was not defect-dependent. This demonstrates that among the many reactions that take place at the gas-solid

interface, the main sensing mechanism can vary significantly also as a function of temperature, leading to selectivity towards different gases as the temperature varies. Similar behaviors (selectivity varying by changing the working temperature) were also observed by Kim et al. [114] towards C_7H_{10} and C_7H_8 using NiO at 350 and 400°C, and by Motsoeneng et al. [115] towards C_3H_7OH and C_2H_5OH using SnO_2 at 75 and 150°C. Kim et al. explained that the tuning of selectivity to p-xylene at 350°C or to toluene at 400°C was achieved by controlling the balance between catalytic promotion of the gas in more active species and the oxidation in less reactive species depending on the temperature of exercise [114]. Motsoeneng et al. showed that the selectivity towards different gases depends both on the morphology of the nanostructures and on the working temperature. Also in this case PL and XPS confirmed that the density of defects in nanostructures depends on their morphology, and influences the response of the sensor [115]. As can be seen, there are various detection mechanisms that often act simultaneously and, although they are being studied, unfortunately the results obtained do not yet paint a homogeneous picture. The importance of the dimensions of the nanomaterial is well established, since the response of the sensor depends on the thickness of the depletion layer (which is fixed) in relation to the thickness of the nanostructure. For this reason thin films perform much better than thick films, and the new 2D materials promise further improvement [116]. The modulation mechanism of the depletion layer is accepted as the source of the electrical response of the sensor and studied extensively. By approximating the bending of the bands with a simple step function, it can be seen that as the thickness of the nanowire decreases closer to the depth of the depletion layer, the more the sensor response increases [117].

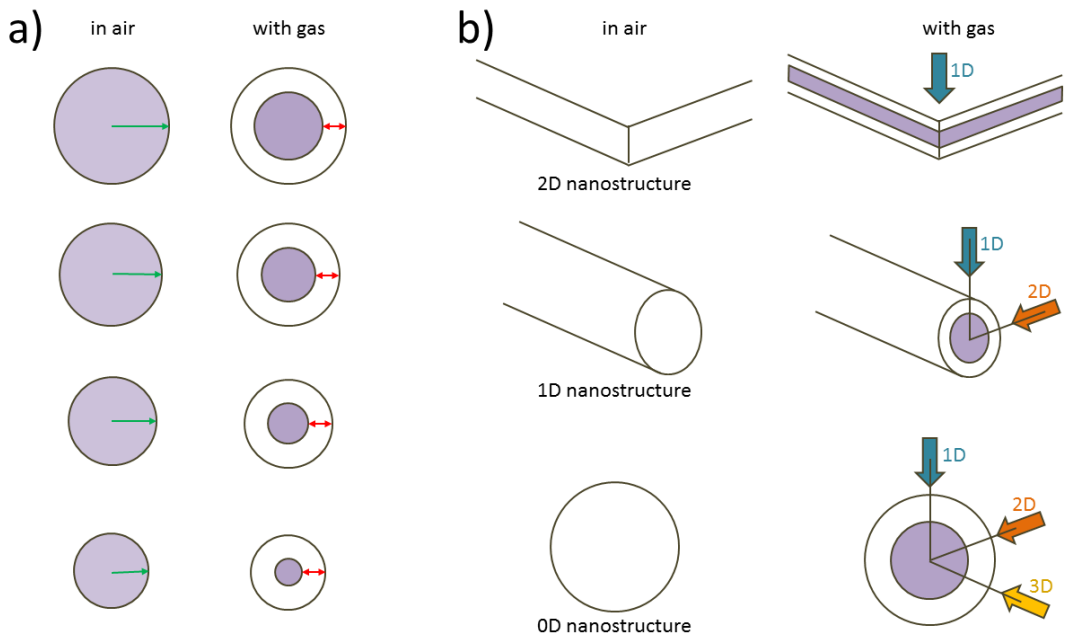

Figure 5.2 – (a) section of a nanowire in air and in the presence of gas. The white annular section is the depletion layer, while the purple colored part contributes to the signal; (b) the modulation of the depletion layer acts on the number of nanometric dimensions.

Fig. 5.2a shows the section of a semiconductor metal oxide nanowire in air (left column) and in the presence of gas (right column). Since the depth of the depletion layer is constant (red arrow), as the radius of the nanowire (green arrow) decreases, the sensor response (ratio between the purple circle on the left and the one on the right) increases. Liu et al. demonstrated that the sensor response reaches its maximum peak when the thickness of the nanostructure equals the depletion layer [118]. Fig. 5.2b illustrates how the effect of the modulation mechanism of the depletion layer differs as the dimensionality of the nanostructures varies. The mechanism acts in a non-negligible way only on the nanometric dimensions of the material, and therefore a 2D structure (a thin plate) will be depleted only in one dimension, while a 1D nanowire will be depleted in two dimensions and a 0D nanoparticle in all three dimensions [119]. The main problem with metal oxides therefore remains selectivity. Many groups work on resistive gas sensors based on different metal oxides, both n-type and p-type, but the results in the literature regarding selectivity are rarely in agreement. In order to

assess whether there is agreement about the selectivity of the main metal oxides towards specific gases, we have carried out a survey of the recent scientific literature, which is shown in Fig. 5.3.

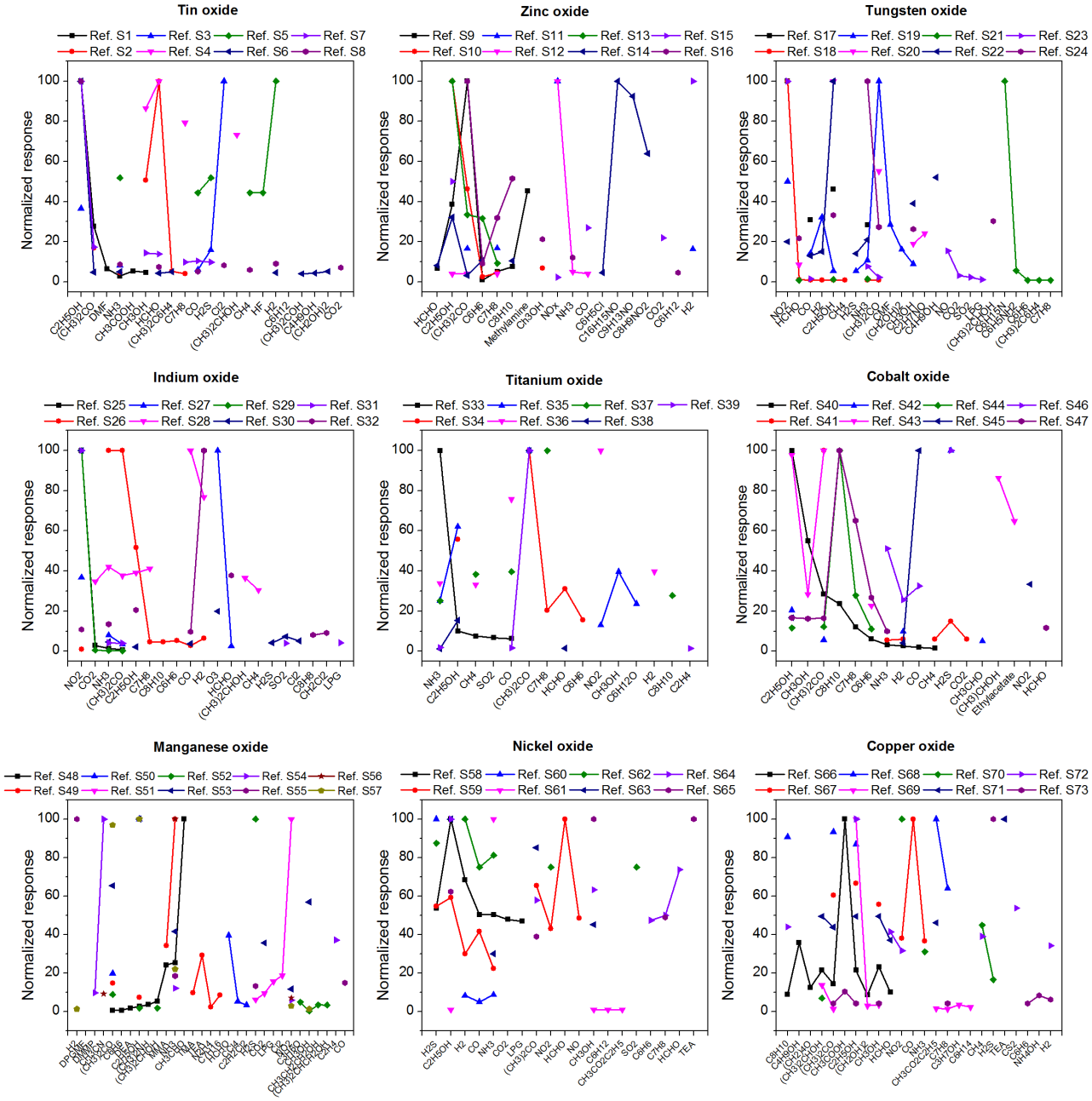

Figure 5.3 – Selectivity of the main metal oxides towards the studied gases. The response in each reference was normalized (the highest response was set to 100).

As can be seen in Fig. 5.3, there is no agreement in the literature for any metal oxides. The maximum agreement reached by the various scientific articles examined is 50% in the case of SnO_2, TiO_2 and In_2O_3, while the minimum agreement is 25% for Co_3O_4 and CuO. This demonstrates that the selectivity of metal oxides depends on many parameters, and it is currently impossible to consider a certain selective metal oxide for a certain gas.

5.4 The brain of the electronic nose: visualization methods and algorithms

A key component of an electronic nose is its "brain": an array of non-selective or low-selective sensors cannot achieve true selectivity if the responses are not intelligently processed and combined. The data processing carried out on the data matrix extracted from a sensor array is fundamental to obtain good performance, but it is also a rather distant topic from material science. For this reason, research groups that were working on traditional gas sensors based on nanowires had to undertake interdisciplinary collaborations or develop their own expertise in this field. However, both processes (developing interdisciplinary collaborations and building your own skills) are complex and time-consuming. This explains why the "brain" of the electronic nose is to date its least developed element despite being the most important. For this reason, together with the different machine learning algorithms, section 2.1 has been inserted to describe the most basic methods that have been used in recent years to demonstrate the capacity for selectivity. These systems have in common the fact that they are visual methods, in which it is necessary for the reader to observe a graph and reason. In this way the human eye and brain (which is still the best pattern recognition system, at least in two dimensions) are exploited as part of the sensing system. In the next subsections, the methods used in the articles studied have been listed according to the objectives they achieve: mere feasibility, qualitative classification, qualitative quantification, real classification, and real

quantification. This distinction will serve to discuss the current state of development of nanowire-based electronic noses, as the level of ability to achieve real-world classification and possibly quantification is a strictly necessary requirement for real-world applications.

5.4.1 Proof of concept

Some publications focus only on the feasibility of an electronic nose by showing how the responses of the sensors that form the array vary as the tested gas or gas mixture varies. This can be done by visual inspection of the trend of a bar plot or a box plot, and how this trend (fingerprint) is different for each gas. Similarly, the different shapes that sensor responses show in a radar plot for different gases can be used to distinguish them. These methods are not based on algorithms of any kind, but on the ability of the human eye and brain to distinguish differences and similarities, so they can only be considered proof of concept.

5.4.2 Principal Component Analysis (PCA)

This very old technique, which is gaining more and more interest in the field of sensors, is a data reduction method used in multivariate statistics. The aim of this technique is to reduce the number of variables describing a data set to a smaller number of latent variables, with a limited loss of information. In practice, it is a linear transformation that projects the N original variables into a new coordinate system (still of dimension N) in which the new variable with the greatest variance is projected onto the first axis, the new variable, second by variance, onto the second axis and so on. In this way it is possible to reduce the number of variables (from N to M <N) while keeping as much

information as possible contained in the original variables. The original purpose (to reduce a too large data set) is usually not what it is used for in the case of e-noses: as we shall see, here it is often used to reduce a small number of variables (6-12) down to two or three in a graph, so that the reader can visualize the data and the relationships between them. Many authors consider these graphs (two-dimensional or three-dimensional, relative to the first 2 or 3 principal components) an easy way to obtain a sort of qualitative classification. When it is possible to distinguish clusters of separate points, each relating to a gas, it is easy to think that a new unknown measure (a new point) can be classified by observing near which cluster it will be positioned. Unfortunately, in addition to being very qualitative, this method assumes the presence of a human operator and the exploitation of her eyes and brain, which are powerful analysis tools but prone to subjectivity and biases. To overcome the qualitative nature of the visual inspection of PCA analysis, several classification methods have been developed that use autonomous algorithms, the output of which is not a graph but a label with the class in which the system classifies the new point.

5.4.3 RGB Encoding

This is not a standard method in the literature, but it is described in this section because it achieves divergent results from other studies: superior to mere classification, but inferior to true quantification.

Furthermore, this method well explains an important concept for electronic noses: the information in a sensor's response signal lies in its dimensionality. In section 1 it has already been explained that a single resistive sensor, with a dimensionless response, is almost completely devoid of selectivity. In this case, combining three responses of this type makes it evident that the

selectivity of the system is sufficient for a perfect classification (at least in the case of the 8 gases analyzed in the paper) and even for an approximate quantification, similar to that of a litmus test.

It should be emphasized that there is no algorithm behind this method, no PCA or other variance optimization technique. The responses are simply normalized and then interpreted as the reg, green and blue channels composing a color.

5.4.4 Linear Discriminant Analysis (LDA)

A slightly more powerful tool that works in a similar way is linear discriminant analysis. This technique is used for dimensionality reduction and visualization, as is PCA, but it is also a reliable classification method. It is a linear transformation from the space of N-dimensions to a space with lower dimensionality M <N, trying to keep as much information as possible, and leaving out the noise instead. In this case the transformation tries to minimize the variance of different groups and maximize their distance, that is, to optimize the separation. This makes it easier to divide the space into regions labelled with a given class (a gas, in our case). Unlike PCA, this algorithm can be considered a supervised method (a method in which a first set of data is used to build the model and then new data is compared to the model) and used as a classifier. In this case the algorithm compares each new data with the model created starting from a data set used to "train" the system, and classifies it by proximity (similarity) to a certain group (a gas, in our case). This method returns a label as an output without the need for any interpretation, and thus operates a true classification. As in all supervised methods, models must be tested on data sets that are completely independent of the training datasets.

5.4.5 Partial Least Squares Discriminant Analysis (PLS-DA)

The most recent interpretation of the acronym PLS stands for "Projection to Latent Structures by means of Partial Least Squares" [120]. This technique is similar to the principal component regression (PCR, based on the PCA seen above) however, instead of finding hyperplanes of maximum variance between the response and the independent variables, it finds a linear regression model by projecting the latent variables and the observable variables into a new space [121]. Also in this case, the new space has the same dimensionality N as the original space, and therefore keeps all the information, even if it distributes it in a different (decreasing) way, trying to maximize the separation between different classes. The response variable is a numerical variable that measures the degree of belonging to a class in the 0 - 1 range (total diversity - total belonging).

An advantage of PLS-DA is that it allows the transformation (similar to PCA) even on a matrix missing of some elements, while previous methods could process an incomplete matrix only by eliminating individuals with missing variables, or by replacing the missing data with estimates. The PLS-DA, on the other hand, is able to work only on known data, even with incomplete matrices.

5.4.6 Artificial Neural Network (ANN)

Artificial neural networks (or just *neural networks*) are based on the concept of artificial neuron proposed in 1943 by McCulloch and Pitts [122]. The first electronic noses were developed using these [123,124], trying to replicate the nature of a mammalian nose insofar as possible. Artificial neural networks are structures of nodes organized in layers, that receive N external signals on a layer of nodes, each connected to various internal nodes of the network (typically organized on several levels) with each single node processing the received signals and transmitting the result of its

elaborations to subsequent levels.

Usually, neural networks comprise three layers:

1) the Input (I) layer receives and processes the input signals, adapting them to the demands of the neurons of the network;

2) the Hidden (H) layer is in charge of the actual processing (and can also be structured with multiple levels of neurons);

3) the Output (O) layer collects the results of the processing of the H layer and checks them with the expected ones.

In the case of electronic noses, a supervised learning method is used, where the system is initially "taught" through a series of labeled data. The most used learning algorithm is the *vanish gradient* method, which allows to find a local minimum of a function in an N-dimensional space. The weights associated with the links between the neuronal layers are initialized to random values and the ANN is made to work with a labeled dataset.

The training of a neural network takes then place in two phases. In the first phase (forward-pass) the input data are given to the input nodes with a forward propagation of the signals through each layer of the network, with the values of the synaptic weights all fixed. In the second phase (backward-pass) the response of the network is compared with the desired output obtaining the error signal. The calculated error is propagated in the reverse direction to that of the synaptic connections. Finally, the synaptic weights are modified in order to minimize the difference between the actual output and the desired output.

5.4.7 Support Vector Machine (SVM)

A support vector machine is a supervised learning model used to analyze data both for classification and for regression. An SVM maps measurements from a first labelled data set to points in a N-dimensional space so as to maximize the width of the gap between the categories. New measurements are then mapped into that same space and predicted to belong to a category based on the area in the space they fall into.

The algorithm works with two classes at a time, looking for a linearly separable hyperplane between them. If there are more than a hyperplane, it looks for the one that maximizes the distance between the points of the two classes it is considering (using support vectors). If there are none, it uses non-linear mapping to bring the training data into a higher dimensionality, so that two classes can always be separated by a hyperplane. This is done using a non-linear kernel, in order to obtain a non-linear classifier without transforming the data too much.

When used for regression, it uses the same principles as for classification, with only a few minor differences. However, the main idea is similar: to minimize error, individualizing the hyperplane (a space of N-1 dimensions) which maximizes the margin, keeping in mind that part of the error can be tolerated.

Using the SVM first as a classifier and then as a regressor (a different and independent regressor for each identified class), excellent results can be obtained both in terms of classification and quantification.

5.5 Fields of application

Unlike a single gas sensor based on metal oxide nanowires, an electronic nose is capable of

detecting and distinguishing many different gases and volatile compounds. This makes it a very transversal tool, suitable for all applications where it is important to quickly understand what an atmosphere is made of, usually produced by a solid product or an organism, but also by industrial processes and complex chains of events. An electronic nose can, for example, be used to assess the freshness of an agrifood product, or carry out a pre-screening by analyzing a patient's breath, or monitor the air quality in different environments (city, home, office, factory...). In this section we will divide the articles published in the literature according to the field in which the authors tested the electronic nose, considering the most important and common fields: generic tests without specific application, agrifood, health and safety fields.

5.5.1 Generic application

The group of Kolmakov proposed a "nanoscopic electronic nose" using an array of four single nanostructures [125]. Four n-type semiconducting nanostructures (SnO_2 and Ni-decorated SnO_2 nanowires, TiO_2 and In_2O_3 thicker nanowires) were tested towards H_2 and CO in conditions of low pressure. The response values of three sensors (SnO_2, Ni- SnO_2 and TiO_2) were plotted as radial plots for a qualitative classification of the two target gases.

The KAMINA platform (a linear microarray of 38 segments contacted singularly) was used with SnO_2 nanowires in order to fabricate an electronic nose [126]. The microarray was tested towards ethanol, isopropanol, and CO using two modalities: in the first only the density of nanowires was varied along the array, while in the second the working temperature also. The discrimination ability (obtained qualitatively through 3D LDA graphs, increases when both parameters are varied.

The same microarray architecture was used with a constant density of pristine SnO_2 nanowires, with only the temperature gradient created by four heaters on the back side of the substrate [127]. The sensors were able to detect 1 part per million (ppmv) of CO, ethanol, isopropanol and toluene. The system was able to classify the four gases at their lower concentration through a 3D LDA plot.

Four resistive sensors based on single nanowires (In_2O_3, SnO_2 and ZnO) and single-walled carbon nanotubes were integrated on separate hotplates, so that their temperature could be controlled individually. Using the responses from the four sensors working at two different temperatures, the electronic nose was able to qualitatively distinguish NO_2, H_2 and ethanol and their concentration [128]. Fig. 5.4 shows the SEM images of the four sensors and the PCA plot obtained using only the three sensors based on metal oxide single nanowires.

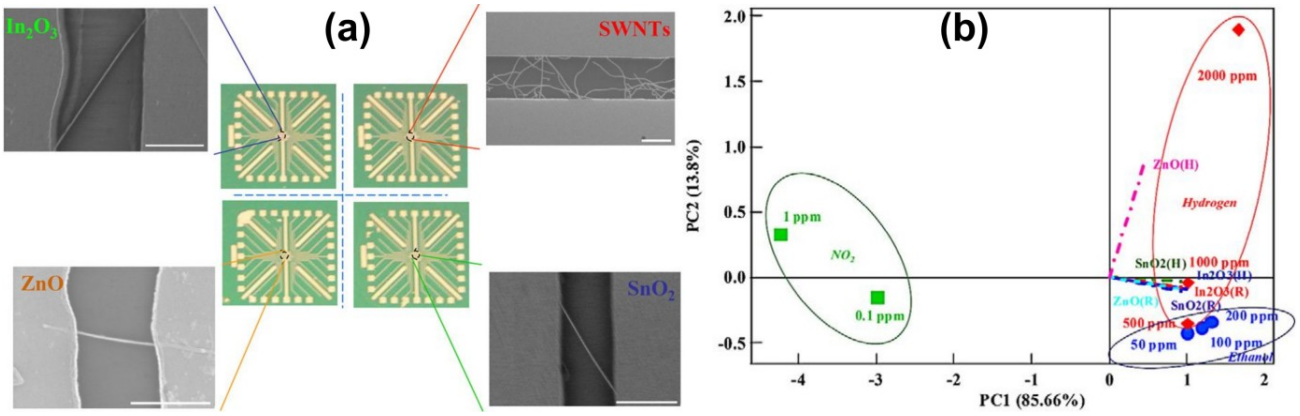

Figure 5.4 – (a) Sensor array chip composed of four individual chemical sensors, including individual In_2O_3 nanowire, SnO_2 nanowire, ZnO nanowire, and SWNT chemical sensor chips; (b) PCA scores and loading plots of the chemical sensor array composed by only the three metal oxide single nanowires. Edited with permission from [128].

The group of Moskovits described an electronic nose strategy on an array of single SnO_2 nanowire whose sensing properties were modified by surface decoration with different metal nanoparticles and different operating temperatures [129]. The sensors selectivity was tested towards

three reducing gases: H_2, CO and ethylene, which were classified qualitatively through LDA plots. The discriminating ability of the e-nose was not affected by the length or diameter of the nanowires composing it.

A different system was proposed, composed of two sensors based on vertical ZnO nanowires with different metal oxide coatings on top of them: CuO and SnO_2 [130]. Different response values of the two sensors towards different concentrations of NO_2 and H_2S gases were plotted in radial graphs, showing different slopes, which could be used to discriminate the gases in a qualitative way.

The same architecture with vertical ZnO nanowires with different coatings, was used also in another work of the same group [131]. In this case the structural template consisted of vertical ZnO NWs coated with SnO_2 on top. Different sensors were obtained sputtering very thin layers of different metals (Pt, Pd and Au) on top of three samples, as active materials for gas sensing. The large area given by the vertical nanowires and the catalytic effect due to the noble metals make the sensors able to detect NO_2 and H_2S at room temperature. An array composed of three sensors with different decorations (Pd, Pt, and Au) was able to discriminate five different gases (H_2S, NO_2, NH_3, H_2, and CO) in a qualitative way (using 2D and 3D PCA plots).

As an alternative to using different materials, different surface decorations or different working temperatures for the realization of the electronic nose, it was also proposed to take advantage of UV lighting of different wavelengths [132]. This theoretical work showed that employing a tunable UV source, the reaction on the nanowires surface can be tuned, achieving selectivity towards different gases. The theory behind the UV-activated gas sensing is shortly presented in terms of the energy balance when the light interacts with the surface of the nanowires.

A more traditional approach, using different nanomaterials assembled via dielectrophoresis

between gold electrodes, was presented [133]. The active materials used are graphene oxide, carbon nanotubes, and CuO nanowires, in an array of 40 sensors. The matrix was exposed to methanol, toluene and ammonia and the evidence for discrimination is that the dynamic resistance of the sensors is different for different gases.

A single SnO_2 nanowire was used in a KAMINA design, exploiting the decreasing diameter of the nanostructure and Pt decoration of its surface [134]. The change in resistance along the segments mirrors the change in the concentration of charge carriers and is used as a variable parameter to build the electronic nose. The microarray was able to recognize acetone and hydrogen, while isopropanol and CO were difficult to discriminate in the LDA plot, because of their overlap.

An array of four heterostructures made of vertical ZnO nanowires with different surface decorations (pristine, SnO_2, In_2O_3 and WO_3) was used as an electronic nose [135]. The electronic nose was able to detect NO_2, H_2S, H_2, NH_3, and CO at room temperature. The discrimination of the gases was obtained through a 2D PCA plot in which the only isolated cluster was that of H_2S. The clusters relative to the other gases overlapped significantly, not allowing any classification.

A sensor based on SnO_2 nanowires was integrated in an array to compare its performance with that of the thin film counterparts, testing it towards water, ethanol and a mixture [136]. The nanowire-based sensor demonstrated performance equal to that of thin film based sensors, with the advantage of greater surface area/volume and flexibility.

An array of three single Mg-doped In_2O_3 nanowires doped with different metal (Au, Ag, Pt) nanoparticles, was used to demonstrate the feasibility of an integrated electronic nose [137]. In this case the sensors were not chemoresistors, but back-gated field-effect transistors (FETs). The parameters of the transistors in the array can be used as features to obtain selectivity at room

temperature, as the authors did for CO, ethanol and hydrogen.

A different design of electronic nose with ZnO nanorods was realized by Ko et al. using electrodeless quartz crystal microbalances [138]. Different patterns of ZnO nanorods were grown on each mibrobalance, working as independent resonators with different frequency. Longer nanostructures increased the quality factor of the resonators, enhancing the sensing performance of the sensor. Coating the ZnO nanorods with different polymers (PMMA, PVP and PVAc), a certain selectivity was achieved, allowing for qualitatively discriminate ethanol, toluene and gasoline in a 2D PCA plot.

Another vertical design was used to fabricate an electronic nose using different nanostructures of different materials. Six different sensors were used different of shapes (helices, rods and zig-zags) made of different metal oxides (TiO_2, ITO, SnO_2 and WO_3) [139]. The array of vertical sensors was used to qualitatively distinguish hydrogen, CO and NO2 using radar plots.

Hu et al. built an array composed of four single nanowires, trying to exploit the different selectivities of the most diverse materials, namely a metal (Pd), two polymers (PPy and PANI) and a semiconductor (ZnO) [140]. Four target gases were selected to test the performance of the array: hydrogen, methanol, CO and NO_2. The authors were able to qualitatively discriminate the four gases, also using blinded experiments where new measurements were compared in the PCA plot with the calibration points, thus also providing a quantitative estimation of the gas concentration. As can be seen in Fig. 5.5, the four sensors were quite selective towards the four tested gases, and this was reflected in the three-dimensional PCA plot. Fig. 5.5c compares the real composition of the tested gases with that estimated by the sensing system.

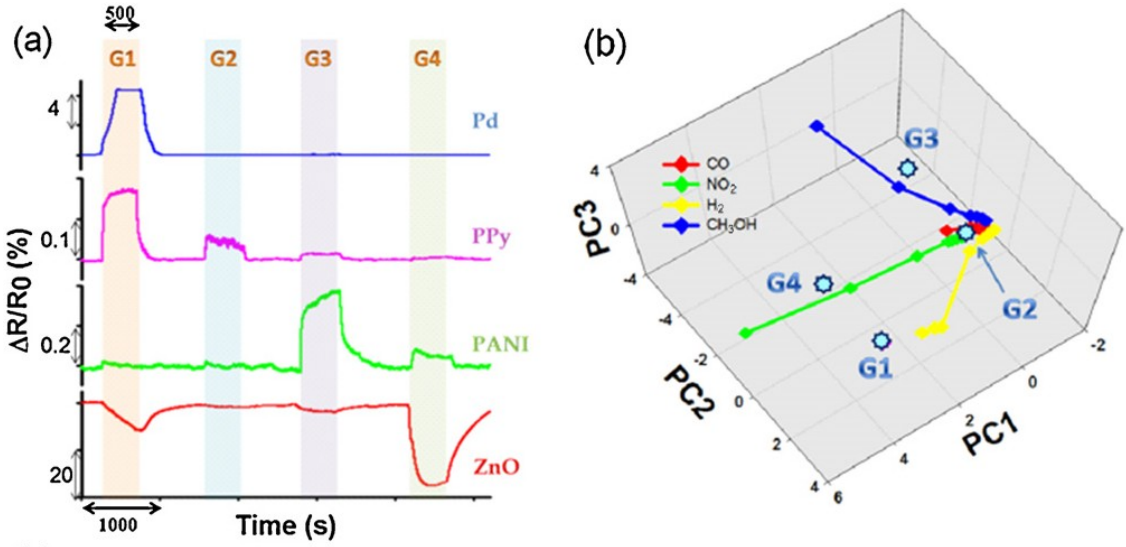

(c)

	Gas 1	Gas 2	Gas 3	Gas 4
Real composition (concentration)	H_2 (2%)	CO (400 ppm)	CH_3OH (5.4%)	NO_2 (5 ppm)
Estimated composition (concentration)	H_2 (≈7.2%)	CO (≈667 ppm)	CH_3OH (≈3.6%)	NO_2 (≈3.3 ppm)

Figure 5.5 – Real-time sensing signals and the corresponding PCA plot. (a) Dynamic percentage response (change in resistance divided by the base resistance) collected from the four sensors during four response-recovery cycles; (b) 3D PCA plot including training points (colored points connected by lines) and test points (four teal octagons labeled G1-G4); (c) Comparison between the real gases injected and the estimates from the sensing system. Modified with permission from [140].

An array of three different on-chip grown ZnO and CuO nanowires was used as a prototypal electronic nose [141]. In practice, by growing ZnO and CuO nanowires directly from the electrodes, three sensors were made that exploit different junctions: ZnO-ZnO, ZnO-CuO and CuO-CuO, as shown in Fig. 5.6a. Using three sensors of the pristine metal oxides, three decorated with Pd nanoparticles and three with Ag nanoparticles, nine sensors were combined (3 junctions x 3 surface decorations). The sensors were able to qualitatively distinguish H_2, CO, and NO_2 in a LDA plot.

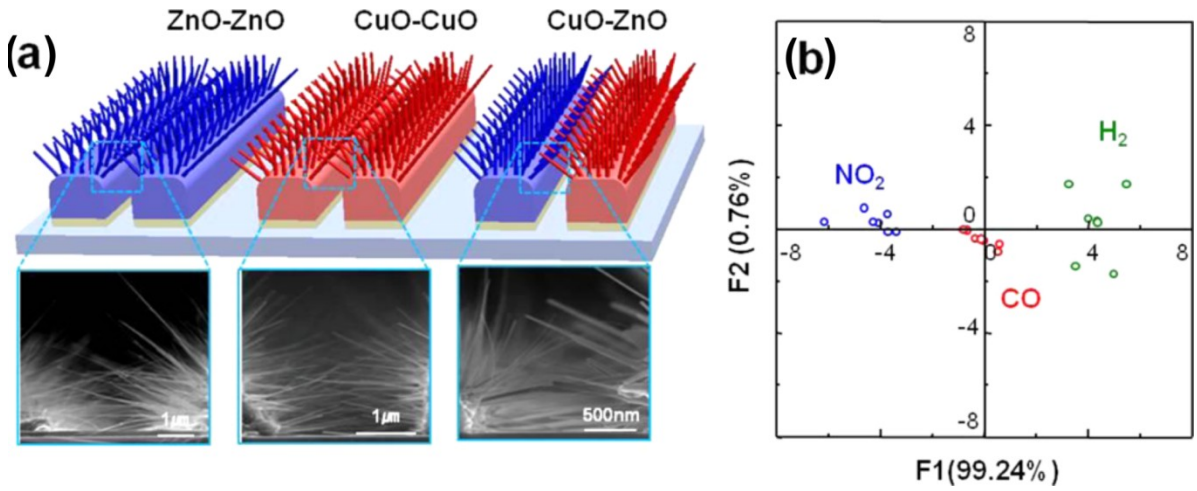

Figure 5.6 – (a) Schematic representation of the crossed-nanowire junction array and corresponding SEM images; (b) LDA analysis classifying the points corresponding to the various gases at 95% confidence level. Reprinted with permission from [141].

A more traditional approach, using different metal oxides (VOx, MnOx, WOx, and NiOx) deposited on finger electrodes [142]. The semiconducting nanostructures were assembled via dielectrophoresis onto electrode arrays and then packaged for easy testing. Looking at the fractional resistance was affected by the presence of ethanol, acetone, methanol and ammonia, the authors were able to discriminate ethanol and ammonia. They are confident that with the help of machine learning algorithm, this setup would be able to achieve real selectivity.

A thicker surface decoration was implemented on ZnO nanowires, realizing almost a core-shell situation [143]. After atomic layer deposition of thin layers (5 nm) of Al_2O_3 and TiO_2, two types of core-shell nanostructures were obtained: ZnO–$ZnAl_2O_4$ and ZnO–Zn_2TiO_4 nanowires, used as sensing elements at room temperature under UV illumination. Using an array comprising pristine ZnO nanowires also, the authors were able to qualitatively discriminate O_2, O_3, CO and NO_2 using bar plots and a 3D PCA plot.

A network of potassium titanate nanowires was used as a chemiresistor to detect acetone and ethanol at room temperature [144]. The network was segmented in eleven different sensors, that are

different because of the intrinsic variation of the density of the nanowires. Combining the response values of the eleven sensors and processing them with LDA, different clusters were found for acetone and ethanol, proving a certain qualitative classification from the system.

The role of metal oxides is different in the work of Song et al., who use polymeric nanowires surface decorated with 3 different catalysts as sensor: Ag, CuO and Mn_2O_3 [145]. Four sensors (including pristine PANI nanowires) were used to obtain an array and achieve a qualitative selectivity. The sensing system was tested with ascorbic acid, dopamine and H_2O_2 in liquid as an electronic tongue, but could also be operated with gases, as an electronic nose. The different analytes and their mixtures were discriminated qualitatively and semi-quantitatively through two-dimensional PCA plots.

Polycrystalline NiO nanowires were used as a chemiresistor to demonstrate that selectivity can be tuned towards different target gas by changing the working temperature of the sensor [146]. The sensor response to hydrogen is larger at 200°C and decreases as the temperature rises, while the response to ethanol increases with temperature, and reaches its maximum at 400°C. In this way, by varying the temperature of the sensor, it is possible to set its selectivity towards one of the target gases.

An electronic nose based on different materials and different shapes was proposed as very sensitive system to detect gases and volatiles [147]. The sensing system was formed by three metal oxides (WO_3, SnO_2 and In_2O_3) in three versions: pristine thin films, Au-decorated thin films and vertical nanowires, thus obtaining a 3x3 array. The classification is shown qualitatively by means of 2D PCA plots. Using only the thin films, the electronic nose is able to discriminate NH_3 and H_2S, while adding the nanowires it can also distinguish NO. On the other hand, it cannot distinguish acetone, benzene, CO and ethanol.

A different approach consisted in using a single SnO_2 nanobelt suspended between two electrodes, acting as a field-effect transistor [148]. Different FET parameters were extracted (I_{ON}, mobility, threshold voltage, subthreshold swing) and used as features to be processed by LDA. The two-dimensional LDA plot shows a qualitative classification of NO, NO_2 and H_2S. After this classification, a possible quantification is proposed, comparing the measurement with the calibration ones.

The on-chip growth of SnO_2 NWs was used to manufacture an array of self-heated gas sensors, in order to simplify the fabrication process and avoid the need of an external heater, reducing the power consumption [149]. Tuning the sensor power, different response values can be obtained, which vary for each gas, and can therefore be considered as fingerprints.

In addition to the intrinsic selectivity of the sensor towards NO_2, the self-heated system could qualitatively discriminate H_2, NH_3, H_2S, and C_2H_5OH.

A chemoresistive electronic nose based on pristine and Au-decorated SnO_2 and WO_3 nanowires was fabricated by electron-beam evaporation at a glancing angle [150]. The back-heated 2x2 array (2 materials x 2 surface decorations) has a sub-ppmv detection limit for NO and NH_3 in 80% relative humidity (RH). A two-dimensional PCA plot demonstrated that the electronic nose is able to well distinguish NO and NH_3, while the other gases (C_2H_5OH, CO, C_7H_8, C_6H_6, and CH_3COCH_3) are too overlapped. The position in the PCA graph of the points relative to NO and NH_3 shows that a quantitative analysis of these two gases would probably also be possible.

Nanowires of different materials have been grown on the same chip exploiting the presence of different membrane with integrated heaters [151]. The ability to locally heat the chip, allowed to grow SnO_2, WO_3 and Ge nanowires on different sensors of the same chip, and later to optimize the

working temperature of each sensor. The electronic nose was able to qualitatively distinguish CO, NO_2 and relative humidity in a 2D PCA plot.

A sensor made of NiO nanowires was made working at different temperature in order to simulate a temperature gradient and a virtual electronic nose [152]. The fingerprints of 7 reducing gases (H_2S, ethanol, H_2, CO, NH_3, CO_2 and LPG) were each combined in a 5D point, and processed by machine learning. The shape of the fingerprints is very similar even changing the gas concentration. Using support vector machines, the system was able to achieve perfect classification and very good quantification (<15% average error).

An array of four sensors based on vertical polycrystalline SnO_2 nanotubes decorated with Pt was proposed as an ultra-lower power electronic nose [153]. The four sensors were top-coated with different materials (Au, Pt, Ni, ITO) in order to change their intrinsic selectivities. The sensor array was tested with relative humidity, NO_2, benzene and H_2. The 3D LQV plots, similar to PCA plots, showed that the points are well dispersed, allowing to classify the gases and probably even to estimate the concentrations.

Three sensors based on SnO_2, WO_3, and Ge nanowires were integrated on the same chip thanks to localized growth driven by local heating [154]. Using different membranes with integrated heaters (Fig. 5.7a), the nanowires were grown directly on the patterned electrodes by chemical vapour deposition (CVD). The responses from the three materials were combined and analyzed through PCA. Fig. 5.7b shows clear qualitative classification of humidity, CO and NO_2 with well-isolated clusters of points for each gas.

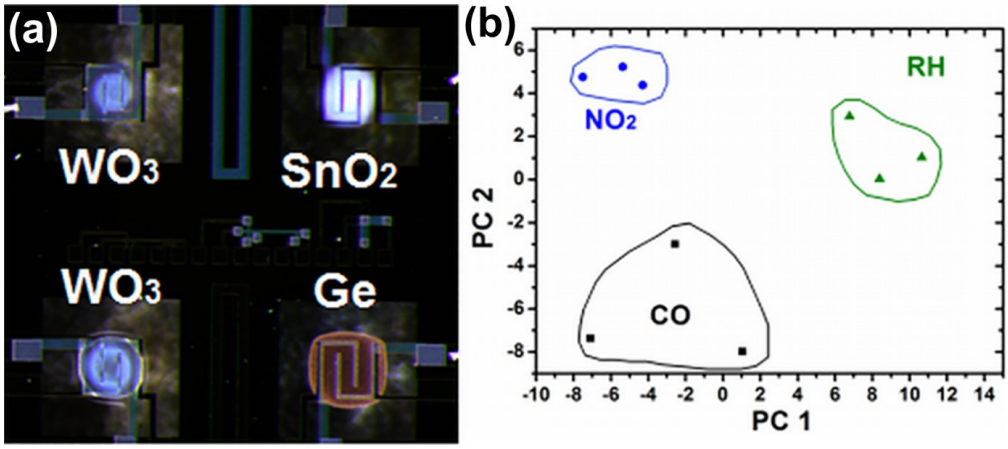

Figure 5.7 - Optical image of the blue tungsten oxide WO_{3-x} NWs, the white SnO_2 NW deposit, and brown coating of Ge; (b) PCA from SnO_2, WO_3, and Ge NW-based gas sensor showing clustered CO, NO_2, and relative humidity points. Reprinted with permission from [154].

A visual sensor (a kind of electronic nose that works like a litmus paper) was manufactured with very simple processing of signals from sensors based on NiO nanowires [155]. The response at each working temperature was just normalized to a 0-255 range in order to be encoded as one of the three channels in the colour-space. The combination of the three channels allowed to easily recognize any of the eight tested gases (NH_3, LPG, H_2S, ethanol, H_2, NO_2, CO and CO_2). A renormalization on each single gas also allowed to reach a qualitative estimate of the gas concentration.

Similar to Sysoev's work [134], but using a temporal rather than spatial thermal gradient, an electronic nose was made using a single SnO_2 nanowire [156]. The responses of the sensor at five different temperatures were combined to greatly increase the intrinsic poor selectivity of the resistive sensor. Using a SVM the nanometric electronic nose achieved a classification of 94.3% and a good estimate of the concentrations (18.4%) for ethanol, H_2, CO, acetone, NH_3 and toluene. NO_2 was sometimes confused at low concentration.

An electronic nose was built that exploits the intrinsic inhomogeneity of a network of ZnO nanorods deposited on a multi-electrode chip [157]. The system was able to detect isopropanol, ethanol and butanol at sub-ppmv concentrations, and separate them well in a 2D LDA plot, as shown in Fig. 5.8. Using the Mahalanobis distance, the authors demonstrated that the separation of points at higher concentrations is greater.

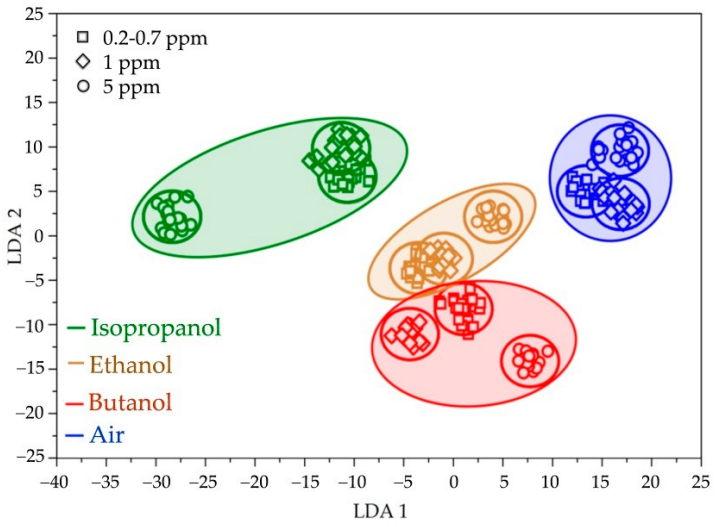

Figure 5.8 - LDA plot showing that the electronic nose can recognize the different gases at different concentrations, from sub-ppmv to 5 ppmv. Reprinted with permission from [157].

A sensor based on SnO_2 nanowires grown directly from the metal electrodes and then decorated with Pt nanoparticles by radiolysis was used as electronic nose by using it at different working temperatures [158]. The thermal fingerprints for each gas (benzene, acetone, H_2, toluene and ethanol) were shown as a function of the gas concentration, and a 3D PCA plot showed that the gas clusters are well separated. Using an SVM, it was possible to obtain a good estimate of the concentration of each gas (approximately 14%).

A sensor based on carbon-doped SnO_2 nanowires was operated in a low range of temperatures in order to use it as an electronic nose [159]. At each temperature the sensor showed a different

intrinsic traditional selectivity, while the combination of the five response values resulted in well separated clusters in a uniform manifold approximation and projection (UMAP) for the gas tested (ethanol, H_2, CO, acetone, NH_3 and toluene). Several classification methods were tested, most of which gave a perfect accuracy of 100%. The use of an SVM gave good estimates for all the gas concentrations, with an error decreasing as the concentration increases.

In a similar approach, a self-heating sensor made of Ag-decorated SnO_2 nanowires was heated at three different levels of power, and the response obtained were combined to be used as an electronic nose [160]. The nanowires were grown directly from the side of the sensor electrodes, and then decorated with Ag nanoparticles by sputtering. The sensor was able to detect H_2S, H_2, NH_3, ethanol and acetone at sub-ppmv concentrations and well separated in a 3D PCA plot. Using an SVM, a good quantification of the gas concentration was achieved. Such an approach could transform a single resistive sensor in a miniaturized electronic nose.

A similar approach using edge-grown SnO_2 nanowires was used to fabricate four sensors to be used in parallel, in a spatial thermal gradient instead of temporal [161]. The four on-chip sensors are patterned at increasing distance (decreasing temperature) from a heater, in the same lithography. The four response signals are collected simultaneously and processed together. A series of radar plots showed different shapes for methanol, IPA, ethanol, NH_3, H_2S and H_2.

In a similar way, two chips with SnO_2 nanowires, one decorated with Ag and one with Pt nanoparticles, were used together to build up a more sensitive electronic nose [162]. The responses from the eight sensors were combined and processed with machine learning algorithms. In a first step, a t-distributed stochastic neighbour embedding (t-SNE) was used to show the relationships between the gas clusters, showing a good separation of the tested gases (acetone, ethanol, H_2, H_2S and NH_3). In a successive step, the gas concentration was estimated by a SVM, obtaining an average

error of 18.3%.

An electronic nose based on ZnO nanowires chemoresistors was realized decorating different sensors with different sensitizers, namely Ni, Co, Mg and Fe [163]. Showing the response of the different sensors (pristine ZnO and sensitized ones) towards H_2S, NO_2, NH_3 and CO, the authors showed that the array has the potential to act as an electronic nose.

Two electronic noses each based on a forest of nanowires of a single material (SnO_2 and ZnO, respectively) working at different temperatures were compared by measuring different gases (acetone, ammonia, ethanol, hydrogen, nitrogen dioxide). Under the same conditions (similar nanowire morphology, same working temperatures and gas concentrations) the SnO_2-based device proved to be better, perfectly classifying all gases and quantifying them with an error of less than 10 ppmv [164].

Kanaparthi and Singh tested a single sensor based on ZnO nanostructures, operating it at 250°C, to detect NH_3, CO_2, and H_2S. When the sensor detected the presence of gas, it was also tested at 300 and 350°C. The three responses were used, together with a simple ternary logic, to classify by random forest the measured gas with an accuracy of 99.8% [165].

Table 5.1 - List of scientific papers on electronic noses based on metal oxide nanowires tested generically in a scientific laboratory.

Metal oxides	Decoration	Target gas	Temperature in °C	Array difference	"Brain"	Reference
SnO_2, TiO_2	Ni	oxygen, H_2, CO	350	materials	radial plots	[125]
SnO_2	-	isopropanol, ethanol, CO	250 - 330	NWs density & temperature	LDA	[126]
SnO_2	-	CO, ethanol, isopropanol, toluene	not available	temperatures	LDA	[127]
In_2O_3, SnO_2, ZnO	-	NO_2, H_2, ethanol	25, 200°C	materials & temperature	PCA	[128]
SnO_2	Ag, Pd	H_2, CO, ethylene	245 - 285	surface decoration & temperature	LDA	[129]
ZnO	Cu, SnO_2	NO_2, H_2S	160	surface coating	radial plot	[130]
ZnO, SnO_2	Pd, Pt, Au	H_2S, NO_2, NH_3, H_2, CO	RT	surface decoration	PCA	[131]
WO_3	-	theoretical	RT	UV with different wavelength	none	[132]
CuO	-	methanol, toluene, NH_3	not available	materials	dynamic plot	[133]
SnO_2	Pd	acetone, isopropanol, CO, H_2	300	width + surface decoration	LDA	[134]
ZnO	SnO_2, In_2O_3, WO_3	NO_2, H_2S, H_2, NH_3, CO	RT	surface decoration	PCA	[135]
SnO_2	-	water-ethanol mix	not available	materials	box plot	[136]
Mg-In_2O_3	Au, Ag, Pt	CO	300 - 400	surface decoration	bar plots	[137]
ZnO	PMMA, PVP, PVAc	ethanol, toluene, gasoline	RT	surface decoration	PCA	[138]
TiO_2, SnO_2, WO_3, ITO	-	H_2, CO, NO_2	250	materials & shapes	radar plots	[139]
ZnO	-	H_2, methanol, CO, NO_2	RT	materials	PCA	[140]

Metal oxides	Decoration	Target gas	Temperature in °C	Array difference	"Brain"	Reference
ZnO-ZnO, CuO-CuO, ZnO-CuO	Pd, Ag	H_2, CO, NO_2	250	materials & surface decoration	LDA	[141]
NiOx, WOx, MnOx, VOx	-	acetone, isopropanol, methanol, ammonia	RT	materials	bar plot	[142]
ZnO	$ZnAl_2O_4$, Zn_2TiO_4	CO, O_2, NO_2, O_3	RT (UV)	surface decoration	bar plots, PCA	[143]
$K_2Ti_6O_{13}$	no	acetone, ethanol	RT	NWs density	LDA	[144]
polyaniline (PANI)	CuO, Mn_2O_3	AA, DA, H_2O_2	not available	surface decoration	PCA	[145]
NiO	-	ethanol, H_2, NH_3, LPG, CO, CO_2	200 - 400	temperatures	bar plots, radar plot	[146]
WO_3, SnO_2, In_2O_3	-	H_2S, NH_3, NO, benzene, CO, ethanol, acetone	168	materials & surface decoration & shape	PCA	[147]
SnO_2	-	NO, H_2S, NO_2	RT	FET parameters	LDA	[148]
SnO2	-	NO_2, H_2, NH_3, H_2S, ethanol	150 - 300	materials	fingerprints	[149]
WO_3, SnO_2	Au	acetone, ethanol, benzene, toluene, NH_3, NO, CO	212	materials & surface decoration	PCA	[150]
SnO_2, WO_3	-	CO, NO_2, humidity	250 - 300	materials	PCA	[151]
NiO	-	C_2H_5OH, H_2, CO, LPG, CO_2, NH_3, H_2S	200 - 400	temperatures	PCA, SVM	[152]
SnO_2	Pt	H_2, NO_2, benzene, humidity	RT	top electrode materials (Au, Pt, Ni, ITO)	ANN	[153]
SnO_2, WO_3	-	CO, NO_2, humidity	250 - 300	materials	PCA	[154]
NiO	-	ethanol, NH_3, H_2, LPG, H_2S, CO, CO_2, NO_2	200 - 300	temperatures	RGB encoding	[155]
SnO_2	-	ethanol, H_2, CO, NO_2, acetone, NH_3, toluene	200 - 400	temperatures	PCA, SVM	[156]
Metal oxides	**Decoration**	**Target gas**	**Temperature**	**Array difference**	**"Brain"**	**Reference**

			in °C			
ZnO	-	ethanol, isopropanol, butanol	~400	NRs density	LDA	[157]
SnO_2	Pt	benzene, acetone, H_2, toluene, ethanol	200 - 400	temperatures	PCA, SVM	[158]
C-SnO_2	C	ethanol, H_2, CO, acetone, NH_3, toluene	150 - 270	temperatures	SVM	[159]
SnO_2	Ag	H_2S, NH_3, H_2, ethanol, acetone	0.6, 0.8, 1 mA	self-heating power	PCA, SVM	[160]
SnO_2	-	methanol, isopropanol, ethanol, NH_3, H_2S, H_2	210 - 450	temperatures	radar plot	[161]
SnO_2	Ag, Pt	acetone, NH_3, ethanol, H_2, H_2S	210 - 400	temperatures & surface decoration	t-SNE, SVM	[162]
ZnO	Ni, Co, Mg, Fe	H_2S, NO_2, NH_3, CO	200	surface decoration	bar plot	[163]
SnO_2, ZnO	-	acetone, NH_3, ethanol, H_2, NO_2	200 - 400	temperatures	PCA, SVM	[164]
ZnO	-	NH_3, CO_2, H_2S	250 - 350	temperatures	NB, SVM, RF, LR	[165]

5.5.2 Agrifood

An individual SnO_2 nanobelt was contacted by multiple electrodes in order to obtain ten segments acting as an array of resistive sensors, some of which were decorated with Pd nanoparticles [166]. Due to the decreasing width and the localized Pd decoration, the sensors had different sensitivities and acted as an electronic nose. In a first step the system proved to be able to distinguish toluene, isopropanol, ethanol and CO. Then, as can be seen in Fig. 5.9, radar charts and an LDA plot showed that the electronic nose was able to qualitatively distinguish the aroma of different alcoholic beverages: glühwein, champagne, vermouth and brandy, all diluted up to 10% ethanol content.

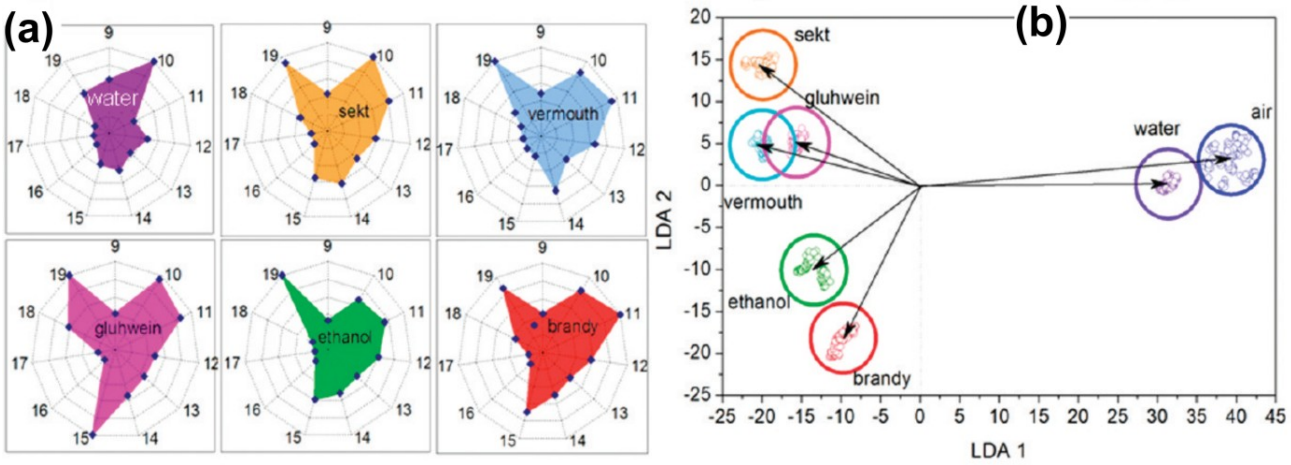

Figure 5.9 - (a) polar plots with the responses of the sensors in the array to the aroma of various alcohol beverages; (b) corresponding LDA plot of the sensor array to the beverages aromas. Reprinted with permission from [166].

SnO_2 nanowires were integrated to a commercial electronic nose (EOS835 from SACMI, Imola, Italy) in order to enhance its performance [167]. In a first phase, the electronic nose was tested on individual gases, namely CO, ethanol, NH_3 and H_2S and the results were shown in a radar plot. Subsequently, the electronic nose was used to assess the quality of green coffee beans, distinguishing mold-contaminated samples from uncontaminated ones.

The same commercial electronic nose was equipped with two (on six) sensors based on SnO_2 nanowires in order to investigate coffee from different origins (India, Indonesia, Santos, Honduras, Nicaragua) roasted following four different programs and grinded [168,169]. A two-dimensional PCA chart showed that the origin of the coffee is more important than the roasting method in generating the aroma of the coffee.

A commercial electronic nose (EOS507, SACMI, Imola, Italy) was equipped also with SnO_2 nanowires and then used for a rapid assessment of tomato paste and vegetable soups, in some cases artificially contaminated with yeasts and bacteria [170]. After 24 hours of inoculation, the electronic nose was able to correctly classify tomato samples spoiled with *C. milleri* yeast and vegetable soup samples contaminated with *E. hormaechei* and *E. coli* in the 98.9 and 100% of cases, respectively.

An α–FOX electronic nose (Alpha MOS, Toulouse, France) using tin oxide, chromium titanium oxide and tungsten oxide sensors with different geometries was used to distinguish five different cultivars of garlic. The odor profiles of the fresh garlic scapes (Sureño, Castaño, Gostoso, Fuego and Morado) were expected to be different because of different amounts of allicins and sulfide compounds. Linear Discriminant Analysis was used to analyze the garlic scapes, proving that the electronic nose is able to distinguish the different cultivars with a correct classification of 53.3% [171].

An e-nose system using eight metal oxide sensors by Parallax Engineering Inc. (Long Beach, CA, USA) was used to measure different climacteric fruits and assess their ripeness. The results were first visually inspected in the form of radar graphs, showing a significant difference between the odour prints of guava, banana and orange samples. The responses of the sensors were then combined and analyzed with the PCA, managing to qualitatively distinguish the three fruits [172].

Three sensors (on six) of a commercial electronic nose EOS835 were replaced with resistive devices based on SnO_2 and ZnO nanowires, and the instrument was used to assess the quality of grated Parmigiano Reggiano (PR) cheese [173]. Different kinds of crust and pulp were mixed with different ratios, and the electronic nose was able to qualitatively classify the pure-pulp samples from those with 5 and 10% of crust, through a two-dimensional PCA plot.

The results from a commercial electronic nose, a panel of nine expert panelists and a gas chromatograph were compared analyzing 25 samples of Parmigiano Reggiano [174]. The EN, based on an array of six metal oxides gas sensors (three of which in the form of nanowires) was used to evaluate the quality of grated PR samples. It was able to qualitatively discriminate between degraded and non-degraded samples (Fig. 5.10a) and recognize the degree of seasoning (Fig. 5.10b), demonstrating that such a fast and sensitive tool would help in the quality control of food products.

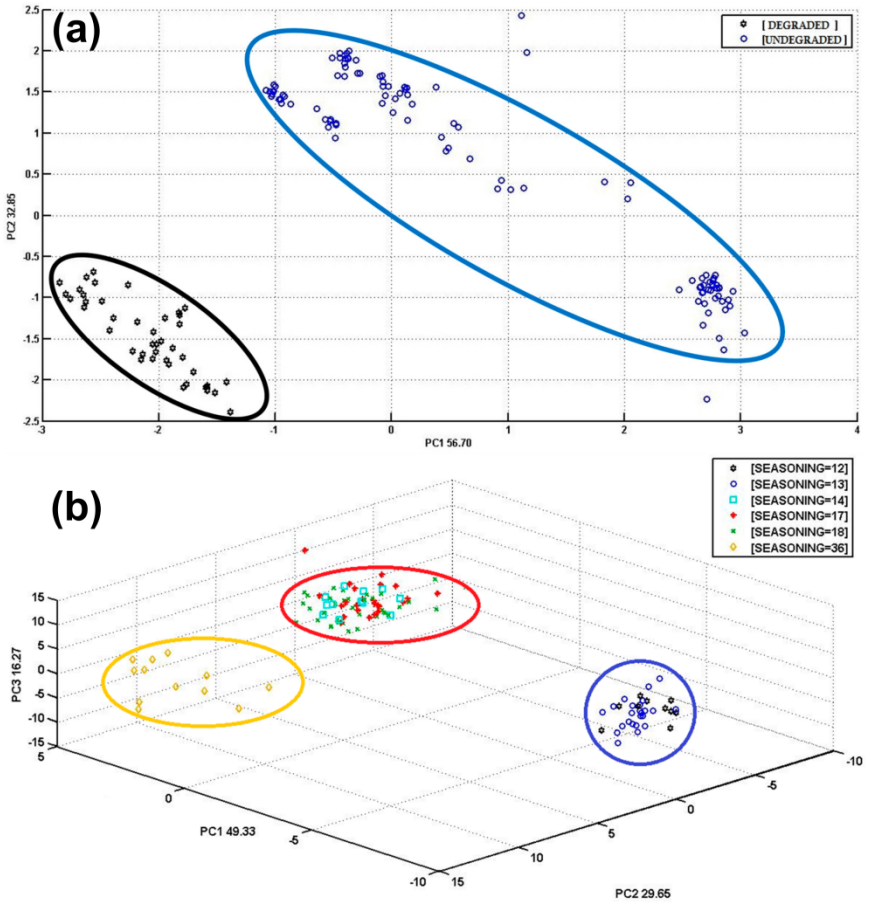

Figure 5.10 - (a) PCA plot of degraded and un-degraded cheese samples in black and blue, respectively; (b) PCA of cheese samples with different ripening times (in months). Edited with permission from [174].

Two conductometric gas sensors, based on ZnO and SnO_2 nanowires grown on alumina substrates, were fabricated and used together to investigate samples of grated Parmigiano Reggiano with different crust content (from 0 to 100%) [175]. The sensing system was able to qualitatively distinguish three groups of points in a PCA plot, relating to samples with 20, 50 and 100% crust content.

The S3 device from the SENSOR laboratory in Brescia was tested by assessing the quality of grated PR and comparing it with the opinions of a panel of experts [176]. The instrument isolated the samples evaluated as "bad" by the panelist from those evaluated as "good" or "flat", proving capable of performing a quality pre-screening.

The same instrument was tested, in parallel with a spectrocolorimeter, to investigate the ripening (from 11 to 36 months) of grated Parmigiano Reggiano [177]. A PCA plot shows that the different ripening categories are quite separate, except the 24 and 30 months, which are overlapping.

An electronic nose that also uses MO nanowires was used to identify possible counterfeits of Parmigiano Reggiano around the world [178]. Several samples of Parmigiano Reggiano from different producers and several samples from European and US competitors were tested. Gas chromatography showed that six volatile compounds were sufficient to discriminate against USA or European competitors of PR. Using the response and response time of selected sensors as features for PLS, the electronic nose was able to distinguish the original PR from competitors with an 80% correct classification. A PLS score plot is shown in Fig. 5.11, demonstrating the classification of PR, European and USA competitors.

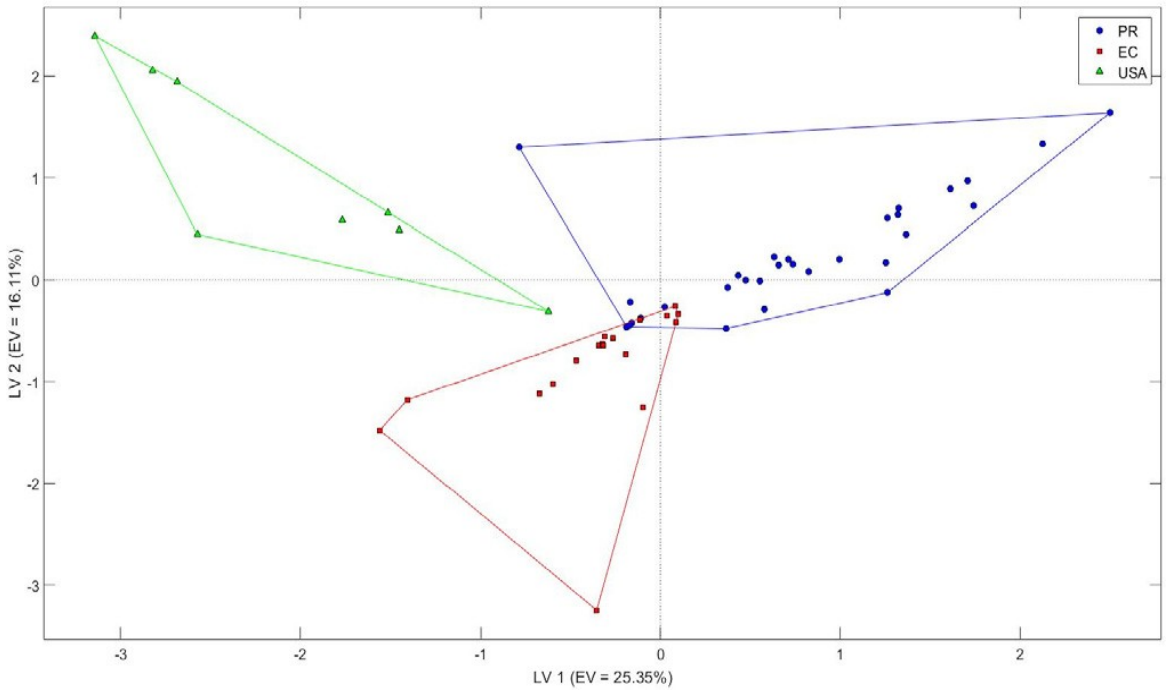

Figure 5.11 - PLS score plot showing the different cheeses. Parmigiano Reggiano is represented by blue circles, European competitors (EC) by red squares and US competitors (USA) by green triangles. Reprinted with permission from [178].

Three nanowires-based gas sensors were used in an electronic nose composed of six sensors in order to recognize different characteristic of grated Parmigiano Reggiano [179]. Classification from PLS-DA and ANNs were evaluated and compared. The electronic nose was used to estimate both the seasoning (12 or 24 months), the rind working process and the percentage of rind present in the grated product. The classification of the seasoning was perfect for ANN, while correct in 94.7% of cases for PLS-DA. The classification of the rind working process was perfect in all cases but the 24-months samples with PLS-DA which gave a 79% correct label. The classification of the rind percentage ranged from 58.8 and 100%.

An electronic nose with three sensors based on MO nanowire (out of a total of eight MO sensors) was used to detect the presence of *Campylobacter jejuni*, for a potential application in the agrifood field [180]. Since the bacteria consume some molecules and their metabolism produces other molecules, their presence can be detected by the headspace. The electronic nose was able to qualitatively follow the bacteria growth and concentration increase in a PCA plot.

A low-power electronic nose using SnO_2, CuO and WO_3 nanowires was used to detect different food preservatives (ethanol, nitrogen dioxide, and ozone) [181]. The three gases overlap on the PCA plot, showing a poor qualitative classification. The integration of the nanowires on micro hotplates allows to foresee the use of pulsed temperature operation.

The S3 electronic nose developed by the group of Brescia was used to assess some characteristics of Parmigiano Reggiano [182]. This work meant to generalize the results obtained in [179]. Using an array of different sensors, the authors identified several different features from each sensor signal, then verified which were the most informative used them to train an ANN. This process in three steps was repeated for each classification (seasoning, rind working process, rind percentage) in order to optimize it. By choosing the best materials and features, a classification

accuracy between 88 and 100% was found. Fig. 5.12 shows four of the many features selected to train the ANN and then to test the electronic nose.

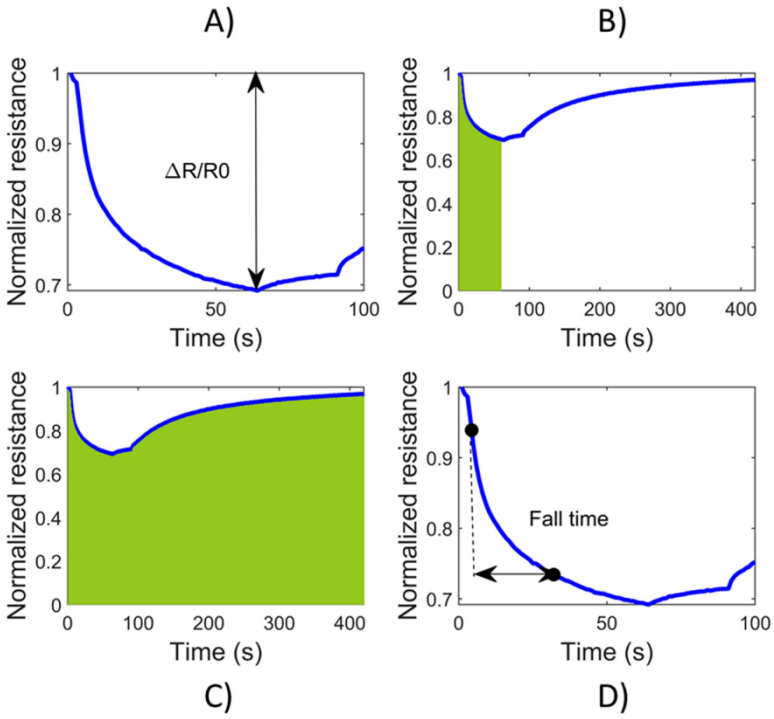

Figure 5.12 - Four features extracted from the normalized signal of nanowire SnO2 sensor: (A) variation of resistance from the baseline (DR/R0); (B) area under the signal up to the minimum (in green); (C) total area under the signal (in green); (D) fall time between 10% and 90% of the signal drop. Reprinted with permission from [182].

A single SnO_2 nanowire was used at three different temperatures in order to mimic an electronic nose. The responses of the single-nanowire chemiresistor at 200, 250 and 300°C were combined and analyzed with principal components analysis. The system proved capable of assessing the freshness of rainbow trout fish according to their total viable count measurement [183]. The PCA graph in Fig. 5.13 where the freshness of the fish is indicated by the color of the points shows a curve indicating the degradation of the fish.

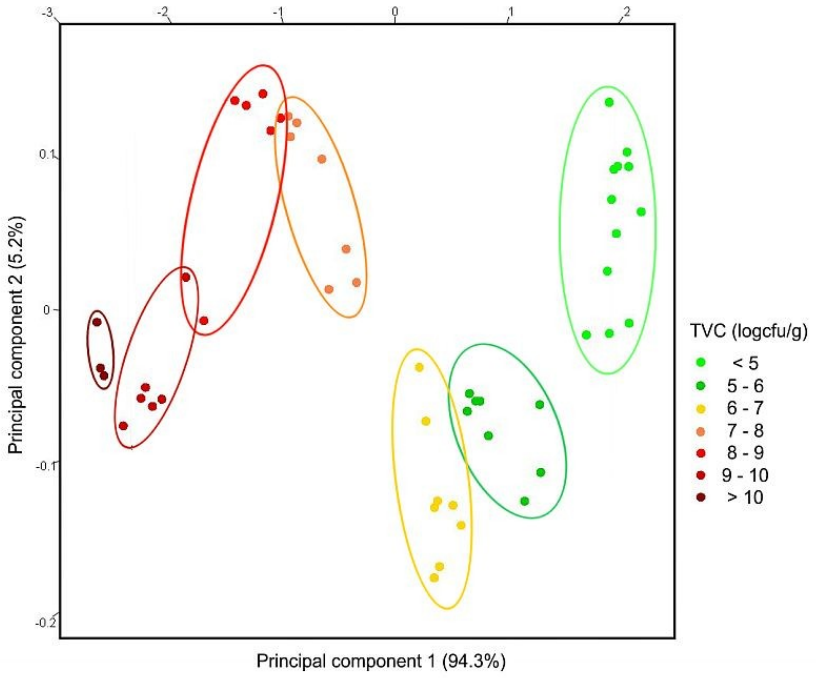

Figure 5.13 - PCA plot of random samples of rainbow trout. The colour of the points indicates the log(TVC) according to the scale on the right. Reprinted with permission from [183].

An electronic nose consisting of a single SnO_2 semiconductor nanowire was used at different temperatures (200-360°C) was used to recognize the degradation state of pig and marble trout samples. Using as features the response of the resistive sensor at 5 different working temperatures, the device was able to recognize the type of sample (meat or fish) in 95.2% of cases, and to evaluate its freshness in 90.5% of cases [184].

An electronic nose compound with four commercial sensors (MQ-138, MQ-135, MQ-3, and TGS 2602) based on SnO_2 was used to recognize whitefly infestation in tomato plants. The electronic nose was able to distinguish healthy plants from stressed ones by means of HCA and PCA [185]. Using gas chromatography-mass spectrometry, the authors found that only infested plants produced 2-nonanol and n-hexadecanoic acid, which have known anti-parasitic properties against nematodes. This suggests that they are emitted by plants in response to the attack of the whitefly and that the sensors can detect this effect.

An array of six commercial SnO_2-based gas sensors were used to detect the presence of *E. coli* in chicken samples [186]. Six statistical features (mean, kurtosis, median, standard derivation, skewness, and variance) were extracted from the measurement of each sensor. Using a random forest, the electronic nose was able to identify fresh and contaminated samples with an accuracy of 99.2% and 98.4%, respectively.

Six composite sensors, based on SiO_2 nanofibers: In_2O_3, SiO_2, ZnO and SiO_2 modified with polyaniline and poly(styrene sulfonate) were used by electrical impedance measurements on analytes related to fish meat degradation (ammonia, methylamine and trimethylamine) [187]. The relative electrical resistance response as a function of frequency was used for multivariate data analysis. The electronic nose was tested in the range 5 - 15 ppmv with ammonia, methylamine and trimethylamine. Using nonlinear interactive document mapping, the device was able to qualitatively distinguish fish samples stored at 0, 24, 30 and 48 hours.

Table 5.2 - List of scientific papers on electronic noses based on metal oxide nanowires applied to agrifood products.

Metal oxides	Decoration	Target gas	Temperature in °C	Array difference	"Brain"	Reference
SnO_2	Pd	isopropyl alcohol, ethanol, toluene, CO, diluted beverages	290	width + surface decoration	radial plot, LDA	[166]
SnO_2	-	NH_3, H_2S, CO, ethanol, coffee	450	materials	radar plot, PCA	[167]
SnO_2	-	coffee roasting	350 - 400	materials	PCA	[168]
SnO_2	-	coffee roasting	350 - 400	materials	PCA	[169]
SnO_2	-	tomato paste + vegetable soup	not available	materials	PCA, LDA	[170]
SnO_2, Cr_2TiO_5, WO_3	-	different garlic cultivars	not available	materials	LDA	[171]
SnO_2	-	banana, guava, orange	not available	materials	PCA	[172]
ZnO, SnO_2	-	Parmigiano cheese	not available	materials	PCA	[173]
ZnO, SnO_2	-	Parmigiano cheese	280 - 500	materials	PCA	[174]
ZnO, SnO_2	-	Parmigiano cheese	350 - 500	materials	PCA	[175]
ZnO, SnO_2	-	grated Parmigiano cheese	not available	materials	PCA	[176]
ZnO, SnO_2	-	Parmigiano cheese	245 - 500	materials	PCA	[177]
ZnO, TiO_2, SnO_2, CuO	Au	Parmigiano and other cheeses	400	materials, signal features	PLS-DA	[178]
SnO_2, CuO	Au	grated Parmigiano cheese	350 - 400	materials	PLS-DA, ANNs	[179]
SnO_2, CuO	Au	Campylobacter jejuni	350 - 400	materials	PCA	[180]
SnO_2, CuO, WO_3	-	ethanol, acetone, nitrogen dioxide, ozone	200 - 400	materials	radial plot, PCA	[181]
SnO_2, CuO	Au	Parmigiano cheese	350 - 400	materials, signal features	ANN	[182]
Metal oxides	**Decoration**	**Target gas**	**Temperature in °C**	**Array difference**	**"Brain"**	**Reference**

SnO_2	-	rainbow trout fish	200 - 300	temperature	PCA	[183]
SnO_2	-	pork, marble trout fish	200 - 360	temperature	PCA, SVM	[184]
SnO_2	-	healthy and infested tomato plants	not available	materials	PCA, HCA	[185]
SnO_2	-	E. Coli on chicken meat	not available	materials	SVM, RF	[186]
SiO_2: In_2O_3, SiO_2, SiO_2: ZnO	PANI, PSS	NH_3, MA, TMA, fish, degraded fish	25°C	materials	IDMAP	[187]

5.5.3 Health

Carmona et al. used an electronic nose to monitor the growth of *E. coli* in water, in order to assess whether it can detect traces of the bacterium in drinking water and thus prevent water-borne diseases [188]. The pH and optical density measurements are very well correlated, while the plot made with the measurements of the electronic nose shows a drift of the points over time that reflects the change in the headspace due to the growth of bacteria.

The same EN, using two nanowire-based sensors, was used to detect the presence of *E. coli* and *L. monocytogenes* in potable water [189]. The system proved capable of detecting the presence of bacteria, and the lines that the dots follow in the PCA plots indicate the potential to track bacterial growth over time in a qualitative way. The lack of a comparison with a technique that measured the concentration of bacteria does not allow to have an estimate, even qualitative, of the limit of detection.

The microbiotic contamination detection performance of an electronic nose was tested against mold, spoilage lactic acid bacteria (LAB) and coliform bacteria [190]. The system was able to follow the growth of mold in coffee beans over time and detect the presence of different types of LAB bacteria compared to an uncontaminated sample. It was also able to detect the presence and growth over time of coliform bacteria in the water of a toilet and well.

An electronic nose consisting of six sensors based on differently decorated WO_3 nanowires was compared with an electronic nose based on six commercial SnO2 sensors, testing them on the breath of smokers from that of non-smokers. [191]. PCA plots showed qualitative classification with both ENs, but the confusion matrix obtained with SVM showed a success rate of 99.09 % and 94.59 % for WO_3 and SnO_2 sensor array, respectively.

An electronic nose based on six sensors, three of which of ZnO and SnO_2 nanowires, was used to analyze the growth of skin microbiota in an artificial sweat solution [192]. Three different microbial blends (each composed by a bacterium, a yeast and a fungus) were inoculated from a concentration of 3.75 and $1.25x10^6$ CFU/mL for prokaryotes and eukaryotes, respectively. A 2D PCA plot shown in Fig. 5.14 demonstrates that the system was able to qualitatively distinguish mixture B (*E. coli*, *Rhodotorula* and FGO3) and detect its development over time. The achieved results show that the electronic nose can discriminate the microorganism blends from the VOCs emitted by the microbial metabolism.

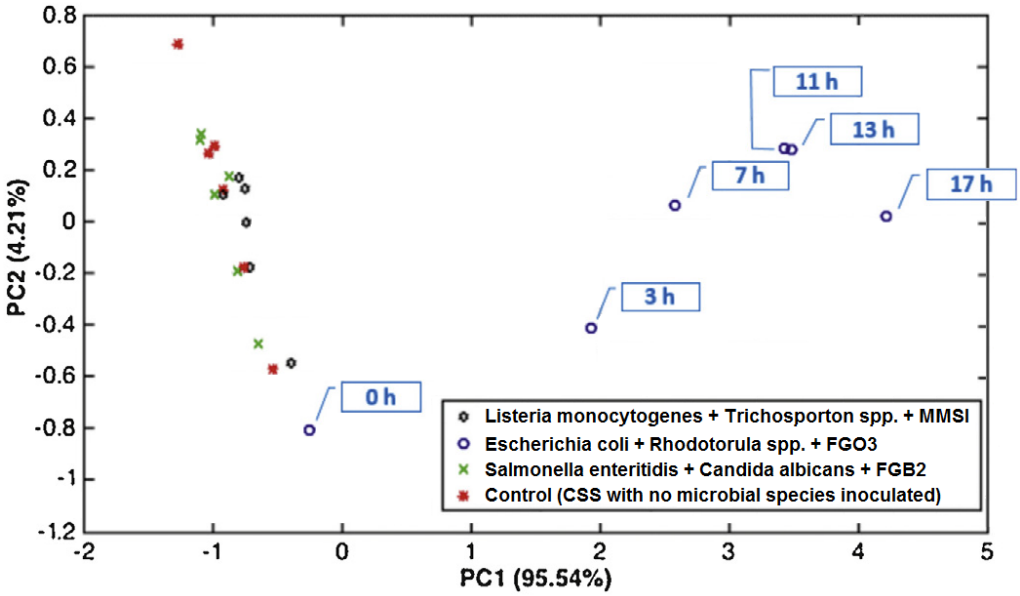

Figure 5.14 - PCA plot of the different microbial blends along the 20 h analysis. Modified with permission from [192].

A similar device was used by the same group to detect the presence of microbiological pollution in water [193]. The electronic nose was able to qualitatively distinguish potable water from water contaminated with pathogenic microorganicsms such as *Escherichia coli*, *Salmonella typhimurium*, *Vibrio cholerae* and *Pseudomonas aeruginosa*, detecting the volatiles they emit (like indole, a volatile typically emitted by *E. coli*).

Five different metal oxides, one p-type (NiO) and four n-type (WO_3, SnO_2, ZnO and Nb_2O_5) were assembled into an electronic nose and used to discriminate between pure and contaminated water [194]. After a first phase in which the performance of each sensor was assessed in detail, the electronic nose was tested on drinking and contaminated water samples, and was able to distinguish them without any training (through a PCA plot). Using a gas chromatograph, the volatiles that most distinguish the samples were found during microbiotic growth over the course of a week.

Six sensors based on MO nanowires, some of which superficially decorated, where used in an electronic nose to discriminate potable water, wastewater and wastewater containing cyanide [195]. An ANN was trained and then used to classify the water samples, achieving a classification rate equal to 97.62%. The main volatiles present in the different waters were found using gas chromatography - mass spectrometry.

Five commercial sensors (Figaro Engineering Inc., Osaka, Japan) each based on a single metal oxide were used to investigate the breath of patients with chronic obstructive pulmonary disease and lung cancer. For each of the two hundred participants, fasting for 2 hours, a measurement of 120 seconds was acquired, then analyzed using different ensemble learning methods. Using XGBoost algorithm the system gave an accuracy, sensitivity, and specificity of 79.3%, 70.0%, and 84.2% respectively for lung cancer detection, and 76.7%, 66.7%, and 83.3% for chronic obstructive pulmonary disease detection [196].

Table 5.3 - List of scientific papers on electronic noses based on metal oxide nanowires applied to the health field.

Metal oxides	Decoration	Target gas	Temperature in °C	Array difference	"Brain"	Reference
SnO_2	-	VOCs from E. Coli	not available	materials	PCA	[188]
ZnO, SnO_2	-	VOCs from bacteria	not available	materials	PCA	[189]
SnO_2	-	coffee, water	not available	materials	PCA	[190]
SnO_2, WO_3	Au, Pt, Pt-Au, Ni, Fe	smokers/non-smokers breath air	not available	materials	radar plot, PCA, SVM	[191]
ZnO, SnO_2	-	skin microbiotas	280 - 500	materials	PCA	[192]
ZnO, SnO_2	-	indole (2,3-benzopyrrole) from E. Coli	400	materials	PCA	[193]
NiO, WO_3, ZnO, SnO_2	Au	water + E. coli	200 - 400	materials	PCA	[194]
SnO_2	Au	water, wastewater + cyanide	not available	materials	PCA, ANN	[195]
SnO_2	-	breath from healthy people and patients diagnosed with chronic obstructive pulmonary disease and lung cancer	not available	materials	XGBoost, AdaBoost, RF	[196]

5.5.4 Security

In order to demonstrate the feasibility of an electronic nose based on 1D nanomaterials, Chen et al. fabricated trinitrotoluene (TNT) sensors based on single-wall carbon nanotubes (SWCNTs) and ZnO nanowires [197]. The sensors were able to detect the presence of TNT down to a few parts per billion (8 and 60 ppbv for SWCNTs and ZnO nanowires, respectively) at room temperature. The responses of the two materials are different (that of SWCNTs is linear up to 1 ppmv, while that of nanowires tends to saturate) and therefore prove to be suitable for use in an electronic nose.

An electronic nose using SnO_2 nanowires and other metal oxides in thin film form was tested with simulants of chemical warfare agents: acetonitrile as a simulant for cyanide compounds and dimethyl methylphosphonate as simulant for the nerve agent Sarin [198]. The specific response intensities of the different materials to the tested gases resulted in a sort of "fingerprint" of the gases, demonstrating the potential as electronic nose.

An integrated sensor array fabricated in the "print and fry" technique and consisting by 16 segments with different densities of SnO_2 nanowires (like the KAMINA approach) was tested to detect explosive materials and the smell of burning from several common materials [199]. During various tests the sensor was shown to distinguish the smell of burning poly propane, poly ethane, beech, polychlorinated biphenyl, cotton and paper, using linear discriminant analysis, with a separation quality of 74.5%. Furthermore, the electronic nose distinguished ammonium nitrate, nitro benzene, nitrotoluene and dinitrotoluene with a separation quality of 53.3% working at 25°C (activated under UV illumination) and 70% relative humidity.

An electronic nose based on a 4x3 array of sensors based on different metal oxides (SnO_2, WO_3, ZnO and TiO_2) with different surface decorations (Al, Ti and Au) was used to detect toxic

gases (NO_2, NO, H_2S) [200]. Using a bar plot of the responses of the twelve sensors as a fingerprint of each gas, the authors demonstrated the feasibility of an electronic nose capable to of qualitatively distinguishing the three target gases.

An array of 16 resistive sensors based on random densities of SnO_2 nanowires was used to distinguish the pre-burning smell of different substances [201]. The electronic nose was working at room temperature in 50% RH, illuminated by ultraviolet light. After a first phase measuring single gases (isopropanol, CO, benzene), the electronic nose was tested with different substances heated up to 200°C. At this temperature the system was able to distinguish cotton, beech and polychlorinated biphenyl. The dynamic resistance of the sensors was used as input features for Linear Discriminant Analysis. The electronic nose successfully discriminated all the substances at pre-burning temperature with a separation quality of 88%. A real field scenario was set up, with the electronic nose inside a real room, far from the heated materials. Also in this case, the system was able to distinguish the materials heated, with a separation quality of 86%. In this way, an alarm can be set to also indicate the type of material that could trigger the fire.

An array of six commercial SnO_2-based gas sensors were used to study wood samples from two types of plants: sugi (*Cryptomeria japonica*) and karamatsu (*Larix kaempferi*) and detect the presence of fungi (*F. palustris* and *T. versicolor*). The electronic nose was able to discriminate in a qualitative way (PCA) the wooden samples infested by the fungi [202].

Nanostructures of Mn_3O_4 were grown by vapor deposition in different atmospheres (O_2 and O_2 + H_2O) in order to study how the growth conditions varied their characteristics and sensing performance [203]. The sensors were tested towards acetonitrile (CH_3CN) and dimethyl methyl phosphonate (DMMP), both used as simulants for cyanide warfare agents. Raising the working temperature from 200 to 300°C, the sensors were able to detect CH_3CN with good selectivity.

Nano-structured composite materials based on Mn_3O_4 have been used as conductometric sensors to detect low concentrations of chemical warfare agents [204]. Pristine Mn_3O_4, Ag/Mn_3O_4 and Au/Mn_3O_4 were tested for di(propylene glycol) monomethyl ether (DPGME), acetonitrile (CH_3CN) and dimethyl methyl phosphonate (DMMP), as well as acetone and ethanol. The sensors proved to be selective towards chemical warfare agent simulants, especially working at 300°C. In particular, the Au/Mn_3O_4 showed a high selectivity for the DPGME

Composite nanostructures of Fe_2O_3/Mn_3O_4 and ZnO/Mn_3O_4 have been used as selective sensors towards ammonia with respect to nitrogen dioxide and acetonitrile (CH_3CN), a toxic gas used as simulant of cyanide warfare agents [205]. Composite nanomaterials are selective towards ammonia and NO_2, while pristine Mn_3O_4 shows a marked selectivity towards CH_3CN between 200 and 300°C.

Composite sensors based on almost one-dimensional CuO/MnO_2 and SnO_2/MnO_2 nanostructures were used to detect di(propyleneglycol) monomethyl ether and dimethyl methyl phosphonate (used as simulants for chemical warfare agents) and hydrogen. Working at 250°C, the metal oxide hetero-nanostructures showed a remarkable selectivity towards the gas chemical warfare agents [206]. The use at three different temperatures (150 - 250°C) could increase the selectivity even more.

Table 5.4 - List of scientific papers on electronic noses based on metal oxide nanowires applied in the field of safety.

Metal oxides	Decoration	Target gas	Temperature in °C	Array difference	"Brain"	Reference
ZnO	-	NO, NO_2, trinitrotoluene	RT	materials	bar plots	[197]
SnO_2	-	chemical warfare agents: acetonitrile (for cyanide) and dimethyl methylphosphonate (Sarin)	450	materials	bar plots, PCA	[198]
SnO_2	-	air, benzene, isopropanol, CO, ammonium nitrate, nitro benzene, nitrotoluene, dinitrotoluene	RT (UV 365nm)	NWs density	LDA	[199]
ZnO	Al, Ti, Au	NO, H_2S and NO_2	200	metal-decoration	none	[200]
SnO_2	-	air, benzene, isopropanol, CO	RT (UV 365nm)	NWs density	LDA	[201]
SnO_2	-	wood, fungi-infested wood	not available	materials	PCA	[202]
Mn_3O_4	-	CH_3CN, DMMP	200 - 300	materials	bar plots	[203]
Mn_3O_4	Au, Ag	ethanol, acetone, CH_3CN, DPGME, DMMP (simulants for chemical warfare agents)	200 - 300	materials	bar plots	[204]
Mn_3O_4	Fe_2O_3, ZnO	NH_3, NO_2, CH_3CN (simulant for chemical warfare agents)	200 - 300	materials	bar plots	[205]
MnO_2	CuO, SnO_2	H_2 and DPGME, DMMP (simulants for chemical warfare agents)	150 -250	materials	bar plots	[206]

5.6 Discussion

Some conclusions can be drawn from the collection of articles discussed. First, despite the large number of scientific articles on gas sensors, nanowires and electronic noses, in the last decade there have been few articles on electronic noses using metal oxide nanowires. It is reasonable to think that this is due to the different technological maturity of the two topics: electronic noses have been studied since the 1980s, while only in the last 15 years has it been possible to integrate nanowires into functional devices.

Metal oxide nanowires are a widely used material for gas sensors. Initially, the focus was on n-type semiconductors, which perform better, but recently p-type semiconductors are also gaining momentum as they are useful for increasing selectivity.

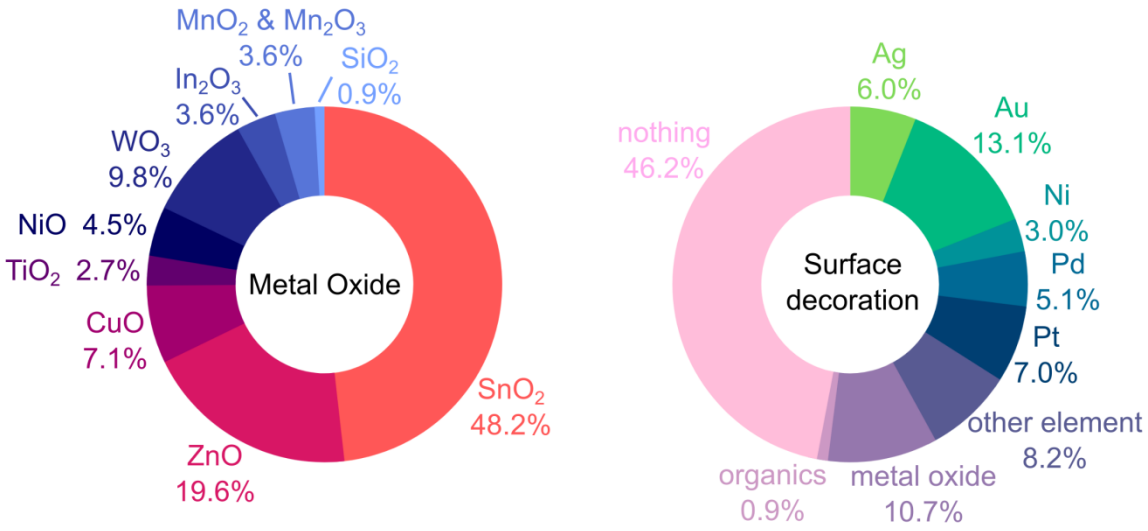

Figure 5.15 - Frequency of use of the different metal oxides in the fabrication of electronic noses based on nanowires (left); frequency of use of different materials as superficial decoration for the MO nanowires (right).

As seen in the left part of Fig. 5.15, this different interest in metal oxides is confirmed by the articles studied here: SnO_2 is by far the most used, followed by ZnO. The other oxides are used in

about one third of cases.

Recently, the performance of gas sensors based on MO nanowires has been greatly improved by decorating their surface with nanoparticles. At first the decoration was carried out with precious metals (Ag, Au, Pt), then it was extended to metal oxides and finally to a wide range of materials. This technological evolution is visible in the right part of Fig. 5.13, in which most of the articles discussed here are not superficially decorated, and the most used nanoparticles are those of Au and Pt. The decoration with metal oxides is receiving great attention also for the possibility of creating p-n junctions and it is growing strongly in recent times.

Using different metal oxides or surface decoration with different materials is the most common way to make a sensor array that is the basis for an electronic nose. Since an electronic nose tries to mimic the olfactory system of mammals, made up of many receptors with different properties, the first devices were born using sensors made of different materials. Even when nanowires began to be used, this approach remained the most common, whether different sensors were used or integrated on a single platform. As can be seen in the left part of Fig. 5.16, the material and the surface decoration (another aspect of the material, if you will) are the basis of almost three quarters of the devices analyzed.

However, as can be seen in the figure, the use of nanowires has broadened the range of parameters that can be used to differentiate the sensors in the array and generate selectivity. Different materials and different signal parameters were already used for macroscopic sensors, but using nanowires it is also possible to vary their density and make them work in a temperature gradient, for example.

Another aspect to consider, which has been used as a framework for this review, is the

application for which the electronic noses were used. Section 3 has been divided into subsections relating to the pure scientific-technological aspect and use in the agrifood, health and safety fields. The proportions of these uses are shown in the right part of Fig. 5.16. It can be clearly seen that in the vast majority of cases the electronic noses are used in the laboratory and tested with pure gases, for purely scientific tests. The lack of real applications may indicate that a technological maturity has not yet been reached.

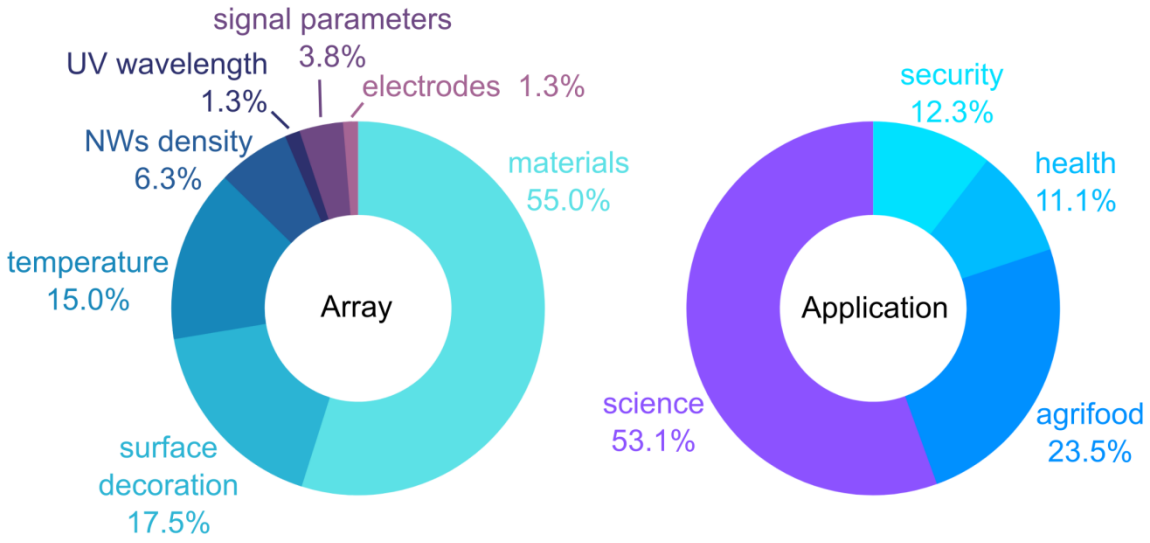

Figure 5.16 - Features that differentiates the sensors in the array that makes up the electronic nose (left); application for which the electronic nose was tested (right).

This fact is confirmed by the graphs in Fig. 5.17. The left side shows the method used to illustrate the final results obtained by the electronic nose.

In some cases these are real machine learning algorithms, often a simple visualization of the points, and sometimes a simple graph of the raw responses. As can be seen, PCA is used in almost half of the cases, which is a method of reducing dimensionality in order to visualize the data, and in this case the electronic nose does not autonomously give any response. The maximum achievable result is the comparison of new measurements with those used for training (qualitative

classification), but it is done by the operator with human eyes and brain, and not by the electronic nose. The real algorithms that give an output (classification or even quantification) are LDA, PLS-DA, SVM and ANN, and together they add up to about a third of the cases studied. In 20% of cases the authors simply indicated the response of the various sensors that make up the electronic nose giving the values or graphing them in box plots, bar plots or radar plots. The case of RGB encoding is similar to a litmus test, which gives an approximate quantification but needs a human operator (like PCA).

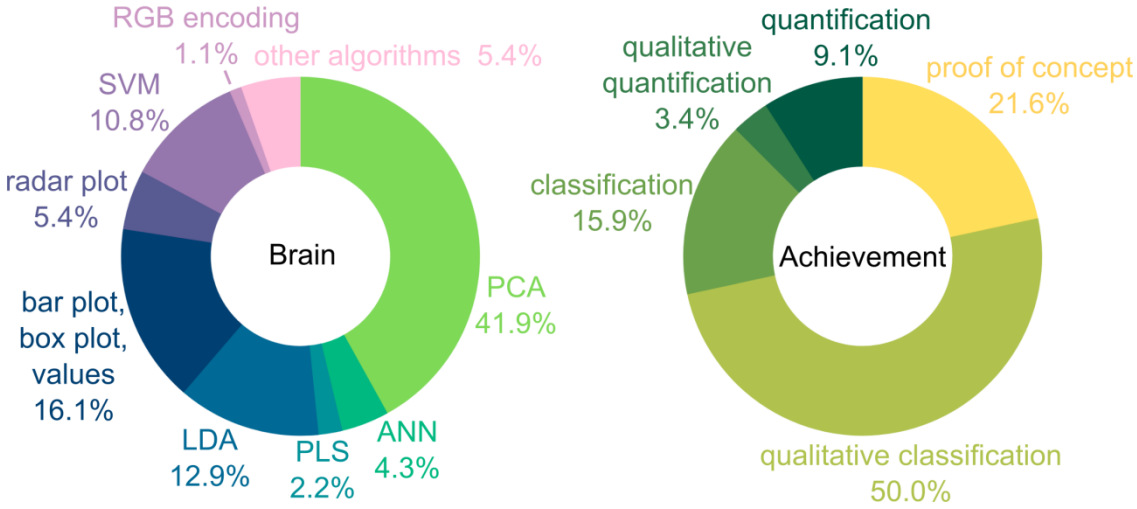

Figure 5.17 - Features that differentiates the sensors in the array that makes up the electronic nose (left); application for which the electronic nose was tested (right).

The right part of Fig. 5.17 shows the type of final information that the electronic nose provides. In 20% of cases there is only a proof of concept, which usually consists of the raw responses from the sensors (a sort of fingerprints). In most cases the device only gives a qualitative classification, i.e. a visual comparison (which needs a human operator, as the system is not capable of it) between the calibration data and any new measurement. Only 9.1% of the ENs provide a real classification obtained autonomously. Although it is the final goal of an electronic nose, only a small part of the systems analyzed is able to give a quantitative estimate autonomously. Depending on the

application, this can be an important defect: in certain contexts, it is sufficient to distinguish different cases (for example patients with a certain pathology from healthy individuals), but in others it is necessary to understand which gas is present and in what concentration (for example a fire sensor that must not misinterpret cooking smells).

5.7 Conclusions and outlook

The scenario depicted by the articles analyzed in this review indicates a recent and not yet fully developed combination of MO nanowires and machine learning algorithms for fabricating electronic noses. There is certainly a lot of potential in this synergy (as demonstrated by the flourishing of innovative approaches), but the results are still limited in most cases. This is likely due to the inherently interdisciplinary nature of this subject, which combines materials science and nanotechnology (growth of nanowires), micromachining (electrodes and device), electronics (signal acquisition and processing), and machine learning (statistical analysis of responses).

Scientific literature shows a much greater development in the aspects related to materials science and nanotechnologies, while the implementation of data mining and artificial intelligence methods is still limited, both for the extraction of features and their analysis. This is probably because the authors are largely experts in resistive gas sensors based on nanostructured metal oxides, who have independently acquired basic knowledge about machine learning, while the opposite situation is not common. This imbalance is demonstrated by the attention given to the growth and characterization of nanomaterials or to the improvement of individual sensors (response intensity, response and recovery time, limit of detection), while little attention is given to features extraction and their processing (in many cases these passages are not even present), which are

equally important for the final performance of an electronic nose.

Another weakness of nanowire based electronic noses is that they are almost always tested under laboratory conditions, with exact concentrations from pure gas cylinders. The few applications with real samples are also carried out under simplified laboratory conditions, without all the possible adversities of field measurements (including the wide variability of real samples). This type of experiment works for single selective sensors to be applied in specific conditions (no or few interfering gases, narrow temperature and humidity range...), but not for electronic noses. This type of device has been designed precisely to identify gases and volatile organic compounds in the presence of many interfering molecules, and therefore field measurements under realistic conditions are needed. The absence of real-world applications in the reviewed literature indicates that research on electronic noses based on metal oxide nanowires is still in its infancy: better fundamental research and wider real-world applications are still needed.

It should be emphasized that several new approaches have recently been developed, both regarding the differentiation of sensors in the array and the choice of features to extract and process. In this sense, the new approaches shown in this excursus, even very different from each other, demonstrate the interest of the scientific community for the topic. Traditional electronic noses, composed of single macroscopic gas sensors, continue to provide interesting results, but the new integrated architectures based on nanowires offer very important advantages in the era internet of things. Given the very wide diffusion and rapid innovation of personal technological tools (smartphones, smartwatches) and the need for sensors to collect information about the world around us, this new generation of electronic noses will surely attract more and more interest also through the synergy of nanoscience and artificial intelligence.

CHAPTER 6. SENSING PERFORMANCE OF THERMAL ELECTRONIC NOSES: A COMPARISON BETWEEN ZNO AND SNO_2 NANOWIRES

This chapter is based on the scientific paper [164]:

"Sensing performance of thermal electronic noses: A comparison between ZnO and SnO_2 nanowires", Nanomaterials, 11 (2021) 2773. Doi: 10.3390/nano11112773.

6.1 Abstract

In recent times, an increasing number of applications in different fields need gas sensors that are miniaturized but also capable of distinguishing different gases and volatiles. Thermal electronic noses are new devices that meet this need, but their performance is still under study. In this work, we compare the performance of two thermal electronic noses based on SnO_2 and ZnO nanowires. Using five different target gases (acetone, ammonia, ethanol, hydrogen and nitrogen dioxide), we investigated the ability of the systems to distinguish individual gases and estimate their concentration. SnO_2 nanowires proved to be more suitable for this purpose with a detection limit of 32 parts per billion, an always correct classification (100%) and a mean absolute error of 7 parts per million.

6.2 Introduction

Nowadays, the need for gas sensors is increasingly clear and important in many fields. Progress brings benefits but also hidden dangers, such as the effect of day-to-day breathing of

harmful gases that ruin health. Air pollution in urban areas is only the most obvious of these dangers to human health [207,208,209]. Numerous industrial and artisanal processes emit gases with negative long-term effects [210,211]. Many materials used for objects that share the spaces inhabited by humans release volatile substances, the dangers of which are not yet known [212]. For these reasons, it is important to be able to monitor the presence of gas in environments and activities related to human life. The availability of tiny sensors that can be integrated into buildings, cars and portable devices, such as cell phones or even wearables, would allow for the creation of wide and capillary networks capable of monitoring the situation at a high level. Sensors of this type would also be important in many other fields, such as food and beverage quality [213,183], agriculture [214], security against terrorism [215] and early medical diagnosis [216]. Metal oxides (MOs) are the ideal candidate for small and cheap devices as they work very well as chemoresistors, i.e., electrical resistors, the value of which changes according to the surrounding atmosphere (the sensor only needs two electrodes, with very simple signal reading) [217,218,219].

Furthermore, the latest generation of chemoresistors use nanostructured materials, which have a very large surface that greatly increases the response intensity. The shape [220] and, more importantly, the dimensions [221] of the nanostructures influence the sensing performance of the sensors; therefore, one of the most used materials are nanowires (NWs). N-type semiconductors have been studied for longer and more thoroughly as they perform better as gas detectors [222,223]. The two materials most studied previously are SnO_2 and ZnO, which are still the most used owing to their superior performance. Unfortunately, the fact that MOs are sensitive to a lot of gases is also a flaw as it is not possible to recognize what the sensor is detecting. In the same way, the simplicity of resistive sensors is also a defect, since the output signal they give is one dimensional and therefore intrinsically non-selective.

The traditional solution to the lack of selectivity is to combine sensors based on different materials in an array, called an electronic nose [224]. This type of device has attracted a lot of interest as it shows a good balance between performance on the one hand and size and cost on the other [225,226]. Despite this, the cost and dimensions of a traditional electronic nose do not yet to allow for its widespread diffusion and integration into everyday devices. To this end, taking up Sysoev's pioneering works [227,228], we have recently developed a new approach that uses the same nanostructured material working at different temperatures instead of different materials, as if it were an electronic nose [229,230,231].

The lower expected selectivity is balanced by the size (it can be a few square millimeters), which allows it to be easily integrated into a smartphone or smartwatch. Despite the great potential of this type of thermal electronic nose, its recent development means that its performance has not yet been studied in detail. In this work, we tested two different thermal electronic noses based on SnO_2 and ZnO nanowires working at five different temperatures. The performance of the two systems was tested against five gases: acetone, ammonia, ethanol, hydrogen and NO_2. The performance was evaluated in two steps: how well the electronic nose could distinguish the different gases and the error in the estimation of the gas concentration.

The sensor based on ZnO nanowires classified 95% of the samples correctly, while the sensor based on SnO_2 nanowires classified all gases perfectly (100%). The mean absolute error on the concentration estimate is low in both cases (7 parts per million for the SnO_2 nanowires and 11 for the ZnO nanowires), but rises to 30 parts per million (ppmv) in the case of the misclassified sample. Hence, SnO_2 nanowires work best as active materials inside a thermal gradient based electronic nose. We emphasize that this preliminary work must be reconsidered according to the boundary conditions of the application for which the electronic nose is to be used.

6.3 Materials and Methods

6.3.1 Synthesis of SnO_2 and ZnO Nanowires

Both tin oxide (SnO_2) and zinc oxide (ZnO) nanowires were grown by means of chemical vapor deposition with modifications to the recipes in order to obtain nanowires of similar size. In both growth processes, an alumina vessel containing the source powder was placed inside a quartz tube in the center of a single-zone furnace (Lingdberg Blue M, Thermo Fisher Scientific, Waltham, MA, USA) at the highest temperature point. The substrate (a 1×3 cm^2 rectangle of silicon wafer with 300 nm of thermally grown oxide and 5–7 nm of gold catalyst) was positioned downstream of the source at the optimum growth distance.

In the case of tin oxide nanowires, the source powder was 99.99% pure tin monoxide (Sigma-Aldrich, St. Louis, MO, USA), and the substrate was placed approximately 3 cm away from it. The quartz tube was pumped at $5 \cdot 10^{-3}$ mbar and purged with high-purity argon (99.999%), and this process was repeated three times to clean the system. Next, the oven was heated up to 850 °C at a rate of 50 °C per minute and held at this temperature for five minutes. Finally, 0.35 standard cubic centimeters (sccm) of oxygen was flowed through the quartz tube, starting the 30 min growth process, after which the system was shut down and cooled naturally.

In the case of zinc oxide nanowires, the source powder was 99.995% pure zinc (Sigma-Aldrich, St. Louis, MO, USA), and the substrate was placed at about 7 cm from it. The quartz tube was cleaned as explained previously and then heated at a rate of 50 °C per minute to a temperature of 730 °C. After five minutes, a mixture of 50 sccm of argon and 2 sccm of oxygen was flowed for 40 min, then the process was finished and the system cooled naturally.

6.3.2 Material Characterization

The morphology of the tin oxide and zinc oxide nanowires was characterized with secondary electron microscopy (SEM) using a Hitachi S-4800 (Tokyo, Japan). The structure was investigated with X-ray diffraction (XRD) using a Philips Xpert Pro (Malvern Panalytical, Malvern, UK) operating at 40 kV with CuKα radiation.

6.3.3 Fabrication of the Sensor

To fabricate the sensor, the nanowires were transferred to another substrate, a 1 × 2 cm^2 piece of silicon wafer with a 300 nm layer of thermally grown oxide. To perform this, each sample with the nanowires was sonicated in dimethylformamide for two seconds to obtain a dispersion, which was then deposited on the new substrate by spinning a few drops at 6000 rpm. On top of the substrate with the dispersed nanowires, a pair of interdigitated Ti/Pt electrodes with a thickness of 10/250 nm was then deposited by means of sputtering and UV lithography. The semiconductor nanowires acting as a bridge between the metal electrodes thus served as a chemoresistor.

6.3.4 Gas Sensor Measurements

Each interdigitated chemoresistive sensor was placed in the measurement chamber on top of a heatable sample holder. The measurement chamber was connected to gas cylinders through mass flow controllers in order to vary the type and concentration of gas to be tested. A pair of micromanipulators was used to contact the sensor electrodes and bring the signal to a multimeter (Keithely 2410, Cleveland, OH, USA) controlled with a home-made data acquisition program (LabView, National Instruments, Austin, TX, USA). The sensors were held at 500 °C for 6 h and powered with 1V in order to stabilize the nanowires and their base resistance [232]. Both sensors showed a linear trend of current versus voltage, demonstrating good ohmic contact. Both sensors with SnO_2 and ZnO nanowires were tested under the exact same conditions: at five different

temperatures (200, 250, 300, 350 and 400 °C) towards the same five gases (acetone, ammonia, ethanol, hydrogen and nitrogen dioxide). Each gas was measured at nine different concentrations, ranging from 5 to 250 parts per million (ppmv), in order to cover the concentrations indicated as dangerous by the institutions [233,234,235,236,237].

The definition $S = R_{AIR}/R_{GAS}$ was used to calculate the response intensity, where R_{GAS} and R_{AIR} are the resistance of the sensor in the presence of the target gas and in air, respectively. The standard definition was used to calculate the limit of detection (LoD): the intercept between the slope of the response as a function of concentration and three times the standard deviation of the signal.

6.3.5 Machine Learning

For each sensor, the response at the five temperatures, calculated as explained in the previous section, was combined into a five-dimensional point. Principal component analysis (PCA) [238] was applied to the five-dimensional points in order to reduce their dimensionality and visualize the relationships between the points relating to the various gases. The distinction of the different gases was instead carried out by a support vector machine [239] with a linear kernel used as a classifier, which worked on all five dimensions.

The points were then passed to five other support vector machines (SVM), one for each gas, depending on how they were classified in the previous step. These SVMs were used as five-dimensional regressors in order to estimate the gas concentration. It should be emphasized that for each point, the regressor relative to the gas that the system has previously classified was used, not the real one, as this can strongly increase the error in the concentration estimate.

6.4 Results and Discussion

6.4.1 Nanowire Characterization

The morphology of the zinc oxide and tin oxide nanowires obtained by chemical vapor deposition was studied with scanning electron microscopy; the SEM images are shown in Figure 6.1.

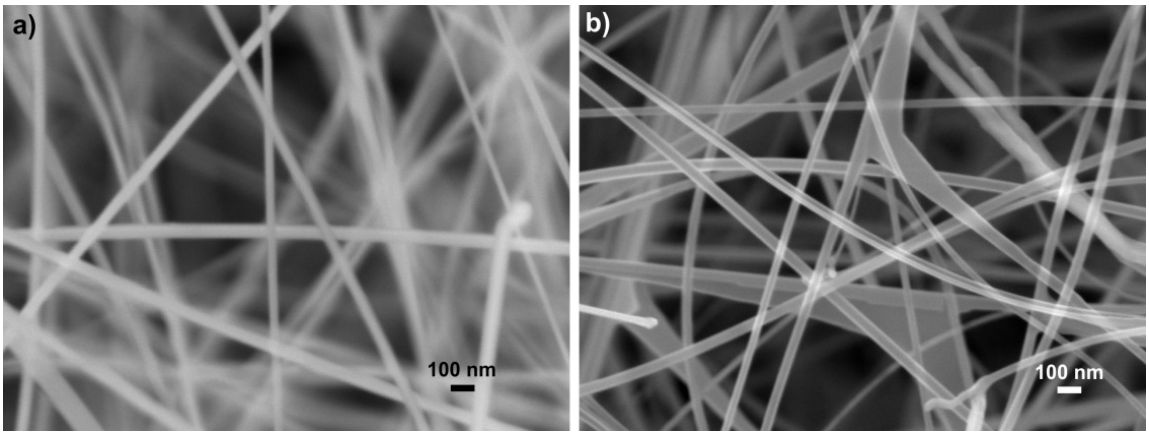

Figure 6.1 – SEM images of the nanowires grown by CVD and used as gas sensors: (a) ZnO nanowires; (b) SnO_2 nanowires.

Figure 6.1a shows the ZnO nanowires which have an average diameter of about 50–60 nm and are very constant and homogeneous. Figure 6.1b instead shows the SnO_2 nanowires, which have an average diameter of around 50–65 nm. In this case, the nanowires tend to create "sails" in some places, even if it is not a very frequent effect. The shape and size of the nanowires are quite similar, which allows for a better comparison of their performance as gas sensors.

The structure of the nanowires was investigated with X-ray diffraction, shown in Figure 6.2. The experimental patterns obtained from the samples grown by CVD (before being transferred to fabricate the sensor) are shown in the upper row (in black), while in the bottom row (in red) the reference patterns from the International Center for Diffraction Data are shown.

It is evident that the experimental pattern in Figure 6.2a agrees with the underlying reference pattern, and each peak can be easily indexed to a hexagonal wurtzite with lattice parameters of a = b

= 3.249 Å and c = 5.206 Å. Similarly, all the diffraction peaks present in the experimental pattern in Figure 6.2b can be easily indexed to the tetragonal phase of SnO_2 with lattice parameters of a = b = 4.742 and c = 3.186 Å and therefore agree well with the standard values in the pattern below. In both experimental patterns, amorphous contributions and peaks from impurities or other phases are absent, confirming the high purity of the crystalline nanowires.

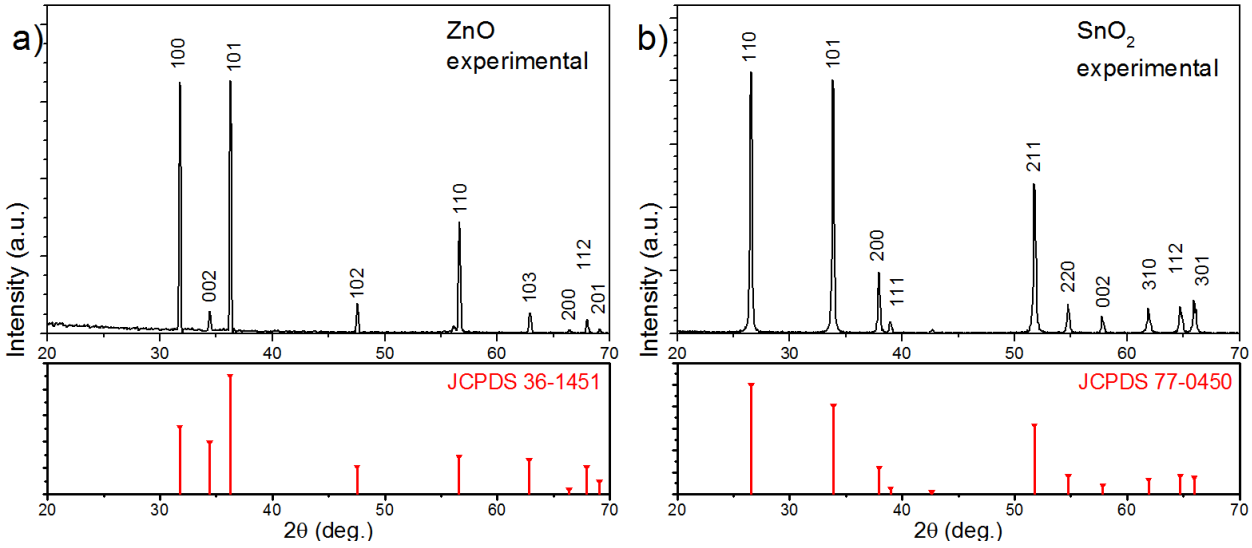

Figure 6.2. XRD patterns of the nanowires grown by CVD: (a) ZnO nanowires and (b) SnO_2 nanowires. The top images show the experimental patterns (in black), while the bottom images show the reference pattern from ICDD (in red).

6.4.2 Gas sensing Measurements

The sensor response was measured for each gas at the five temperatures (200–400 °C) in the traditional way, and the limit was calculated at each temperature. Since the sensor signal is louder at low temperatures, the LoD at 200 °C is the largest for each gas. For this reason, we considered this value as the limit of detection of the thermal electronic nose. The detection limits of the electronic nose based on ZnO nanowires were found to be 0.7, 2.1, 1.8, 1.5 and 0.9 parts per million

respectively for acetone, ammonia, ethanol, hydrogen and nitrogen dioxide. The corresponding detection limits for the SnO_2 nanowire-based electronic nose were 0.9, 1.2, 0.8, 0.2 and 0.4 parts per million. The average LoD is therefore 0.7 ppmv for the ZnO nanowires and 1.4 ppmv for the SnO_2 ones. This also partly stems from the higher resistivity of the ZnO nanowires, which makes the signal noisier.

The five response values, calculated at the five temperatures according to the definition given in Section 2.4, were then combined together in five-dimensional points of this type: $P_A = (R_A^{200°C}, R_A^{250°C}, R_A^{300°C}, R_A^{350°C}, R_A^{400°C})$ and $P_B = (R_B^{200°C}, R_B^{250°C}, R_B^{300°C}, R_B^{350°C}, R_B^{400°C})$. A single response as a one-dimensional signal is inherently non-selective. Instead, the five responses combined contain a lot of information, not only the five values but also all the correlations between them. This can be seen in Figure 6.3a: if we compare the response of a sensor at a single temperature for gas A and for gas B (one of the plots in blue on the left and the corresponding in red in the right column), it is not possible to recognize the gas in question. If, on the other hand, we combine the five responses of the left column into the radar plot in blue in the center of Figure 6.3a and those of the right column into the radar plot in red, we can clearly see the difference, since the two forms relating to the two gases are clearly different.

The radar plot relative to a gas increases in amplitude as the concentration of the gas increases, but retains the same shape. It should be emphasized that radar plots are used only to be able to easily compare the responses of the thermal electronic nose to different gases: the machine learning algorithms work in 5D (using the points P_A and P_B, like in Figure 6.3b). Unfortunately, it is impossible to compare too many overlapping shapes in a radar plot. Since 5D space is impossible to visualize, the best way to see relationships be-tween responses related to different gases is to perform a principal component analysis, which reduces dimensionality (in our case from 5D to 3D

or 2D) while keeping as much information as possible. Figure 3c shows how the two radar plots (blue and red) in Figure 6.3a appear in a PCA graph after reducing from five to three dimensions: each radar graph becomes a single point, which contains almost all the information of the five responses at different temperatures.

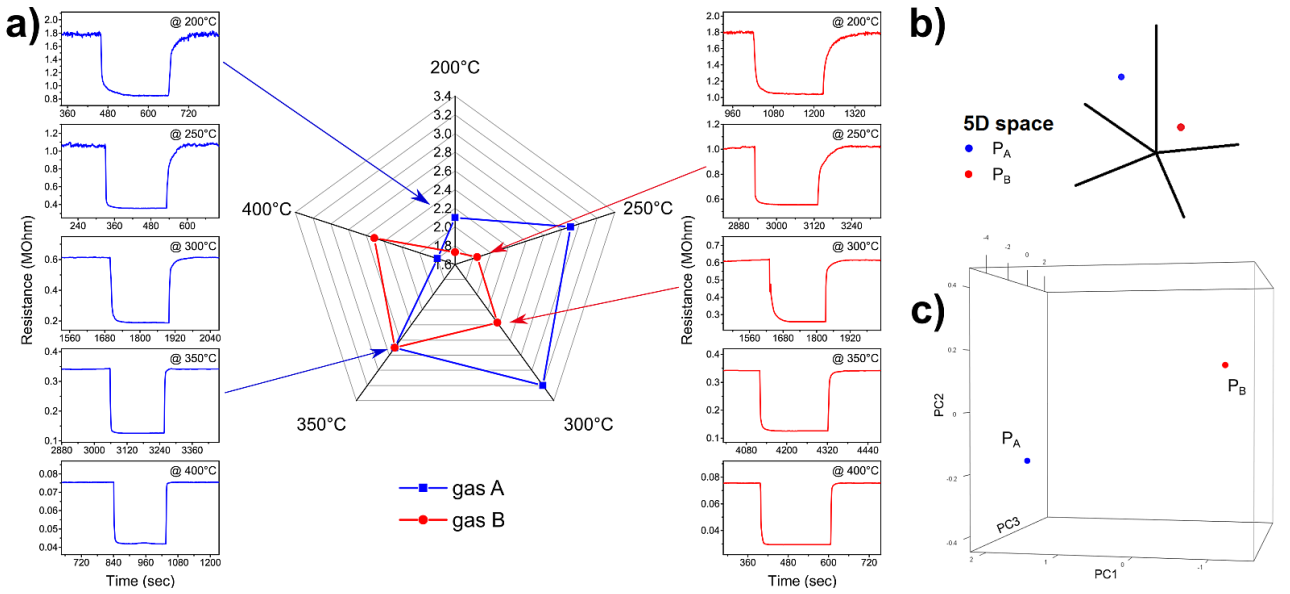

Figure 6.3 – Procedure for combining the five sensor responses at different temperatures: (a) the responses calculated in the five graphs in each column (blue and red) are combined into a radar plot (blue and red, respectively); (b) the five response values become a five-dimensional point; (c) which, in our case, is reduced to three dimensional by PCA.

In this way, it is possible to plot many points relative to different gases and clearly perceive the relationships between points of different gases or of the same gas at different concentrations. The greater the distance between the two points in the graph, the greater the measures from which they derive are different from each other.

6.4.3 Qualitative Distinction

As the first step, we plotted the responses of the sensors as radar plots to qualitatively evaluate how selective the two sensors are. The graphs obtained with the sensor based on SnO_2 nanowires are

shown in the upper row of Figure 6.4, while those obtained with the sensor based on ZnO nanowires are shown in the lower row.

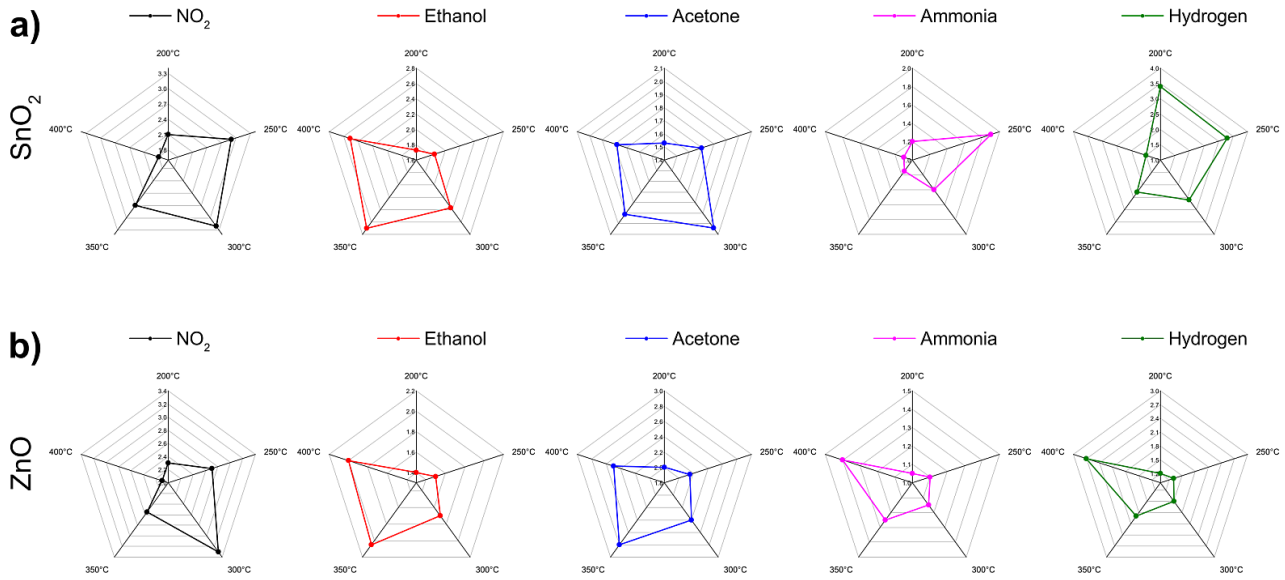

Figure 6.4 – Radar plots obtained by measuring 100 ppmv of each gas at five temperatures: (a) with the sensor based on SnO_2 nanowires; (b) with the sensor based on ZnO nanowires.

As can be seen, the radar plots shown in the upper row of Figure 6.4 are quite different from each other and therefore seem to indicate a good selectivity of the sensor. On the bot-tom row, however, the last two radar plots look quite similar. In reality, the responses to hydrogen are much greater, as can be seen from the scale of the radar plot, but the selectivity (classification of the different gases) is based only on the shape and not on the size of the plot.

Unfortunately, this method does not work well if one wants to compare different points of each gas because the graph becomes confusing with more than 3–4 plots. For this reason, we used the principal component analysis on the five-dimensional points obtained from the sensor responses, and the results are shown in Figure 6.5.

Although both methods (radar plots and PCA plots) are just approximations of the 5D situation, the PCA plots shown in Figure 6.5 can show many points more clearly. In Figure 6.5, the components PC2 and PC3 are shown since the component PC1 is mainly due to the variation in gas concentration; therefore, the figure shows the best point of view to appreciate the separation between the different target gases. The difference between the graph obtained with the SnO_2 nanowires (left) and the one obtained with the ZnO nanowires (right) is remarkable since in the first graph the points relating to each gas seem clearly more separated.

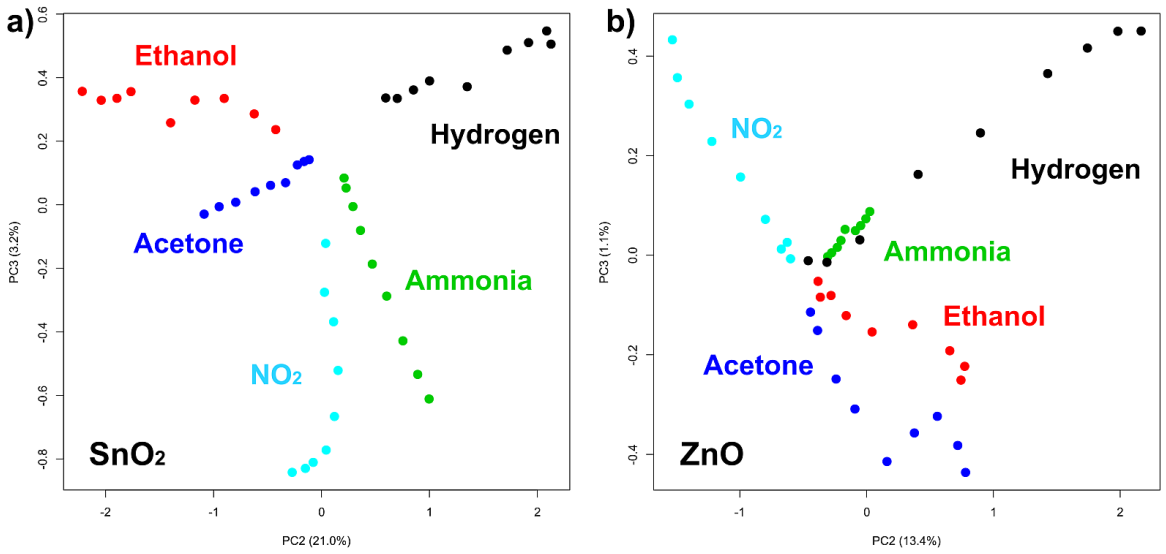

Figure 6.5 – PCA plots showing measurements of the five gases obtained with (a) the sensor based on SnO_2 nanowires and (b) the sensor based on ZnO nanowires.

In order to try to improve the distinction between gases, we attempted to normalize each group of five responses (each radar plot, or each point in the PCA) to its highest value. In this way, we expected the specificity of each gas (the shape of its radar plot) to be more important than the concentration in the comparison for the classification of the gas.

In each image, the view that best separates the points of the different gases was chosen. As can be seen, the points in Figure 6.6a separate even better than in Figure 6.5a, demonstrating that

normalization helps classification by reducing the contribution due to gas concentration. Unfortunately, the effect is minimal in Figure 6a, in which it seems that some gases are still not very separated.

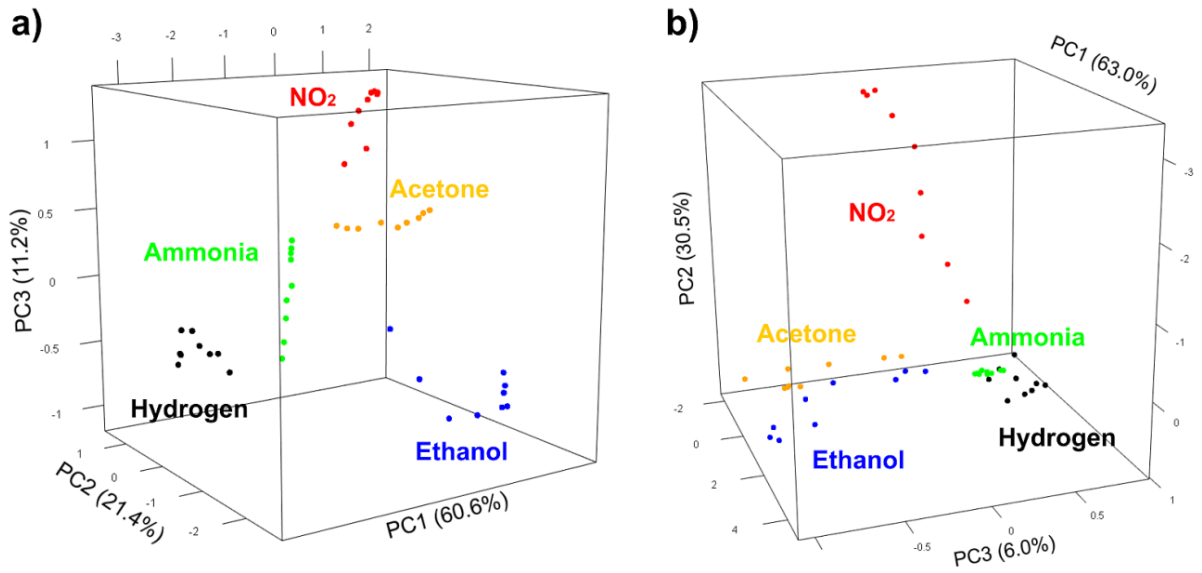

Figure 6.6 – PCA plots showing the measurements after normalization obtained with (a) the sensor based on SnO_2 nanowires and (b) the sensor based on ZnO nanowires.

However, it should be emphasized that these are only dimensional reductions of the true five-dimensional space, which is also limited by our visual perception. Hence, to have an objective vision that is not approximate and not distorted by human perception, we used machine learning algorithms that work directly in five dimensions.

6.4.4 Classification

A support vector machine, used as a classifier, was used as the "brain" for the distinction between gases. This machine learning algorithm is supervised, meaning it needs data to "learn" how to classify. For this reason, five different concentrations for each gas (5, 20, 50, 150 and 250 ppmv)

were used as the training dataset. Four other concentrations (10, 30, 100 and 200 ppmv) were then used to test the performance of the sensing system.

The 5D points of the training set are used by the algorithm to identify hyperplanes (4D spaces) that divide the 5D space into zones related to each gas. Once this map has been created (as a sort of calibration), the next points are automatically compared with the map and classified according to the zone of 5D space they fall into.

The results of the classification obtained with the sensor based on SnO_2 nanowires are shown in Table 6.1.

Table 6.1 – Confusion matrix obtained with the sensor based on SnO_2 nanowires.

		Estimated				
		Acetone	Ammonia	Ethanol	Hydrogen	NO_2
	Acetone	4				
	Ammonia		4			
True	Ethanol			4		
	Hydrogen				4	
	NO_2					4

As can be seen from the confusion matrix in Table 6.1, all measured points were correctly classified; therefore, the sensor based on SnO_2 nanowires perfectly distinguished the tested gases, albeit at different concentrations.

The same procedure was carried out with the five-dimensional points obtained from the responses of the sensor based on ZnO nanowires, and the results are reported in Table 6.2.

Table 6.2 – Confusion matrix obtained with the sensor based on ZnO nanowires.

		Estimated				
		Acetone	Ammonia	Ethanol	Hydrogen	NO_2
	Acetone	4				
	Ammonia		4		1	
True	Ethanol			4		

Hydrogen	3	
NO_2		4

In this case, 19 out of 20 points are correctly classified, but one is misclassified. To be exact, the system mistakes the lowest concentration point of hydrogen for ammonia. This is in accordance with Figures 6.5b and 6.6b, where the ammonia points are very close to the low concentration points relating to hydrogen.

It should be emphasized that this result is a much more advanced step than those in Section 6.4.2, since the thermal electronic nose in this case is able to distinguish gases autonomously, without a human having to observe any image and deduce anything. In fact, while the colors in Figures 6.5 and 6.6 were given knowing a priori which gas it was, in this case, once trained, the electronic nose understands by itself which gas is being measured. The electronic nose based on ZnO nanowires correctly recognized the gas only in 95% of cases, while the one based on SnO_2 nanowires recognized them all perfectly (100%).

6.4.5 Quantification

Once the gas was recognized with the classifier, the data were split based on the gas that the system recognized (right or wrong) and passed to another support vector machine. The five support vector machines, each related to a gas, worked as regressors in the five-dimensional space to estimate the gas concentration. The regression results are shown in Figure 6.7.

Figure 6.7a shows the estimated concentration from the thermal electronic nose based on SnO_2 nanowires. The true concentration is on the abscissa, while on the ordinate there is the estimate of the electronic nose; therefore, the diagonal represents the perfect result. The estimates are all very close to the diagonal, with a very low error. The mean absolute error (MAE) is in fact less than 10 parts per million for all gases. Furthermore, at low concentrations, the estimates are always higher

than the true concentration, and this is positive for the sensor: a possible threshold alarm would trigger with some false positives, but it would not risk tripping in the presence of gas.

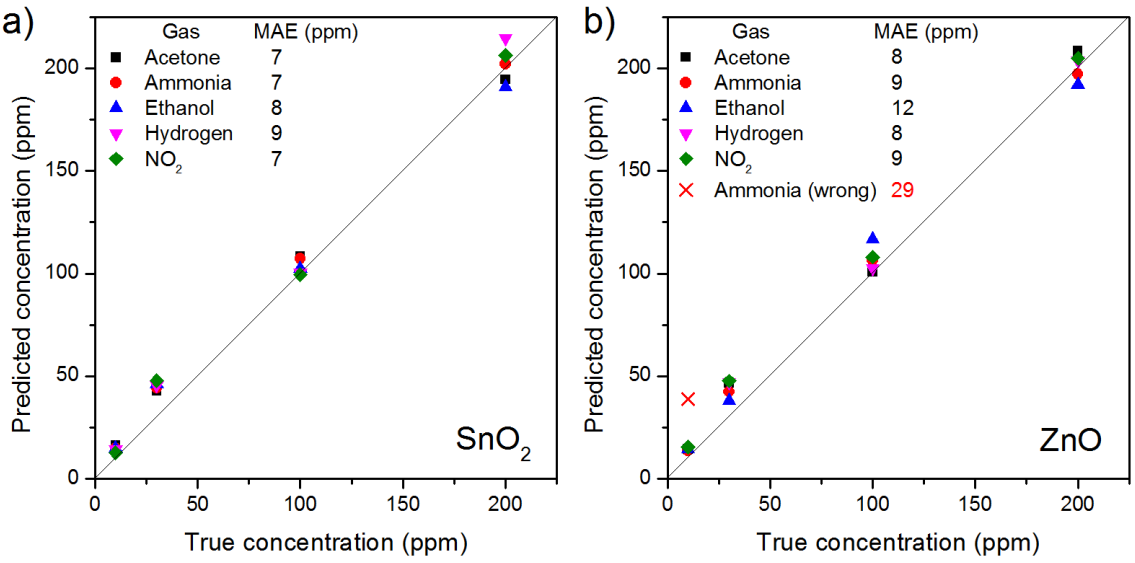

Figure 6.7 – Predicted gas concentration as a function of the true concentration by the thermal electronic nose based on (a) SnO_2 nanowires and (b) ZnO nanowires.

The situation is worse in Figure 6.7b, which was obtained with the responses of the electronic nose based on the ZnO nanowires. In this case, the error on the estimate is generally greater, even if it remains good. The error increases significantly if we consider the wrongly classified measurement, since in this case 10 ppmv of hydrogen was confused as 40 ppmv of ammonia. It is therefore clear that classification is the most important step as it strongly influences the performance of gas concentration quantification.

6.5 Conclusions

The performance of two thermal electronic noses, identical in every respect except for the active material used as a sensor (ZnO and SnO_2 nanowires, respectively), were studied regarding

five gases (acetone, ammonia, ethanol, hydrogen and nitrogen dioxide). Nine different concentrations were measured for each gas from 5 to 250 ppmv in order to test the performance along the entire concentration range around the hazard threshold. The electronic nose based on ZnO nanowires showed a correct classification in 95% of cases and an error that was influenced by the misclassifications. The detection system based on SnO_2 nanowires, on the other hand, classified perfectly (100%) and estimated the concentration of all five gases with a mean absolute error of less than 10 ppmv. The electronic nose based on SnO_2 nanowires at different temperatures is therefore a good candidate for a gas detection system that is selective and small enough to be integrated into smartphones and other devices.

CHAPTER 7. NANOSENSOR BASED ON THERMAL GRADIENT AND MACHINE LEARNING FOR THE DETECTION OF METHANOL ADULTERATION IN ALCOHOLIC BEVERAGES AND METHANOL POISONING

This chapter is based on the scientific paper [240]:

"Nanosensor based on thermal gradient and machine learning for the detection of methanol adulteration in alcoholic beverages and methanol poisoning", Sensors, 22 (2022) 5554. Doi: 10.3390/s22155554.

7.1 Abstract

Methanol, naturally present in small quantities in the distillation of alcoholic beverages, can lead to serious health problems. When it exceeds a certain concentration, it causes blindness, organ failure, and even death if not recognized in time. Analytical techniques such as chromatography are used to detect dangerous concentrations of methanol, which are very accurate but also expensive, cumbersome, and time-consuming. Therefore, a gas sensor that is inexpensive and portable and capable of distinguishing methanol from ethanol would be very useful. Here, we present a resistive gas sensor, based on tin oxide nanowires, that works in a thermal gradient. By combining responses at various temperatures and using machine learning algorithms (PCA, SVM, LDA), the device can distinguish methanol from ethanol in a wide range of concentrations (1–100 ppmv) in both dry air and under different humidity conditions (25–75% RH). The proposed sensor, which is small and inexpensive, demonstrates the ability to distinguish methanol from ethanol at different

concentrations and could be developed both to detect the adulteration of alcoholic beverages and to quickly recognize methanol poisoning.

7.2 Introduction

Methanol, alcohol produced naturally (in minimal quantities) in the distillation and production of alcoholic and even non-alcoholic beverages, can be highly toxic to human health. Methanol poisoning, which usually occurs by ingestion, can lead to irreversible tissue damage, especially to the eyes and nervous system, or even death [1]. This happens because methanol is metabolized by the body to form formic acid, formate, and formaldehyde [2], which are very toxic [3]. Outbreaks of methanol poisoning occur frequently in many countries, with hundreds of deaths due to adulterated alcohol [4]. Examples include the 959 cases in Iran (October 2018) [5], 237 in Cambodia (May 2018) [6], 45 deaths in Malaysia (October 2018) [7], and more than 250 deaths in India (February 2019) [8,9]. Furthermore, methanol is often used as a solvent or chemical raw material in chemical laboratories and plants [10], which creates a risk of intoxication even by inhalation or absorption from the skin [11].

Methanol intoxication is usually detected in the blood by analytical techniques such as gas-liquid chromatography and blood gas analysis [12], which require qualified personnel and are costly in terms of both time and money. For these reasons, they are not readily available, especially in non-urban areas and in developing countries, where out-breaks are more frequent [13]. Levels of methanol intoxication can also be determined non-invasively in exhaled breath [14], such as what is performed daily by law enforcement with ethanol [15]. Although the average concentration of methanol in the breath of healthy people is less than 1 ppmv, concentrations up to 10 ppmv may be found in some cases [14], while concentrations above 150 ppmv are considered a symptom of severe

intoxication [1]. The recommended airborne exposure limit (REL) by the American National Institute for Occupational Safety (NIOSH), Occupational Safety and Health Administration (OSHA), and American Conference of Governmental Industrial Hygienists (ACGIH) is 200 ppmv averaged over a 10-h work shift [16].

The challenge is therefore to distinguish methanol from ethanol and quantitatively estimate their amount with a small, inexpensive, and portable device. Similarly, such a device would also be important for screening alcoholic beverages in order to prevent methanol poisoning. Gas chemosensors are ideal candidates for this application, as they are simple to make and use, inexpensive, and miniaturizable [17]. Chemoresistive sensors based on metal oxide nanostructures have been shown to detect various analytes at concentrations below parts per million (ppmv) in a very short time [18]. Unfortunately, these materials are not very selective even if their morphology and structure are optimized to increase porosity and reactivity [19].

Due to this poor selectivity, it is difficult to distinguish two similar molecules such as ethanol and methanol. Although SnO_2 is one of the metal oxides with the best properties and therefore most used for gas sensors, even the finest nanostructures such as cross-linked porous nanosheets [20] and hollow nanoparticles [21] exhibit very similar responses to these two gases, making them difficult to distinguish. Therefore, chemoresistors are usually joined in arrays called *electronic noses*, which exploit different materials to obtain good selectivity [22,23]. The interest in electronic noses leads to the study of the most innovative materials, such as graphene and graphene oxide, and the use of algorithms such as the support vector machine (SVM) allows one to obtain good quantitative results [24].

Most resistive electronic noses use different metal oxides (SnO_2, ZnO, WO_3) and different surface decorations with metal nanoparticles (Ag, Pt, Pd) to obtain good performance also in the

detection of ethanol and methanol [25]. Being composed of different sensors based on different materials (metal oxides, polymers, small conjugated molecules, and others) that require different working conditions, heaters, and electrodes for individual signal acquisition, current electronic noses are still rather complex and ex-pensive.

Here we describe a gas sensor, based on tin oxide (SnO_2) nanowires, that aims at selectivity, not using different materials but rather different operating temperatures. The detection mechanism is based on the chemical reactions that take place on the surface of the nanowires, where the volatile molecules react by releasing or absorbing electrons, changing the resistance of the sensor. The material response changes with both the temperature and volatile compound concentration. This produces a "thermal/chemical fingerprint" which can be the basis of an electronic nose [26].

This approach has already been demonstrated on agrifood products by evaluating the freshness of meat and fish [27,28]. In practice, we join the responses at different temperatures (as if they came from different sensors) and combine them in multidimensional points. Analyzing them with machine learning algorithms and multivariate statistical analysis techniques (principal component analysis, support vector machine, linear discriminant analysis), we demonstrate that the sensor is not only able to distinguish ethanol and methanol, but also to estimate their concentration. Considering the aforementioned hazard and intoxication thresholds, the sensor was tested in a concentration range of 1 to 100 ppmv.

The sensor has been tested with different concentrations of ethanol and methanol under more realistic and difficult conditions (relative humidity of 25 to 75%) and proved to be able to distinguish the two alcohols under any conditions. This performance makes the nanowire-based sensor an excellent candidate for rapid and inexpensive screening for the presence of methanol in both intoxicated patients and potentially adulterated beverages.

7.3 Materials and Methods

7.3.1 Synthesis of SnO_2 Nanowires

A forest of tin oxide nanowires was initially grown by chemical vapor deposition (CVD). An alumina boat filled with pure tin monoxide was placed as an evaporation source in the center of an oven (Lindberg Blue M, Thermo Fisher Scientific, Waltham, MA, USA) where the temperature is highest. Close to it (1 cm), a silicon substrate of approximately 1×2 cm^2 was placed, on which a thin gold film (thickness of approximately 5 nm) acted as a catalyst. The quartz tube was then pumped down to 10^{-2} mbar and purged with high-purity argon (99.999%), repeating these two steps three times, and finally, the system was pumped down to $8 \cdot 10^{-3}$ mbar. While the system was in a vacuum, the temperature was increased from room temperature (23 °C) up to 800 °C at a rate of 25 °C/min and then the oven was held at 800 °C for five minutes. At this point, an oxygen flow of 0.35 standard cubic centimeters (sccm) was injected into the system in order to start the growth of the nanowires. The growth of the nanostructures, which follows the gold-catalyzed vapor liquid solid (VLS) mechanism [29], lasted 30 min, after which the system was shut down and allowed to cool. At the end of the growth process, the sample surface showed a homogeneous white film.

7.3.2 Nanowires Characterization

The morphology of the SnO_2 nanowires was studied by secondary electron microscopy (SEM) with a Hitachi S-4800 (Tokyo, Japan). The structure of the nanowires was investigated by X-ray diffraction (XRD) using a Philips Xpert Pro diffractometer (Malvern Panalytical, Malvern, UK) working at 40 kV with CuKα radiation.

7.3.3 Sensor Fabrication

The nanowires were transferred to another substrate via sonication and drop-coating. The sample with the nanowire forest obtained from the CVD was ultrasonicated in dimethylformamide for ten seconds to obtain a dispersion of nanowires. A few drops of this dispersion were deposited on a piece of silicon wafer with a 300 nm layer of thermally grown oxide. Two interdigitated Ti/Pt electrodes were then deposited via sputtering and UV lithography on top of the nanowires, so that they formed a chemiresistor. The device was subjected to eight-hour thermal annealing at 500 °C in nitrogen in order to stabilize the structure and electrical characteristics [18].

7.3.4 Gas Sensor Measurements

The chemoresistive sensor was placed on a heatable sample holder in a vacuum chamber connected to high-purity gas cylinders through mass flow controllers and a mixing chamber. Two microprobes were connected to the metal electrodes in order to read the resistance of the nanowires with a multimeter (Keithely 2410, Cleveland, OH, USA) controlled by data acquisition software (LabView, National Instruments, Austin, TX, USA). The sensor was tested at five different temperatures (180–300 °C) over a concentration range of ethanol and methanol ranging from 1 to 100 ppmv. The sensor response was defined as $S = R_{air}/R_{gas}$, where R_{air} and R_{gas} are the resistance of the sensor in the air and in the presence of gas, respectively. The measurements on the liquid mixtures were carried out by placing the sensor approximately 1 cm above the vessel with the alcohol mixture in the measurement chamber, letting the system reach equilibrium.

7.3.5 Machine Learning Techniques

Since a resistive sensor provides a one-dimensional response (a single pure number, a ratio between two electrical values), it is inherently non-selective. For this reason, the sensor responses at five different working temperatures (180, 210, 240, 270, and 300 °C) were combined to create 5-

dimensional points to be processed with multivariate statistical analysis techniques [26]. The 5D points obtained were analyzed with different techniques in order to evaluate different aspects of the sensor performance. Principal component analysis (PCA) was used to graphically visualize the relationships between gas measurements, as it reduces the dimensions (from five to two) while maintaining as much in-formation as possible. Linear discriminant analysis (LDA) was used to quantitatively evaluate the sensor's ability to distinguish the two gases, as it maximizes the separation between classes (in our case the two gases at different concentrations). To confirm the classification of the LDA, a Euclidean UPGMA clustering was also used. The support vector machine (SVM) was used to obtain an estimate of the gas concentration through linear regression. SVM regression measurements were performed using concentrations 1, 3, 5, 10, 20, 50, and 100 ppmv as the training set and 2, 4, 8, 15, 30, and 80 ppmv as the test set. The classification of the measurements with LDA in humidity and the measurements of alcoholic mixtures were carried out with cross-validation, using all the possible per-mutations of training and test data.

7.4 Results and Discussion

7.4.1 Nanowires Characterization

The nanowires that made up the white layer obtained from CVD were initially studied by secondary electron microscopy to study the morphology of the nanomaterial. Figure 7.1a confirms that the material is a forest composed of long, thin nanowires arranged chaotically. The nanowires are several microns long and have constant and rather homogeneous diameters of approximately 40–70 nm. Figure 7.1a is blurred because of the accumulated charge due to the very high electrical resistance of the nanowires.

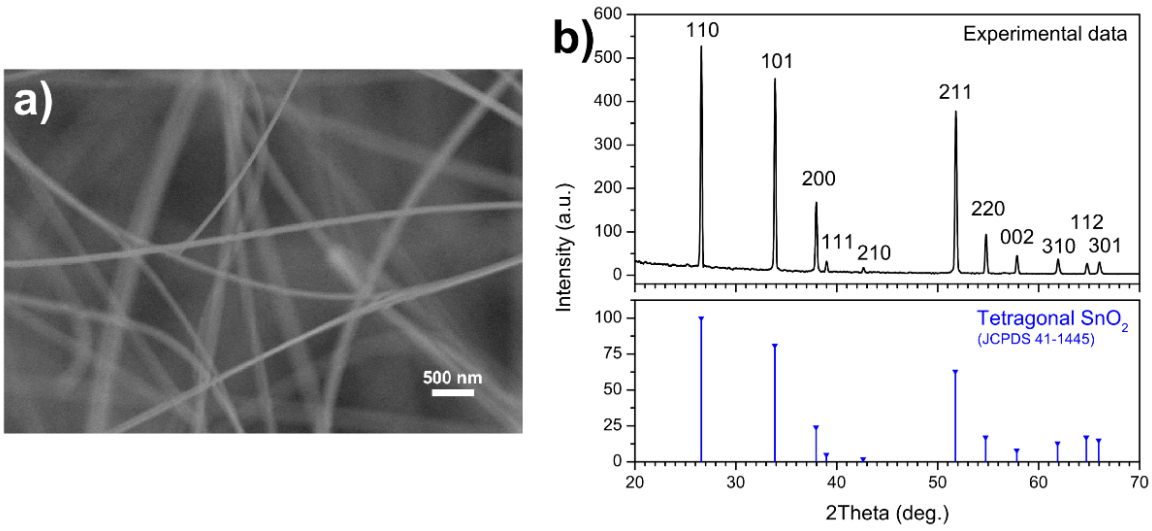

Figure 7.1 – (a) SEM image and (b) XRD pattern of the SnO_2 nanowires.

The composition and structure of the nanowires were investigated by means of X-ray diffraction. The top pattern in Figure 7.1b shows many intense and sharp peaks, which can be easily assigned to the reflections of the SnO_2 tetragonal phase, with lattice parameters of a = b = 4.742 and c = 3.186 Å. As can be seen in the pattern in the lower part of Figure 7.1b (in blue), the experimental peaks aptly match those in the reference JCPDS n. 77-0450. The pattern in Figure 7.1b does not show other phases besides the tetragonal SnO_2, nor peaks due to impurities or amorphous contributions, and therefore confirms the good crystallinity of the nanowires.

7.4.2 Traditional Gas Measurements

The performance of the gas sensor based on SnO_2 nanowires was initially studied in a traditional way. The dynamic response of the device at various temperatures is shown in Figure 7.2a,b. The sensor was subjected to different concentrations of ethanol (Figure 7.2a) and methanol (Figure 7.2b) ranging from 1 to 100 ppmv. Both graphs show that the response increased rapidly when the gas was injected and decreased even more rapidly when the gas was replaced by dry air. The intensity of the response increases with increasing gas concentration, as expected, and the signal

fully recovers when dry air is injected, with no noteworthy drifts. The graphs in Figure 7.2c,d show the response of the sensor as a function of the gas concentration (ethanol in Figure 7.2c and methanol in Figure 7.2d).

The response clearly increases with concentration, initially more markedly and then more slowly, and increases with increasing operating temperature. The graphs in Figure 7.2, although different, are quite similar: The response increases with the gas concentration and temperature for both ethanol and methanol. The traditional analysis of the sensor response does not allow us to distinguish the two gases.

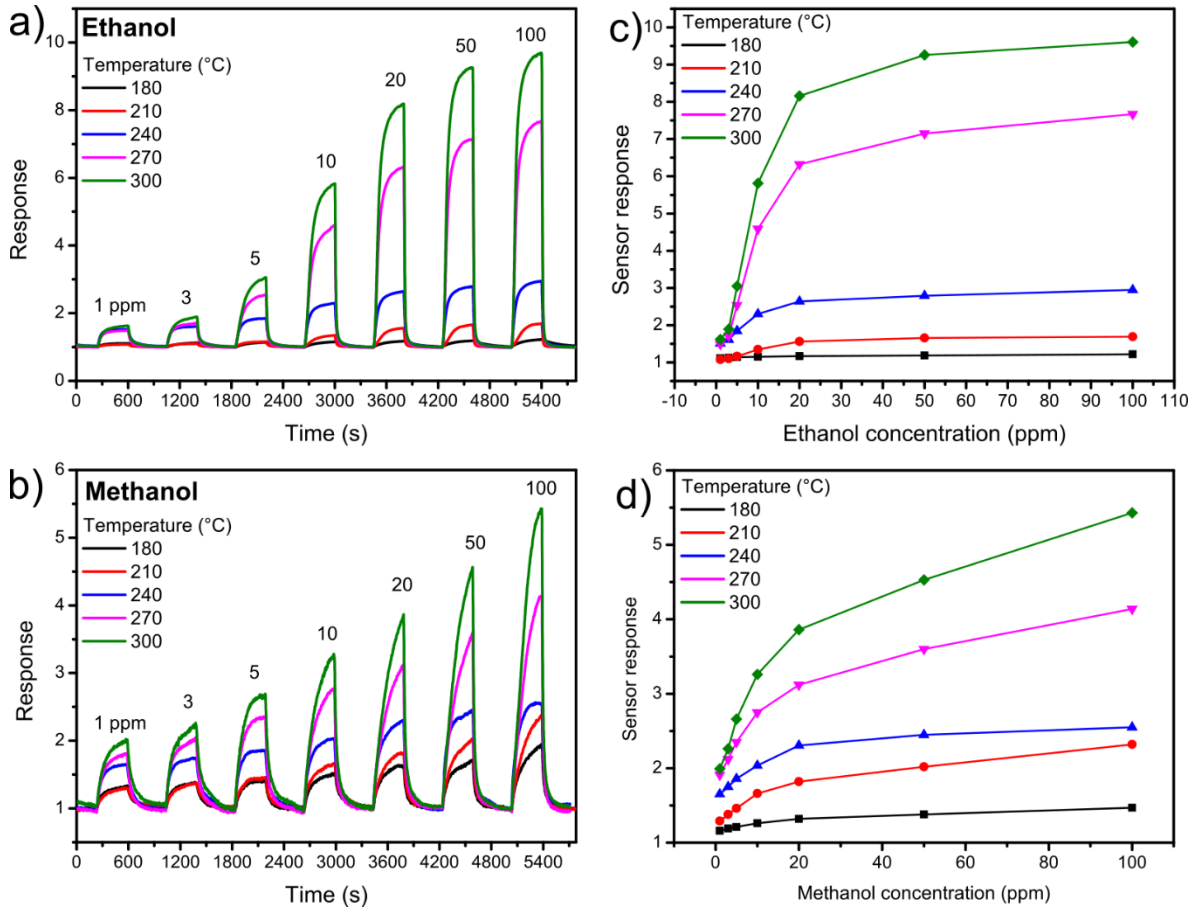

Figure 7.2 – Dynamic response of the sensor to different concentrations of (a) ethanol and (b) methanol at different temperatures; response as a function of gas concentration for (c) ethanol and (d) methanol at different operating temperatures.

7.4.3 Machine Learning: Visualization and Classification

To achieve selectivity and to be able to distinguish ethanol from methanol, the responses of the sensor at the five temperatures were combined in 5D points and analyzed with different techniques of multivariate statistics and machine learning. The first technique used is principal component analysis (PCA), a technique that allows the dimensions to be reduced from five to two (so that points can be visualized) while retaining maximum information from the original data. The graph of the first two main components is shown in Figure 7.3, where the points relating to ethanol are green and those relating to methanol are violet. It is clear that the points relating to the two gases lie on different lines, and it is therefore easy to distinguish them qualitatively. The points of each gas lie on a line because they are measurements at different concentrations: The leftmost points are the measurements at 1 ppmv, and moving to the right, the points are relative to measurements at higher concentrations, up to 100 ppmv (they are the same concentrations as in Figure 7.2a,b). Figure 7.3 intuitively demonstrates that the sensor is able to distinguish the points relating to the two gases, but it is not enough. For this reason, linear discriminant analysis (LDA) was also used, which is shown in the inset of Figure 7.3 and confirms how the points relating to the two gases are clearly distinct, also in a quantitative way. This means that the gas sensor is able to distinguish the two gases despite the different concentrations tested.

7.4.4 Machine Learning: Quantification

To assess the danger of methanol poisoning or an adulterated drink, it is necessary not only to detect its presence, but also its concentration (in the breath or in the drink). To obtain an estimate of the gas concentration, a support vector machine (SVM) was used, a supervised technique that uses the first set of data as “calibration” [30,31]. The data used for Figure 7.2 was used as a training set,

while other concentrations (2, 4, 8, 15, 30, and 80 ppmv) were used to test the sensor performance in estimating the gas concentration.

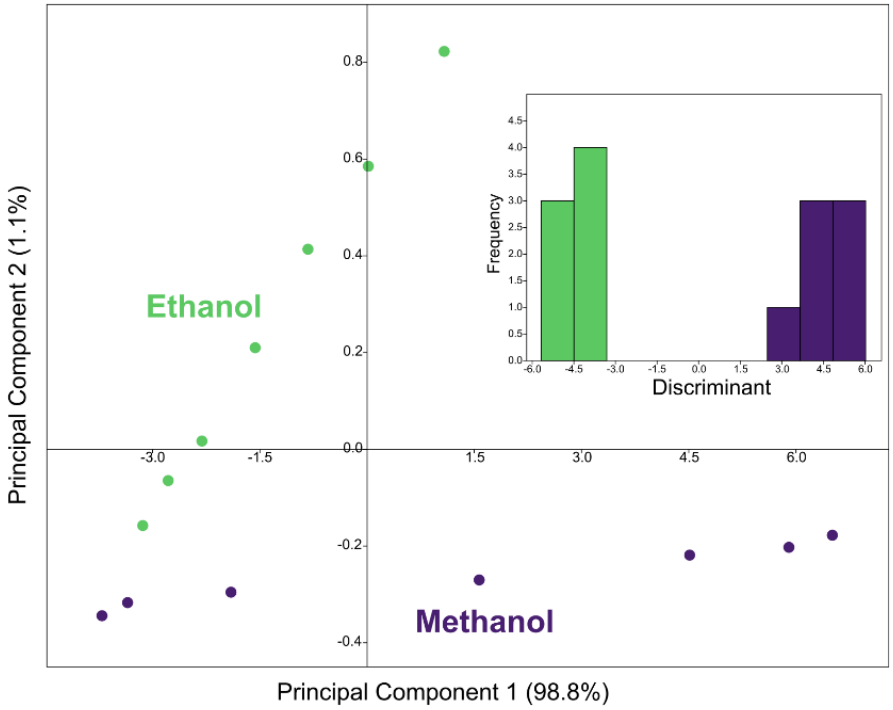

Figure 7.3 – Plot of the first two main components illustrating the measurements at different concentrations (1 to 100 ppmv) of ethanol (in green) and methanol (in violet). Inset: Linear discriminant analysis of the points relating to the two gases, which shows how they are separated and distinguishable.

The concentrations of the test dataset were chosen halfway between those of the training dataset in order to make the work more difficult for the sensor and to obtain the estimate in the worst realistic conditions. The linear support vector machine performed a regression in the five-dimensional space and the sensor provided the estimates shown in Figure 7.4.

The X-axis shows the nominal concentration tested, while the estimate provided by the sensor is shown on the Y-axis. The diagonal therefore represents the perfect estimate: The closer a point is to it, the more correct the estimate is. The blue dots in Figure 7.4a are related to ethanol, and are very close to the diagonal, demonstrating good sensor accuracy. In fact, the mean absolute error of

the sensor on the ethanol concentration is only 3.1 ppmv. The green dots in Figure 7.4b refer to methanol, and are also close to the diagonal, confirming an accurate estimate for methanol as well.

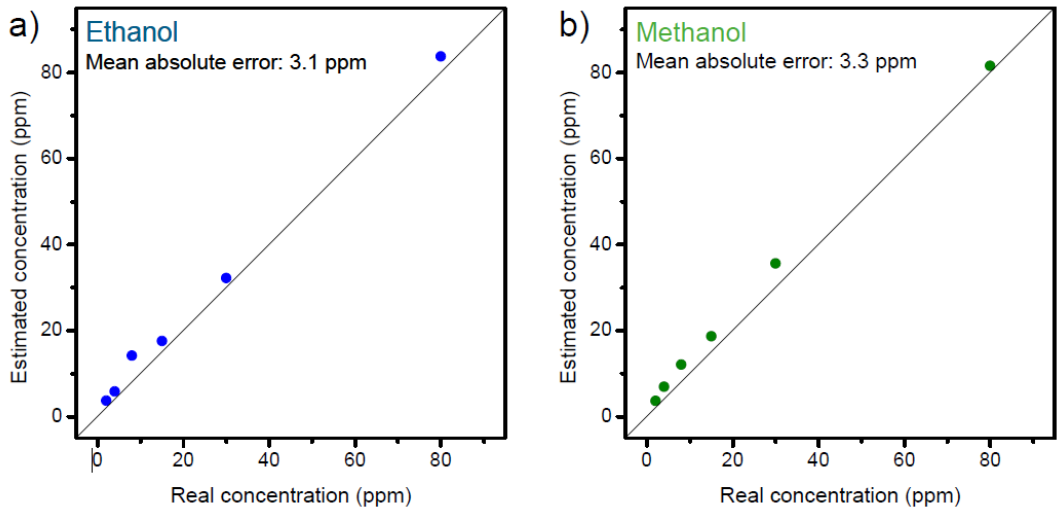

Figure 7.4 – Estimation of the concentration of (a) ethanol and (b) methanol, obtained with a linear regression by means of a support vector machine.

The mean absolute error for methanol is 3.3 ppmv. It can be seen in both plots that the sensor estimate is always higher than the nominal value, and this is useful since it is more dangerous to underestimate the methanol concentration than to overestimate it, whether in the case of an intoxicated person or an adulterated drink.

7.4.5 Relative Humidity

The measurements shown in the previous graphs were obtained in dry air, but both the breath and the headspace of a drink have high relative humidity. For this reason, the sensor has been tested in different relative humidity conditions, in order to understand how its performance varies. To statistically evaluate the performance of the sensor, three concentrations of each gas (1, 10, and 100 ppmv) were chosen, and each measurement was repeated eight times, in order to evaluate the

repeatability of the measurement. This procedure was repeated at different relative humidity values: 0, 25, 50, and 75%.

The five-dimensional space was reduced by principal components analysis, and Figure 7.5 shows the results in 2D plots. Figure 7.5a shows the points in dry air (0% relative humidity, RH), and the groups of points related to each concentration of each gas are colored differently (shades of blue for ethanol and green for methanol).

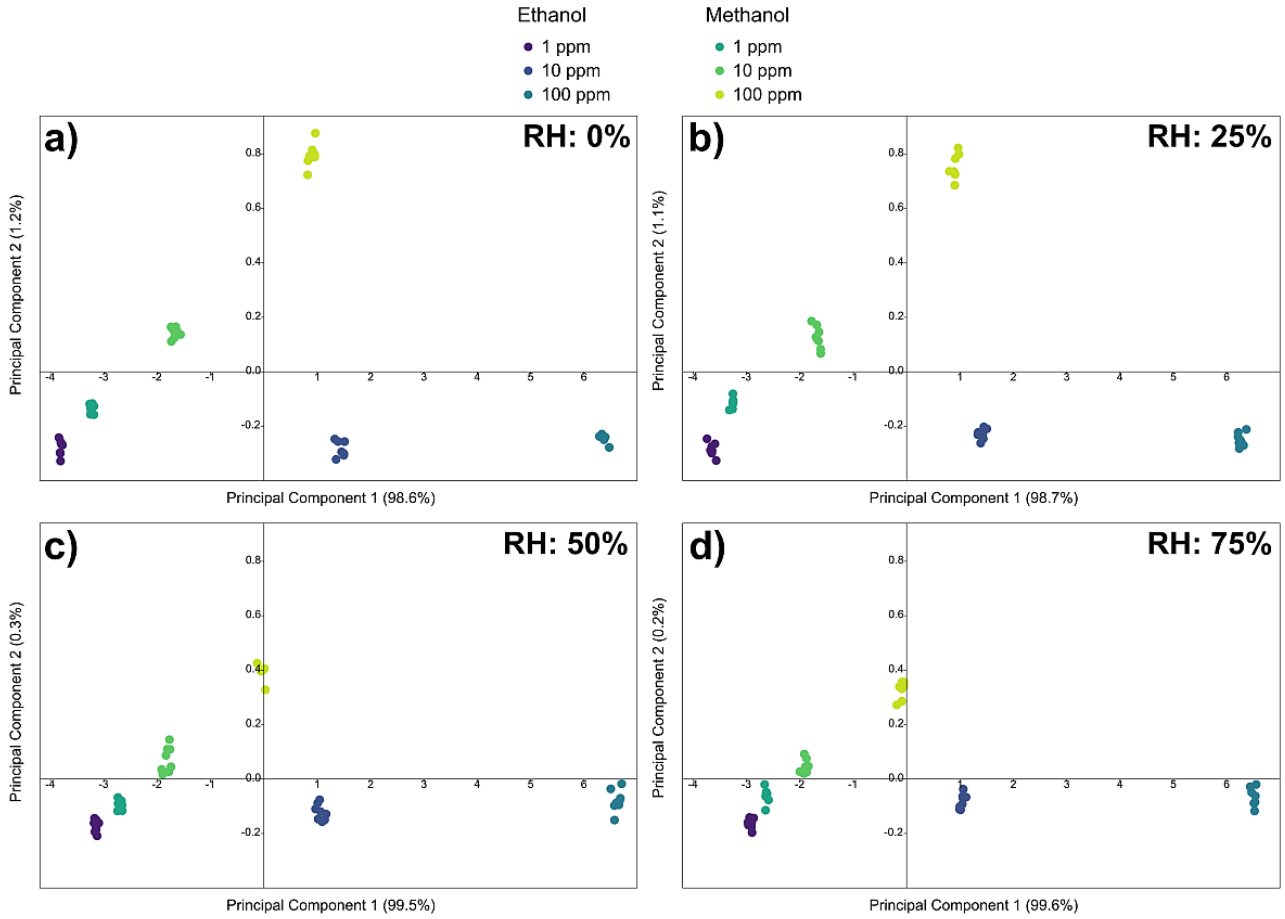

Figure 7.5 – Plots of the principal components for concentrations of 1, 10, and 100 ppmv of ethanol and methanol at (a) 0%, (b) 25%, (c) 50%, and (d) 75% relative humidity.

At the bottom, from left to right, there are the concentrations of ethanol (1, 10, and 100 ppmv), while from the bottom left, going up diagonally, there are the concentrations of methanol, in the

same order. In Figure 7.5b, there are the points obtained at 25% RH, in Figure 7.5c those at 50% RH, and in Figure 7.5d those at 75% RH. The arrangement of the point groups is roughly always the same.

To better compare the performance under various humidity conditions, the graphs were made with the same dimensions. The distribution of the groups of points is similar in the four graphs, but it can be noticed how, as the relative humidity increases, the groups of points tend to become closer. On the one hand, the points relating to the highest concentrations of ethanol move upwards slightly, closing the gap with those of methanol. On the other hand, the points relating to methanol at higher concentrations drop a lot towards those of ethanol and towards the lower concentrations on the left. Qualitatively, this shows that the discrimination between the various concentrations of the various gases becomes a little more difficult. Unfortunately, PCA plots are purely qualitative and influenced by the perception of the human eye. To obtain a less subjective idea of the sensor performance, linear discriminant analysis was applied, the results of which are shown in Table 7.1.

Table 7.1 – Confusion matrix of the classification of the different types of measurements (type of gas and its concentration).

		Estimated					
		Ethanol			**Methanol**		
		1 ppmv	10 ppmv	100 ppmv	1 ppmv	10 ppmv	100 ppmv
True	1 ppmv	8					
	10 ppmv		8				
	100 ppmv			8			
	1 ppmv				8		
	10 ppmv					8	
	100 ppmv						8

Only one table is shown since the results in the four relative humidity conditions are the same and indicate an accuracy of 100%. Table 7.1 therefore summarizes the classification of the sensor

for the various measurements, demonstrating that the device is able to distinguish the gas and its concentration in all humidity conditions.

7.4.6 Experimental Measurements in Realistic Conditions

To verify its performance under realistic conditions, the sensor was tested on mixtures of alcohol in distilled water. Since most of the spirits consumed in the world (whiskey, gin, vodka, cachaça, tequila, grappa) have an alcohol content of approximately 40°, we have simulated bottles of this type by making alcohol mixtures at 40° in distilled water. Since 100 mL of methanol is considered the minimum lethal dose in humans [32], we made three types of samples: Ten samples contained a water/ethanol solution (40%), simulating a safe commercial distillate; in ten samples, 100 mL of ethanol was replaced with methanol; and in another ten samples, 50 mL of ethanol was replaced with methanol (to simulate a less dangerous dose). A graph of the first two principal components is shown in Figure 7.6, in order to illustrate the relationships between the clusters of points relative to the different mixtures. The ellipses indicate 90% confidence intervals. The points from mixtures containing methanol are partially overlapped, while the points from mixtures with only ethanol are distinct from the others. The partial overlap between the ellipses of the samples with 50 and 100 mL of methanol is due to the limitedness of the 2D graph. To quantitatively verify the sensor performance in realistic conditions, linear discriminant analysis was used, which showed a correct classification in 100% of cases. This means that the sensor can perfectly distinguish the three classes of alcoholic mixtures, but above all, more importantly, the safe mixtures (without methanol) from the toxic ones (with methanol).

Although more tests must certainly be performed, we believe that these results demonstrate the ability of the electronic nose based on a thermal gradient to also face ap-plications in the field of food safety.

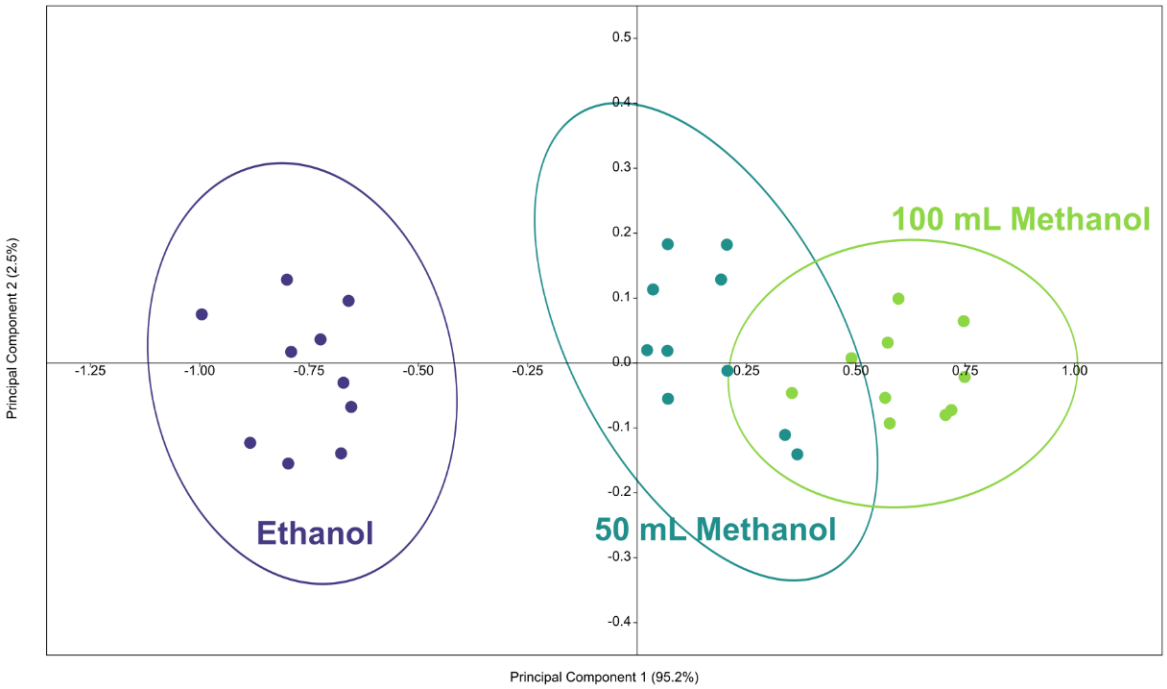

Figure 7.6 – Principal components plot for alcoholic mixtures at 40° of pure ethanol in distilled water, with 50 mL of methanol, and 100 mL of methanol.

7.5 Conclusions

A single chemoresistive sensor based on SnO_2 nanowires was used to distinguish methanol from ethanol and measure its concentration. The responses of the sensor at five working temperatures were combined in five-dimensional points in order to then be processed with multivariate statistical analysis and machine learning techniques. Using principal component analysis, linear discriminant analysis, and a support vector machine, the sensor was able to accurately distinguish methanol from ethanol and measure the concentration of the two gases with an average error of 3 parts per million in approximately 2–3 min. The sensor has proven the ability to distinguish the type of gas and its concentration in all conditions of relative humidity. The sensor correctly classified 100% alcoholic mixtures at 40° (simulating vodka, whiskey, gin) in real conditions. These performances demonstrate that this approach can be effective in detecting

methanol-intoxicated patients or detecting the presence of methanol in alcoholic beverages in lieu of more expensive and time-consuming analytical techniques.

CHAPTER 8. OPTIMIZATION OF GAS SENSORS MEASUREMENTS BY DYNAMIC HEADSPACE ANALYSIS SUPPORTED BY SIMULTANEOUS DIRECT INJECTION MASS SPECTROMETRY

This chapter is based on the scientific paper [241]:

"Optimization of gas sensors measurements by dynamic headspace analysis supported by simultaneous direct injection mass spectrometry", Sensors and Actuators B: Chemical, 347 (2021) 130580. Doi: 10.1016/j.snb.2021.130580

8.1 Abstract

Dynamic headspace extraction is frequently used in gas sensors measurements. Although the distortion of headspace composition is a possible artefact, its influence in sensors signals interpretation has not been deeply studied. In this paper, taking advantage of the on-line combination of a quartz microbalance gas sensor array with a proton transfer reaction mass spectrometer, we have been able to track the evolution of the concentration of volatile compounds along 60 seconds of extraction of the headspace of differently treated tomato paste. An electric equivalent circuit model of the dynamic headspace sampling has been introduced. Proton transfer reaction mass spectrometer signals show that VOCs are characterized by a large diversity of the evolution of the concentration in the sensors cell.

Sensors signals do not follow the concentration of volatile compounds, but they grow approaching a steady value. The contrasting behavior between sensors and the concentration of most of VOCs is explained considering that water is the dominant component in the tomato paste sample

and that water is one of those compounds whose concentration in the sensor cell steadily grows. Analysis of variance demonstrates that in this experiment the largest separation between classes occurs when the concentration of compounds in the sensor cell reached its peak. Thus, although the sensor signals continue to rise, the information content of the signals decay. This finding suggests that measurement protocols need to be adjusted according to the properties of the sample and that the actual measurement time could be much shorter than predicted from the behavior of sensor signal and typically used.

8.2 Introduction

The optimization of measurement protocols is a preeminent element of gas sensors applications. However, in spite of this evident importance, topics such as sample conditioning and uptake are seldom investigated. In most of the cases, procedures previously optimized for analytical methods, such as gas-chromatography and mass spectrometry, are uncritically transferred to gas sensors with little consideration of the peculiar properties of these devices [242].

The standard arrangement of sensors in closed cells requires the transfer of the gaseous sample typically mixed with a carrier gas. In case of liquid or solid samples, the measurement procedure is typically based on dynamic headspace extraction. This method is directly derived by gas-chromatography practice where samples (either liquid or solid) are enclosed in sealed vials endowed with a pierceable septum [243]. Vials are kept at constant temperature in order to establish the equilibrium composition of the headspace; then, the headspace is sampled by a flow of a carrier gas (typically N_2) and transferred to the sensors cell. The extraction of the headspace disrupts the equilibrium between gas and liquid/solid phase and a competition between the extraction of volatile compounds and the evaporation of molecules occurs after the extraction of the first quota of volatile

molecules. In gas-chromatography the injected volumes are small and the extraction time is short, thus it is reasonable to assume that it does not affect the actual concentration of volatile compounds [244].

On the other hand, the response times of sensors are usually longer and the perturbation of the headspace composition cannot be neglected. Most of the attention in the past literature has been given to the reproducibility of sample extraction methods [242]. This is a very important concern: although nominally similar, differently extracted samples are likely to be perceived by the sensors as belonging to distinct classes. In comparison, one of the most striking properties of natural olfaction is the capability to identify samples disregarding the modality in which the odor occurs, and it is common experience that odors can be identified even against variable background or at variable concentration [245]. Artificial olfaction systems are still quite distant from this abstraction capability; rather, sensors provide signals linked to sample composition. Furthermore, in complex matrices the evaporation enthalpies proper of each compound, combined with the effects of non-ideal behavior of real mixtures, make the modification of headspace unpredictable.

In this paper, the effects of sampling time on sensors response have been investigated and a three-class experiment has been designed. The experiment was aimed at classifying samples in three classes of tomato paste: pristine, inoculated with *Penicillium expansum* then stored at 8°C for one week, and inoculated with *Penicillium expansum* stored for one week at 8°C under exposure to vapors of thyme essential oil. Thyme essential oil is known to inhibit the growth of microorganisms and thus to protect food from spoilage [246,247].

Beside their intrinsic potential interest, the three groups of samples are supposed to be sufficiently different to provide the basis to study the influence of measurement time and the evolution of volatile compounds during the direct headspace extraction. Gaseous samples were

analyzed by an array of quartz microbalances coated with porphyrinoids [248] connected in series with a Proton Transfer Reaction Time of Flight Mass Spectrometer (PTR-ToF-MS) [249]. Such a setup enables the simultaneous measurement of the same sample with both techniques. The combination of electronic nose and PTR-ToF-MS has been recently demonstrated to be an effective methodology to study complex mixtures such as the culture media of red blood cells infected with *plasmodium falciparum* [250].

Results show that the concentration of volatile organic compounds (VOCs) in the headspace quickly reaches a peak followed by a progressive depletion of compounds in the carrier. The interpretation of signals has been corroborated by an equivalent circuit model of dynamic headspace sampling which shows that the ratio between the speed of filling of sensor cell and the rate of the evaporation of the VOC is crucial to determine the behavior of concentration of VOCs. The use of equivalent circuits to describe sensor responses has been recently demonstrated in case of Langmuir isotherm adsorption [251].

However, due to the abundance of water vapor and the non-negligible sensitivity of sensors to humidity, the variation of VOCs content is not immediately visible in sensor signals. Here it is shown that, in spite of the progressive increase of sensor signal that demonstrates an accumulation of molecules onto the sensor surface, the information content measured by variance analysis shows a synchronous peak with the VOCs content in the headspace. Tomato paste inoculated/not-inoculated with a common spoiling microorganism and treated/non-treated with thyme oil as possible inhibitor has been chosen as relevant case study.

These results provide an input to the design of gas sensors arrays in experiments where dynamic headspace extraction is used.

8.3 Materials and methods

8.3.1 Tomato paste samples

Samples were prepared from commercial tomato paste, same brand bought over the counter. Samples were inoculated with *Penicillium expansum* (10^6 UFC/ml) and stored at 8°C for a week. A part of samples was exposed to a proper concentration of vapors of essential oil of thyme (*Thymus vulgaris*) during the storage, with the aim of inhibiting the fungus growth. After one week storage at 8°C, the inhibition effect of thyme vapor was verified by visual inspection and confirmed by microbiological measurements: inoculated samples showed between 4 and 5 times the original fungal load while samples stored under thyme vapors had only between two and three times the original fungal load [248]. Eventually three groups of samples were prepared: pristine tomato paste, inoculated tomato paste and inoculated tomato paste stored under thyme oil vapors. Ten samples were prepared for each group, to be analyzed simultaneously by e-nose and PTR-ToF-MS.

8.3.2 Headspace analysis

Samples were handled by a multipurpose GC automatic sampler (Autosampler, Gerstel GmbH, Mulheim am Ruhr, Germany). Headspace VOCs from the samples were delivered by a nitrogen carrier to the gas sensors measurement cell and to the PTR-ToF-MS connected in series. VOC measurements were performed in 20 mL vials. Samples were stored at 4°C then, before analysis, they were incubated for 30 min at 37°C and measured for 70 s in direct mode. A constant flow of 150 sccm of zero air produced by the gas calibration unit (Ionicon Analytik GmbH, Innsbruck, Austria) was applied for the dilution of the headspace and preventing the memory effects between measurements.

8.3.3 Proton Transfer Reaction Mass Spectrometry

The headspace of tomato paste samples was analysed by direct injection in a PTR-ToF-MS 8000 apparatus (Ionicon Analytik GmbH, Innsbruck, Austria) after passing a Gas Sensor Array. The instrumental conditions in the drift tube were as follows: drift voltage 538 V, drift temperature 110°C, drift pressure 2.80 mbar, producing a reduced electric field E/N=130 Td (1 Td = 10^{-17} Vcm^2), where E is the electric field and N is the gas number density (molecules/cm^3). In order to increase the sensitivity, an ion funnel was operated at the end of the drift tube [252]. The sampling time per channel of ToF acquisition was 0.1 ns, amounting to 350,000 channels for a mass spectrum ranging up to m/z = 350. Every single spectrum is the sum of 30030 acquisitions lasting 33 μs each, resulting in a time resolution of 1 s.

8.3.4 Sensor Array

The gas sensor array was an ensemble of six quartz microbalances (QMB). In these sensors, a mass change (Δm) on the quartz surface results in a frequency changes (Δf) of the electrical output signal of an oscillator circuit at which each sensor is connected. In the low-perturbation regime, Δm and Δf are linearly proportional [253]. QMBs had a fundamental frequency of 20 MHz, corresponding to a mass resolution of the order of a few nanograms. The six sensors were functionalized with molecular films of 5,10,15,20-tetrakis-(4-butyloxyphenyl)porphyrins, but differentiated by the metal complexed at the molecular core: copper, cobalt, zinc, magnesium, manganese chloride, and iron chloride. Metalloporphyrins were synthesized following literature methods [254].

The sensors were used with an in-house designed and manufactured sensor system where the gas sensors are complemented by temperature and relative humidity sensors. Each QMB is connected to an oscillator circuit, and the frequency of the oscillators outputs are measured respect to a temperature compensated reference quartz that allows for a frequency resolution of 0.1 Hz.

Digital electronics is implemented in a Field Programmable Gate Array. A single USB connection provides both the power supply and the data connection. Functions and data acquisition are controlled with a software running in Matlab.

8.3.5 Data processing and statistical analysis

Data processing of PTR-ToF-MS spectra included dead time correction, external calibration and peak extraction steps performed according to a procedure described elsewhere [255]. The baseline of the mass spectra was removed after averaging the whole measurement, and peak detection and peak area extraction were performed by using a modified Gaussian to fit the data [256]. To determine the concentrations of volatile compounds in ppbvv (part per billion by volume) the formulas described by Lindinger et al. [257] were used assuming a constant reaction rate coefficient ($k = 2\times10^{-9}$ cm^3/s) for H_3O^+ as primary ion.

The statistical significance of PTR-MS peaks and sensors signals was evaluated with the non-parametric Kruskal-Wallis rank sum test followed by Bonferroni correction in case of multiple comparisons. Variance analysis and multivariate analysis were performed in Matlab R2020a.

8.4 Results and discussion.

Ten samples for each of three classes (pristine tomato paste, inoculated tomato paste, and inoculated tomato paste treated with thyme oil) were closed in vials. Measurements were taken with an autosampler keeping the sample at the constant temperature of 40°C and using nitrogen as gas carrier.

The headspace was sampled for 70 s and delivered to the electronic nose and the PTR connected in series. In dynamic sampling the headspace of a vial containing the sample is extracted by a carrier flow and transferred into a cell where the detector, either sensors or mass spectrometer injector, are placed. During the transfer, the concentration in the vial is diluted by the carrier flow. The time behavior of the VOCs concentration in the sensor cell depends on several factors including the evaporation of VOCs inside the vial, the dilution of the headspace in the carrier and the filling of the sensor cell. The whole process can be adequately represented by a RC circuit made of three blocks, each representing one of the factors previously mentioned. The model is shown in Figure 8.1. The capacitors in the circuit represent the volumes of vial and the sensor cell, the voltage is the saturation pressure of the volatile compound and the resistors define the transfer of molecules into the different compartments. The complete and detailed analysis of circuit in Figure 8.1A and the dimensioning of circuit elements to the real case is are out of the scope of this paper. Here we are interested to qualitatively study the behavior of the output voltage which represents the pressure of the VOC in the chamber. The shape of the dynamic concentration at which sensors and PTR are exposed depends on the balance between the three above mentioned processes. Carrier flow and sensor cell filling are maintained constant, while the evaporation rate of different VOCs may be extremely variable. To study the different time evolution of VOCs, we calculated V_{cell} at different ratio between the time constant of sensor chamber filling (R_{cell}*C_{cell}) and the time constant of headspace formation (R_{evap}*C_{vial}). The carrier is activated, closing the switch, only after that the charge of C_{vial} is completed. In practice, it corresponds to start the measure of the headspace after that the headspace reached the equilibrium condition. The circuit in figure 1A has was been simulated in MATLAB 2020b/Simscape Electrical environment.

Figure 8.1B shows the behavior of V_{cell} for different ratio of time constants. When the cell filling is faster than the evaporation rate, the behavior is non-linear characterized by an overshoot.

On the other hand, when the evaporation rate is faster than the filling of the cell the concentration at which sensors are exposed, it grows progressively.

In a mixture of compounds, such as in the tomato paste, we expect a diversity of behaviors.

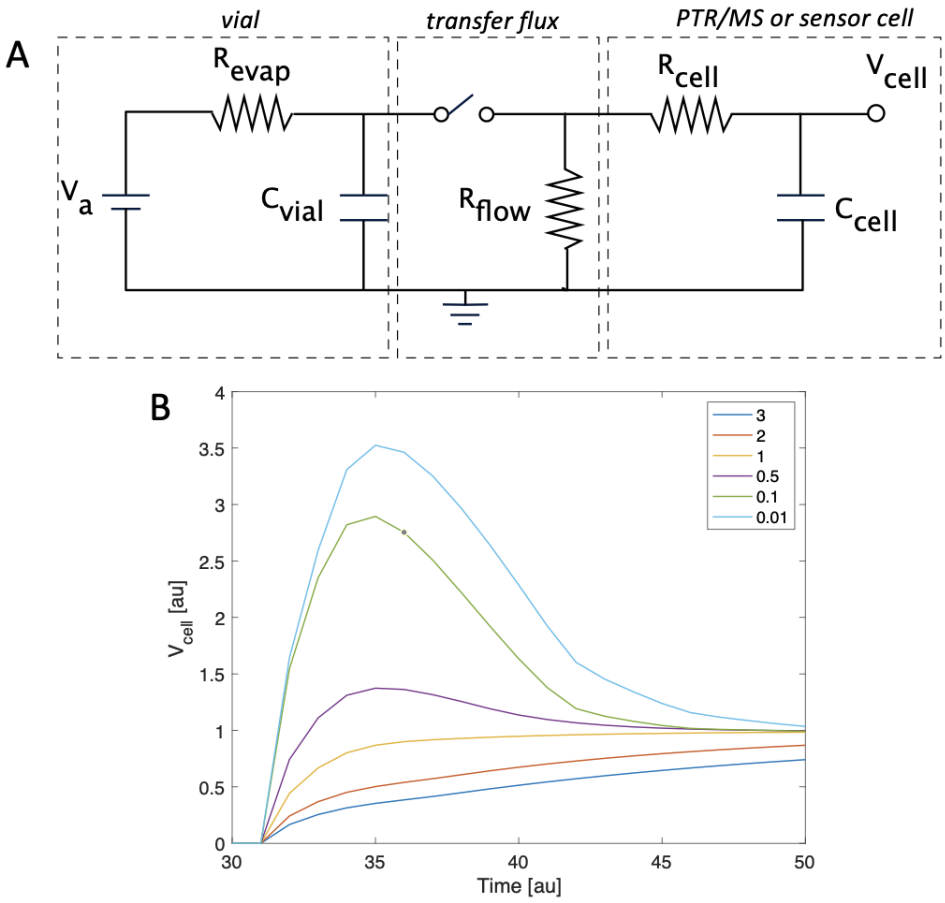

Figure 8.1 – A: electric equivalent model of the evolution of volatile compounds in a sensor (or detector) cell. B: output voltage, representing the concentration in the sensor's cell, as a function of the time constant ratio between the sensor cell filling (R_{cell}*C_{cell}) and the time constant of headspace formation (R_{evap}*C_{vial}).

The real time response of PTR-ToF-MS data gives the chance to better study the evolution of the concentration of compounds in the sensors or the detector cell. PTR-ToF-MS detected 131 different peaks. For each peak the average in the 30 measurements was evaluated. To understand the different time behavior of the peaks, the time evolution has been clustered by a k-means algorithm

in 6 classes. For the scope we were interested to study the shape of the signal evolution. The time evolution of the 131 peaks was analyzed with principal component analysis to evidence the differences between the peaks. Figure 8.2 shows the scores plot of the PCA. For each group the peaks signal evolution is also shown. To focus the attention on the shape of the behavior, the peaks signals was normalized in the [0-1] interval.

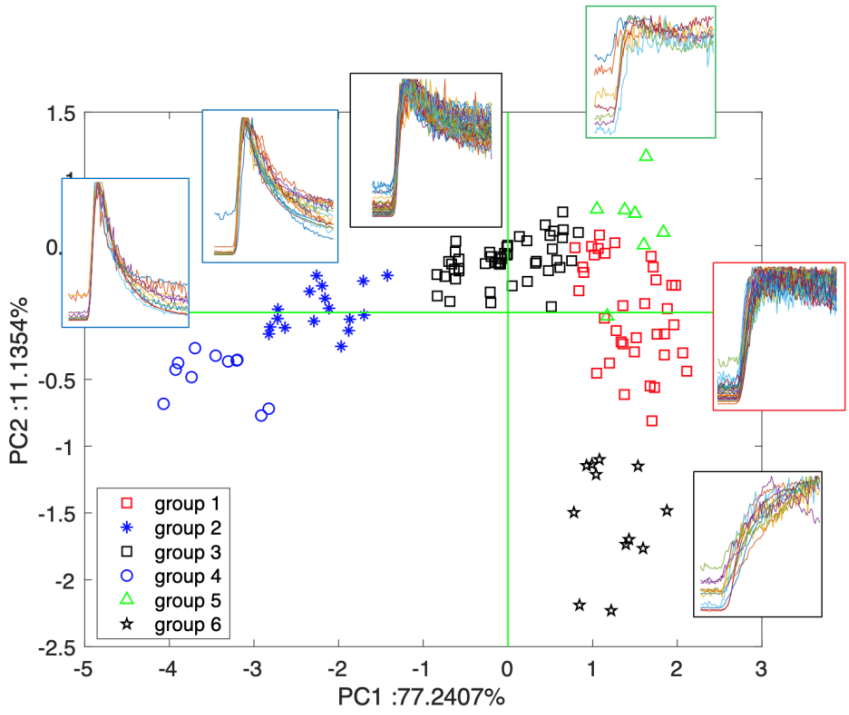

Figure 8.2 – PCA of peaks time evolution reveals the different time constant of evaporation process of the different VOCs. Groups have been defined by k-means clustering of normalized peaks signal. (see text)

Sensors signals on the other hand do not show the behavior of PTR-ToF-MS peaks. Figure 8.3 shows the sensors signals recorded during the exposure to all samples. The signals are scaled for the frequency at the time of sample injection, so the frequency shift to the adsorption of molecules in the sample is considered. Sensors signals are rather reproducible, and considering the working mechanism of quartz microbalances, the sensors signals suggest a progressive increase of the

amount of absorbed molecules. The end of exposure and the beginning of cleaning with a stream of technical air is also visible in Figure 8.3 and it shows a prompt start of the desorption process.

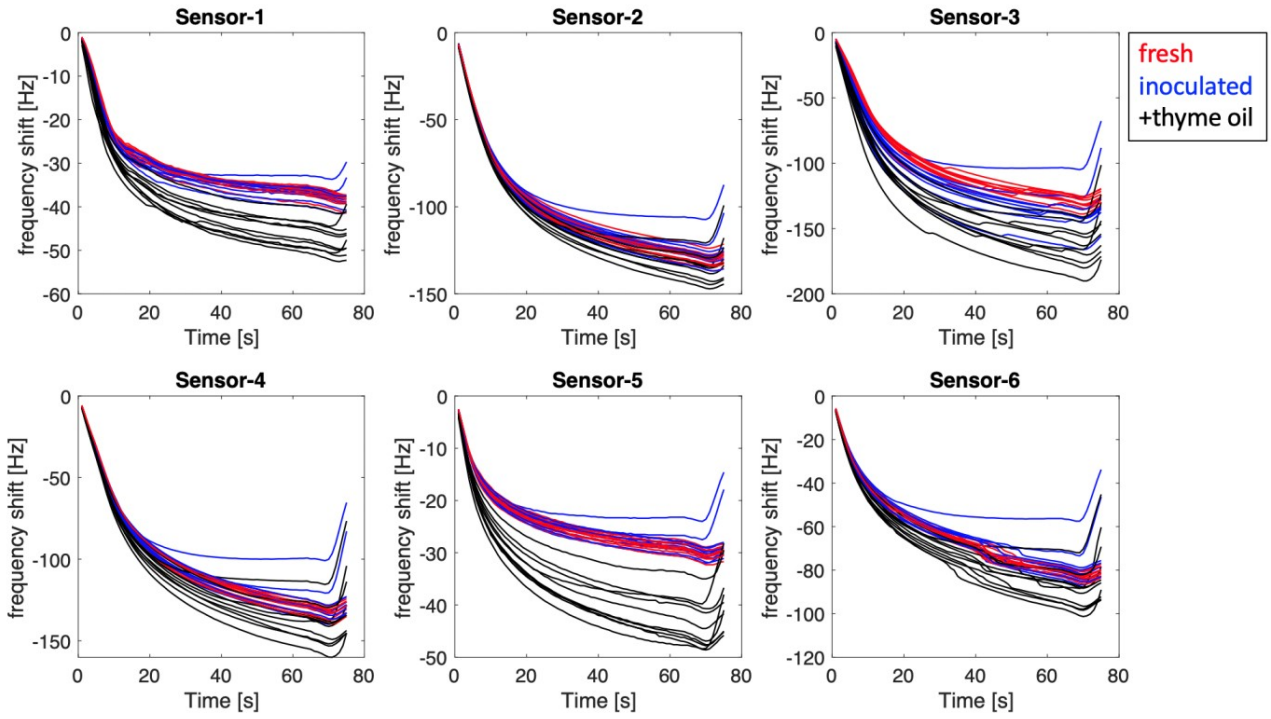

Figure 8.3 – Evolution of sensors signals during the exposure to samples. In each plot the signals of the same sensor are compared. A certain tendency to separate the three classes can be observed. Samples treated with thyme oil show higher signals which make them clearly identifiable respect to the other two classes.

In this experiment we were interested in studying the variation in the information content of the sensor signal during the exposure. The interpretation of adsorption processes suggests that the information of sensor signal increases during the exposure to the sample. Indeed, the behavior of sensors in figure 8.3 shows a progressive increase of the signals and an apparent increase of the differences between classes. This is immediately perceived for class 3 (samples added with thyme oil), while the differences between the other two classes are less recognizable from a visual comparison of the signals. Sensors signals seem to be more influenced by the compounds lying in the right side of the plot in Figure 8.2. However, a more accurate appraisal of the evolution of sensors signals can be acquired calculating, by variance analysis, the probability of class separation

as a function of time. The probability of null hypothesis (p-value) was calculated with data collected at different experimental times from the first second after the beginning of the exposure up to 75 seconds later, immediately before to switch the inlet flow to the technical air background. The p-value has been calculated with the non-parametric Kruskal-Wallis rank sum test.

Figure 8.4 shows the behavior of the p-value respect to the exposure time.

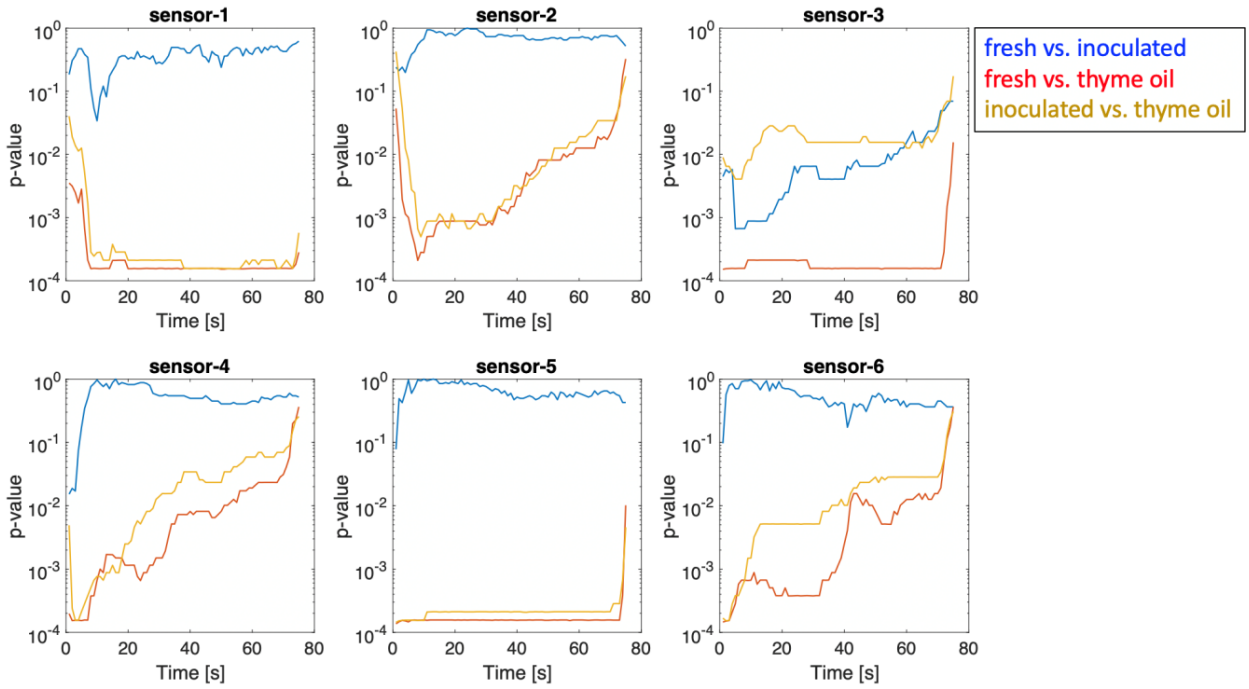

Figure 8.4 – Time evolution of the p-value calculated for the mutual separation between classes, for each sensor, as a function of the time from the beginning of exposure.

The analysis of variance shows that, except sensor 3, all sensors separate oil-thyme treated samples respect to the others. Largest difference between classes is captured about 10 s after the beginning of exposure. This behaviour is similar with the concentration evolution of the slowly evaporating compounds plotted at the left side of Figure 8.2. Thus, it may be interpreted as a clear consequence of the evolution of the headspace during its dynamic extraction. Moreover, the

evolution of the differences between classes are also rather variable suggesting that the composition of the headspace also changes during the headspace extraction.

Variance analyses of PTR-ToF-MS mass peaks, similar to those reported for sensors, showed the largest difference between classes in correspondence of the peak of concentration shown in Figure 8.2. Since the main interest of this study is to compare PTR-ToF-MS signals with those of sensors, the analysis was restricted to the most abundant mass peaks. In particular, 29 mass peaks whose average abundance was above 10 ppbv were selected for further analysis. The list of the selected mass peaks is shown in Table 1. Most of these compounds are characterized by a nonlinear evolution of the PTR-ToF-MS signal, labelled as groups 2, 3 and 4 in figure 8.2. Few compounds show a progressive increase of the concentration (groups 1 and 6 in fig. 8.2).

It is interesting to observe that different mass peaks showed a different behaviour of p-value. Moreover, for the same mass peak the behaviour of p-values with respect to the separation between different classes may be different too. This result is rather expected considering that each volatile compound is characterized by a proper evaporation rate and contributes differently to the separation between the classes. In addition, it should be taken into consideration that a PTR-ToF-MS mass peak could consist of different monomers with different physicochemical properties.

The consequences of the headspace variable composition to sensors and PTR-ToF-MS signals can be efficiently studied by multivariate analysis of the datasets. The number of samples does not enable a reliable classification of data, and on the other hand a classifier might also hide the changes occurring along the time. Rather, it is more useful and convenient to study the correlation among variables (either sensors or PTR-ToF-MS mass peaks) and to display the variation of the relationship between data, and Principal Component Analysis (PCA) is an adequate tool for this scope.

Table 8.1 – List of selected mass peaks whose mean abundance is larger than 10 ppbv. The time behaviour of the PTR-ToF-MS signals is attributed to one of the 6 classes shown in figure 8.2. For each mass smallest and largest abundances are also listed.

	m/z	Chemical formula	Concentration behaviour (group in fig. 2)	Largest abundance [ppbv]	Smallest abundance [ppbv]	Average abundance [ppbv]
1	31.018	$CH_2O.H^+$	2	224.78	2.09	162.51
2	34.037	$C^{13}H3OH.H^+$	3	272.25	0.38	196.45
3	39.023	$C_3H_3^+$	2	62.92	1.21	32.52
4	41.039	$C_3H_5^+$	3	338.59	3.45	184.09
5	43.018	$C_2H_3O^+$	3	110.42	4.10	65.84
6	43.029	$CH_2N_2.H^+$	2	111.06	0.72	73.92
7	43.054	C3H7+	3	266.07	1.33	123.69
8	45.990	NO2+??	4	31.67	3.59	16.35
9	46.037	$C^{13}CH_4O.H^+$	2	85.40	1.31	35.52
10	48.053	$C_2H_5O.H^+$	3	202.82	0.40	72.70
11	55.038	$(H_2O)_3.H^+$	6	72.28	37.44	58.55
12	55.054	$C_4H_7^+$	3	41.58	2.66	15.24
13	57.070	$C_4H_9^+$	3	339.48	2.04	146.84
14	59.049	$C_3H_6O.H^+$	2	1186.09	13.36	629.43
15	61.012	$C_2H_4S.H^+$	4	33.86	0.14	17.95
16	61.028	$C_2H_4O_2.H^+$	3	186.63	6.22	97.58
17	64.029	$C^{13}CCH_6S.H^+$	4	256.18	0.10	138.80
18	67.055	$C_5H_7^+$	1	67.45	0.31	15.26
19	71.086	$C_5H_{11}^+$	3	59.06	0.32	18.62
20	73.065	$C_4H_8O.H^+$	2	277.46	0.80	112.65
21	75.044	$C_3H_6O_2.H^+$	2	96.07	0.65	63.00
22	87.081	$C_5H_{10}O.H^+$	2	28.53	0.24	14.26
23	89.060	$C_4H_8O_2.H^+$	3	26.53	0.37	17.57
24	91.056	$C_4H_{10}S.H^+$	1	156.64	0.34	31.70
25	97.029	$C_5H_4O_2.H^+$	1	36.70	0.43	18.41
26	119.086	$C_9H_{11}^+$	1	83.87	0.11	17.74
27	135.116	$C_{10}H_{15}^+$	1	604.84	0.16	119.48
28	138.136	$C_9{}^{13}CH_{17}^+$	1	222.87	0.09	50.01
29	153.128	$C_{10}H_{16}O.H^+$	6	82.01	0.12	20.38

Kruskal-Wallis test was performed for each mass peak at each time of measurement. Figure 8.5 shows the evolution of the p-value with time for each selected mass peak.

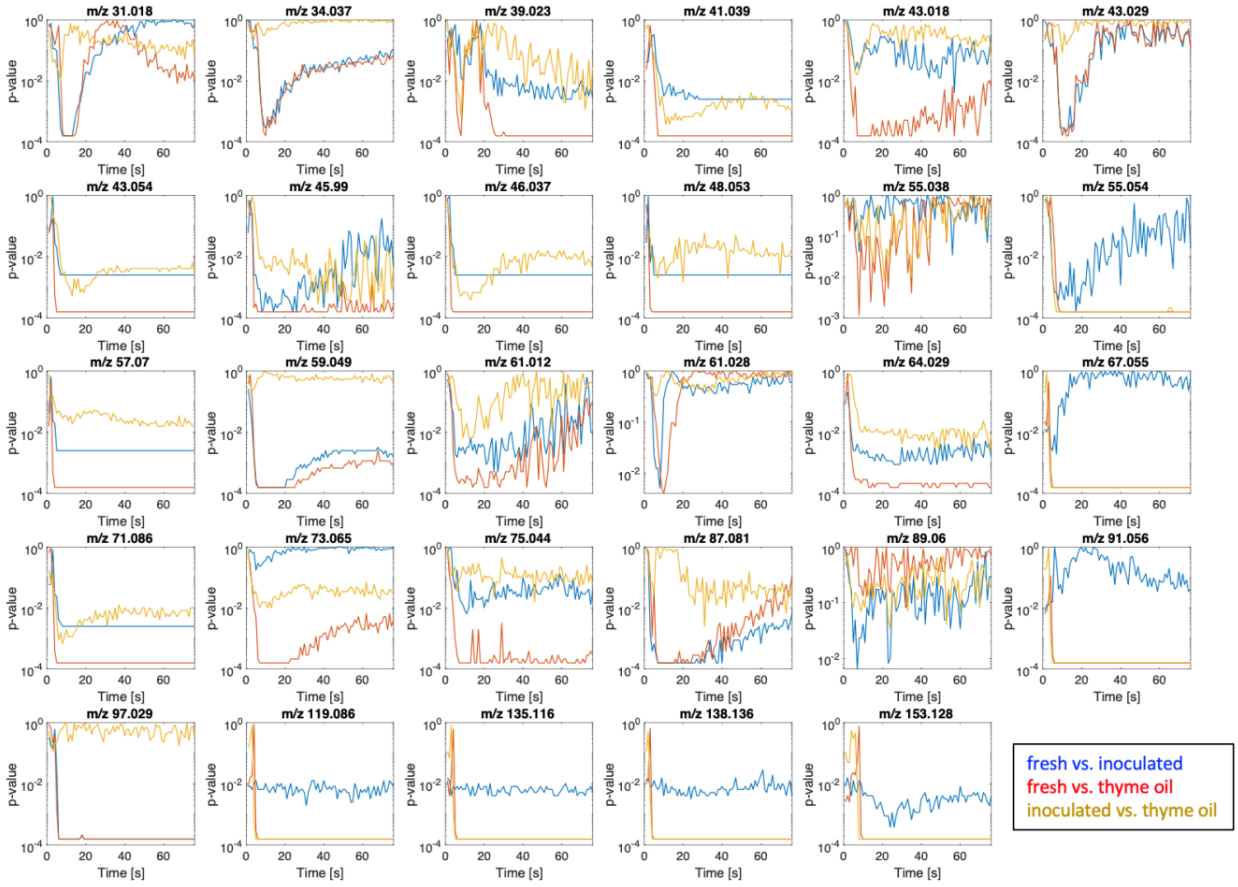

Figure 8.5 – Time evolution of the p-value calculated for the mutual separation between classes and for each PTR-ToF-MS mass peak whose mean abundance is larger than 10 ppbv.

Figures 8.6 and 8.7 show the plots of the first two principal components calculated with the data of sensors and most abundant PTR-ToF-MS mass peaks. PCA was calculated on standardized data where each variable is normalized to zero mean and unitary variance.

The scores plots of sensors data (Figures 8.6A and 8.6B) show that the separation of the three classes achieved at 10 s is almost completely lost at 60 s. This is particularly evident for inoculated and thyme oil treated samples. In contrast, the data of pristine paste are closely clustered even after

60 s. The different effect of time on the three classes suggests that also the qualitative composition of headspace changes during the measurement. A further demonstration is offered by the radically different loadings plots (Figures 8.6C and 8.6D). To correctly interpret the loadings plot it is necessary to consider that the sensors signals are negative, thus a larger response means a larger negative signal.

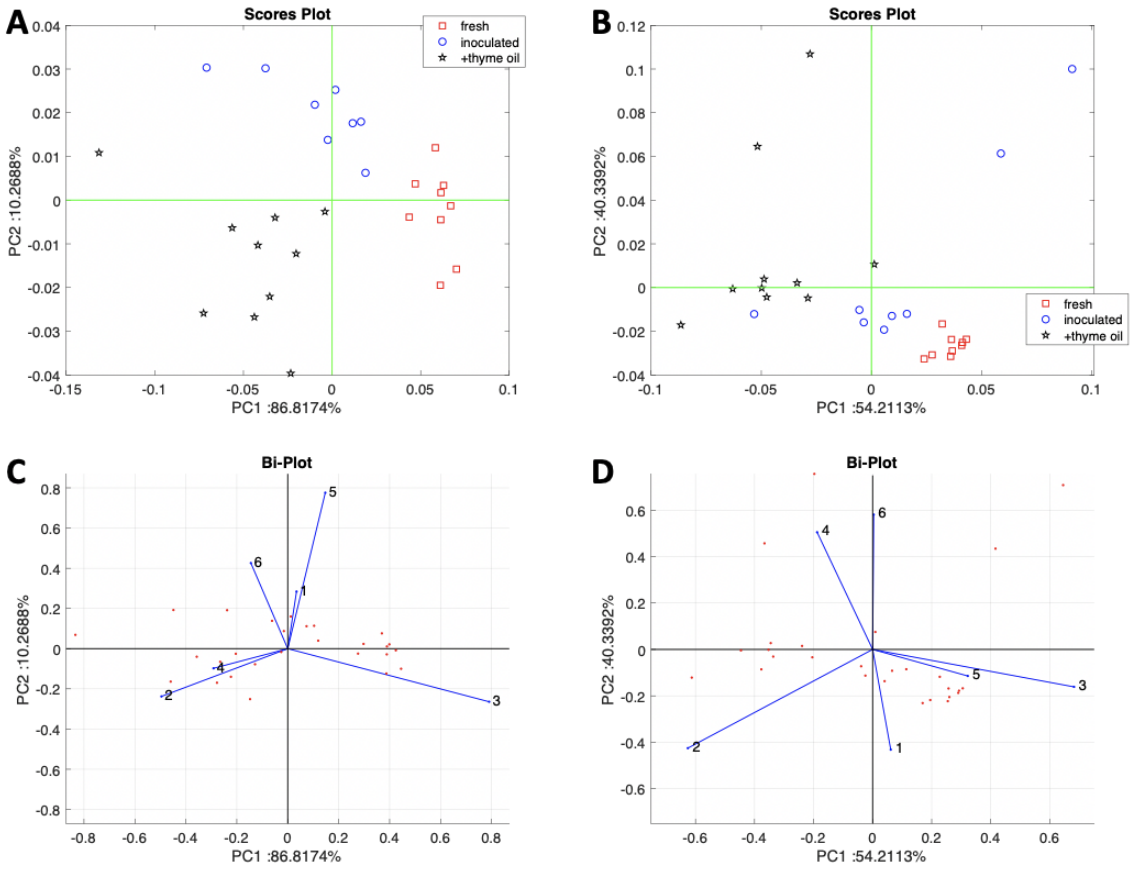

Figure 8.6 – PCA of sensors data. A) scores plot with data at t=10 s; B) scores plot with data at t= 60 s; C) loadings plot with data at t=10 s; D) loadings plot with data at t=60 s.

The scores plot at 10 s is dominated by sensors 3, 5, and 2, where each of these sensors points towards a different class. At 60 s the relationship between sensors and classes is almost lost and only sensor 2 retains its correlation with the group of thyme oil treated samples. Rather than the changes of scores plot, the variations in loadings plots indicate the changes of the headspace composition.

Figures 8.6C and 8.6D show that for some sensors the relationship between sensors and classes at short and long time changes. PTR-ToF-MS data scores plots are less affected by the decrease of concentration of VOCs. The scores plots calculated with data taken at after 10 and 60 seconds are indeed rather similar (Figures 8.7A and 8.7B). More evident are the changes in the loadings plots (Figures 8.7C and 8.7D). At 10 s all masses contribute either to thyme oil treated or to pristine paste samples, except variable 23, corresponding to m/z 89.060 attributed to $C_4H_8O_2.H^+$. At 60 s the role of variable 16 respect to inoculated samples emerges; this variable corresponds to m/z 61.028 whose formula is ($C_2H_4O_2.H^+$).

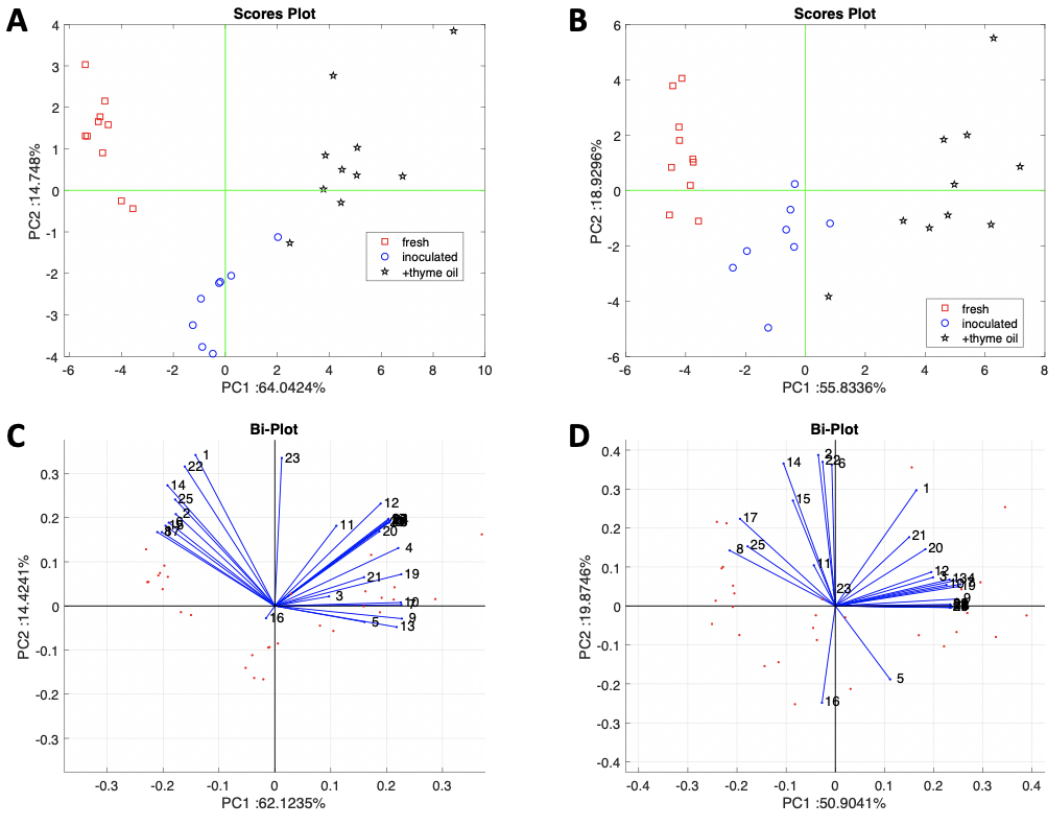

Figure 8.7 – PCA of PTR-ToF-MS data. Analysis has been restricted to those masses whose mean abundance is larger than 10 ppbv (Table 8.1). A) scores plot with data at t=10 s; B) scores plot with data at t= 60 s; C) loadings plot with data at t=10 s; D) loadings plot with data at t=60 s.

Sensors and PTR-ToF-MS data were differently affected by the variation of headspace abundance. The behaviour of sensors data was unexpected because, as shown in figure 8.3, in spite of the variable headspace composition, sensors signals are characterized by a progressive increase of the amount of absorbed molecules. This behaviour can be explained considering that the measured samples are characterized by a non-negligible amount of water. Indeed, as typical in many foodstuffs, water is by far the more abundant component of the matrix. Due to its large concentration in the food matrix, water vapour, instead of decreasing as the other VOCs, steadily increased during the measurement. The relative humidity of the sample was measured by a humidity sensor placed in the sensors cell. Humidity sensors data correlate with the m/z 55.038, that is identified as water cluster and is related to headspace humidity.

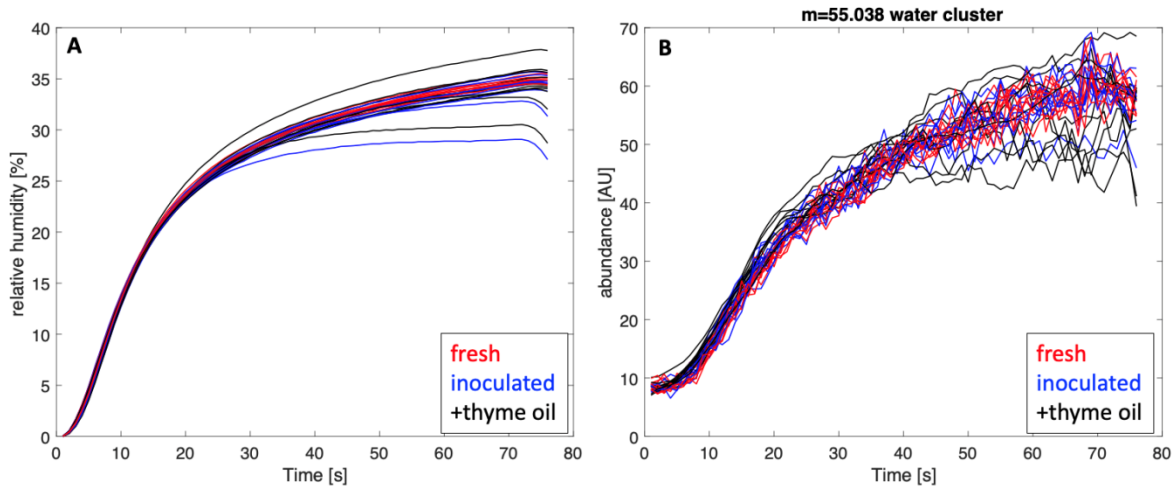

Figure 8.8 – Evolution of relative humidity (panel A) and abundance of m/z 55.038, identified as water cluster (panel B) in all measured samples. Curves are coloured according to their class.

Figure 8 shows the relative humidity as measured by the humidity sensor of the electronic nose (Figure 8A) and the abundance of m/z 55.038 measured by PTR-ToF-MS (Figure 8B). The two signals are obviously proportional to each other: the linear correlation coefficient between the two sets is larger than 0.99. No relationship between the humidity of the sample and any class was found

in Figure 8. The absence of relationship between humidity and classes is also visible in Figure 5, where m/z 55.038 is a variable with the largest p-value and that in practice does not discriminate the different classes.

Even if the sensitivity to water, in terms of Hz/ppmv, may be small respect to that towards other VOCs, the actual concentration of water can well exceed that of VOCs. In these samples the contribution of water in the sensors signal is not negligible and after the peak of VOCs concentration, sensors surface continues to accumulate water molecules and the sensor signal keeps increasing.

Eventually, the analysis of variance at different times provides a valid methodology to determine the optimal measurement time respect to the subtraction of relative humidity contribution which requires a long exposure of sensors. Short exposures, besides maximizing the information content of sensor signals, also reduce the burden of unwanted absorbed water molecules that could also induce drift effects in sensor signals.

8.5 Conclusions

In gas sensors it is common opinion that optimal sensor response is obtained when the sensor signal reaches a steady value. In this paper it has been shown that although the sensor signal progressively increases during the exposure to the sample, the information content of the signal itself, here represented by classes separation, may decrease. Thus, the behaviour of sensor signals is not always completely representative of the phenomena underlying the sensor response. This behaviour may be simply explained by the fact that these sensors are sensitive to volatile compounds and to humidity. In high humidity samples, such as many food products, the concentration of water vapour may continuously grow during head-space extraction while volatile compounds, a minor

component in the sample, quickly reach a maximum concentration and possibly decrease if sampled from a finite volume.

Taking advantage of the on-line connection of gas sensors and PTR-ToF-MS, the sensor response has been directly compared with the sample composition at the same time. An electric equivalent circuit of the dynamic headspace sampling has been introduced. VOCs concentration in sensors and detector cells follows different evolutions depending on the evaporation rate of the volatile compounds.

For most of the compounds, the concentration at which the sensors are exposed shows a peak a few seconds after the beginning of the measurement. It has been shown here that the sensor response at the time of maximum concentration corresponds to the largest information content, allowing for a clear separation of the three classes. Among the compounds whose concentration in the sensor cells is monotonically growing we found humidity. Thus, a simple explanation of sensor response has been provided where sensor are considered sensitive to the total volatile compounds and the relative humidity.

Eventually, this study suggests that in electronic nose experiments an optimal measurement time may exist at which the information content of sensors signals is largest. If the sample is not homogeneous but it includes compounds with different evaporation enthalpies, the optimal time may be, in principle, different for each class. The use of a PTR-ToF-MS in series with gas-sensor cells is a valuable tool to better understand and support the optimisation of gas-sensors arrays. Because of cost and size, it is obviously not an alternative to gas sensors. However, photoionization detectors (PIDs) which are fast, sensitive and non-selective can efficiently complement gas sensors applications by providing the information about the time evolution of total VOCs and thus the time at which the sensor signal could be most informative and reliable. Recent improvements in PID

design are expected to result in low-cost miniaturized devices that could be easily implemented in gas sensor arrays [258].

CHAPTER 9. DETECTION OF MACKEREL FISH SPOILAGE WITH A GAS SENSOR BASED ON ONE SINGLE SnO_2 NANOWIRE

This chapter is based on the scientific paper [218]:

"Detection of mackerel fish spoilage with a gas sensor based on one single SnO_2 nanowire", Chemosensors, 9 (2021) 1–10. Doi: 10.3390/chemosensors9010002

9.1 Abstract

A chemosensor consisting of one single tin oxide nanowire is used to determine the freshness status of mackerel fish (*Scomber scombrus*) in a quick and non-invasive way. The tiny chemo-resistive sensor is first tested with pure ammonia and then used to measure the total volatile basic nitrogen from different samples of fish at different degrees of freshness. The sensor has proved capable of determining the freshness of a sample in few seconds compared to traditional methods such as microbial count and chromatography, which take hours. The sensor response is well correlated with the total viable count (TVC), proving that the total volatile basic nitrogen is a good way to quickly test the bacterial population in the sample. After calibrating the sensor (following the degradation of the fish during almost two days), it has been tested with random double-blind samples, proving that it can well discriminate the degree of freshness of the fish preserved at different temperatures.

9.2 Introduction

Food has a profound impact on people's health, chronic disease risk, and longevity. Better nutritional quality is achieved also by consuming more fresh products instead of highly processed foods with additives (artificial food colors, preservatives, etc.). Unfortunately, fresh food is subject to deterioration quite rapidly, and this has important repercussions not only on the food industry, but also on the health of consumers, with social and health costs [259,260]. Recently, the globalization and the centralization of many production chains has led to greater distances between the production areas and the consumer and more complex supply chains [261]. Fish is a food that, also thanks to its healthy properties, is consumed more and more all over the world [262]. For these reasons, it is increasingly important to develop cheaper and faster non-invasive methods to assess fish freshness during real time. Until a few years ago, panels of human experts evaluating appearance, smell, and texture were used [263,264], but this type of procedure is laborious and not always reliable, which is why the use of sensors has recently become essential.

The main factor limiting the shelf life of fresh fish is the activity of microorganisms. For this reason, an estimate of total vital counts (TVC) is generally used as a reference and as a definitive index [265]. After the death of the fish, the amount of microorganisms on its surface increases and gradually spreads to various tissues [266]. Several methods have been used to measure the freshness of the fish [263,267]. As microorganisms degrade fish tissues, they convert trimethylamine oxide into $(CH_3)_3N$ (trimethylamine or TMA) and $(CH_3)_2NH$ (dimethylamine or DMA). At the same time, NH_3 (ammonia) is produced through the de-composition of urea and amino acids by bacteria [268]. These volatiles are collectively referred to as TVB-N (total volatile basic nitrogen), and their concentration is considered a good indicator of fish freshness. Among the most used and accurate systems to analyze volatile compounds are the headspace methods, which consist of extracting the volatiles and then separating them and identifying them with chromatographic techniques [263]. Unfortunately, these methods are time-consuming and require trained personnel and equipment

accessible only in the laboratory. So, this type of analysis can only be done on a sample basis, guaranteeing the freshness of only a small part of the products. Therefore, it is important to develop non-invasive sensors that are small, cheap, and fast, in order to be able to extensively monitor the supply chain in real time. A suitable tool for this task, as it is able to distinguish complex gas mixtures, is the electronic nose: an array of sensors whose responses are combined together [269,270]. These devices are able to distinguish complex mixtures of volatile organic compounds that make up the aroma of an agro-food product. Electronic noses are able to distinguish complex mixtures of volatiles and there-fore many different agro-food products [271,272,273]. In this case, it is not necessary to evaluate subtle nuances but to measure a very precise marker (the TVB-N), and therefore a single sensor can be smaller, cheaper, and easily integrated. Chemoresistors based on semiconducting metal oxides (SMOs) are ideal candidates for this task: their dimensions are less than one micron, and they are very simple, since they are basically a resistance that varies by reacting to the atmosphere around them. Therefore, they can be easily integrated into portable or wearable devices (mobile phones or smart watches) or into containers used for transporting fish. The mechanism underlying their detection performance was presented by Seyama [274], and the latest generation consists of SMO nanostructures. The enormous surface/volume ratio of the nanostructures (usually nanowires, NWs) greatly improves the detection performance, allowing gases to be detected down to ranges below ppmv (parts per million). Nanowires can be used as a porous thin film [275] that is grown directly from the electrodes [276] or even contacted individually [277].

In the present work, the latter method will be used in order to exploit the sensitivity and the speed of response and recovery of a single nanowire. Using the microbial count as a reference, the nanosensor has been shown to be able to measure mackerel freshness non-invasively, quickly, and accurately.

9.3 Materials and Methods

9.3.1 Synthesis of SnO_2 Nanowires

The tin oxide (SnO_2) nanowires were grown in a horizontal quartz tube placed inside a furnace (Lindberg Blue M, Thermo Fisher Scientific, Waltham, Massachusetts, USA) by chemical vapor deposition (CVD). An alumina boat filled with pure tin monoxide was used as an evaporation source and placed in the center of the furnace at its maximum temperature. A silicon wafer square (about 1 × 1 cm^2) was used as substrate, deposited with a thin gold film (about 5 nm) acting as a catalyst, and positioned 1 cm from the alumina boat. The quartz tube was cleaned by pumping it down to 10^{-2} mbar and purging it with high-purity (99.999%) argon. This cycle was repeated three times, and finally, the system was pumped down to its limit pressure. Then, the temperature was increased from room temperature (26 °C) to 850 °C with a slope of 25 °C per minute, and the furnace was left for five minutes at 850 °C to thermalize. Then, an oxygen flow of 0.35 standard cubic centimeters (sccm) was flowed into the system, starting the process. Growth of the NWs lasted 30 min; then, the system was shut down and allowed to cool. Once the growth was complete, the samples showed a soft and homogeneous white film.

9.3.2 Material Characterization

The thin white film grown via CVD was characterized by X-ray diffraction (XRD) using a Philips Xpert Pro (PANalytical, Westborough, Massachusetts, USA) working at 40 kV with CuKα radiation. Transmission electron microscopy (TEM) investigation was carried out using a JEM-100CX (JEOL, Tokyo, Japan) operating at 90 kV, and secondary electron microscopy (SEM) images were acquired with a Hitachi S-4800 (Hitachi, Krefeld, Germany).

9.3.3 Fabrication of the Sensor

Then, a piece of the white thin film (a forest of spaghetti-like nanowires) was sonicated in dimethylformamide for two seconds. The resulting dispersion was dropped onto a Si/SiO_2 wafer by spinning it at 6000 rpm in order to obtain the desired NW density. A matrix of Ti/Pt (10/250 nm) electrodes was patterned on the dispersed nanowires using the standard UV lithography technique on the whole wafer. The pairs of electrodes connected by nanowires were found by combining two tests: resistance measurement and optical microscopy. The best candidates for single nanowire devices were characterized by SEM imaging to verify their morphology, and the best was chosen to be used as a gas sensor.

9.3.4 Gas Sensor Measurements

The single-nanowire sensor was measured in a home-built system comprising a measuring chamber with heatable sensor holder and micro-probes, gas flow controllers connected to high-purity gas bottles, and a multimeter (Keithely 2410, Keithely, Cleveland, Ohio, USA) connected to a data acquisition program (LabView, National Instruments). The device was first thermally conditioned for 4 h at 500 °C in nitrogen while powered at 1V to stabilize the nanostructures and their base resistance. This is to ensure that the electrical properties of the nanostructures do not change during subsequent measurements [278]. Then, the electrical contact of the SnO_2 nanowire with the titanium/platinum electrodes was studied by analyzing the I-V curves. Good linear behavior was found, which demonstrated good ohmic contact. The sensor resistance drops from 4.25 to 1.43 to 0.66 MΩ when measured at 200, 250, and 300 °C.

The sensor was operated under a voltage of 1V, while different temperature values (200, 250, and 300 °C) were set by the heater on the sample holder. Different concentrations of ammonia (10, 5, 2, 1, and 0.5 parts per million, ppmv) were tested while maintaining the total gas flow of 400 sccm. The sensor response was defined as $S = R_{air}/R_{gas}$, where R_{gas} and R_{air} are the resistance of the

sensor with ammonia or in air, respectively. The speed of the single nanowire sensor is measured using the definition of response and recovery times: the time necessary to reach 90% of the maximum response and to get down to 90% of the complete recovery, respectively. The limit of detection (LoD) was calculated as $3 \cdot noise_{rms}/slope$, where $noise_{rms}$ is the standard deviation of the sensor signal and slope is the derivative of the sensor response as a function of ammonia concentration.

9.3.5 Mackerel Spoilage Measurements

Several small cubes of mackerel fish weighting 20 g were cut from a fresh fillet using disposable gloves and autoclaved tools. Each cube is kept in a different glass jar until the measurement with the gas sensor (some at room temperature = 25 °C and some in a fridge at 4 °C). Every two hours, a fish sample was inserted into the sensing chamber to deter-mine its TVB-N, and immediately afterwards, it was subjected to microbial analysis in order to compare the two measurements. The total viable count (TVC) was evaluated using a spread plate method [279] on a plate count agar and agar base (Oxoid CM0463 and 0055, Thermo Fisher Scientific, Waltham, Massachusetts, USA). Then, the plates were counted after an incubation time of 48 h at 30 °C.

9.4 Results and Discussion

9.4.1 Nanowires Characterization

The SnO_2 nanowires composing the white soft layer obtained by CVD were first investigated by scanning electron microscopy to characterize their morphology. A SEM image of the spaghetti-like nanowires is shown in Figure 9.1A.

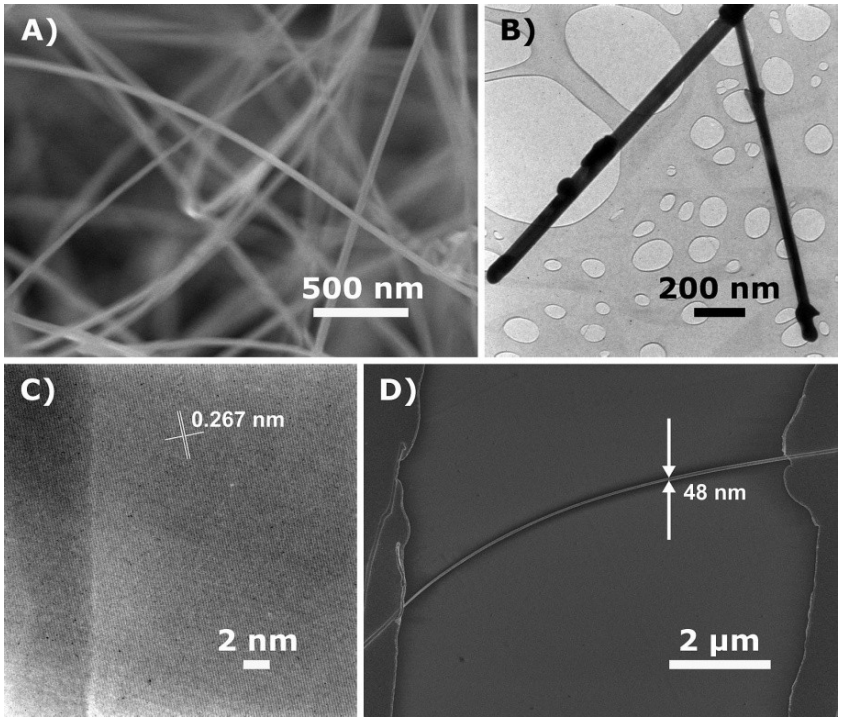

Figure 9.1 – (A) SEM image of the SnO_2 nanowires forest; (B) TEM image of two nanowires; (C) HR-TEM image of a nanowire lattice; (D) SEM image of the sensor: a single SnO_2 nanowire bridging two metallic electrodes.

As can be seen, the nanowires are long, smooth, and straight, with an average diameter of 50 nm. Figure 9.1B shows a TEM image of two nanowires, confirming their smooth and straight shape, their single-crystallinity, and their constant diameter. The HR-TEM of a nanowire in Figure 9.1C shows inter-planar fringes of 0.269 nm, corresponding to the (101) crystal planes of tetragonal SnO_2 structure. Figure 9.1D illustrates a single nanowire bridging two metal electrodes. The gap between the Ti/Pt pads is 8 µm wide, while the diameter of the nanowire is approximately 48 nm.

The composition and structure of the nanowires were also determined by X-ray diffraction, as shown in Figure 9.2.

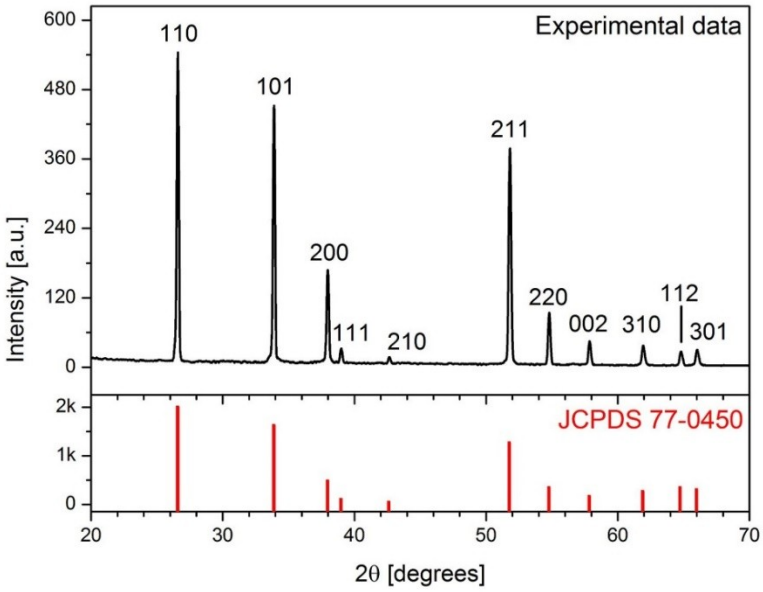

Figure 9.2 – XRD patterns. Top: pattern of SnO_2 nanowires used as a single-nanowire sensor; bottom (red online): reference pattern of tetragonal SnO_2 (JCPDS 77-0450).

All the diffraction peaks in the pattern can be readily indexed to the tetragonal phase of SnO_2 with lattice parameters of a = b = 4.742 Å and c = 3.186 Å, which agree well with the reported values (JCPDS no. 77-0450). No amorphous contributions or impurity peaks can be observed nor other phases of SnO_2, confirming the high purity of the nanowires.

9.4.2 Ammonia Sensing Performance

In order to check the sensor performance at different working temperatures, the resistance of the single SnO_2 nanowire was dynamically measured at three temperature values: 200, 250, and 300 °C. The plots are shown in Figure 9.3.

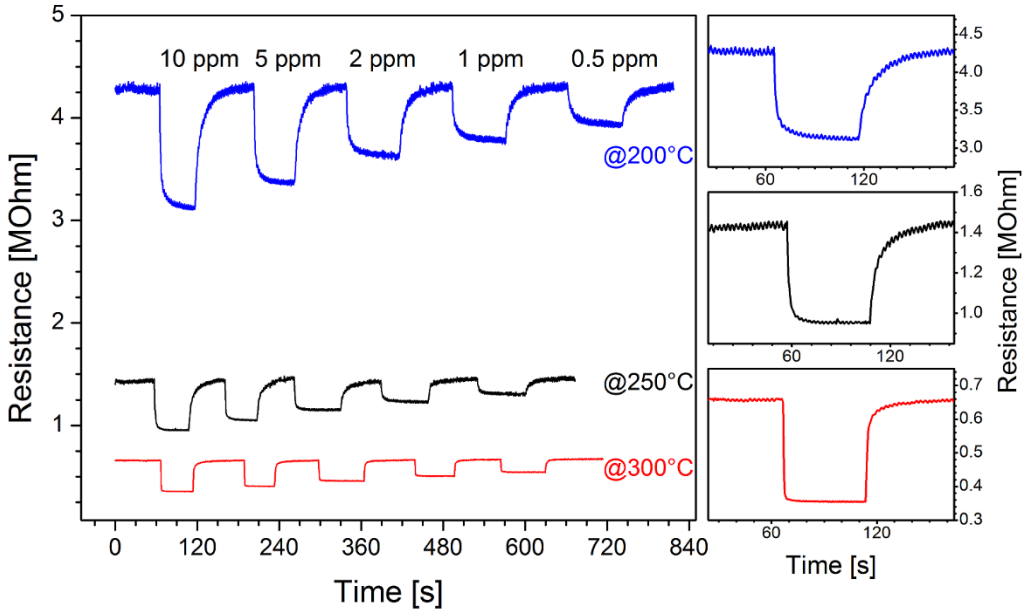

Figure 9.3 – Left: dynamic resistance at different temperature values, during the injection of different concentrations of ammonia. Right: magnification of the response to 10 ppmv of ammonia at each working temperature.

The resistance of the nanowire decreases with increasing temperature (from 4.3 MOhm at 200 °C to 0.7 MOhm at 300 °C). Therefore, the power consumed by the sensor is always of the order of μW: 0.23 μW at 200 °C and 1.43 μW at 300 °C.

At any working temperature, the resistance of the nanosensor is constant in the air and decreases sharply when ammonia gas is injected into the system. The resistance re-turns to its previous value when the ammonia flow is stopped and air is returned to the system. This behavior can be easily explained, as SnO_2 is an n-type semiconductor, and it is very reactive to its surroundings [280], mainly to reducing gases such as ammonia [281]. The sensing mechanism is well known: as soon as the nanowire is exposed to air, oxygen is adsorbed on its surface in the form of O^- and O^{2-}, draining electrons from the NW and increasing its resistance. When ammonia molecules are flowed onto the nanowire surface, they react with the adsorbed oxygen atoms, releasing electrons back to the nanostructure and decreasing the nanostructure resistance:

$$2\ NH_3 + 3\ O^-_{(ads)} \rightarrow N_2 + 3\ H_2O + 3e^- \qquad (9.1)$$

It can easily be seen that the intensity of the response decreases with decreasing gas concentration (ammonia is injected at 10, 5, 2, 1, and 0.5 ppmv, in order).

The responses were calculated by averaging the values obtained from three measurement runs such as that shown in Figure 9.3, which were carried out on three different days. The values obtained are shown in Figure 9.4, where the root mean square error (RMSE) is indicated for each concentration at each temperature.

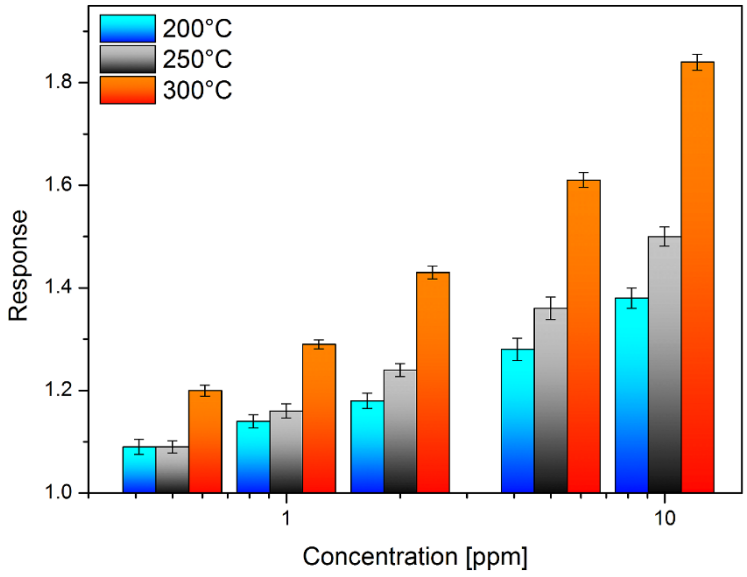

Figure 9.4 – Sensor response as a function of ammonia concentration at three working temperatures.

The response values calculated from the three graphs are shown in Figure 9.4 in order to be compared. The response is higher when the sensor works at a higher temperature.

Another thing that can be seen in Figure 9.3 is how both the response and the recovery of the sensor start very abruptly, but then, the behavior changes according to the temperature at which the

device is working. These parameters have also been calculated (as explained in Section 9.3.4.) so that they can be quantitatively compared, and they are shown in Figure 9.5.

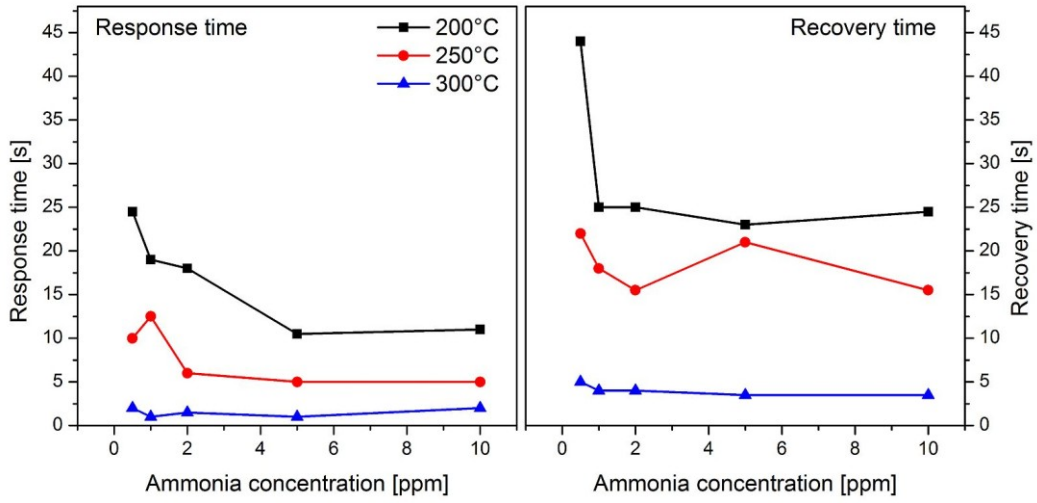

Figure 9.5 – Response times (left) and recovery times (right) as a function of the ammonia concentration for three working temperatures.

As can be seen, response times are always lower than 25 s, while recovery times are lower than 45 s and in general longer than response times in the same conditions. Both parameters seem to decrease somewhat as the gas concentration increases but without a marked trend. It is clear that the sensor speed increases as the operating temperature in-creases, and the best conditions are achieved at 300 °C, with response times around 2 s and response times around 4 s. The limit of detection was calculated applying the definition given in Section 9.3.4, and the obtained results are shown in Figure 9.6.

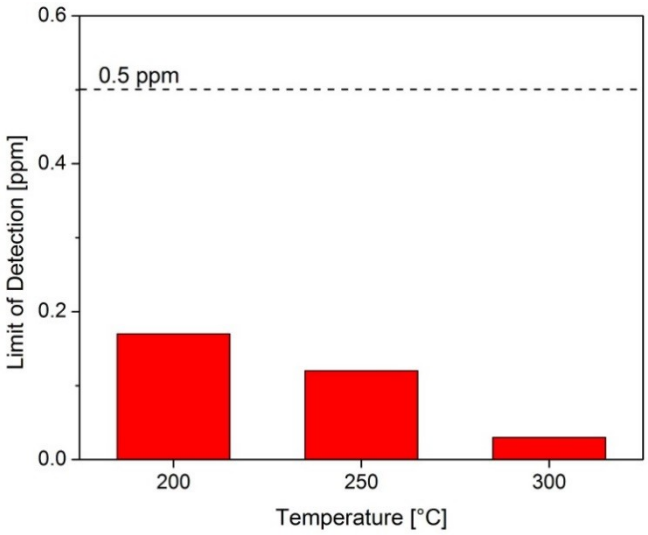

Figure 9.6 – Limit of detection of the single-nanowire (NW) sensor to ammonia at three working temperatures.

The LoD of the single nanowire device is always less than 1 ppmv and decreases with increasing temperature: 170, 120, and 30 ppbv at 200, 250, and 300 °C, respectively. This results from a higher response (Figure 4) and a higher signal-to-noise ratio (Figure 9.3).

In light of the performance obtained by the nanosensor by measuring ammonia, a working temperature of 300 °C was chosen for the subsequent measurements. At this temperature, all sensor parameters are optimized: higher response, faster response and recovery, and lower limit of detection.

9.4.3 Mackerel Fish Spoilage Measurements

The response of the gas sensor and the total viable count are plotted together in Figure 9.7. At the beginning, the TVC starts around 3×10^4 cfu/g and grows slowly; then, it reaches its maximum slope around 18 h, and finally, around 30 h, it seems to stabilize around 3×10^9 cfu/g.

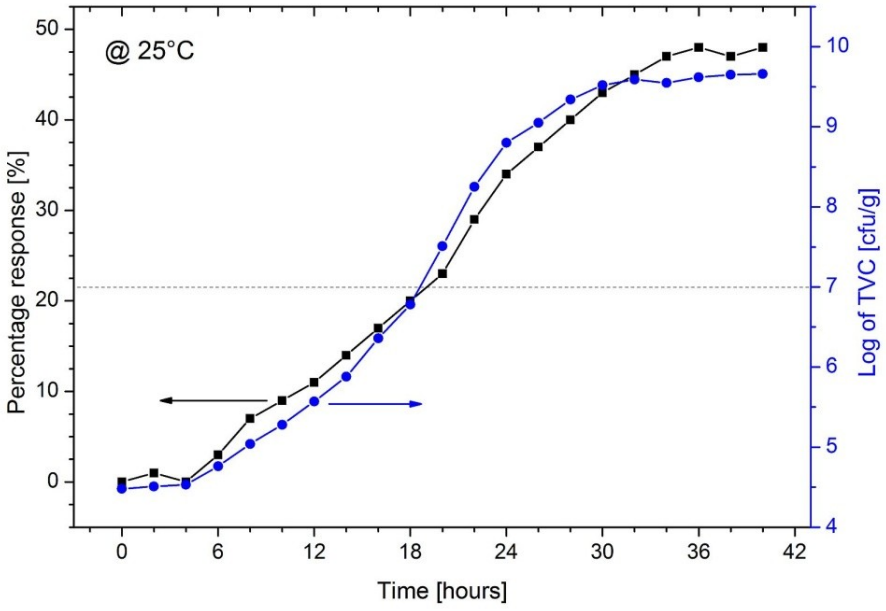

Figure 9.7 – Sensor response (black squares, left scale) and bacterial population (blue circles, right scale) in fresh mackerel fish over a period of 40 h at room temperature (25 °C).

The nanosensor response follows a similar behavior, increasing with a smaller slope and with a less sharp stabilization at the end. It is clear that the sensor response can be considered a good approximation of the total viable count. The horizontal dotted line identifies the threshold considered as the end of the shelf life of the fish both in the literature [263,282] and for institutions [283]. In our case, this limit was reached after 18 h of storage at room temperature. The correlation between the gas sensor response and the total viable count is shown in Figure 9.8.

As can be seen, the two signals are well correlated (correlation coefficient = 0.992) with a small error (RMSE = 2.17%). The root mean square error increases at log(TVC) values higher than 7.5, while below this value, it is much smaller. In particular, it is mini-mum for log(TVC) values from 6.4 to 7. Since the standard threshold used to distinguish the end of shelf life in literature is log(TVC) = 7, the sensor is more accurate than the total RMSE indicates, and the gas sensor can be calibrated using the total viable count as a reference.

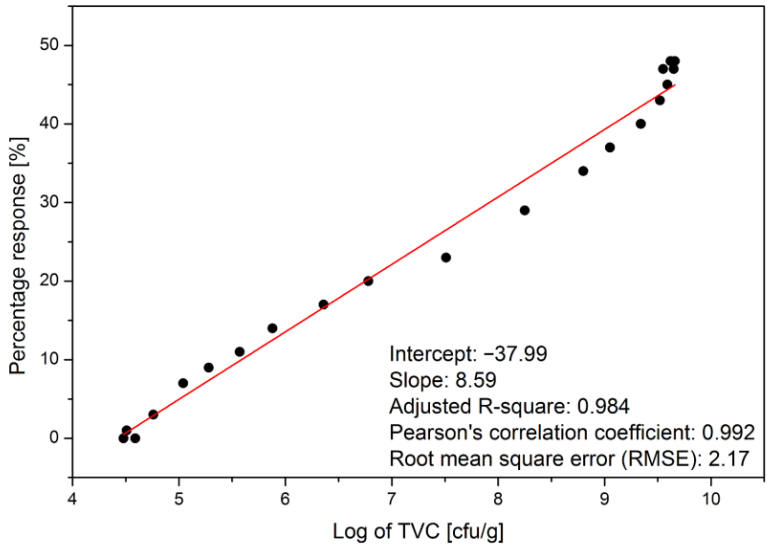

Figure 9.8 – Correlation between the gas sensor response and the total viable count.

To check how the shelf life of the fish is prolonged by storing it in a domestic refrigerator, spoilage measurements were repeated on samples stored at 4 °C, and the results are shown in Figure 9.9.

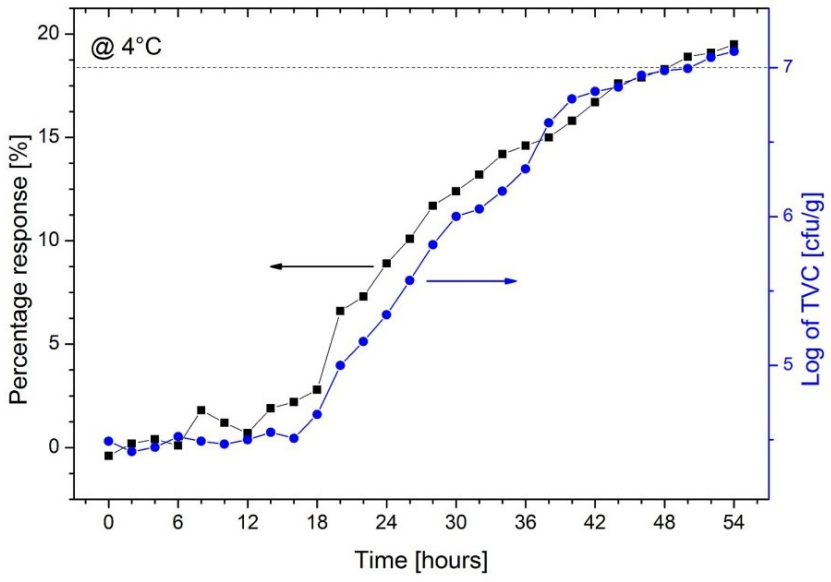

Figure 9.9 – Sensor response (black squares, left scale) and bacterial population (blue circles, right scale) in fresh mackerel fish over a period of 40 h at 4 °C.

Comparing the plots in Figure 9.9 with those in Figure 9.7, it is clear that the deterioration of the mackerel is going much more slowly. Both the gas response and TVC increase very slowly for up to 18 h; then, the slope increases for both signals. The correlation be-tween the two signals is good also in this case (correlation = 0.991), so that also, in this case, the gas response can be considered a good approximation of the total viable count. It appears evident that in this case, the threshold of 10^7 cfu/g is reached much later, around 48 h of storage.

To check if the sensor calibration works, mackerel samples stored at both 25 and 4 °C were measured at a random spoilage level. The results obtained are shown in Figure 9.10.

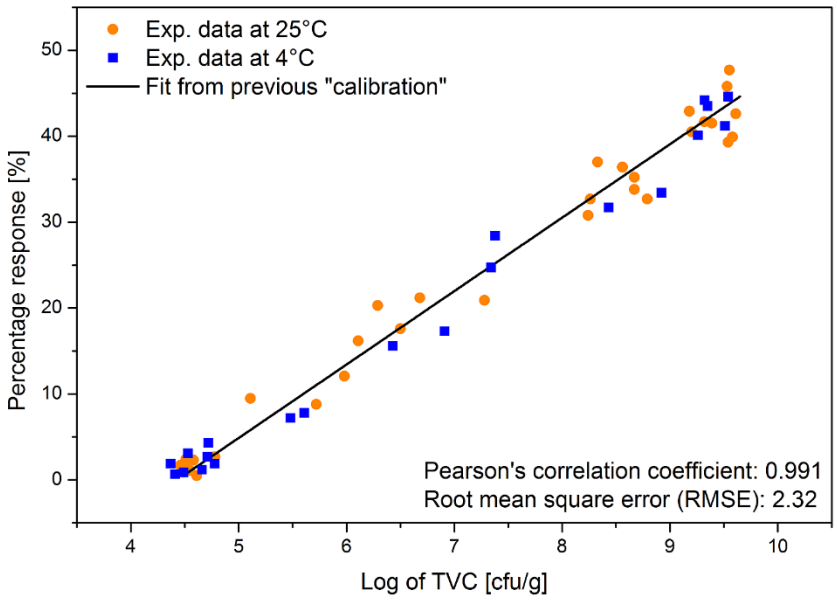

Figure 9.10 – Correlation between sensor response and total viable count (TVC) for measurements of samples at random spoilage level.

Figure 9.10 shows that there is a good correlation between the response obtained from the single-nanowire sensor and the bacterial population obtained from the TVC. The Pearson's correlation coefficient is 0.991, while the root mean square error on the sensor response is 2.32%. Samples stored at room temperature or in the fridge do not appear to have different trends. This

confirms that the response of the resistive nanosensor is a good measure of the level of deterioration of the mackerel.

9.5 Conclusions

A single SnO_2 nanowire was used as resistive gas sensor to assess the spoilage of mackerel fish. Performance was initially tested by measuring ammonia concentrations from 0.5 to 10 ppmv at three different operating temperatures. At the optimal temperature (300 °C), the sensor responds and recovers quickly (2 and 4 s, respectively) with a limit of detection of 30 ppbv. Then, the nanosensor was used to monitor mackerel deterioration over time. The response of the sensor follows well the concentration of the microorganisms while the fish deteriorates, with a correlation of 0.992. The sensor was tested with double-blind measurements of samples stored at 25 °C and 4 °C, and it was able to assess the mackerel quality in all cases.

CHAPTER 10. QUANTITATIVE ASSESSMENT OF TROUT FISH SPOILAGE WITH A SINGLE NANOWIRE GAS SENSOR IN A THERMAL GRADIENT

This chapter is based on the scientific paper [183]:

"Quantitative assessment of trout fish spoilage with a single nanowire gas sensor in a thermal gradient", Nanomaterials, 11 (2021) 1604. Doi: 10.3390/nano11061604.

10.1 Abstract

The response of a single tin oxide nanowire was collected at different temperatures to create a virtual array of sensors working as a nano-electronic nose. The single nanowire, acting as a chemiresistor, was first tested with pure ammonia and then used to determine the freshness status of trout fish (*Oncorhynchus mykiss*) in a rapid and non-invasive way. The gas sensor reacts to total volatile basic nitrogen, detecting the freshness status of the fish samples in less than 30 s. The sensor response at different temperatures correlates well with the total viable count (TVC), demonstrating that it is a good (albeit indirect) way of measuring the bacterial population in the sample. The nano-electronic nose is not only able to classify the samples according to their degree of freshness but also to quantitatively estimate the concentration of microorganisms present. The system was tested with samples stored at different temperatures and classified them perfectly (100%), estimating their log(TVC) with an error lower than 5%.

10.2 Introduction

Microbial growth is important in food as it reduces the shelf life and increases the risk of foodborne illness. Fresh food is even more susceptible to this problem as it deteriorates rapidly and this affects not only the food industry but also the health of consumers, with social and health costs [284,285]. Production chains and distribution networks have expanded and become more complicated and this has increased the time by which food reaches the consumer [286]. Fish is a health food that is increasingly consumed around the world, often fresh or thawed [287]. Fish and fish products are considered "health food products" as they contain a large number of high-grade proteins (including all vital amino acids). Rainbow trout is a sustainable fish labeled a "best choice" by the EPA and FDA for its healthiness and low mercury content. Its consumption is widespread also thanks to the fact that it is a fish that lives in both fresh and marine water [288]. Rainbow trout production has grown exponentially since the 1950s, as reported by FAO statistics [289]. The quality of fresh fish is therefore a major concern for both the industry and consumers [290]. Initially, groups of human experts used to assess the appearance, smell and texture of the fish [291,292] but this procedure was laborious and time-consuming and there-fore sensors capable of doing this automatically and objectively are being studied. Different methods have been used to evaluate the degree of freshness of the fish [291,293]. It is important that the sensor is small (portable), cheap (to deploy many along the production and distribution chain or to integrate one into the packaging) and fast (to measure in real time). After the death of the fish, the microorganisms on its surface multiply and gradually spread to various tissues [294]. The proliferation of microbes is a major cause of fish spoilage. In fact, the total viable count (TVC) is commonly used as a reference and definitive index [295]. During this process, microbes degrade trimethylamine N-oxide (TMAO) into trimethylamine (TMA) and ammonia [296]. At the same time, bacteria decompose urea and amino acids and produce NH_3 (ammonia) [297]. For these reasons, gas sensors usually measure total volatile basic nitrogen (TVB-N) consisting of ammonia, TMA and dimethylamine (DMA), which is commonly

used as a freshness criterion for fish [298]. The most precise and accurate method to analyze volatile compounds is to extract the volatiles and then identify them by separation with chromatographic techniques [288]. Unfortunately, this takes a significant amount of time, trained personnel and expensive equipment that is only accessible in a laboratory. This type of analysis can therefore be done only on a sample basis and guarantees the freshness of the products only in a statistical way. Monitoring the agri-food chain in a widespread manner requires the creation of sensors that are small, cheap and fast. Gas sensors are less invasive than other types of sensors and resistive devices are usually simpler and cheaper. Metal oxide chemoresistors are ideal candidates for this purpose: their size is a few microns and they are cheap because they are very simple. After thick and then thin films [299], the latest generation uses nanostructures, i.e., structures in which at least one dimension is of the order of nanometers [300]. The most commonly used nanostructures are nanowires (quasi-one-dimensional structures). The tiny diameter of the nanowires (NWs) causes the interaction on their surface to affect a large part of the wire section [301]. This way, the response is much higher and the limit of detection (LoD) is in parts per billion (ppbv). Silicon and metal oxide nanowires have been studied as ammonia sensors [302,303,304,305,306,307]. Nanowires are commonly used as a porous thin film on which metal electrodes are deposited [308,309] but they can also be grown directly from the electrodes [310,311] or even contacted individually [312]. A single nanowire has already been used to measure the freshness of mackerel samples but used in a traditional way as a simple chemiresistor [218].

In this work, a single tin oxide nanowire was used and made to work at three different temperatures. The responses were combined in a virtual array, which, working as an electronic nose, was able to evaluate the freshness of the tested fish. The response of the gas detection system to the TVB-N was compared with the total life count, proving capable of measuring the freshness of the rainbow trout quickly and precisely.

10.3 Materials and methods

10.3.1 Synthesis of SnO_2 nanowires

A forest of tin oxide (SnO_2) nanowires was grown by a chemical vapor deposition. An alumina boat filled with pure tin monoxide was used as the evaporation source, placed in the center of a horizontal quartz tube inside a Lindberg Blue M oven (Thermo Fisher Scientific, Waltham, MA USA) at its maximum temperature. A piece of silicon wafer (about 1×3 cm^2) was deposited with a thin gold film (about 5 nm) and placed 1 cm from the alumina boat. Silicon and gold, respectively, act as a substrate and catalyst for the growth of nanowires. The quartz tube was pumped to 10^{-2} mbar and purged with high-purity argon (99.999%) three times and then the system was pumped up to its pressure limit. The temperature was raised from room temperature to 850 °C with a ramp of 25 °C per minute and the oven was left at 850 °C for five minutes. A flow of 0.35 standard cubic centimeters of oxygen then flowed through the system, starting the process. The growth process lasted 30 min and finally the system was shut down and allowed to cool. At the end of the process, the samples were covered with a soft and homogeneous white layer composed of SnO_2 nanowires.

10.3.2 Material Characterization

The CVD-grown tin oxide nanowire forest was characterized by X-ray diffraction (XRD) using a Philips Xpert Pro (Malvern Panalytical, Malvern, UK) operating at 40 kV with CuKα radiation. Secondary electron microscopy (SEM) and transmission electron microscopy (TEM) images were acquired with a Hitachi S-4800 (Tokyo, Japan) and a JEM-100CX (JEOL, Tokyo, Japan), respectively.

10.3.3 Fabrication of the Sensor

A square of the substrate with the forest of nanowires (approximately 1 × 1 cm^2) was sonicated in dimethylformamide for two seconds and the resulting dispersion was drop cast onto a Si/SiO_2 wafer by spinning it at 6000 rpm. An array of Ti/Pt (10/250 nm) electrodes was deposited on top of the dispersed nanowires using UV lithography. Using a resistance measurement and optical microscopy, pairs of adjacent electrodes connected by nanowires were found. These electrode pairs were characterized by SEM to find cases where a single nanowire was connecting the metal pads.

10.3.4 Gas Sensor Measurements

The single nanowire sensor was tested in a system consisting of a measuring chamber with a heatable holder and microprobes. The measuring chamber was connected to high-purity gas cylinders through mass flow controllers. The microprobes were connected to a multimeter (Keithely 2410, Cleveland, OH, USA) interfaced with a data acquisition program (LabView, National Instruments, Austin, TX, USA). Initially the device was kept at 500 °C in nitrogen for 4 h while it was powered at 1 V in order to stabilize the nanostructures and their intrinsic resistance. This procedure served to stabilize the electrical properties of the nanostructures so that they did not change over time [300]. The electrical contact of the semiconductor nanowires with the metal electrodes was studied by analyzing the I-V curves. The good linear behavior found proved a good ohmic contact.

The sensor worked under a voltage of 1 V at three different temperature values (200, 250, 300 °C) towards low concentrations of ammonia (0.1–5 parts per million, ppmv) with a total gas flow maintained at 400 sccm. The sensor response was calculated with the standard definition $S = R_{air}/R_{gas}$, where R_{gas} and R_{air} were, respectively, the resistance of the sensor in the presence of ammonia and in air. The response time of the device was also calculated in the standard way as the

time it took to reach 90% of the maximum response. Similarly, the recovery time was calculated as the time to reach 90% of complete recovery. The limit of detection (LoD) was calculated as $3 \cdot SD_{noise}$/sensitivity, where SD_{noise} was the standard deviation of the sensor signal and sensitivity was the derivative of the sensor response as a function of the gas concentration [313].

10.3.5 Trout Spoilage Measurements

The fresh rainbow trout fish were purchased from a fish farm in Verona (Italy) and kept on ice for less than 1 h upon arrival in the laboratory. Several pieces of trout weighing 20 g were cut from the fresh fish using disposable gloves and autoclaved tools. Each piece was stored in a separate vessel until the measurement with the gas sensor. A few samples were stored at room temperature (25 °C) and a few in the refrigerator (4 °C). A sample was placed in the sensing chamber initially every hour then every three hours and finally every six hours to measure the emitted TVB-N. Immediately after measuring with the gas sensor, the sample was subjected to a microbial analysis in order to compare the two measurements. The total viable count (TVC) was performed using a spread plate technique [299] on a plate count agar and agar base (Oxoid CM0463 and 0055, Hampshire, UK). The plates were counted after an incubation time of 48 h at 30 °C.

10.3.6 Multivariate Statistics and Data Mining

A principal component analysis (PCA) was applied to the response values of the gas sensor at three different temperatures combined together. In this case, the PCA did not reduce the dimensionality but only served to visualize the spatial relationships between the points in a more evident way. The same three-dimensional points were used to quantitatively estimate the TVC value of the fish samples by means of a linear kernel support vector machine [314] used as a regressor.

The points measured (double-blind) were randomly divided into two sets, train (32 points) and test (18 points), in order to calibrate the system and then evaluate its quantification performance.

10.4 Results and Discussion

10.4.1 Characterization of the Nanowires

The morphology of the spaghetti-like SnO_2 nanowires obtained by CVD was studied by scanning electron microscopy. An SEM image of the nanowire layer is shown in Figure 10.1a.

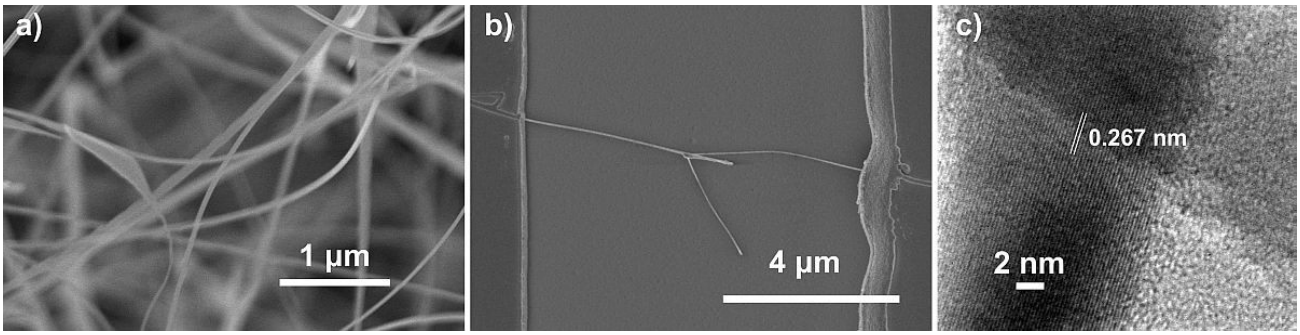

Figure 10.1 – (a) SEM image of the SnO_2 nanowires grown by CVD (magnification 30 k); (b) SEM image of the sensor: a single SnO_2 nanowire bridging the metallic electrodes on the sides (magnification 12 k); (c) TEM image of two crossing nanowires.

Figure 10.1a shows long and thin nanowires with a constant diameter whose average value was 40–80 nm. The SEM image in Figure 10.1b shows the single nanowire that was used as a sensor by connecting the two electrodes to the sides. The nanowire forks in the center of the space between the two electrodes. The diameter of the nanowire was approximately 57 nm on the left side and 33 nm on the right side. The thin diameter of the right side and the probable potential barrier in the center contributed to the improvement of the sensor performance. Figure 10.1c shows a TEM image of two crossing nanowires. The interplanar fringes of 0.267 nm corresponded with the crystalline planes (101) of the tetragonal SnO_2 structure. The image confirms that the nanowires were monocrystalline with no amorphous layers.

The composition and structure of the SnO_2 nanowires were also confirmed by the X-ray diffraction pattern shown in Figure 10.2.

All of the diffraction peaks present in the pattern could be easily indexed to the tetragonal phase of SnO_2 with lattice parameters of a = b = 4742 Å and c = 3186 Å and therefore agree well with the standard values (JCPDS n. 77-0450). The absence of amorphous contributions, impurity peaks or other SnO_2 phases confirmed the high purity of the nanowires.

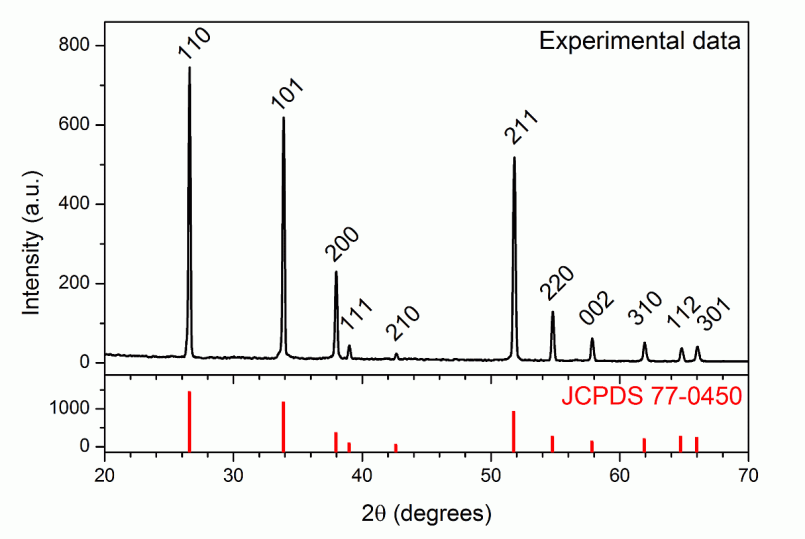

Figure 10.2 – XRD pattern of SnO_2 nanowires grown on the substrate (one of which was used as a single nanowire sensor). The tetragonal SnO_2 reference pattern (JCPDS 77-0450) is shown below (red in line).

10.4.2 Ammonia-Sensing Performance

The sensor performance was initially tested with low ammonia concentrations (0.1 to 5 ppmv). The dynamic resistance of the sensor was tested at three different temperatures (200, 250 and 300 °C). The three answers obtained then composed the 3D signal processed by the machine learning algorithms. The dynamic resistance plots at different temperatures are shown in Figure 10.3a.

The resistance of the nanosensor was constant in air and, at any working temperature, it dropped sharply when ammonia gas was flushed into the chamber. When the ammonia flow was stopped and pure air was returned into the system, the resistance returned to its original value. This behavior is typical of *n*-type semiconductors [300], in response to reducing gases such as ammonia [301].

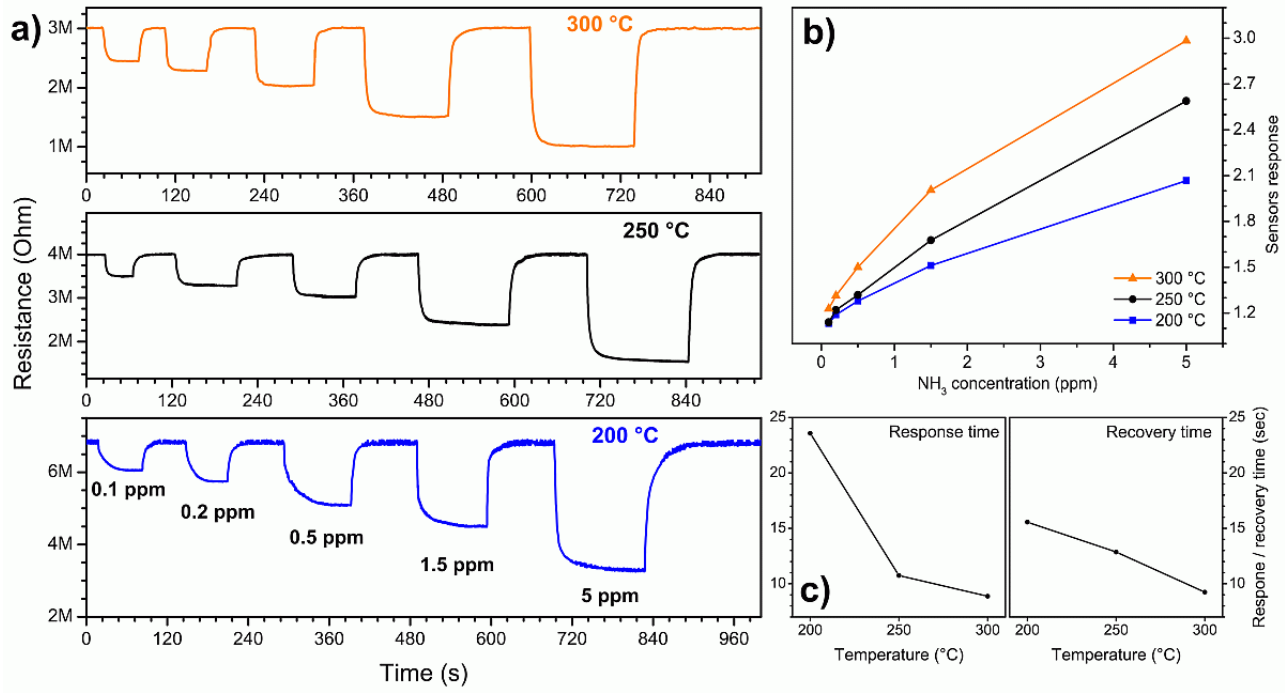

Figure 10.3 – (a) Dynamic resistance at three temperature values during the injection of different concentrations of ammonia; (b) sensor response as a function of the ammonia concentration for different working temperatures; (c) response and recovery times as a function of the sensor working temperature.

The detection mechanism is known in the literature: when the nanowire is exposed to air, oxygen is adsorbed in the form of O^- and O^{2-}, draining electrons from its interior to form chemical bonds on the surface. Decreasing the number of charge carriers increases the sensor resistance. When the ammonia molecules landed on the surface of the nanostructure, they reacted with the adsorbed oxygen atoms breaking their chemical bond and releasing electrons into the nanowire. The increase in the number of charge carriers decreased the resistance of the sensor. The three graphs in

Figure 10.3a show that the resistance variation was proportional to the ammonia concentration. It can also be seen how, as the temperature increased, the air resistance of the sensor decreased and the response and recovery became faster. Figure 10.3b shows the sensor response (calculated as explained in Section 10.3.4) as a function of the gas concentration for the three temperatures tested. The response increased with the concentration almost linearly and was greater for higher working temperatures. The speed of the sensor is quantified in Figure 10.3c where the average response time and recovery time at each temperature are shown as defined in Section 10.3.4. Both times decreased according to the working temperature. The response time was higher than the recovery time at 200 °C but at higher temperatures it became shorter or comparable. In general, the response and recovery times were very fast: at the lowest temperature they were, respectively, 24 and 15.5 s while at higher temperatures they were always less than 13 s. The limit of detection (calculated as specified in Section 10.3.4) was very low at all temperatures tested: 13.4, 4.9 and 1.8 ppbv at 200, 250 and 300 °C, respectively [313].

10.4.3 Trout Fish Spoilage Measurements

The sensor was then used to measure the freshness of the rainbow trout samples stored at 25 °C. As the sensor measured the volatiles emitted by the fish sample (mainly TVB-N, i.e., ammonia, dimethylamine and trimethylamine), it was not possible to compare the response with a known concentration. For this reason, together with the sensor response, Figure 10.4 also shows the microbial count used as a reference.

The responses of the gas sensor are read on the left scale while the total viable count is on the right of Figure 4. The response of the sensor increased as the working temperature increased, as in the case of ammonia. At all temperatures, the response increased over time, slowly over the first six hours and then faster. The TVC increased similarly, starting at a value of 4.2 (note that the log of the

TVC was plotted), reaching the maximum slope at around 20 h and exceeding a value of 10 after 60 h. The response of the single nanowire resistive sensor could be considered to be a good indirect measure of the microbial count and therefore of the freshness of the fish. The dashed horizontal green line identifies the threshold considered as the end of the shelf life of the fish both in literature [315,316] and for the authorities [317,318]. The threshold was exceeded approximately after 22 h and 40 min of storage at room temperature (25 °C).

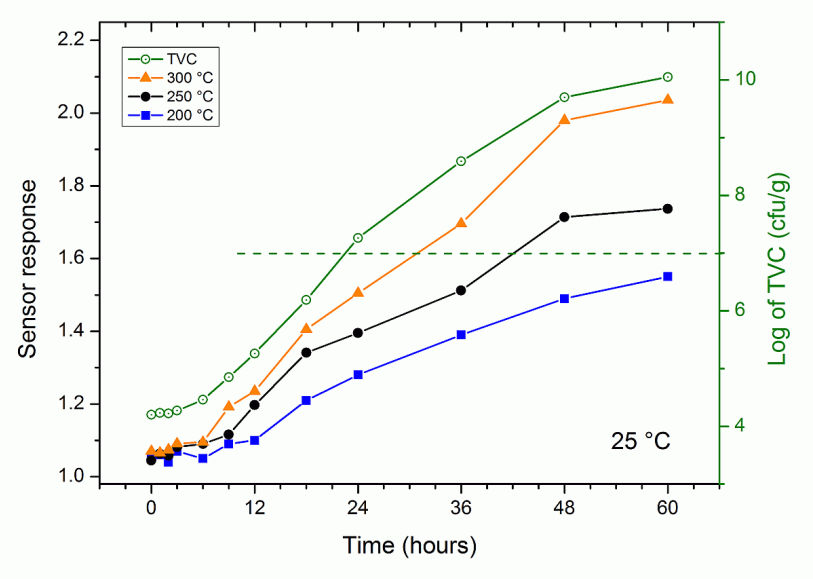

Figure 10.4 – Sensor response (solid symbols, left scale) and bacterial population (green open circles, right scale) in fresh trout fish kept at room temperature (25 °C) over a period of 60 h.

Also in this case the responses of the gas sensor are read on the left scale, while the total viable count on the right. The sensor was also tested with rainbow trout samples stored at 4 °C for 84 h. Figure 10.5 shows the sensor response at 200, 250 and 300 °C and the microbial count detected on the samples over time. During the first 12 h, the microbial count remained more or less constant at around a value of 4.2, then began to rise almost linearly to reach a value of 7.84 after 84

h. The edibility threshold in this case was reached after approximately 64 h. The response of the gas sensor behaved in a similar way at all temperatures.

The trend of the response of the gas sensor at the various temperatures in Figures 10.4 and 10.5 was very similar to that of the microbial count. This could be explained by the fact that TVB-N is the metabolic product of the microbes responsible for the degradation of fish [319] and meat [320]. To evaluate how effective the response of the single nanowire gas sensor could be as a measure of fish freshness, a series of samples stored at different temperatures were measured in a double-blind capacity.

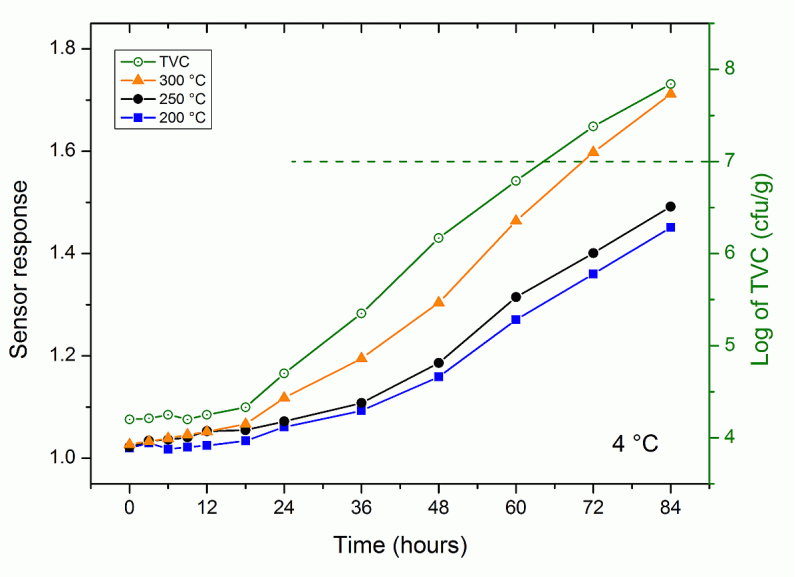

Figure 10.5 – Sensor response (solid symbols, left scale) and bacterial population (green open circles, right scale) in fresh trout fish kept at 4 °C over a period of 60 h.

For each sample, the response of the gas sensor was first measured and immediately afterwards the microbial analysis was carried out in order to have a comparison under the same conditions. The measurements are shown in Figure 6 where the response is reported as a function of the logarithm of the total viable count. The response was linear at all working temperatures with Pearson's correlation coefficients of r were greater than 0.99 in all cases. The error decreased as the

temperature rose but was always less than 10%. This demonstrated that the sensor response could be considered to be a good indirect measure of the TVC.

The three responses of the single nanowire gas sensor were combined to obtain a sort of virtual electronic nose following the approach already tested previously [321]. The 3D points obtained also included the correlations between the various answers and were therefore much more informative than a single response. A principal component analysis (PCA) is commonly used to increase the interpretability while minimizing information loss [322]. In this case, the three-dimensional points were processed with the PCA in order to visually evaluate how they were spatially correlated.

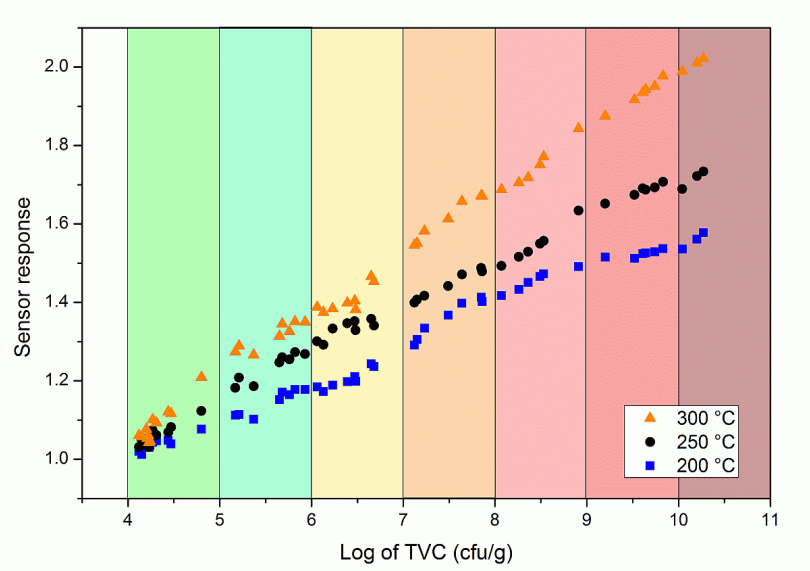

Figure 10.6 – Double-blind measurements of the sensor response as a function of the total viable count in rainbow trout samples.

The PCA graph in Figure 10.7 shows the points divided by color according to the TVC value. Each group of points is colored according to a unit interval of the logarithm of the TVC, as shown in Figure 10.6. It can be seen that the points are arranged in a zigzag line that goes down to a log value (TVC) of 6–7, then goes up to 8, goes down to 10 and then goes up again. Each group of points is

well separated from the others, with a possible small overlap only with the immediately preceding or following group. This overlap was expected as the measurement of the microbial count was continuous and therefore the points along the zigzag line ought to have also been continuous. This was evident in the point clouds of the intervals 7–8, 8–9 and 9–10, which concatenated well along the imaginary zigzag line. Figure 10.7 demonstrates that the single nanowire sensor was very sensitive and accurate as it not only distinguished the spoiled fish samples (over the threshold of 10^7 cfu/g) but also the various stages of the degradation process as measured by the total viable count.

To obtain an automatic quantitative estimate by the nanosensor, a support vector machine was used as a regressor [29]. In this way, the three responses of the gas sensor were automatically transformed into an estimate of the TVC and therefore of the degree of freshness of the fish. Figure 10.8 shows the regressor estimates against the "true" values (obtained from the TVC measurements). Clearly, the diagonal represents an estimate identical to the TVC value and therefore a perfect functioning of the nanosensor.

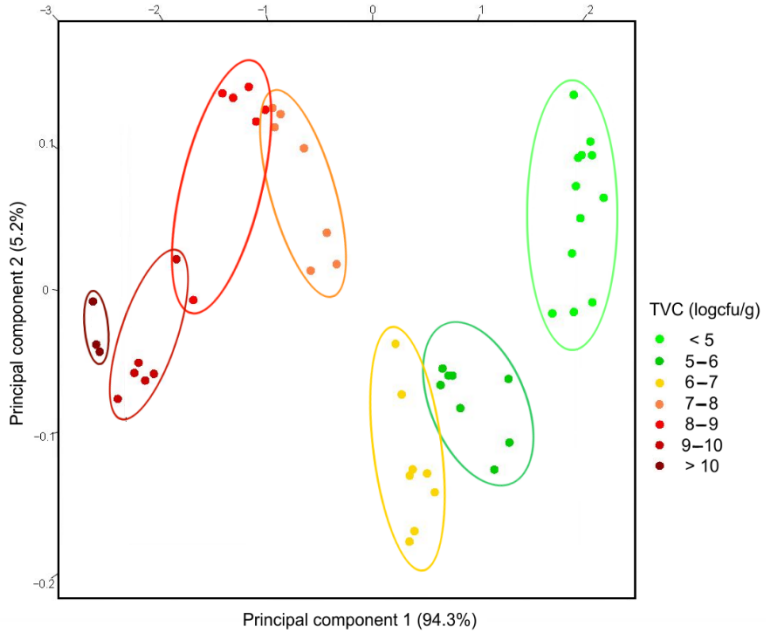

Figure 10.7 – PCA plot of random samples of rainbow trout. The color indicates the log(TVC) with the same scale of the X-axis in Figure 10.6.

The points in Figure 10.8 are all very close to the diagonal, indicating a very good estimate of the freshness of the fish. The average error obtained on all points was less than 5%, demonstrating that the single nanowire gas sensor approximated the microbial count measurement very well.

The points were collected in the two colored areas. The green zone indicates a TVC value that allowed the consumption of fish while the red zone indicates that the fish had deteriorated. This again meant that the sensor was in perfect agreement with the microbial count and could be used as a tool to ascertain the freshness of the rainbow trout samples. It should be noted that the results were obtained under laboratory conditions with samples collected from only one fish. It is reasonable to expect a larger error when working in the field on different fish.

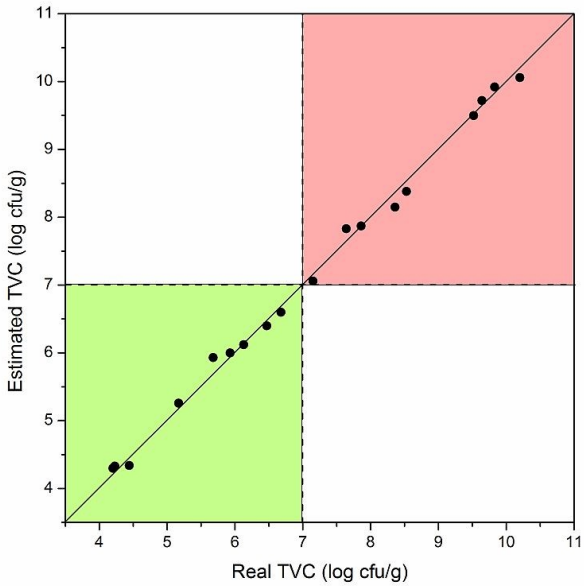

Figure 10.8 – Estimates of the TVC values versus the actual measured TVC values for random rainbow trout samples. The green color indicates the area in which the microbial load was compatible with consumption while the red one indicates that the fish had deteriorated.

The single nanowire gas sensor is in fact tiny and portable (while the TVC can only be done in a laboratory equipped by trained personnel) and takes less than half a minute (while the TVC usually takes days). For this reason, we consider that the proposed sensor could be ideal to assess the freshness of fish during its shelf life.

10.5 Conclusions

A SnO_2 single nanowire gas sensor was used to assess the deterioration of rainbow trout fish. The performance was initially tested by measuring ammonia concentrations from 0.1 to 5 ppmv at three different operating temperatures. The sensor responded quickly even at very low concentrations. The responses of the nanosensor at different temperatures were then used to monitor trout spoilage over time. The gas sensor response proved to be a good approximation of the total viable count at all working temperatures. The use of machine learning algorithms allowed the determination of the spoilage stage of the fish and the estimation of its total viable count.

Considering the tiny size (tenths of a millimeter), economy, ease of use and speed, the single nanowire gas sensor would be ideal as a non-invasive tool for monitoring the freshness of rainbow trout along its production and distribution chain.

CHAPTER 11. SINGLE NANOWIRE GAS SENSOR ABLE TO DISTINGUISH FISH AND MEAT AND EVALUATE THEIR DEGREE OF FRESHNESS

This chapter is based on the scientific paper [184]:

"Single nanowire gas sensor able to distinguish fish and meat and evaluate their degree of freshness", Chemosensors, 9 (2021) 249. Doi: 10.3390/chemosensors9090249

11.1 Abstract

A non-invasive, small and fast device is needed for food freshness monitoring, as current techniques do not meet these criteria. A resistive sensor composed of a single semiconductor nanowire was then used at different temperatures, combining the responses and processing them with multivariate statistical analysis techniques. The sensor, very sensitive to ammonia and total volatile basic nitrogen, proved to be able to distinguish samples of fish (marble trout, *Salmo trutta marmoratus*) and meat (pork, *Sus scrofa domesticus*) both stored at room temperature and 4°C in the refrigerator. Once separated, the fish and meat samples were classified by degree of freshness/degradation with two different classifiers. The sensor classified the samples (trout and pork) correctly in 95.2% of cases. The degree of freshness was correctly assessed in 90.5% of cases. Considering only the errors with repercussions (when a fresh sample was evaluated as degraded, or a degraded sample was evaluated as edible) the accuracy rises to 95.2%. Considering the size (less than a square millimeter) and the speed (less than a minute), this type of sensor could be used to monitor food production and distribution chains.

11.2 Introduction

Food safety is important nowadays, especially when it comes to fresh food. Fresh foods are healthier but are also more prone to rapid degradation. This has important repercussions both in terms of food losses along the distribution chain, and on the health of consumers and therefore on the health system [323,324]. The modern development of longer distribution chains is not suitable for this type of food, as it extends the time that passes before the consumer has the product at home, and therefore increases the possibility of degradation [325]. Fish and meat products are fresh products that represent optimal growth media for a large variety of spoiling microorganisms. The metabolic activity of these microbes can lead to the production of ammonia, biogenic amines, nitrogen compounds, alcohols, ketones, aldehydes, esters, gases (CO_2), and other molecules, responsible for unpleasant odors [326]. For this reason, the number of microorganisms present for each gram of sample is used as a reference value when evaluating the degradation of a product and is called the total viable count (TVC). Since after fishing or slaughter the microorganisms reproduce and their number increases greatly as they spread to the various tissues [327], the TVC measurement can be considered a standard [328].

Fortunately, the volatiles produced by the microorganisms can also be used to assess the degradation status of the product in a non-invasive way. An instrument capable of detecting these volatiles can give a rough estimate of the number of microorganisms on the meat or fish, and therefore of its state of freshness/degradation [329,330]. A sufficiently sensitive device would be able to detect these volatiles at a very initial state, when the proliferation of microorganisms has not yet degraded the product. In this way it could be used to monitor the quality of the product along its distribution chain, from production to sale to the final consumer. A group of volatile molecules widely used to measure the degradation of meat and fish is the so-called total volatile basic nitrogen (TVB-N). The main components of this group are trimethylamine $(CH_3)_3N$ (TMA), dimethylamine $(CH_3)_2NH$ (DMA) and ammonia NH_3 [331].

There are already tools capable of accurately analyzing these volatile compounds: they extract them, separate them and identify them with chromatographic techniques and mass spectrometry [332]. This type of technique can identify every single compound present in the headspace, so that it can be linked to the metabolic processes of spoilage microorganisms. Unfortunately, the other side of the coin is the complexity, size and cost of this equipment, but above all the time taken by highly qualified personnel. For this reason, it is not possible to use these techniques on a large scale, to monitor products along the production and distribution chain. For this purpose, it is necessary to develop sensors that are fast and inexpensive, so that they can be used extensively. Resistive gas sensors based on metal oxide nanowires are a strong candidate, as they are tiny, simple and inexpensive [333,334]. The mechanism is based on the chemical reactions that take place on the surface of the nanowires, where the volatile molecules react by releasing or absorbing electrons and thus influencing the resistance of the sensor. It has already been shown that such sensors can detect ammonia TVB-N at very low concentrations and thus evaluate the freshness of mackerel fish [183]. Unfortunately, a resistive sensor gives a one-dimensional response that cannot have selectivity and can therefore only be calibrated and used for a single food product at a time.

To overcome this problem, here the responses obtained by the sensor at different working temperatures are combined and processed with multivariate statistical analysis techniques (principal component analysis, PCA) and machine learning algorithms (support vector machine, SVM) [335]. In this way the sensor is able to distinguish different products (specifically marble trout and pork) with a first classifier, and then independently evaluate, by means of two different classifiers, the degradation status of meat and fish. The distinction between meat and fish occurs correctly in 95.2% of cases, with only one misclassification per food. The degree of freshness/degradation of the sample is correctly indicated in 85.7% of cases for trout and in 95.2% of cases for pork. If only the

classification as edible/inedible is considered, the classification is correct in 95.2% of cases for both types of food.

11.3 Materials and methods

11.3.1 Synthesis of SnO_2 nanowires

Initially a layer of tin oxide nanowires (SnO_2) was grown by means of chemical vapor deposition (CVD) in a horizontal tube of quartz placed inside an oven (Lindberg Blue M, Thermo Fisher Scientific, Waltham, MA, USA). The nanowires were grown using an alumina boat filled with pure tin monoxide, placed in the center of the furnace, at its maximum temperature as the evaporation source. The nanostructures were grown on a silicon substrate of about 1x1 cm^2, deposited with a thin gold film (about 5 nm thick) acting as a catalyst and positioned 1 cm from the alumina boat. The quartz tube was pumped down to 10^{-2} mbar and then purged with high purity argon (99.999%) three times and finally the system was pumped to limit the pressure. The temperature was then increased from 26°C (room temperature) to 850°C at a rate of 25°C/min and the oven was held at 850°C for five minutes. The growth of the nanowires began by injecting an oxygen flow of 0.35 standard cubic centimeters per minute (sccm) into the system. The growth of the nanostructures following the vapor liquid solid (VLS) mechanism [336] lasted 30 minutes, then the system was shut down and allowed to cool. At the end of the growth process the substrate showed an evident soft and homogeneous white film.

11.3.2 Nanowires Characterization

The morphology of the metal oxide nanowires was investigated by scanning electron microscopy (SEM) with a Hitachi S-4800 (Tokyo, Japan) and by transmission electron microscopy (TEM) using a JEM-100CX (JEOL, Tokyo, Japan) operating at 90 kV. The structure of the SnO_2

nanowires was characterized by X-ray diffraction (XRD) using a Philips Xpert Pro (Malvern Panalytical, Malvern, UK) diffractometer working at 40kV with CuKα radiation.

11.3.3 Sensor fabrication

A piece of substrate with grown SnO_2 nanowires was then treated under ultrasounds in dimethylformamide (DMF) for two seconds. Some drops of the resulting dispersion were spread on an entire Si/SiO_2 wafer, while spinning it at 6000 rpm, in order to optimize the nanowire density. A Ti/Pt (10/250 nm) two-dimensional array composed of square electrodes was deposited on top of the dispersed nanowires using sputtering and UV lithography on the whole wafer. Titanium was used as an adhesion layer in this case, but this choice must be weighed in light of its influence on the performance of the device [337,338,339]. By observing the gap between all the pairs of electrodes under an optical microscope and measuring their resistance, pairs of electrodes bridged by one or more nanowires were found. Observing the candidates with the best characteristics by means of SEM microscopy, the pairs were verified in order to choose the single nanowire devices and check their characteristics (arrangement, length, morphology, diameter...).

11.3.4 Gas sensor measurements

The single nanowire sensor was placed on a small heatable plate in a chamber connected to gas flow controllers connected to high purity gas cylinders. The electrodes were contacted with microprobes connected, through a multimeter (Keithely 2410, Cleveland, OH, USA), to a data acquisition program (LabView, National Instruments, Austin, TX, USA). The sensor was initially heat treated for 8 hours at 500°C in nitrogen while being fed with 1V, in order to stabilize the structure and its resistance so that they do not change during the experiments [340]. The sensor showed good ohmic contact between the nanowire and the metal electrodes and its resistance

dropped from 7.5 MOhm at 200°C down to 122 kOhm at 360°C. The sensor was initially tested with different ammonia concentrations (5 to 0.1 ppmv) while heated to various temperatures (200 - 360°C).

The most common definition in literature has been used for the sensor response, that is $S = R_{air}/R_{NH3}$, where R_{air} and R_{NH3} are respectively the resistance of the sensor in air and in the presence of ammonia. The speed of the single nanowire sensor is evaluated using a common definition of response and recovery times: t_{RESP} is the time it takes to reach 90% of the maximum response, and t_{REC} is the time to go down to 90% of the full recovery. The limit of detection (LoD), that is the minimum detectable concentration, was calculated as 3 • N / D, where N is the noise of the sensor signal (its standard deviation) in air and D is the derivative of the sensor response as a function of the ammonia concentration.

11.3.5 Meat and fish spoilage measurement

The two foods (one marble trout and one piece of pork) were cut into cubes weighing about 20g from a larger fresh piece, using disposable gloves and autoclaved tools. Each sample was stored individually, in a glass jar, until the moment of measurement. A part of the samples was stored at room temperature (about 26°C) and another part instead in a refrigerator at a temperature of 4°C. At each measurement (initially every hour, then three, six and finally twelve hours) a sample was placed in the measurement chamber to determine the response of the gas sensor, and immediately afterwards it was subjected to microbial analysis, in order to compare the two measurements. The total viable count (TVC) was assessed using a spread plate method [341] on a plate count agar and agar base (Oxoid CM0463 and 0055). The plates were then counted after an incubation time of 48 h at 30°C.

11.3.6 Machine learning

Since the single response of the resistive sensor is inherently non-selective, the responses at the five working temperatures were combined to create 5-dimensional points that could be processed and analyzed with multivariate statistical analysis techniques [342]. The 5D points were used both for visualization via principal component analysis (PCA) and for classification and quantification with support vector machine (SVM). The samples used for PCA are those measured initially, to monitor the degradation of the samples over time. Subsequently other samples were randomly measured in order to reach a sufficient number of data to be divided into two groups: two thirds for the training group and one third for the test group. The SVM is used as a classifier in two successive steps: a first classifier is used to identify whether the sample is fish or meat (marble trout or pork), and subsequently two classifiers are used on the subgroups identified as fish and meat, in order to evaluate their degree of freshness. All SVM classifiers are always used with a linear kernel.

11.4 Results and discussion

11.4.1 Nanowires characterization

The SnO_2 nanowire forest was initially studied by scanning electron microscopy in order to investigate the morphology of the nanostructures. The nanowires that make up the forest, shown in Fig. 11.1a, have diameters around 40-65 nm and are several microns long. Many of the nanowires shown are blurred due to the charging effect due to their high electrical resistance.

The TEM image in Fig. 11.1b shows the tip of a single nanowire on a carbon membrane. The nanowire is straight and with a constant diameter. The structure of the nanowires was investigated through X-ray diffraction. All peaks shown in the X-ray pattern of Fig. 11.2 (black, top) can be easily indexed as the tetragonal phase of SnO_2, with lattice parameters of a = b = 4.742 and c =

3.186 Å, which are in good agreement with the values reported as reference (JCPDS n. 77-0450, red, bottom).

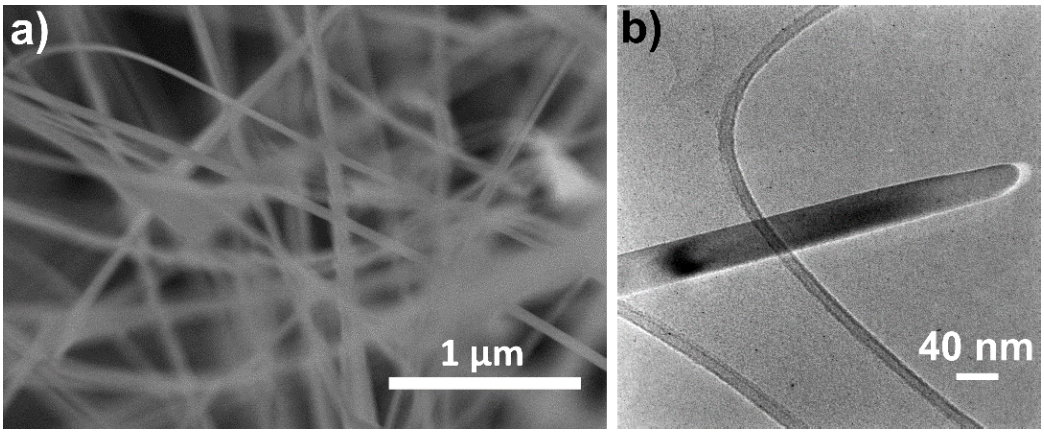

Figure 11.1 – a) SEM image of the SnO_2 nanowires forest; b) TEM image of a nanowire tip.

There are no phases other than the tetragonal one of SnO_2, nor peaks due to impurities or amorphous contributions, confirming the good crystallinity of the nanowires.

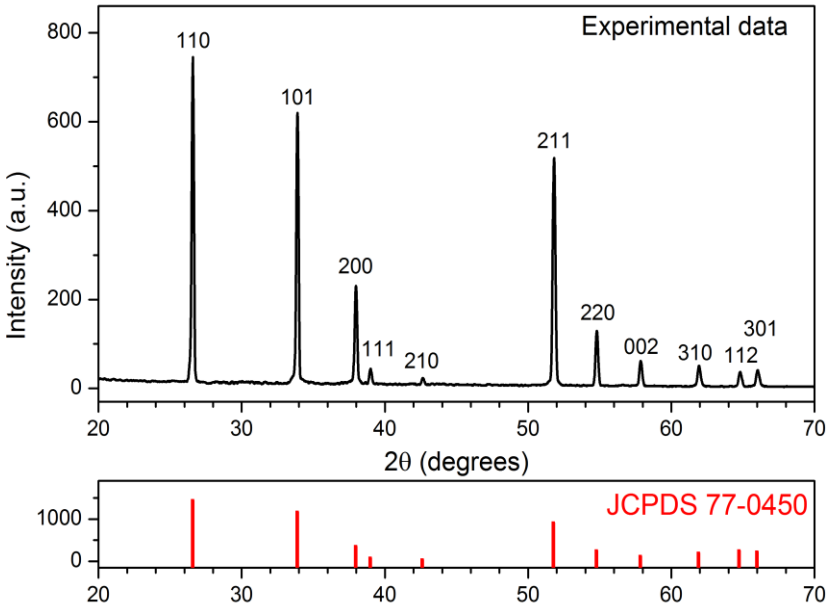

Figure 11.2 – XRD patterns. Top (black): experimental pattern of the SnO_2 nanowires used to fabricate the single-nanowire sensor; Bottom (red online): reference pattern of tetragonal SnO_2 (JCPDS 77-0450).

11.4.2 Ammonia sensing performance

The sensing properties of the single nanowire sensor were initially tested by measuring different concentrations of ammonia, as this volatile is part of the TVB-N, which is a known marker of meat and fish degradation [343]. Low concentrations were measured, from 5 to 0.1 ppmv. The measurements were carried out at five different temperatures, from 200 to 360°C, in order to subsequently combine the obtained responses and process the data with multivariate statistical analysis. Fig. 11.3a shows the current as a function of time as the different ammonia concentrations (indicated by the gray background) are injected into the measurement chamber. As can be seen, as the ammonia is flowed onto the nanowire, the current rapidly increases, and quickly returns to its base value as the ammonia is evacuated.

As can be seen in Fig. 11.3a, the sensor is very stable after the heat treatment carried out before the measurements. It can be seen in the figure that both the response and the recovery become faster as the working temperature of the sensor increases. Average response times decrease from 48 to 8 seconds, while average recovery times decrease from 43 to 6 seconds. Fig. 11.3b shows the response values for the various ammonia concentrations at the five working temperatures. As can be seen, the response increases with increasing gas concentration with a slightly less than linear trend in most cases. The response at the lowest temperature is the most linear, while the response to the highest temperature is the one that tends to saturation. Fig. 11.3c shows a three-dimensional diagram of the sensor, with the SnO_2 nanowire (in white) acting as a bridge between the two metal electrodes (in blue). Fig. 11.3d instead shows a top view SEM image of the nanowire constituting the sensor. The behavior shown in Fig. 11.3a, with the current increasing as ammonia is injected, is typical of n-type semiconductors in response to reducing gases.

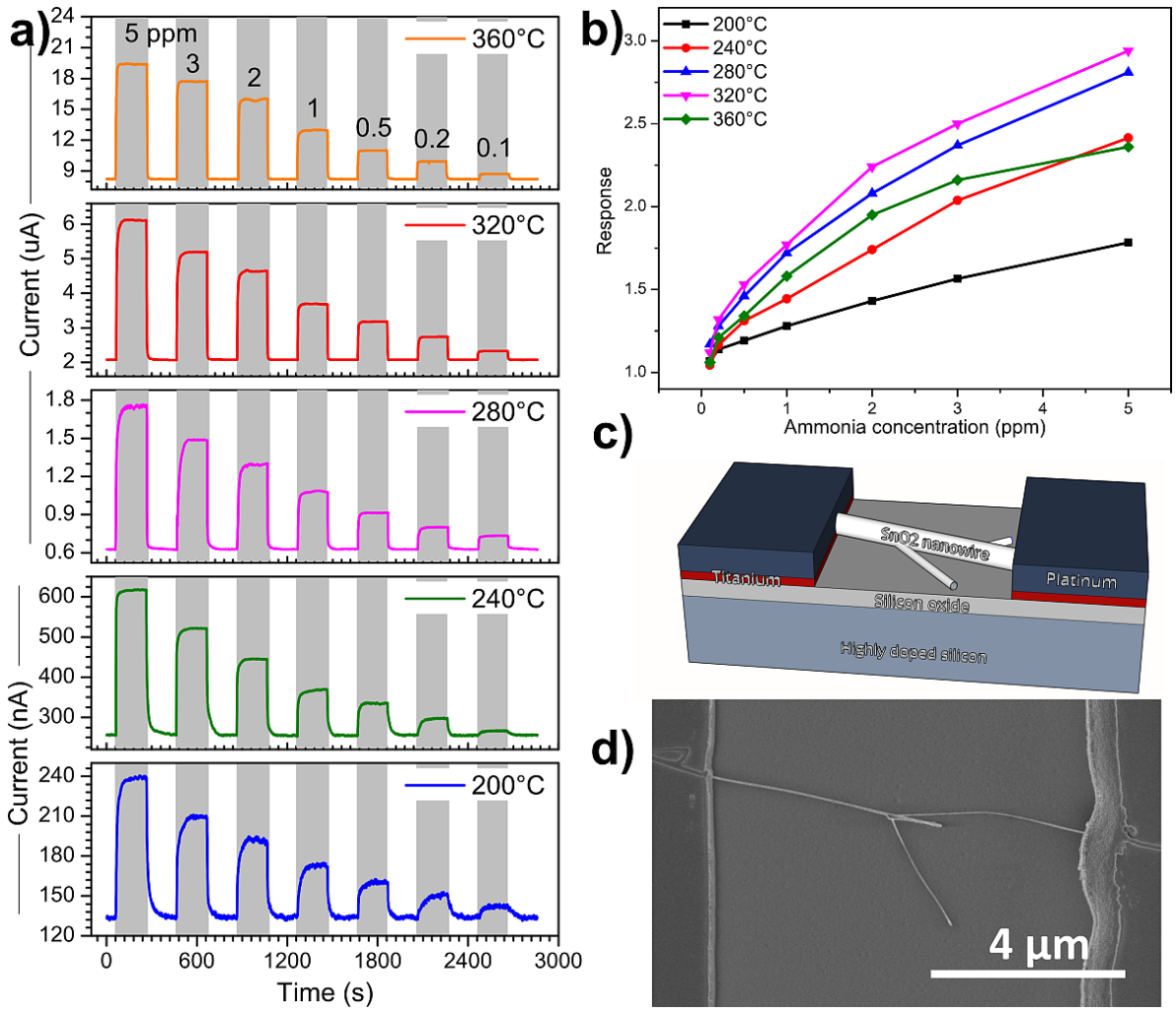

Figure 11.3 – a) dynamic current at different temperatures during the injection of different ammonia concentrations; b) sensor response as a function of gas concentration at different temperatures; c) three-dimensional model of the single nanowire sensor; d) SEM image of the single nanowire sensor.

Tin oxide is in fact a semiconductor in which the charge carriers are electrons, and it is very sensitive to the atmosphere that surrounds it [344], especially to reducing gases such as ammonia [345]. When the sensor is exposed to air, the oxygen reacts on the surface of the SnO_2 by draining electrons from the nanowire, and thus decreasing the current flowing through it. The ammonia molecules, on the other hand, react with the oxygen absorbed on the surface, releasing the electrons in the nanowire and thus increasing the current flowing through it [346,347]:

$$2\ NH_3 + 3\ O^-_{(ads)} \rightarrow N_2 + 3\ H_2O + 3e^- \qquad (11.1)$$

The last parameter calculated regarding the ammonia detection performance is the limit of detection, calculated according to the definition given in section 11.3.4. The calculated value decreases with increasing temperature, from 70 ppbv at 200°C to 18 ppbv at 360°C. This very low value is important for the sensor to detect the low concentrations present in the early stages of meat and fish degradation.

11.4.3 Measurements on marble trout and pork samples

The sensor response and the total viable count measured on marble trout samples stored at room temperature are plotted in Fig. 11.4a. The response of the sensor at any working temperature increases over time, as does the microbial count. The total viable count increases its slope after about ten hours and reaches the threshold value after about 23 hours. This value, indicated by the dashed horizontal green line, is considered the consumability limit of the sample in literature [331,348] and for health regulations [349].

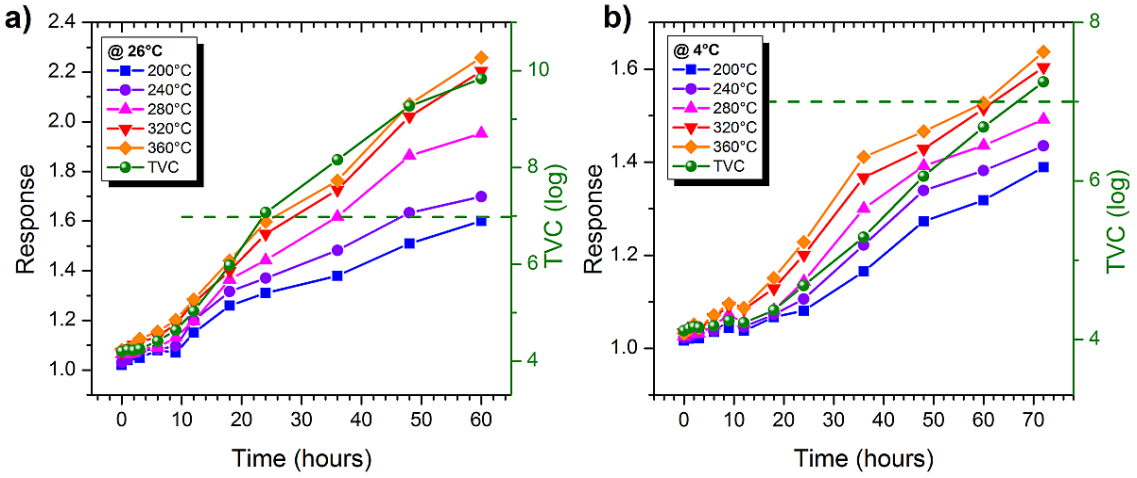

Figure 11.4 – a) Sensor response (colored symbols, left scale) and bacterial population (green spheres, right scale) in marble trout samples stored at room temperature over a period of 60 hours; b) Sensor response (colored symbols, left scale) and bacterial population (green spheres, right scale) in fresh marble trout stored at in a refrigerator over a period of 72 hours.

A similar behavior is followed in Fig. 11.4b, which shows the sensor responses and the total viable count measured on marble trout samples stored in a refrigerator at 4°C. In this case the curves rise more slowly, and the microbial count reaches the threshold value after about 66 hours. In both cases the response of the gas sensor at various temperatures follows the curve of the TVC quite closely. This good correlation, already demonstrated elsewhere [218], shows that the response of the resistive sensor can be used as an indirect measure of the microbial count and therefore of the state of degradation of the food sample.

Fig. 11.5a shows the sensor response and total viable count measured on pork samples stored at room temperature. Also in this case the curves increase over time, demonstrating the progressive degradation of the meat. The TVC graph increases the slope after about ten hours and reaches the consumability threshold after about 40 hours.

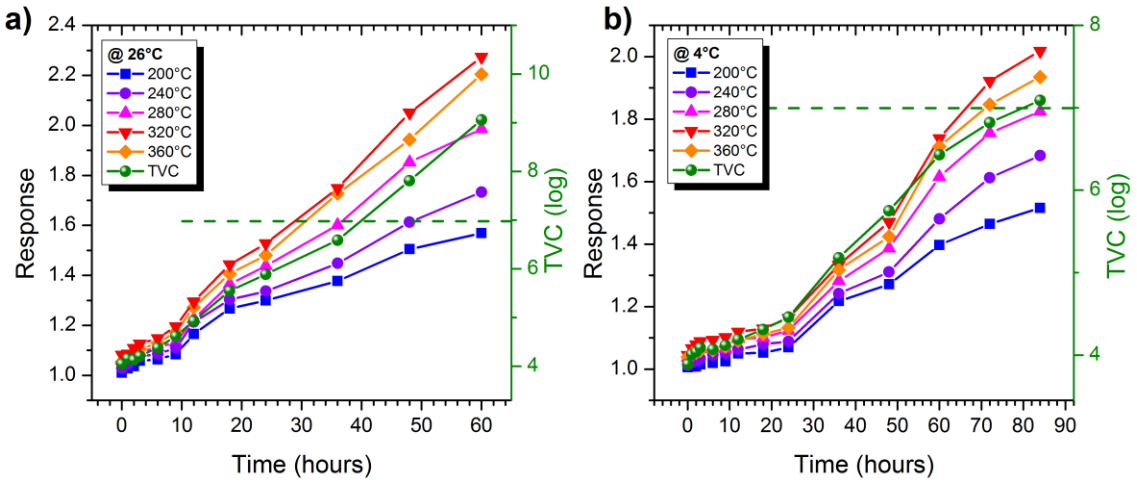

Figure 11.5 – a) Sensor response (colored symbols, left scale) and bacterial population (green spheres, right scale) in pork samples stored at room temperature over a period of 60 hours; b) Sensor response (colored symbols, left scale) and bacterial population (green spheres, right scale) in fresh marble trout stored at in a refrigerator over a period of 84 hours.

Fig. 11.5b shows the resistive sensor response and TVC of pork samples stored in a refrigerator at 4° C. The slope of the curves is low up to about 24 hours and then increases, and the microbial count reaches the threshold after about 80 hours.

11.4.4 Distinction between meat and fish

In the previous section we saw that the response of the resistive gas sensor, at any working temperature, could be used as an indirect measure of the total viable count, both on marble trout and pork samples. Unfortunately, the sensor response lends itself to calibration for only one sample type and could not be used to distinguish different food samples. For this reason, the responses at five different temperatures were combined and processed through multivariate statistical analysis. Initially, we used principal component analysis to visualize the relationship between meat and fish points over time. The aim was to see if the two foods had two different trends, and also to see if the samples stored at different temperatures differed in any way. The top samples are those measured initially (at the beginning of the plots in Figs. 11.4 and 11.5) and then the points drop down as time passes.

The position of the points is given by the PCA of the 5D points obtained by combining the responses collected at various temperatures, while their color reflects the TVC measurement. Moving down the principal component 1 (vertically) the points become darker, indicating a higher TVC (legend on the right in the figure) and therefore greater degradation as time passes, as expected. The two groups of points, relating to fish and meat, are easily distinguishable, and rather separate from each other. This is a good indication that they are classifiable. Unfortunately, however, it is not possible to distinguish between samples stored in the refrigerator and those stored at room temperature.

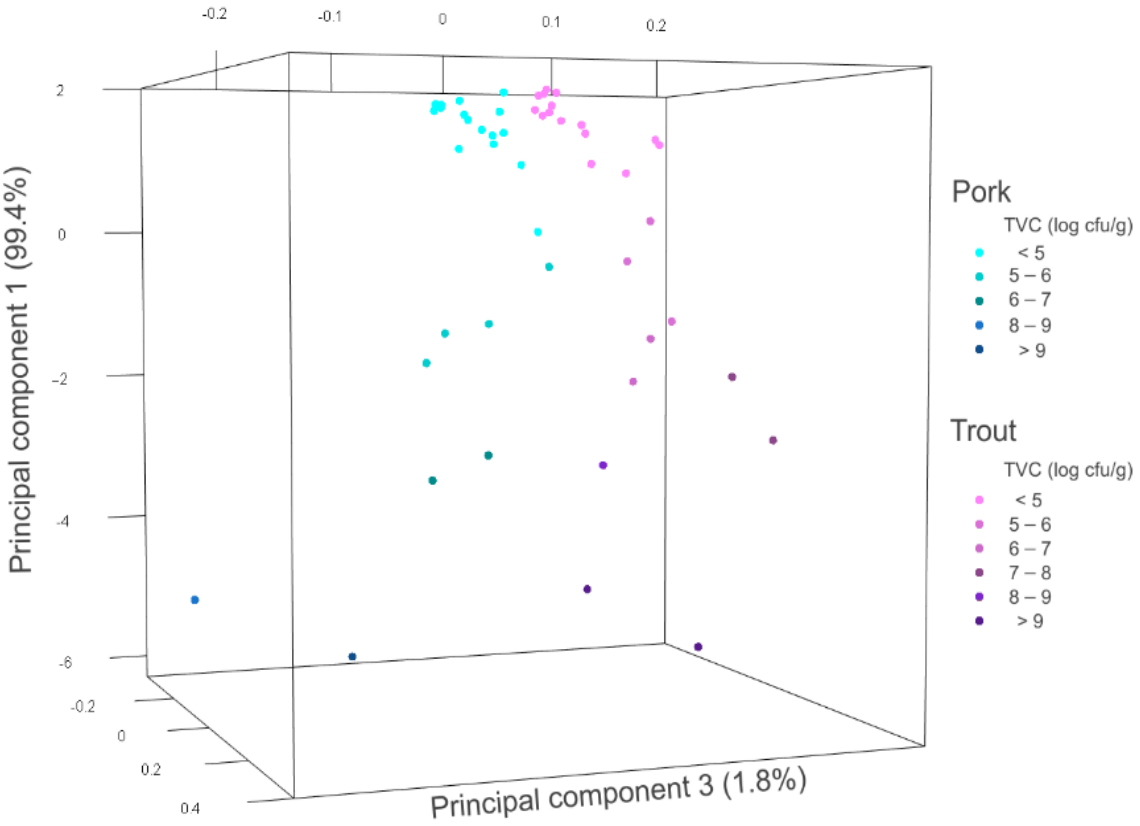

Figure 11.6 – Principal component analysis of meat and fish samples over time. Shades of blue (cyan to navy) indicate points for pork samples, while shades of purple (pink to violet) indicate points for marble trout samples.

Based on these results, a support vector machine was then used to classify the fish and meat samples. This algorithm uses a first data set to map the five-dimensional space according to the classes, and then compares the new data with the map to classify them. The results of this classification are shown in the confusion matrix in Table 11.1.

Table 11.1 – Confusion matrix of the classification between meat and fish using the single nanowire gas sensor.

	True		
Estimated	Sample	Pork	Trout
	Pork	**20**	1
	Trout	1	**20**

For both meat and fish, the sensor correctly classified 20 out of 21 samples tested for 95.2% accuracy. The two misclassified points are both related to degraded food samples, with TVC greater than or close to 8.

11.4.5 Estimation of the degree of freshness of food

Once the sensor distinguished the samples by type (marble trout or pork), the points relating to the two foods were processed with two other classifiers based on support vector machines, one for fish and one for meat. In this case, instead of using the "food type" label of the training dataset points (as the classifier used previously), the "degree of freshness" label was used, which was assigned according to the TVC value. The classification results for the pork samples are shown in the confusion matrix in Table 11.2.

Table 11.2 – Confusion matrix of classification regarding the state of freshness of pork samples. The background color gives an idea of the seriousness of a possible misclassification.

Pork		Estimated TVC (log cfu/g)					
		< 5	5 – 6	6 – 7	7 – 8	8 – 9	> 9
True TVC (log cfu/g)	< 5	**9**					
	5 – 6		**4**				
	6 – 7			**2**			
	7 – 8				**2**		
	8 – 9		1			**2**	
	> 9						**1**

The sensor classified the degree of freshness of pork samples very well, with an accuracy of 95.2%. Only one sample was classified in the wrong degree of freshness, and that was what was

called pork, while in reality it was a sample of marble trout. Unfortunately, as can be seen from the background color of the misclassified sample cell, the error is significant as the sample is considered fresh, while in reality it is rather degraded. Evidently the misclassification in the previous step has strong repercussions on the results of this classification.

The estimate of the degree of freshness of the marble trout samples is shown in Table 11.3.

Table 11.3 – Confusion matrix of classification regarding the state of freshness of marble trout samples. The background color gives an idea of the seriousness of a possible misclassification.

Marble trout		Estimated TVC (log cfu/g)					
		< 5	5 – 6	6 – 7	7 – 8	8 – 9	> 9
True TVC (log cfu/g)	< 5	**9**					
	5 – 6		**3**				
	6 – 7			**2**			
	7 – 8			1	**2**	1	
	8 – 9						1
	> 9						**2**

It is immediately evident that the classification in this case is worse, as three samples are incorrectly classified, for an accuracy of 85.7%. One of the three misclassified samples is the one that was incorrectly classified in the previous step, and is therefore, in reality, a pork sample. While three misclassified samples may seem like a lot, we have to consider different degrees of severity of the misclassifications. In fact, the only major error is that which estimates a degraded sample as fresh. In the other two cases, however, degraded samples were evaluated as even more degraded, and therefore were minimal errors. The severity is highlighted in the table by the background color: a green background means that fresh samples are still considered fresh and degraded samples are considered degraded, even if with different freshness classes (misclassification without consequences). A yellow background means that a fresh sample is considered degraded and would

therefore lead to food waste. Finally, a red background means that a degraded sample is considered fresh, which could lead to food poisoning. Given these considerations, we can say that the sensor makes one important error on the 21 samples of pork and one major error on the 21 samples of marble trout. In both cases, therefore, the system estimates the freshness of the food with an accuracy of 95.2%. If, on the other hand, we consider all types of errors, including those without repercussions, then the system estimates the freshness of pork and marble trout with an accuracy of 95.2 and 85.7%, respectively. It should be emphasized that these results were obtained from a single trout and a single piece of pork. We expect that testing samples from more than one animal of each type, the uncertainty of the measurement may increase. On the other hand, the greater number of samples would help train the support vector machine better, and this should improve performance. The balance between these two effects will be evaluated in future work. In any case, considering the small size and low cost of the device, this performance indicates that the single nanowire gas sensor may be a candidate as a fast and non-invasive method of estimating the freshness of meat and fish.

11.5 Conclusions

A single SnO_2 nanowire, used as a resistive sensor, allows to evaluate the freshness of different foods. By combining the sensor responses at five different temperatures and processing them with multivariate statistical analysis (PCA) and machine learning (SVM) techniques, the sensor is able to distinguish between marble trout and pork samples, and to estimate their state of freshness. The sensor recognized the type of sample (meat or fish) in 95.2% of cases. Furthermore, it recognized the degradation status in 90.5% of cases (85.7% of cases for trout and 95.2% of cases for pork). Considering that in a couple of cases the misclassification had no repercussions as it considered the degraded samples even more degraded, the sensor overall recognized whether the sample was edible in 95.2% of cases. Considering the size (less than a square millimeter), the low

cost, the speed and the non-invasiveness, the gas sensor has proved to be ideal as a monitoring tool along the meat and fish production and distribution chain.

CHAPTER 12. DISCUSSION

The activities planned in the three phases of the doctoral project were all successful.

The hydrothermal growth of different morphologies of metal oxides has led to the selection of some nanostructures that are particularly interesting from a sensor point of view.

In Chapter 3 an n-type semiconductor such as ZnO, grown in the form of porous coral-like nanosheets and nanoplates demonstrated good performance in detecting NO_2, a dangerous gas as well as a radical responsible for the oxidative damage of proteins. The ultrathin nanoplates demonstrated a very intense response, with a detection limit of a few ppt and excellent selectivity. Response times of a few tens of seconds, good short- and long-term stability (3 months) in air and little dependence on air humidity are other advantages that make this sensor suitable for our purposes.

In Chapter 4 a p-type semiconductor oxide such as V_2O_5 demonstrated good performance as a sensor of ammonia, another hazardous gas that is also an indicator of bacterial breakdown of protein-rich foods such as poultry, fish, and meat. V_2O_5, grown by means of surfactant in the form of 2D nanosheets, demonstrated good crystallinity and a good surface/volume ratio. The sensor response, selective for ammonia over ethylene and other possible interferents, is rapid and stable even after four months. The detection limit of ammonia is about 0.4 ppmv, sufficient for agri-food applications. Considering that the performance of p-type semiconductors is usually lower, the material proves to be suitable for our purposes.

The analysis of the state of the art regarding electronic noses based on metal oxide nanowires in Chapter 5 served to understand the scientific and technological context and to identify the strengths and unsolved problems in the development of these devices. Nanowires (1D nanostructures) are among the most widely used materials, and their study has increased exponentially in recent decades like that of gas sensors and electronic noses. Unfortunately, despite

several studies on how the material, morphology and structure of the nanostructures affect the performance of the sensors, the literature reports very conflicting results regarding the intrinsic selectivity of individual gas sensors. This means that the elements of an array cannot be chosen a priori, but an electronic nose must be tested and possibly optimized following experimental feedback. The analysis of the published articles also reveals that the multidisciplinarity necessary to create this type of instrument is still developing, since the requirements of a sensor expert are not those of a computer scientist, and the dialogue is still ongoing. Despite the presence of many algorithms that can be used as the "brains" of electronic noses, only now are the first quantitative results beginning to be seen after many proof-of-concepts. As with single chemoresistive sensors, the most widely used materials are n-type semiconductors, such as ZnO and SnO_2, and only recently is surface functionalization used to modify the properties of individual devices in the array. The study confirms the wide range of possible applications of such a transversal tool, from security to health and the agri-food field.

Chapter 6 compares the performance of two thermal electronic noses based on the most used metal oxides (because they perform better as gas sensors), namely ZnO and SnO_2. The two devices, identical in terms of architecture, dimensions and morphology of the nanomaterials, have similar performances on the gases tested, proving to be able to classify gases with an accuracy of at least 95% and an error of less than 10 ppmv. However, tin oxide is slightly better as it classifies perfectly (100%) and with a better concentration error (7.5 instead of 10ppmv). This case study demonstrates how sensor materials should be chosen according to the application, i.e. target gases and possible interferents, in order to optimize the performance of the electronic nose.

Chapter 7 reports the first work bridging experiments with gas cylinders in the laboratory and measurements on food and drink. Specifically, the instrument was used to distinguish ethanol and methanol at low concentrations and measure their concentration under different relative humidity conditions. This is useful both for recognizing a possible methanol intoxication from human breath and for recognizing an adulterated alcoholic beverage and thus preventing

intoxication. After the measurements with pure gases, the electronic nose was tested on simulated drinks (spirits at 40% alcohol), in some of which some of the ethanol had been replaced with methanol. Even under these realistic conditions, the tool was able to distinguish safe drinks from adulterated and potentially intoxicating ones.

Testing gas sensors and electronic noses with gas cylinders in the laboratory is very different from measuring the headspace of a product. Although similar, the measurement procedure with food is much more complicated both because the sample is not a gas but a mixture, and because the mixture is not originally gaseous, but is dynamically emitted by a solid or liquid food. Since an electronic nose does not recognize the molecules of the gas or mixture it is measuring, it is necessary to support it with an analytical technique that allows understanding its functioning in more detail. In Chapter 8 a study aimed at distinguishing three differently treated commercial tomato sauces served as a case study in this regard. An electronic nose and proton transfer reaction mass spectrometry simultaneously measured samples of unaltered sauce inoculated with a mushroom and treated with thyme essential oil. While the signals from the 6 gas sensors always have the same trend (growth and beginning of saturation), the different masses detected by the PTR-MS are divided into classes with different behaviours, indicating a dynamic evolution of the headspace. By studying the discriminating ability of the sensors over time, it can be seen that it has a maximum after about 10 seconds, and a trend similar to that of some classes of molecules detected with PTR-MS. Principal component analysis (PCA) shows that the PTR-MS is able to distinguish the three tomato sauces well both after 10 seconds and after 60 seconds, while the electronic nose succeeds initially, but loses this ability after 60 seconds, despite the strongest signal. This is explained by the fact that, despite the evolution of the headspace, they contain abundant water vapor which does not help to discriminate between the three different sauces. In summary, a large part of the sensor signal that continues to increase is due to water, which is noise instead of information. On the contrary, as can be seen from the PTR-MS graphs, the molecules carrying information and managing to separate the three classes have a peak after 10 seconds, due to the evolution of the

headspace. This work has shed light on the procedural aspects of measurements with electronic noses on food samples, in order to improve their performance.

The first measurements of real food samples are described in Chapter 9, where a single nanowire SnO_2 sensor is used to quickly and non-invasively assess the freshness of mackerel samples. Initially, the performance of the sensor in detecting ammonia even at low concentrations was evaluated, as it is produced in the decomposition of urea and amino acids by bacteria. The sensor responds sharply and quickly (less than half a minute) at all temperatures and displays a limit of detection of less than 0.2 ppmv. The measurements of mackerel samples were carried out over time on samples stored at room temperature (25°C) and in the fridge (4°C). Microbial counts were used as the reference standard technique, and gas sensor measurements showed good correlation with total viable count measurements. The gas sensor therefore proves to be able to evaluate the freshness of the fish in a rapid and non-invasive way, closely approximating the TVC value of the mackerel.

Chapter 10 takes it a step further by measuring the freshness of trout samples using a single nanowire sensor, but using it as a serial thermal electronic nose, rather than a simple gas sensor. Again the sensor consisted of a single nanowire of tin oxide, and was initially tested for the detection of ammonia, as this is the major component, together with dimethylamine and trimethylamine, of total volatile basic nitrogen (TVB-N), a common marker for measuring fish degradation. The measurements made at different temperatures with the sensor followed well the trend over time of the microbial count measurements on samples both stored at 25°C and at 4°C in the fridge. The electronic nose gave very good results, managing to estimate the total viable count with an error of less than 5% and correctly distinguishing all edible from non-edible samples.

The last step towards the full potential of the miniaturized electronic nose based on metal oxide nanowires is illustrated in Chapter 11, where a single nanowire sensor is used in a broader way, i.e. to distinguish the sample between meat and fish, and evaluate the freshness. This is an important step because, unlike a gas sensor, the electronic nose can distinguish multiple food

products, and then evaluate the freshness of each sample depending on how it has been classified. In this case, measurements at five different temperatures were used, and a first classifier distinguished pork samples from trout samples with greater than 95% accuracy. This classification was then used to send the sample to two other classifiers, one for pork samples and one for trout samples, which assessed the TVC of the sample and rated its freshness. Again the accuracy exceeded 95%, demonstrating that the electronic nose was able to distinguish foods and estimate their freshness successfully.

CHAPTER 13. CONCLUSION

The doctoral program proceeded quite regularly despite the sometimes difficult surrounding conditions (see Covid19). All the stages were addressed as initially planned and successfully completed, providing a large amount of scientific results on gas sensors, miniaturized electronic noses and their use in the agri-food sector.

Chemoresistive sensors based on metal oxide nanostructures, both n-type and p-type, have demonstrated good performance in detecting gases and VOCs useful in the agri-food field. Perhaps the most important parameter is the detection limit, since the sensitivity of analytical techniques such as mass spectrometry is orders of magnitude higher. Optimization of the growth processes to obtain ultra-thin nanostructures and functionalization with nanoparticles or with organic molecules help to decrease the limit of detection to a sufficient level. Furthermore, the fact that chemoresistive sensors simultaneously detect all the gases and VOCs emitted by an agri-food sample is an advantage here since the different contributions are integrated into a more intense signal and making the detection limit less critical.

The use of these sensors in a thermal gradient has demonstrated potential for the fabrication of miniaturized electronic noses capable of distinguishing different target gases from possible interferents and estimating their concentrations with minimal error. The use of different metal oxides and different morphologies has allowed to tune the selectivity of the electronic noses towards the desired target gases and the study of the different usable algorithms has allowed to choose the most suitable ones for the application.

Simultaneous use with the PTR-MS has allowed a deeper understanding of the measurement process of gas sensors in measuring the headspace of agro-food products and optimized the performance to extract the maximum information in the signal versus the noise.

When used with simulated food samples or real thermal electronic noses they have demonstrated good performance, being able to detect the presence of methanol in adulterated spirits, distinguish between meat and fish and estimate their freshness (in terms of microbial count) with minimal error, both that the samples were kept at room temperature or in the fridge. These performances, combined with the low cost, speed and non-invasiveness, make thermal electronic noses based on semiconductor metal oxide nanostructures an ideal tool for evaluating the freshness and quality of agri-food products.

PUBLICATIONS

During the PhD the following scientific articles have been published:

Main articles

These articles constitute the main stages of the doctorate course and illustrate the path covered, from the work on nanostructured sensors to electronic noses up to applications on agri-food products.

1. L. Van Duy, T.T. Nguyet, C.M. Hung, D.T.T. Le, N. Van Duy*, N. Duc Hoa*, F. Biasioli, M. Tonezzer , C. Di Natale, Ultrasensitive NO_2 gas sensing performance of two dimensional ZnO nanomaterials: Nanosheets and nanoplates, Ceramics International, 47 (2021) 28811–28820. Doi: 10.1016/j.ceramint.2021.07.042

2. L. Van Duy, T.T. Nguyet, D.T.T. Le*, N.V. Duy, H. Nguyen, F. Biasioli, M. Tonezzer, C. Di Natale* , N.D. Hoa*, Room Temperature Ammonia Gas Sensor Based on p-Type-like V_2O_5 Nanosheets towards Food Spoilage Monitoring, Nanomaterials, 13 (2023) 146 Doi: 10.3390/nano13010146

3. M. Tonezzer*, D. Thi Thanh Le, L. Van Duy, N. Duc Hoa, F. Gasperi, N. Van Duy*, F. Biasioli, Electronic noses based on metal oxide nanowires: A review, Nanotechnology Reviews, 11 (2022) 897–925. Doi: 10.1515/ntrev-2022-0056

4. M. Tonezzer*, C. Armellini, L. Toniutti, Sensing performance of thermal electronic noses: A comparison between ZnO and SnO_2 nanowires, Nanomaterials, 11 (2021) 2773. Doi: 10.3390/nano11112773

5. M. Tonezzer*, N. Bazzanella, F. Gasperi, F. Biasioli, Nanosensor Based on Thermal Gradient and Machine Learning for the Detection of Methanol Adulteration in Alcoholic Beverages and Methanol Poisoning, Sensors, 22 (2022) 5554. Doi: 10.3390/s22155554

6. L. Quercia, I. Khomenko, R. Capuano, M. Tonezzer, R. Paolesse, E. Martinelli, A. Catini, F. Biasioli, C. Di Natale*, Optimization of gas sensors measurements by dynamic headspace

analysis supported by simultaneous direct injection mass spectrometry, Sensors and Actuators B: Chemical, 347 (2021) 130580. Doi: 10.1016/j.snb.2021.130580

7. M. Tonezzer*, Detection of mackerel fish spoilage with a gas sensor based on one single SnO2 nanowire, Chemosensors, 9 (2021) 1–10. Doi: 10.3390/chemosensors9010002

8. M. Tonezzer*, N.X. Thai, F. Gasperi, N. Van Duy*, F. Biasioli, Quantitative assessment of trout fish spoilage with a single nanowire gas sensor in a thermal gradient, Nanomaterials, 11 (2021) 1604. Doi: 10.3390/nano11061604

9. M. Tonezzer*, Single nanowire gas sensor able to distinguish fish and meat and evaluate their degree of freshness, Chemosensors, 9 (2021) 249. Doi: 10.3390/chemosensors9090249

Secondary articles

These papers are part of the doctorate and have been published with UniTN and AES affiliation, but being less relevant to the track, they have not been described in the thesis.

1. N.X. Thai, M. Tonezzer*, L. Masera, H. Nguyen, N.V. Duy*, N.D. Hoa, Multi gas sensors using one nanomaterial, temperature gradient, and machine learning algorithms for discrimination of gases and their concentration, Analytica Chimica Acta 1124 (2020) 85-93. Doi: 10.1016/j.aca.2020.05.015

2. N.X. Thai, N. Van Duy*, C.M. Hung*, H. Nguyen, M. Tonezzer, N. Van Hieu, N. Duc Hoa, Prototype edge-grown nanowire sensor array for the real-time monitoring and classification of multiple gases, Journal of Science: Advanced Materials and Devices 5 (2020) 409-416. Doi: 10.1016/j.jsamd.2020.05.005

3. V.Q. Khue, T.Q. Huy*, V.N. Phan, A. Tuan-Le, D.T.T. Le, M. Tonezzer, N.T.H. Hanh, electrochemical stability of screen-printed electrodes modified with Au nanoparticles for detection of methicillin-resistant *Staphylococcus aureus*, Materials Chemistry and Physics 255 (2020) 123562. Doi: 10.1016/j.matchemphys.2020.123562

4. Q.K. Vu, Q.H. Tran*, N.P. Vu, T-L. Anh, T.T.L. Dang, M. Tonezzer, T.H.H. Nguyen, A label-free electrochemical biosensor based on screen-printed electrodes modified with gold

nanoparticles for quick detection of bacterial pathogens, Materials Today Communications 26 (2021) 101726. Doi: 10.1016/j.mtcomm.2020.101726

5. J-Y. Kim, S.S. Kim*, M. Tonezzer*, Selective gas detection and quantification using a resistive sensor based on Pd-decorated soda-lime glass, Sensors and Actuators, B: Chemical, 335 (2021) 129714. Doi: 10.1016/j.snb.2021.129714

6. Q.K. Vu, T.H. Nguyen, A‑T. Le, N.P. Vu, X.D. Ngo, T.K. Nguyen, T.T. Nguyen, C.V. Pham, T.L. Nguyen, T.L.T. Dang, M. Tonezzer, Q.H. Tran*, Enhancing Electron Transfer and Stability of Screen-Printed Carbon Electrodes Modified with AgNP-Reduced Graphene Oxide Nanocomposite, Journal of Electronic Materials 51 (2022) 1004-1012. Doi: 10.1007/s11664-021-09402-9

7. R. Guarino*, F. Mo*, Y. Ardesi, A. Gaiardo*, M. Tonezzer*, S. Guarino, G. Piccinini, Modelling electronic transport in monocrystalline metal oxide gas sensors: from the surface kinetics to the experimental response, Sensors and Actuators B: Chemical, 373 (2022) 132646. Doi: 10.1016/j.snb.2022.132646

8. N. Van Duy*, D.T.T. Trang, D.T.T. Le, C.M. Hung, M. Tonezzer, H. Nguyen, N.D. Hoa, Enhancement of NH_3 gas sensing with Ag-Pt co-catalyst on SnO_2 nanofilm towards medical diagnosis, Thin Solid Films, 767 (2023) 139682. Doi: 10.1016/j.tsf.2023.139682

9. M. Tonezzer*, L. Masera, N.X. Thai, H. Nguyen, N.V. Duy*, N.D. Hoa, Miniaturized multisensor system with a thermal gradient: Performance beyond the calibration range, Journal of Science: Advanced Materials and Devices, 8 (2023) 100562. Doi: 10.1016/j.jsamd.2023.100562

10. D.T.T. Le*, D.T.N. Tram, D.V. Minh, M. Tonezzer, T.V.D. Ngoc, C.T. Xuan, C.M. Hung, N.V. Duy, N.D. Hoa*, Eco-friendly facile synthesis of Co_3O_4-Pt nanorods for ethylene detection towards fruit quality monitoring, Sensors and Actuators A: Physical 362 (2023) 114607. Doi: 10.1016/j.sna.2023.114607

Other articles

Although these articles were published during the PhD, they are not part of it.

1. T.Q. Huy*, P.T.M. Huyen, A-T. Le, M. Tonezzer*, Recent advances of silver nanoparticles in cancer diagnosis and treatment, Anti-Cancer Agents in Medicinal Chemistry 20 (2020) 1276-1287. Doi: 10.2174/1871520619666190710121727

2. M. Tonezzer*, L. Van Duy*, Gas Sensors, Encyclopedia of Sensors and Biosensors: Volume 1-4, First Edition 1-4 (2022) 185-208. 10.1016/B978-0-12-822548-6.00113-8

3. N. Van Duy*, N.X. Thai, T.M. Ngoc, D.T.T. Le, C.M. Hung, H. Nguyen, M. Tonezzer, N. Van Hieu, N.D. Hoa*, Design and fabrication of effective gradient temperature sensor array based on bilayer SnO_2/Pt for gas classification, Sensors and Actuators B: Chemical 351 (2022) 130979. Doi: 10.1016/j.snb.2021.130979

4. A. Tahira, Z.H. Ibupoto*, M. Montecchi, L. Pasquali, M. Tonezzer, A. Nafady, H.F. Khalil, R. Mazzaro, V. Morandi, M. Vagin, A. Vomiero, Role of cobalt precursors in the synthesis of Co_3O_4 hierarchical nanostructures toward the development of cobalt-based functional electrocatalysts for bifunctional water splitting in alkaline and acidic media, Journal of the Chinese Chemical Society 69 (2022) 681-691. Doi: 10.1002/jccs.202200012

5. M.D. Albaqami, A.A. Alothman, A. Nafady, S. Medany, A.A. Shah, U. Aftab, M.H. Ibupoto, A.B. Mallah, A. Tahira, M. Tonezzer*, B. Vigolo, Z.H. Ibupoto*, Utilization of polyvinyl amine hydrolysis product in enhancing the catalytic properties of Co_3O_4 nanowires: toward potentiometric glucose bio-sensing application, Journal of Materials Science: Materials in Electronics 33 (2022) 11555-11568. Doi: 10.1007/s10854-022-08128-6

6. A.G. Solangi, T. Pirzada, A.A. Shah, I.A. Halepoto, A.S. Chang, Z.A. Solangi, M.Y. Solangi, U. Aftab, M. Tonezzer, A. Tahira, A. Nafady, S.S. Medany, Z.H. Ibupoto, Phytochemicals of mustard (*Brassica Campestris*) leaves tuned the nickel-cobalt bimetallic oxide properties for enzyme-free sensing of glucose, Journal of the Chinese Chemical Society 69 (2022) 1608-1618. Doi: 10.1002/jccs.202200270

7. M.A. Bhatti, A. Tahira, A.A. Shah, U. Aftab, B. Vigolo, A.R. Khattab, A. Nafady, I.A. Halepoto, M. Tonezzer, Z.H. Ibupoto*, Facile synthesis of a luminescent carbon material from

yogurt for the efficient photocatalytic degradation of methylene blue, RSC Advances 12 (2022) 25549-25564. Doi: 10.1039/D2RA04749G

8. A. Romano, L. Cappellin, I. Cuccui, S. Bogialli, I. Khomenko, M. Tonezzer, F. Biasioli, P. Pastore, O. Allegretti*, Exploring volatile organic compound emission from thermally modified wood by PTR-ToF-MS, Analyst 147 (2022) 5138-5148. Doi: 10.1039/D2AN01376B

9. B. Shaikh, M.A. Bhatti, A.A. Shah, A. Tahira, A.K. Shah, A. Usto, U. Aftab, S.I. Bukhari, S. Alshehri, S.N.U.S. Bukhari, M. Tonezzer, B. Vigolo, Z.H. Ibhupoto*, Mn_3O_4@ZnO Hybrid Material: An Excellent Photocatalyst for the Degradation of Synthetic Dyes including Methylene Blue, Methyl Orange and Malachite Green, Nanomaterials 12 (2022) 3754. Doi: 10.3390/nano12213754

10. M.Y. Solangi, U. Aftab, A. Tahira, A. Hanan, M. Montecchi, L. Pasquali, M. Tonezzer, R. Mazzaro, V. Morandi, A.J Laghari, A. Nafady, M. I. Abro, M. Emo, B. Vigolo, E. Dawi, E. Mustafa, Z.H. Ibupoto*, In-situ growth of nonstoichiometric $CrO_{0.87}$ and Co_3O_4 hybrid system for the enhanced electrocatalytic water splitting in alkaline media, published online on International Journal of Hydrogen Energy.

REFERENCES

[1] F.J. Pérez Elortondo, M. Ojeda, M. Albisu, J. Salmerón, I. Etayo, M. Molina, Food quality certification: An approach for the development of accredited sensory evaluation methods, Food Qual. Prefer. 18 (2007) 425-439. Doi: 10.1016/j.foodqual.2006.05.002

[2] E. Ibanez and A. Cifuentes, New analytical techniques in food science, Crit. Rev. Food Sci. Nutr. 41 (2001) 413–450. Doi: 10.1080/20014091091878

[3] N. Funazaki, A. Hemmi, S. Ito, Y. Asano, Y. Yano, N. Miura, N. Yamazoe, Application of semiconductor gas sensor to quality control of meat freshness in food industry, Sens. Actuators B Chem. 25 (1995) 797-800. Doi: 10.1016/0925-4005(95)85177-1

[4] A.T. John, K. Murugappan, D.R. Nisbet and A. Tricoli, An Outlook of Recent Advances in Chemiresistive Sensor-Based Electronic Nose Systems for Food Quality and Environmental Monitoring, Sensors 21 (2021) 2271. Doi: 10.3390/s21072271

[5] A. Loutfi, S. Coradeschi, G.K. Mani, P. Shankar, J.B.B. Rayappan, Electronic noses for food quality: A review, J. Food Eng. 144 (2015) 103-111. Doi: 10.1016/j.jfoodeng.2014.07.019

[6] L. Van Duy, T.T. Nguyet, C.M. Hung, D.T.T. Le, N. Van Duy, N. Duc Hoa, F. Biasioli, M. Tonezzer, C. Di Natale, Ultrasensitive NO_2 gas sensing performance of two dimensional ZnO nanomaterials: Nanosheets and nanoplates, Ceramics International, 47 (2021) 28811–28820. Doi: 10.1016/j.ceramint.2021.07.042

[7] M. K. Sohal et al., "Ultrasensitive yttrium modified tin oxide thin film based sub-ppbv level NO2 detector," Sensors Actuators B Chem., vol. 329, p. 129169, Feb. 2021.

[8] E.A. Nunes Simonetti, T. Cardoso de Oliveira, ´A. Enrico do Carmo Machado, A. A. Coutinho Silva, A. Silva dos Santos, L. de Simone Cividanes, TiO_2 as a gas sensor: the novel carbon structures and noble metals as new elements for enhancing sensitivity – a Review, Ceram. Int. (2021). Doi: 10.1016/j.ceramint.2021.03.189.

[9] L. Zhang et al., "Hexagonal ZnO nanoplates/graphene composites with excellent sensing performance to NO_2 at room temperature," Appl. Surf. Sci., vol. 537, p. 147785, Jan. 2021.

[10] C. Han et al., "Construction of In_2O_3/ZnO yolk-shell nanofibers for room-temperature NO_2 detection under UV illumination," J. Hazard. Mater., vol. 403, p. 124093, Feb. 2021.

[11] R. R. Kumar et al., "Ultrasensitive and light-activated NO_2 gas sensor based on networked MoS_2/ZnO nanohybrid with adsorption/desorption kinetics study," Appl. Surf. Sci., vol. 536, p. 147933, Jan. 2021.

[12] D. Chavez et al., "High sensitivity of flexible graphene composites decorated with V_2O_5 microbelts for NO_2 detection," Mater. Res. Bull., vol. 133, p. 111052, Jan. 2021.

[13] R. R. Kumar, T. Murugesan, T.-W. Chang, and H.-N. Lin, "Defect controlled adsorption/desorption kinetics of ZnO nanorods for UV-activated NO_2 gas sensing at room temperature," Mater. Lett., vol. 287, p. 129257, Mar. 2021.

[14] C. M. Hung, D. T. T. Le, and N. Van Hieu, "On-chip growth of semiconductor metal oxide nanowires for gas sensors: A review," J. Sci. Adv. Mater. Devices, vol. 2, no. 3, pp. 263–285, 2017.

[15] W. Wang et al., "Metal–organic framework-derived Cu_2O–CuO octahedrons for sensitive and selective detection of ppbv-level NO_2 at room temperature," Sensors Actuators B Chem., vol. 328, p. 129045, Feb. 2021.

[16] C. Zhang, Y. Luo, J. Xu, and M. Debliquy, "Room temperature conductive type metal oxide semiconductor gas sensors for NO_2 detection," Sensors Actuators A Phys., vol. 289, pp. 118–133, Apr. 2019.

[17] S. Nundy, T. Eom, K.-Y. Song, J.-S. Park, H.-J. Lee, Hydrothermal synthesis of mesoporous ZnO microspheres as NO_X gas sensor materials — calcination effects on microstructure and sensing performance, Ceram. Int. 46 (2020) 19354–19364. Doi: 10.1016/j.ceramint.2020.04.278.

[18] S.N. Birajdar, P.V. Adhyapak, Palladium-decorated vanadium pentoxide as NOx gas sensor, Ceram. Int. 46 (2020) 27381–27393. Doi: 10.1016/j. ceramint.2020.07.223.

[19] N. Van Hieu, N. Van Duy, P. T. Huy, and N. D. Chien, "Inclusion of SWCNTs in Nb/Pt co-doped TiO_2 thin-film sensor for ethanol vapor detection," Phys. E Low-dimensional Syst. Nanostructures, vol. 40, no. 9, pp. 2950–2958, Aug. 2008.

[20] V. L. Patil, S. A. Vanalakar, P. S. Patil, and J. H. Kim, "Fabrication of nanostructured ZnO thin films based NO_2 gas sensor via SILAR technique," Sensors Actuators B Chem., vol. 239, pp. 1185–1193, Feb. 2017.

[21] Y. Kang, F. Yu, L. Zhang, W. Wang, L. Chen, and Y. Li, "Review of ZnO-based nanomaterials in gas sensors," Solid State Ionics, vol. 360, p. 115544, Feb. 2021.

[22] X. Yue, Z. Li, S. Zhao, A new electrochemical sensor for simultaneous detection of sulfamethoxazole and trimethoprim antibiotics based on graphene and ZnO nanorods modified glassy carbon electrode, Microchem. J. 159 (2020) 105440. Doi: 10.1016/j.microc.2020.105440.
[23] V. Gerbreders, M. Krasovska, I. Mihailova, A. Ogurcovs, E. Sledevskis, A. Gerbreders, E. Tamanis, I. Kokina, I. Plaksenkova, ZnO nanostructure-based electrochemical biosensor for Trichinella DNA detection, Sens. Bio-Sensing Res. 23 (2019) 100276. Doi: 10.1016/j.sbsr.2019.100276.
[24] S. Murali, P.K. Dammala, B. Rani, R. Santhosh, C. Jadhao, N.K. Sahu, Polyol mediated synthesis of anisotropic ZnO nanomaterials and composite with rGO: application towards hybrid supercapacitor, J. Alloys Compd. 844 (2020) 156149. Doi: 10.1016/j.jallcom.2020.156149.
[25] P. Dammala, J. Machado, B. Rani, S. Murali, S. Devi, M. Niraj Luwang, N.K. Sahu, Synthesis of biphasic nanomaterials based on ZnO and SnO_2: application towards photocatalytic degradation of acid red dye, Nano-Structures & Nano-Objects 18 (2019) 100292. Doi: 10.1016/j.nanoso.2019.100292.
[26] Y. Wang, Y. Zhou, H. Ren, Y. Wang, X. Zhu, Y. Guo, X. Li, Room-temperature and humidity-resistant trace nitrogen dioxide sensing of few-layer black phosphorus nanosheet by incorporating zinc oxide nanowire, Anal. Chem. 92 (2020) 11007–11017. Doi: 10.1021/acs.analchem.9b05623.
[27] Y. Zhou, Y. Wang, Y. Wang, X. Li, Y. Guo, The impact of carrier gas on room-temperature trace nitrogen dioxide sensing of ZnO nanowire-integrated film under UV illumination, Ceram. Int. 46 (2020) 16056–16061. Doi: 10.1016/j. ceramint.2020.03.156.
[28] P.P. Ortega, C.C. Silva, M.A. Ramirez, G. Biasotto, C.R. Foschini, A.Z. Sim˜oes, Multifunctional environmental applications of ZnO nanostructures synthesized by the microwave-assisted hydrothermal technique, Appl. Surf. Sci. 542 (2021) 148723. Doi: 10.1016/j.apsusc.2020.148723.
[29] N. Huang, Y. Cheng, H. Li, L. Zhao, Z. He, C. Zhao, F. Liu, L. Ding, Selective-detection NO at room temperature on porous ZnO nanostructure by solid-state synthesis method, J. Colloid Interface Sci. 556 (2019) 640–649. Doi: 10.1016/j.jcis.2019.07.013.
[30] S. ¨Oztürk, N. Kılınç, Z.Z. ¨Oztürk, Fabrication of ZnO nanorods for NO_2 sensor applications: effect of dimensions and electrode position, J. Alloys Compd. 581 (2013) 196–201. Doi: 10.1016/j.jallcom.2013.07.063.
[31] L. Van Duy, N. Van Duy, C.M. Hung, N.D. Hoa, N.Q. Dich, Urea mediated synthesis and acetone-sensing properties of ultrathin porous ZnO nanoplates, Mater, Today Commun 25 (2020) 101445. Doi: 10.1016/j.mtcomm.2020.101445.
[32] L. Van Duy, N.H. Hanh, D.N. Son, P.T. Hung, C.M. Hung, N. Van Duy, N.D. Hoa, N. Van Hieu, Facile hydrothermal synthesis of two-dimensional porous ZnO nanosheets for highly sensitive ethanol sensor, J. Nanomater. 2019 (2019) 1–7. Doi: 10.1155/2019/4867909.
[33] L.V. Thong, L.T.N. Loan, N. Van Hieu, Comparative study of gas sensor performance of SnO_2 nanowires and their hierarchical nanostructures, Sensor. Actuator. B Chem. 150 (2010) 112–119. DOI: 10.1016/j. snb.2010.07.033.
[34] N.T. Thang, L.T. Hong, N.H. Thoan, C.M. Hung, N. Van Duy, N. Van Hieu, N. D. Hoa, Controlled synthesis of ultrathin MoS_2 nanoflowers for highly enhanced NO_2 sensing at room temperature, RSC Adv. 10 (2020) 12759–12771. Doi: 10.1039/D0RA00121J.
[35] L.J. Vasquez-Elizondo, J.C. Rendón-Ángeles, Z. Matamoros-Veloza, J.López-Cuevas, K.Yanagisawa, Urea decomposition enhancing the hydrothermal synthesis of lithium iron phosphate powders: Effect of the lithium precursor, Adv. Powder Tech. 28 (2017) 1593-1602.
[36] D. Wang, N. Dong, Y. Niu, S. Hui, A Review of Urea Pyrolysis to Produce NH_3 Used for NOx Removal, Journal of Chemistry 2019 (2019) 6853638.
[37] S. Agarwal, P. Rai, E.N. Gatell, E. Llobet, F. Güell, M. Kumar, K. Awasthi, Gas sensing properties of ZnO nanostructures (flowers/rods) synthesized by hydrothermal method, Sensor. Actuator. B Chem. 292 (2019) 24–31. Doi: 10.1016/j.snb.2019.04.083.
[38] C.M. Hung, N.D. Hoa, N. Van Duy, N. Van Toan, D.T.T. Le, N. Van Hieu, Synthesis and gas-sensing characteristics of α-Fe_2O_3 hollow balls, J. Sci. Adv. Mater. Devices. 1 (2016) 45–50. Doi: 10.1016/j.jsamd.2016.03.003.
[39] L.V. Thong, L.T.N. Loan, N. Van Hieu, Comparative study of gas sensor performance of SnO_2 nanowires and their hierarchical nanostructures, Sensor. Actuator. B Chem. 150 (2010) 112–119. Doi: 10.1016/j. snb.2010.07.033.
[40] P.-S. Cho, K.-W. Kim, J.-H. Lee, NO_2 sensing characteristics of ZnO nanorods prepared by hydrothermal method, J. Electroceram. 17 (2006) 975–978. Doi: 10.1007/s10832-006-8146-7.
[41] F.-T. Liu, S.-F. Gao, S.-K. Pei, S.-C. Tseng, C.-H.J. Liu, ZnO nanorod gas sensor for NO_2 detection, J. Taiwan Inst. Chem. Eng. 40 (2009) 528–532. Doi: 10.1016/j.jtice.2009.03.008.
[42] J.X. Wang, X.W. Sun, Y. Yang, C.M.L. Wu, N–P transition sensing behaviors of ZnO nanotubes exposed to NO_2 gas, Nanotechnology 20 (2009) 465501, https://doi. org/10.1088/0957-4484/20/46/465501.

[43] R.K. Sonker, S.R. Sabhajeet, S. Singh, B.C. Yadav, Synthesis of ZnO nanopetals and its application as NO_2 gas sensor, Mater. Lett. 152 (2015) 189–191, https://doi. org/10.1016/j.matlet.2015.03.112.
[44] X. Chen, Y. Shen, W. Zhang, J. Zhang, D. Wei, R. Lu, L. Zhu, H. Li, Y. Shen, In-situ growth of ZnO nanowire arrays on the sensing electrode via a facile hydrothermal route for high-performance NO_2 sensor, Appl. Surf. Sci. 435 (2018) 1096–1104. Doi: 10.1016/j.apsusc.2017.11.222.
[45] K. Shingange, H.C. Swart, G.H. Mhlongo, Au functionalized ZnO rose-like hierarchical structures and their enhanced NO_2 sensing performance, Phys. B Condens. Matter 535 (2018) 216–220. Doi: 10.1016/j. physb.2017.07.039.
[46] H. Wang, M. Dai, Y. Li, J. Bai, Y. Liu, Y. Li, C. Wang, F. Liu, G. Lu, The influence of different ZnO nanostructures on NO_2 sensing performance, Sensor. Actuator. B Chem. 329 (2021) 129145. Doi: 10.1016/j.snb.2020.129145.
[47] T.V.A. Kusumam, V.S. Siril, K.N. Madhusoodanan, M. Prashantkumar, Y. T. Ravikiran, N.K. Renuka, NO_2 gas sensing performance of zinc oxide nanostructures synthesized by surfactant assisted Low temperature hydrothermal technique, Sensors Actuators A Phys 318 (2021) 112389. Doi: 10.1016/ j.sna.2020.112389.
[48] C. Zhang, G. Liu, X. Geng, K. Wu, M. Debliquy, Metal oxide semiconductors with highly concentrated oxygen vacancies for gas sensing materials: a review, Sensors Actuators A Phys 309 (2020) 112026. Doi: 10.1016/j. sna.2020.112026.
[49] H.M. Tan, C. Manh Hung, T.M. Ngoc, H. Nguyen, N. Duc Hoa, N. Van Duy, N. Van Hieu, Novel self-heated gas sensors using on-chip networked nanowires with ultralow power consumption, ACS Appl. Mater. Interfaces 9 (2017) 6153–6162. Doi: 10.1021/acsami.6b14516.
[50] L. Van Duy, T.T. Nguyet, D.T.T. Le, N.V. Duy, H. Nguyen, F. Biasioli, M. Tonezzer, C. Di Natale, N.D. Hoa, Room Temperature Ammonia Gas Sensor Based on p-Type-like V_2O_5 Nanosheets towards Food Spoilage Monitoring, Nanomaterials, 13 (2023) 146. Doi: 10.3390/nano13010146
[51] B. Timmer, W. Olthuis, and A. Van Den Berg, "Ammonia sensors and their applications - A review," Sensors Actuators, B Chem., vol. 107, no. 2, pp. 666–677, 2005, doi: 10.1016/j.snb.2004.11.054.
[52] V. Mounasamy, G. K. Mani, K. Tsuchiya, and S. Madanagurusamy, "Preparation of free-standing V_2O_5 nanosheets for ammonia sensing application: A potential candidate for flexible sensors," J. Sci. Adv. Mater. Devices, vol. 7, no. 2, p. 100415, Jun. 2022, doi: 10.1016/j.jsamd.2021.100415.
[53] T. Lindgren, "A case of indoor air pollution of ammonia emitted from concrete in a newly built office in Beijing," Build. Environ., vol. 45, no. 3, pp. 596–600, 2010, doi: 10.1016/j.buildenv.2009.07.014.
[54] M. Mahdinia, S. H. Adeli, A. Mohammadbeigi, H. Heidari, F. Ghamari, and A. Soltanzadeh, "Respiratory Disorders Resulting From Exposure to Low Concentrations of Ammonia: A 5-Year Historical Cohort Study," J. Occup. Environ. Med., vol. 62, no. 8, pp. e431–e435, 2020, doi: 10.1097/JOM.0000000000001932.
[55] W. Chen, M. Metsälä, O. Vaittinen, and L. Halonen, "The origin of mouth-exhaled ammonia," J. Breath Res., vol. 8, no. 3, 2014, doi: 10.1088/1752-7155/8/3/036003.
[56] L. R. Narasimhan, W. Goodman, and C. K. N. Patel, "Correlation of breath ammonia with blood urea nitrogen and creatinine during hemodialysis," Proc. Natl. Acad. Sci. U. S. A., vol. 98, no. 8, pp. 4617–4621, 2001, doi: 10.1073/pnas.071057598.
[57] M. Aydin and C. N. Harvey-Woodworth, "Halitosis: a new definition and classification," Br. Dent. J., vol. 217, no. 1, pp. E1–E1, Jul. 2014, doi: 10.1038/sj.bdj.2014.552.
[58] S. DuBois et al., "Breath ammonia testing for diagnosis of hepatic encephalopathy," Dig. Dis. Sci., vol. 50, no. 10, pp. 1780–1784, 2005, doi: 10.1007/s10620-005-2937-6.
[59] D. J. Kearney, T. Hubbard, and D. Putnam, "Breath ammonia measurement in Helicobacter pylori infection," Dig. Dis. Sci., vol. 47, no. 11, pp. 2523–2530, 2002, doi: 10.1023/A:1020568227868.
[60] N. T. Brannelly, J. P. Hamilton-Shield, and A. J. Killard, "The Measurement of Ammonia in Human Breath and its Potential in Clinical Diagnostics," Crit. Rev. Anal. Chem., vol. 46, no. 6, pp. 490–501, 2016, doi: 10.1080/10408347.2016.1153949.
[61] K.-H. Kim, R. Pal, J.-W. Ahn, and Y.-H. Kim, "Food decay and offensive odorants: A comparative analysis among three types of food," Waste Manag., vol. 29, no. 4, pp. 1265–1273, Apr. 2009, doi: 10.1016/j.wasman.2008.08.029.
[62] Z. Ma et al., "Highly Sensitive, Printable Nanostructured Conductive Polymer Wireless Sensor for Food Spoilage Detection," Nano Lett., vol. 18, no. 7, pp. 4570–4575, Jul. 2018, doi: 10.1021/acs.nanolett.8b01825.
[63] Z. Yuan et al., "Trace-Level, Multi-Gas Detection for Food Quality Assessment Based on Decorated Silicon Transistor Arrays," Adv. Mater., vol. 32, no. 21, p. 1908385, May 2020, doi: 10.1002/adma.201908385.
[64] C. Wang, Z. Yu, X. Zhao, H. Lu, and Q. Wang, "Rapid response to amine vapor based on fluorescent light-up sensor for real-time and visual detection of crawfish and fish freshness," Dye. Pigment., vol. 189, p. 109228, May 2021, doi: 10.1016/j.dyepig.2021.109228.

[65] N. M. Shaalan, F. Ahmed, O. Saber, and S. Kumar, "Gases in Food Production and Monitoring: Recent Advances in Target Chemiresistive Gas Sensors," Chemosensors, vol. 10, no. 8, p. 338, Aug. 2022, doi: 10.3390/chemosensors10080338.
[66] C.-T. Lee and Y.-S. Wang, "High-performance room temperature NH_3 gas sensors based on polyaniline-reduced graphene oxide nanocomposite sensitive membrane," J. Alloys Compd., vol. 789, pp. 693–696, Jun. 2019, doi: 10.1016/j.jallcom.2019.03.124.
[67] P. F. M. Pereira, P. H. de Sousa Picciani, V. Calado, and R. V. Tonon, "Electrical gas sensors for meat freshness assessment and quality monitoring: A review," Trends Food Sci. Technol., vol. 118, no. November 2020, pp. 36–44, 2021, doi: 10.1016/j.tifs.2021.08.036.
[68] A. T. John, K. Murugappan, D. R. Nisbet, and A. Tricoli, "An outlook of recent advances in chemiresistive sensor-based electronic nose systems for food quality and environmental monitoring," Sensors, vol. 21, no. 7, 2021, doi: 10.3390/s21072271.
[69] V. Galstyan, M. Bhandari, V. Sberveglieri, G. Sberveglieri, and E. Comini, "Metal Oxide Nanostructures in Food Applications: Quality Control and Packaging," Chemosensors, vol. 6, no. 2, p. 16, Apr. 2018, doi: 10.3390/chemosensors6020016.
[70] F. Meng et al., "MoS_2 -Templated Porous Hollow MoO_3 Microspheres for Highly Selective Ammonia Sensing via a Lewis Acid-Base Interaction," IEEE Trans. Ind. Electron., vol. 69, no. 1, pp. 960–970, Jan. 2022, doi: 10.1109/TIE.2021.3053902.
[71] P. S. Chauhan, A. Mishra, G. Bhatt, and S. Bhattacharya, "Enhanced He gas detection by V_2O_5-noble metal (Au, Ag, and Pd) nanocomposite with temperature dependent n- to p-type transition," Mater. Sci. Semicond. Process., vol. 123, p. 105528, Mar. 2021, doi: 10.1016/j.mssp.2020.105528.
[72] N. Singh, A. Umar, N. Singh, H. Fouad, O. Y. Alothman, and F. Z. Haque, "Highly sensitive optical ammonia gas sensor based on Sn Doped V_2O_5 Nanoparticles," Mater. Res. Bull., vol. 108, pp. 266–274, Dec. 2018, doi: 10.1016/j.materresbull.2018.09.008.
[73] X. Xing, X. Xiao, L. Wang, and Y. Wang, "Highly sensitive formaldehyde gas sensor based on hierarchically porous Ag-loaded ZnO heterojunction nanocomposites," Sensors Actuators B Chem., vol. 247, pp. 797–806, Aug. 2017, doi: 10.1016/j.snb.2017.03.077.
[74] V. Mounasamy, G. K. Mani, K. Tsuchiya, and S. Madanagurusamy, "Nanoimprint assisted free standing porous vanadium oxide nanosheet based ammonia sensor," Appl. Surf. Sci., vol. 541, p. 148271, Mar. 2021, doi: 10.1016/j.apsusc.2020.148271.
[75] M. Berouaken et al., "Room temperature ammonia gas sensor based on V_2O_5 nanoplatelets/Quartz crystal microbalance," Appl. Phys. A, vol. 126, no. 12, p. 949, Dec. 2020, doi: 10.1007/s00339-020-04129-6.
[76] H. Choi, Y. J. Kwon, J. Paik, J.-B. Seol, and Y. K. Jeong, "P-Type Conductivity of Hydrated Amorphous V_2O_5 and Its Enhanced Photocatalytic Performance in ZnO/ V_2O_5 /rGO," ACS Appl. Electron. Mater., vol. 1, no. 9, pp. 1881–1889, 2019, doi: 10.1021/acsaelm.9b00397.
[77] A. D'Amico and C. Di Natale, "A contribution on some basic definitions of sensors properties," IEEE Sens. J., vol. 1, no. 3, pp. 183–190, 2001, doi: 10.1109/JSEN.2001.954831.
[78] M. Benkahoul, M. K. Zayed, A. Solieman, and S. N. Alamri, "Spray deposition of V_4O_9 and V_2O_5 thin films and post-annealing formation of thermochromic VO_2," J. Alloys Compd., vol. 704, pp. 760–768, May 2017, doi: 10.1016/j.jallcom.2017.02.088.
[79] R. T. Rasheed et al., "Synthesis, characterization of V_2O_5 nanoparticles and determination of catalase mimetic activity by new colorimetric method," J. Therm. Anal. Calorim., vol. 145, no. 2, pp. 297–307, Jul. 2021, doi: 10.1007/s10973-020-09725-5.
[80] D. Meng et al., "In-situ growth of V_2O_5 flower-like structures on ceramic tubes and their trimethylamine sensing properties," Chinese Chem. Lett., vol. 31, no. 8, pp. 2133–2136, Aug. 2020, doi: 10.1016/j.cclet.2019.12.021.
[81] D. Meng, T. Qiao, G. Wang, X. San, and F. Meng, "One-step synthesis of rGO/V_2O_5 flower-like microsphere composites with enhanced trimethylamine sensing properties," Mater. Lett., vol. 299, p. 130023, Sep. 2021, doi: 10.1016/j.matlet.2021.130023
[82] H. Dhoundiyal, P. Das, and M. C. Bhatnagar, "Electrical and magnetic properties of V_2O_5 microstructure formed by self-assembled nanorods," Phys. B Condens. Matter, vol. 603, p. 412622, Feb. 2021, doi: 10.1016/j.physb.2020.412622.
[83] G. Zhang, L. Ren, D. Hu, S. Zhang, and H. Gu, "Fabrication of mesoporous carbon hollow spheres intercalated three-dimensional network structure V_2O_5 nanosheets with enhanced electrochemical performance," J. Alloys Compd., vol. 781, pp. 407–414, Apr. 2019, doi: 10.1016/j.jallcom.2018.12.096.

[84] H. Zhang, Y. Rong, W. Jia, H. Chai, and Y. Cao, “Simple solvent-free synthesis of rod-like Cu-doped V_2O_5 for high storage capacity cathode materials of lithium ion batteries,” J. Alloys Compd., vol. 802, pp. 139–145, Sep. 2019, doi: 10.1016/j.jallcom.2019.06.192.
[85] N. H. Hanh, T. M. Ngoc, L. Van Duy, C. M. Hung, N. Van Duy, and N. D. Hoa, “A comparative study on the VOCs gas sensing properties of Zn_2SnO_4 nanoparticles, hollow cubes, and hollow octahedra towards exhaled breath analysis,” Sensors Actuators B Chem., vol. 343, p. 130147, Sep. 2021, doi: 10.1016/j.snb.2021.130147.
[86] Z. Wang et al., “Oxygen-defective V_2O_5 nanosheets boosting 3D diffusion and reversible storage of zinc ion for aqueous zinc-ion batteries,” Appl. Surf. Sci., vol. 562, p. 150196, Oct. 2021, doi: 10.1016/j.apsusc.2021.150196.
[87] Y. Qi et al., “Ag-functionalized exfoliated V_2O_5 nanosheets: a flexible and binder-free cathode for lithium-ion batteries,” J. Mater. Sci., vol. 54, no. 19, pp. 12713–12722, Oct. 2019, doi: 10.1007/s10853-019-03806-z.
[88] X. H. Yang, H. Xie, H. T. Fu, X. Z. An, X. C. Jiang, and A. B. Yu, “Synthesis of hierarchical nanosheet-assembled V_2O_5 microflowers with high sensing properties towards amines,” RSC Adv., vol. 6, no. 90, pp. 87649–87655, 2016, doi: 10.1039/C6RA18848F.
[89] D. Surya Bhaskaram, R. Cheruku, and G. Govindaraj, “Reduced graphene oxide wrapped V_2O_5 nanoparticles: green synthesis and electrical properties,” J. Mater. Sci. Mater. Electron., vol. 27, no. 10, pp. 10855–10863, Oct. 2016, doi: 10.1007/s10854-016-5194-x.
[90] S. Wang, T. Yu, Y. Li, H. Fu, and C. Sun, “General methods for large-scale production of nanostructured V_2O_5 with controlled morphologies,” Mater. Res. Bull., vol. 111, pp. 284–288, Mar. 2019, doi: 10.1016/j.materresbull.2018.11.008.
[91] N. M. Abd-Alghafour, N. M. Ahmed, and Z. Hassan, “Fabrication and characterization of V_2O_5 nanorods based metal–semiconductor–metal photodetector,” Sensors Actuators A Phys., vol. 250, pp. 250–257, Oct. 2016, doi: 10.1016/j.sna.2016.09.001.
[92] C. M. Hung, L. Van Duy, D. T. Thanh Le, H. Nguyen, N. Van Duy, and N. D. Hoa, “ZnO coral-like nanoplates decorated with Pd nanoparticles for enhanced VOC gas sensing,” J. Sci. Adv. Mater. Devices, vol. 6, no. 3, pp. 453–461, Sep. 2021, doi: 10.1016/j.jsamd.2021.05.005.
[93] P. Cao et al., “Design of flower-like V_2O_5 hierarchical nanostructures by hydrothermal strategy for the selective and sensitive detection of xylene,” J. Alloys Compd., vol. 815, p. 152378, Jan. 2020, doi: 10.1016/j.jallcom.2019.152378.
[94] P. Zhang, G. Pan, B. Zhang, J. Zhen, and Y. Sun, “High sensitivity ethanol gas sensor based on Sn - doped ZnO under visible light irradiation at low temperature,” Mater. Res., vol. 17, no. 4, pp. 817–822, Jul. 2014, doi: 10.1590/1516-1439.235713.
[95] D. Sun, Q. Liu, Z. Liu, G. Gui, and Z. Huang, “Adsorption and oxidation of NH_3 over V_2O_5/AC surface,” Appl. Catal. B Environ., vol. 92, no. 3–4, pp. 462–467, Nov. 2009, doi: 10.1016/j.apcatb.2009.09.005.
[96] W. C. Ko, K. M. Kim, Y. J. Kwon, H. Choi, J. K. Park, and Y. K. Jeong, “ALD-assisted synthesis of V_2O_5 nanoislands on SnO_2 nanowires for improving NO_2 sensing performance,” Appl. Surf. Sci., vol. 509, p. 144821, Apr. 2020, doi: 10.1016/j.apsusc.2019.144821.
[97] P. Cao et al., “Highly ordered mesoporous V_2O_5 nanospheres utilized chemiresistive sensors for selective detection of xylene,” Mater. Sci. Eng. B, vol. 265, p. 115031, Mar. 2021, doi: 10.1016/j.mseb.2020.115031.
[98] N. M. Abd-Alghafour, G. A. Naeem, A. S. Ibraheam, N. Afzal, S. M. Mohammad, and R. F. Muslim, “Fabrication and characterization of ethanol gas sensor based on hydrothermally grown V_2O_5 nanorods,” Optik (Stuttg)., vol. 222, p. 165441, Nov. 2020, doi: 10.1016/j.ijleo.2020.165441.
[99] A. A. Mane, P. S. Maldar, S. H. Dabhole, S. A. Nikam, and A. V. Moholkar, “Effect of substrate temperature on physicochemical and gas sensing properties of sprayed orthorhombic V_2O_5 thin films,” Measurement, vol. 131, pp. 223–234, Jan. 2019, doi: 10.1016/j.measurement.2018.08.042.
[100] Y. Vijayakumar et al., “V2O5 nanofibers: Potential contestant for high performance xylene sensor,” J. Alloys Compd., vol. 731, pp. 805–812, Jan. 2018, doi: 10.1016/j.jallcom.2017.10.056.
[101] H. Fu, X. Yang, X. An, W. Fan, X. Jiang, and A. Yu, “Experimental and theoretical studies of V_2O_5@TiO_2 core-shell hybrid composites with high gas sensing performance towards ammonia,” Sensors Actuators B Chem., vol. 252, pp. 103–115, Nov. 2017, doi: 10.1016/j.snb.2017.05.027.
[102] T. Yang, H. Yu, B. Xiao, Z. Li, and M. Zhang, “Enhanced 1-butylamine gas sensing characteristics of flower-like V_2O_5 hierarchical architectures,” J. Alloys Compd., vol. 699, pp. 921–927, Mar. 2017, doi: 10.1016/j.jallcom.2017.01.028.
[103] A. A. Mane, S. A. Nikam, and A. V. Moholkar, “NO_2 gas sensing properties of sprayed composite porous MoO_3-V_2O_5 thin films,” Mater. Chem. Phys., vol. 216, pp. 294–304, Sep. 2018, doi: 10.1016/j.matchemphys.2018.05.043.

[104] X. Yang et al., "Synthesis of Au decorated V_2O_5 microflowers with enhanced sensing properties towards amines," Powder Technol., vol. 339, pp. 408–418, Nov. 2018, doi: 10.1016/j.powtec.2018.08.024.
[105] J. Wu et al., "Electrospun hollow CuO modified V_2O_5 nano-string of pearls with improved acetone sensitivity," Chem. Phys. Lett., vol. 727, pp. 19–24, Jul. 2019, doi: 10.1016/j.cplett.2019.04.043.
[106] V. Modafferi, S. Trocino, A. Donato, G. Panzera, and G. Neri, "Electrospun V_2O_5 composite fibers: Synthesis, characterization and ammonia sensing properties," Thin Solid Films, vol. 548, pp. 689–694, Dec. 2013, doi: 10.1016/j.tsf.2013.03.137.
[107] V. Modafferi et al., "Highly sensitive ammonia resistive sensor based on electrospun V_2O_5 fibers," Sensors Actuators B Chem., vol. 163, no. 1, pp. 61–68, Mar. 2012, doi: 10.1016/j.snb.2012.01.007.
[108] M. Tonezzer, D. Thi Thanh Le, L. Van Duy, N. Duc Hoa, F. Gasperi, N. Van Duy, F. Biasioli, Electronic noses based on metal oxide nanowires: A review, Nanotechnology Reviews, 11 (2022) 897–925. Doi: 10.1515/ntrev-2022-0056
[109] Research carried out on the Scopus search engine on October 7, 2021.
[110] Seyama T, Kato A, Fujishi K, Nagatani M, A new detector for gasous components using semiconductive thin films. Anal. Chem. 1962; 34:1502.
[111] Kim J-H, Mirzaei A, Osada M, Kim HW, Kim SS. Hydrogen sensing characteristics of Pd-decorated ultrathin ZnO nanosheets, Sensors Actuators, B Chem. 2021;329:129222. Doi: 10.1016/j.snb.2020.129222.
[112] Navale S, Shahbaz M, Mirzaei A, Kim SS, Kim HW. Effect of Ag Addition on the gas-sensing properties of nanostructured resistive-based gas sensors: an overview, Sensors 2021;21:6454. Doi: 10.3390/s21196454.
[113] Tshabalala ZP, Mokoena TP, Jozela M, Tshilongo J, Hillie TK, Swart HC, et al.. TiO_2 Nanowires for Humidity-Stable Gas Sensors for Toluene and Xylene, ACS Appl. Nano Mater. 2021; 4:702-716. Doi: 10.1021/acsanm.0c02963.
[114] Kim T-H, Jeong S-Y, Moon YK, Lee J-H. Dual-mode gas sensor for ultrasensitive and highly selective detection of xylene and toluene using Nb-doped NiO hollow spheres. Sens. Actuators, B 2019;301:127140. Doi: 10.1016/j.snb.2019.127140.
[115] Motsoeneng RG, Kortidis I, Ray SS, Motaung DE. Designing SnO_2 nanostructure-based sensors with tailored selectivity towards propanol and ethanol vapors, ACS Omega 2019;4:13696−13709. Doi: 10.1021/acsomega.9b01079.
[116] Neri G. Thin 2D: the new dimensionality in gas sensing, Chemosensors 2017;5:21. Doi: 10.3390/chemosensors5030021.
[117] Tonezzer M, Hieu NV. Size-dependent response of single-nanowire gas sensors, Sens. Actuators, B 2012;163:146-152. Doi: 10.1016/j.snb.2012.01.022.
[118] Liu J, Lv J, Xiong H, Wang Y, Jin G, Zhai Z, et al. Size effect and comprehensive mathematical model for gas-sensing mechanism of SnO_2 thin film gas sensors, J. Alloys Compd. 2022;898:162875. Doi: 10.1016/j.jallcom.2021.162875.
[119] Tonezzer M, Dang TTL, Bazzanella N, Nguyen VH, Iannotta S. Comparative gas-sensing performance of 1D and 2D ZnO nanostructures, Sensors Actuators, B Chem. 2015;220:1152-1160. Doi: 10.1016/j.snb.2015.06.103.
[120] S. Wold, M. Sjöström, L. Eriksson, PLS-regression: a basic tool of chemometrics. Chemometrics and Intelligent Laboratory Systems 2001; 58:109–130. Doi:10.1016/S0169-7439(01)00155-1
[121] Handbook of Partial Least Squares. Esposito Vinzi V, Chin WW, Henseler J, Wang H, editors. Springer Handbooks of Computational Statistics. ISBN 978-3-540-32827-8
[122] McCulloch WS, Pitts W. A logical calculus of the ideas immanent in nervous activity. Bull. Math. Biol. 1943; 5:115-133. Doi: 10.1007/BF02459570
[123] Gardner JW, Bartlett PN. A brief history of electronic noses. Sensors Actuators, B Chem. 1994;18-19:211-220. Doi: 10.1016/0925-4005
[124] Haugen J-E, Kvaal K. Electronic nose and artificial neural network. Meat Science 1998; 49:S273-S286. Doi: 10.1016/0925-4005 (94) 87085-3
[125] Sysoev VV, Button BK, Wepsiec K, Dmitriev S, Kolmakov A. Toward the nanoscopic "electronic nose": hydrogen vs carbon monoxide discrimination with an array of individual metal oxide nano- and mesowire sensors. Nano Lett. 2006; 6:1584-1588. Doi: 10.1021/nl060185t
[126] Sysoev VV, Goshnick J, Schneider T, Strelcov E, Kolmakov A. A gradient microarray electronic nose based on percolating SnO_2 nanowire sensing elements. Nano Lett. 2007; 7:3182-3188. Doi: 10.1021/nl071815+
[127] Sysoev VV, Kiselev I, Schneider T, Bruns M, Sommer M, Haibcht W, et al. The gas-sensing characteristics of percolating 2D SnO_2 nanowire mats as a platform for electronic nose devices. AIP Conf. Proc. 2009; 1137:403-404. Doi: 10.1063/1.3156563

[128] Chen P-C, Ishikawa FN, Chang H-K, Ryu K, Zhou C. A nanoelectronic nose: a hybrid nanowire/carbon nanotube sensor array with integrated micromachined hotplates for sensitive gas discrimination. Nanotech. 2009;20:125503. Doi: 10.1088/0957-4484/20/12/125503

[129] Baik JM, Zielke M, Kim MH, Turner KL, Wodtke AM, Moskovits M. Tin-oxide-nanowire-based electronic nose using heterogeneous catalysis as a functionalization strategy. ACS Nano 2010; 4:3117–3122. Doi:10.1021/nn100394a.

[130] Chen J, Su H, Zhou W. Gas discrimination by ZnO nanowire arrays with different metal oxide coatings. Proc. IEEE Conf. Nanotechnol. 2011; 34–37. Doi:10.1109/NANO.2011.6144459.

[131] Chen J, Wang K, Zhou W. Vertically aligned ZnO nanorod arrays coated with SnO2/noble metal nanoparticles for highly sensitive and selective gas detection. IEEE Trans. Nanotechnol. 2011;10:968–974. Doi:10.1109/TNANO.2010.2091423.

[132] Mwakikunga BW, Malwela T, Hillie KT, Ndlovu G. Towards an electronic nose based on nano-structured transition metal oxides activated by a tuneable UV light source. Proc. of IEEE Sensors 2011;6127403:1109–1112. Doi: 10.1109/ICSENS.2011.6127403

[133] MacNaughton S, Sonkusale S, Surwade S, Ammu S, Manohar S. Electronic nose based on graphene, nanotube and nanowire chemiresistor arrays on silicon. Proc. IEEE Sensors. 2011;125–128. Doi:10.1109/ICSENS.2011.6127182.

[134] Sysoev VV, Strelcov E, Kar S, Kolmakov A. The electrical characterization of a multi-electrode odor detection sensor array based on the single SnO_2 nanowire. Thin Solid Films 2011;520:898–903. Doi:10.1016/j.tsf.2011.04.179.

[135] Su H, Chen J, Wang K, Ayyad AA, Zhou W. The Electronic Nose: The Effect of Metal Oxide Modifications to Well-Aligned ZnO Nanowire Arrays for Highly Sensitive and Selective Gas Detection. 2012;126–129. Doi:10.5162/imcs2012/1.4.5.

[136] Sberveglieri G, Concinca I, Comini E, Falasconi M, Ferroni M, Sberveglieri V. Synthesis and integration of tin oxide nanowires into an electronic nose. Vacuum 2012;86:532-535. Doi: 10.1016/j.vacuum.2011.10.004

[137] Zou X, Wang J, Liu X, Wang X, Jiang Y, Wang Y, et al. Rational design of sub-parts per million specific gas sensors array based on metal nanoparticles decorated nanowire enhancement-mode transistors. Nano Lett. 2013; 13:3287-3292. Doi: 10.1021/nl401498t

[138] Ko W, Jung N, Lee M, Yun M, Jeon S. Electronic nose based on multipatterns of ZnO nanorods on a quartz resonator with remote electrodes. ACS Nano. 2013;7:6685–6690. Doi:10.1021/nn4027245.

[139] Hwang S, Kwon H, Chhajed S, Byon JW, Baik JM, Im J, et al. A near single crystalline TiO_2 nanohelix array: enhanced gas sensing performance and its application as a monolithically integrated electronic nose. Analyst 2013; 138:443–450. Doi:10.1039/C2AN35932D.

[140] Hu Y, Lee H, Kim S, Yun M. A highly selective chemical sensor array based on nanowire/nanostructure for gas identification. Sensors Actuators, B Chem. 2013;181:424–431. Doi: 10.1016/j.snb.2013.01.084.

[141] Park WJ, Choi KJ, Kim MH, Koo BH, Lee JL, Baik JM. Self-assembled and highly selective sensors based on air-bridge-structured nanowire junction arrays. ACS Appl. Mater. Interfaces. 2013;5:6802–6807. Doi:10.1021/am401635e.

[142] DeMeo D, MacNaughton S, Wang Z, Zhang X, Sonkusale S, Vandervelde TE. Heterogeneous metal-oxide nanowire micro-sensor array for gas sensing. Mater. Res. Express. 2014;1. Doi:10.1088/2053-1591/1/2/025002.

[143] Wongchoosuk C, Subannajui K, Wang C, Yang Y, Güder F, Kerdcharoen T, et al. Electronic nose for toxic gas detection based on photostimulated core-shell nanowires. RSC Adv. 2014;4:35084–35088. Doi:10.1039/c4ra06143h.

[144] Burmistrov IN, Varezhnikov AS, Musatov VY, Lashkov AV, Gorokhovsky AV, Yudinceva TI, et al. Room temperature gas sensing with potassium titanate nanowires. 2015 IEEE SENSORS - Proc. 2015;1–4. Doi:10.1109/ICSENS.2015.7370586.

[145] Song E, Choi J-W. Multi-analyte detection of chemical species using a conducting polymer nanowire-based sensor array platform. Sens. Actuators B Chem. 2015; 215:99-106. Doi: 10.1016/j.snb.2015.03.039.

[146] Tonezzer M, Le DTT, Huy TQ, Iannotta S. Dual-selective hydrogen and ethanol sensor for steam reforming systems. Sens. Actuators, B 2016;236:1011-1019. Doi: 10.1016/j.snb.2016.04.150.

[147] Moon HG, Jung Y, Han SD, Shim Y-S, Shin B, Lee T, et al. Chemiresistive electronic nose toward detection of biomarkers in exhaled breath. ACS Appl. Mater. Interfaces 2016; 8:20969-20976. Doi: 10.1021/acsami.6b03256

[148] Cai B, Song Z, Tong Y, Tang Q, Shaymurat T, Liu Y. A single nanobelt transistor for gas identification: Using a gas-dielectric strategy. Sensors. 2016;16:1–11. Doi:10.3390/s16060917.

[149] Tan HM, Manh Hung C, Ngoc TM, Nguyen H, Duc Hoa N, Van Duy N, et al. Novel self-heated gas sensors using on-chip networked nanowires with ultralow power consumption. ACS Appl. Mater. Interfaces. 2017; 9:6153–6162. Doi:10.1021/acsami.6b14516.
[150] Moon HG, Jung Y, Han SD, Shim YS, Jung WS, Lee T, et al. All villi-like metal oxide nanostructures-based chemiresistive electronic nose for an exhaled breath analyzer. Sensors Actuators, B Chem. 2018;257:295–302. Doi:10.1016/j.snb.2017.10.153.
[151] Domènech-Gil G, Pardo A, Romano-Rodríguez A, Hrachowina L, Seifner MS, Barth S, et al. Different nanowire materials localized growth and in-situ integration for electronic nose applications. Proc. 2018 12th Spanish Conf. Electron Devices, CDE 2018. 2018;6:8–11. Doi:10.1109/CDE.2018.8597020.
[152] Tonezzer M, Le DTT, Iannotta S, Hieu NV. Selective discrimination of hazardous gases using one single metal oxide resistive sensor. Sens. Actuators B Chem. 2018; 277:121-128. Doi: 10.1016/j.snb.2018.08.103
[153] Chen J, Chen Z, Boussaid F, Zhang D, Pan X, Zhao H, et al. Ultra-low-power smart electronic nose system based on three-dimensional tin oxide nanotube arrays. ACS Nano. 2018;12:6079–6088. Doi:10.1021/acsnano.8b02371.
[154] Hrachowina L, Domènech-Gil G, Pardo A, Seifner MS, Gràcia I, Cané C, et al. Site-specific growth and in situ integration of different nanowire material networks on a single chip: toward a nanowire-based electronic nose for gas detection. ACS Sensors. 2018;3:727–734. Doi:10.1021/acssensors.8b00073.
[155] Tonezzer M, Dang LTT, Tran HQ, Iannotta S. Multiselective visual gas sensor using nickel oxide nanowires as chemiresistor. Sensors Actuators, B Chem. 2018;255:2785–2793. Doi:10.1016/j.snb.2017.09.094.
[156] Tonezzer M. Selective gas sensor based on one single SnO_2 nanowire, Sens. Actuators B Chem. 2019;288:53-59. Doi: 10.1016/j.snb.2019.02.096
[157] Bobkov A, Alexey Varezhnikov A, Plugin I, Fedorov FS, Trouillet V, Geckle U, et al. The multisensor array based on grown-on-chip zinc oxide nanorod network for selective discrimination of alcohol vapors at sub-ppmv range. Sensors 2019; 19:4265. Doi: 10.3390/s19194265
[158] Tonezzer M, Kim J-H, Lee J-H, Iannotta S, Kim SS. Predictive gas sensor based on thermal fingerprints from Pt-SnO_2 nanowires. Sens. Actuators B Chem. 2019; 281:670-678. Doi: 10.1016/j.snb.2018.10.102
[159] Tonezzer M, Izidoro SC, Moraes JPA, Dang LTT. Improved gas selectivity based on carbon modified SnO_2 nanowires. Front. Mater. 2019; 6:277. Doi: 10.3389/fmats.2019.00277
[160] Ngoc TM, Duy NV, Hung CM, Hoa ND, Nguyen H, Tonezzer M, et al. Self-heated Ag-decorated SnO_2 nanowires with low power consumption used as a predictive virtual multisensor for H_2S-selective sensing. Anal. Chim. Acta 2019; 1069:108-116. Doi: 10.1016/j.aca.2019.04.020
[161] Thai NX, Van Duy N, Hung CM, Nguyen H, Tonezzer M, Van Hieu N, et al. Prototype edge-grown nanowire sensor array for the real-time monitoring and classification of multiple gases. J. Sci. Adv. Mater. Devices. 2020; 5:409–416. Doi: 10.1016/j.jsamd.2020.05.005.
[162] Thai NX, Tonezzer M, Masera L, Nguyen H, Duy NV, Hoa ND. Multi gas sensors using one nanomaterial, temperature gradient, and machine learning algorithms for discrimination of gases and their concentration. Anal. Chim. Acta 2020; 1124:85-93. Doi: 10.1016/j.aca.2020.05.015
[163] Sinju KR, Ramgir NS, Pathak A, Debnath AK, Muthe KP. Multiple sensor array based on ZnO nanowires for electronic nose applications towards toxic gases. AIP Conf. Proc. 2020;2265. Doi:10.1063/5.0017841.
[164] Tonezzer M, Armellini C, Toniutti L. Sensing performance of thermal electronic noses: A comparison between ZnO and SnO_2 nanowires. Nanomaterials 2021;11:2773. Doi: 10.3390/nano11112773.
[165] Kanaparthi S, Singh SG. Discrimination of gases with a single chemiresistive multi-gas sensor using temperature sweeping and machine learning. Sensors Actuators, B Chem. 2021;348:130725. Doi: 10.1016/j.snb.2021.130725.
[166] Sysoev VV, Strelcov E, Sommer M, Bruns M, Kiselev I, Habicht W, et al. Single-nanobelt electronic nose: Engineering and tests of the simplest analytical element. ACS Nano. 2010;4:4487–4494. Doi:10.1021/nn100435h.
[167] Ponzoni A, Zappa D, Comini E, Sberveglieri V, Faglia G, Sberveglieri G. Metal oxide nanowire gas sensors: Application of conductometric and surface ionization architectures. Chem. Eng. Trans. 2012;30:31–36. Doi:10.3303/CET1230006.
[168] Sberveglieri V, Pulvirenti A, Comini E, Carmona EN. What happens at the aroma of coffee beans after roasting? MOX nanowire technology by novel electronic nose to discover the finger print. Int. J. Smart Sens. Intell. Syst. 2014; 7:1-4. Doi: 10.21307/IJSSIS-2019-052
[169] Sberveglieri V, Núñez E, Zappa D, Comini E, Pulvirenti A. Classification of different roasting processes by MOX nanowire. Procedia Eng. 2014; 87:572-575. Doi: 10.1016/j.proeng.2014.11.553
[170] Sberveglieri G, Zambotti G, Falasconi M, Gobbi E, Sberveglieri V. MOX-NW electronic nose for detection of food microbial contamination. Proc. IEEE Sensors 2014; 2014:1376-1379. Doi: 10.1109/ICSENS.2014.6985268

[171] Messina V, Sance M, Grigioni G, de Reca NW. Optimization of metal oxide gas sensor in electronic nose to monitor odor profiles of garlic scape. IEEE Sens. J. 2014; 14:1765. Doi: 10.1109/JSEN.2014.2303147
[172] Kanade A, Shaligram AD. Development of an e-nose using metal oxide semiconductor sensors for the classification of climacteric fruits. IJSER 2104;5:467.
[173] Sberveglieri V, Carmona EN, Pulvirenti A. Nanowire sensor array for the rapid quality control on grated Parmigiano Reggiano. Proc. AISEM Conference 2015; 2015:7066773. Doi: 10.1109/AISEM.2015.7066773
[174] Sberveglieri V, Bhandari MP, Carmona EN, Betto G, Sberveglieri G. A novel MOS nanowire gas sensor device (S3) and GC-MS-based approach for the characterization of grated parmigiano reggiano cheese. Biosensors. 2016;6. Doi:10.3390/bios6040060.
[175] Zappa D, Sberveglieri V, Comini E, Barisani F, Sberveglieri G. Synthesis and characterization of zinc and tin oxide nanowires for the detection of Parmigiano Reggiano cheese. Proc. Int. Conf. Sens. Technol. ICST. 2016;2016-March:178–182. Doi:10.1109/ICSensT.2015.7438387.
[176] Bhandari MP, Carmona EN, Galstyan V, Sberveglieri V. Quality evaluation of Parmigiano Reggiano cheese by a novel nanowire device S3 and evaluation of the VOCs profile. Procedia Eng. 2016;168:460–464. Doi:10.1016/j.proeng.2016.11.126.
[177] Sberveglieri V, Bhandari MP, Carmona EN, Betto G, Soprani M, Malla R, et al. Spectrocolorimetry and nanowire gas sensor device S3 for the analysis of Parmigiano Reggiano cheese ripening. Proc. ISOEN 2017, 7968861. Doi: 10.1109/ISOEN.2017.7968861
[178] Abbatangelo M, Núñez-Carmona E, Sberveglieri V. Application of a novel S3 nanowire gas sensor device in parallel with GC-MS for the identification of Parmigiano Reggiano from US and European competitors. J. Food Eng. 2018; 236:36-43. Doi: 10.1016/j.jfoodeng.2018.05.009
[179] Abbatangelo M, Núñez-Carmona E, Sberveglieri V, Zappa D, Comini E, Sberveglieri G. Application of a novel S3 nanowire gas sensor device in parallel with GC-MS for the identification of rind percentage of grated Parmigiano Reggiano. Sensors. 2018;18. Doi:10.3390/s18051617.
[180] Núñez-Carmona E, Abbatangelo M, Sberveglieri V. Innovative sensor approach to follow Campylobacter jejuni development. Biosensors 2019; 9:bios9010008. Doi: 10.3390/bios9010008
[181] Zappa D. Low-power detection of food preservatives by a novel nanowire-based sensor array. Foods. 2019;8. Doi:10.3390/foods8060226.
[182] Abbatangelo M, Núñez-Carmona E, Sberveglieri V, Zappa D, Comini E, Sberveglieri G. An array of MOx sensors and ANNs to assess grated Parmigiano reggiano cheese packs' compliance with CFPR guidelines. Biosensors. 2020;10. Doi:10.3390/BIOS10050047.
[183] Tonezzer M, Thai NX, Gasperi F, Duy NV, Biasioli F. Quantitative assessment of trout fish spoilage with a single nanowire gas sensor in a thermal gradient. Nanomater. 2021;22:1604. Doi: 10.3390/nano11061604
[184] Tonezzer M. Single nanowire gas sensor able to distinguish fish and meat and evaluate their degree of freshness. Chemosensors 2021;9249. Doi: 10.3390/chemosensors9090249.
[185] Cui S, Cao L, Acosta N, Zhu H, Ling PP. Development of portable e-nose system for fast diagnosis of whitefly infestation in tomato plant in greenhouse. Chemosensors 2021;9:297. Doi: 10.3390/chemosensors9110297.
[186] Astuti SD, Tamimi MH, Pradhana AAS, Alamsyah KA, Purnobasuki H, Khasanah M, et al. Gas sensor array to classify the chicken meat with E. coli contaminant by using random forest and support vector machine. Biosens. Bioelectron. 2021;9:100083. Doi: 10.1016/j.biosx.2021.100083.
[187] Andre RS, Facure MHM, Mercante LA, Correa DS. Electronic nose based on hybrid free-standing nanofibrous mats for meat spoilage monitoring. Sensors Actuators, B Chem. 2022;353:131114. Doi: 10.1016/j.snb.2021.131114.
[188] Carmona EN, Sberveglieri V, Ponzoni A, Zappa D, Pulvirenti A. Detection of microbial contamination in potable water by nanowire technology. Int. J. Smart Sens. Intell. Syst. 2014;7:2–5. Doi:10.21307/IJSSIS-2019-054.
[189] Carmona EN, Sberveglieri V, Comini E, Zappa D, Pulvirenti A. Nanowire technology for the detection of microorganisms in potable water. Procedia Eng. 2014;87:1453–1456. Doi:10.1016/j.proeng.2014.11.723.
[190] Sberveglieri V, Nunez Carmona E, Comini E, Ponzoni A, Zappa D, Pirrotta O, Pulvirenti A. A novel electronic nose as adaptable device to judge microbiological quality and safety in foodstuff. BioMed Res. Int. 2014;2014:529519. Doi: 10.1155/2014/529519
[191] Saidi T, Welearegay TG, Zaim O, Leon OG, Ionescu R, El Bari N, Bouchikhi B. Ability of discrimination of breath from smoker and non-smoker volunteers by using an electronic nose based on WO_3 nanowires and SnO_2 sensors. ISOEN 2017 - ISOCS/IEEE Int. Symp. Olfaction Electron. Nose, Proc. 2017;15–17. Doi:10.1109/ISOEN.2017.7968881.

[192] Núñez Carmona E, Sberveglieri V, Ponzoni A, Galstyan V, Zappa D, Pulvirenti A, CominiE. Detection of food and skin pathogen microbiota by means of an electronic nose based on metal oxide chemiresistors. Sensors Actuators, B Chem. 2017;238:1224–1230. Doi:10.1016/j.snb.2016.09.086.
[193] Soprani M, Ponzoni A, Sberveglieri V, Carmona EN, Bhandari MP, Betto G, Sberveglieri G. Real-time chemical gas sensing of pathogenic microorganisms pollution in wastewater. ISOEN 2017 - ISOCS/IEEE Int. Symp. Olfaction Electron. Nose, Proc. 2017;17–19. Doi:10.1109/ISOEN.2017.7968877.
[194] Zappa D, Bertuna A, Comini E, Kaur N, Poli N, Sberveglieri V, Sberveglieri G. Metal oxide nanostructures: preparation, characterization and functional applications as chemical sensors. Beilstein J. Nanotechnol. 2017; 8:1205–1217. Doi:10.3762/bjnano.8.122.
[195] Soprani M, Duina G, Malgaretti M, Abbatangelo M, Sberveglieri V. Array of semiconductor nanowires gas sensor for IoT in wastewater management. 2018;68–71. Doi: 10.1109/METROI4.2018.8438882
[196] Binson VA, Subramoniam M, Mathew L. Detection of COPD and Lung Cancer with electronic nose using ensemble learning methods. Clin. Chim. Acta 2021;523:231-238. Doi: 10.1016/j.cca.2021.10.005.
[197] Chen PC, Sukcharoenchoke S, Ryu K, De Arco LG, Badmaev A, Wang C, Zhou C. 2,4,6-Trinitrotoluene (TNT) chemical sensing based on aligned single-walled carbon nanotubes and ZnO nanowires. Adv. Mater. 2010; 22:1900–1904. Doi:10.1002/adma.200904005.
[198] Ponzoni A, Comini E, Concina I, Ferroni M, Falasconi M, Gobbi E, Sberveglieri V, Sberveglieri G. Nanostructured metal oxide gas sensors, a survey of applications carried out at SENSOR Lab, Brescia (Italy) in the security and food quality fields. Sensors 2012;12:17023-17045. Doi: 10.3390/s121217023
[199] Adib M, Sommer M. UV excited SnO2 nanowire based printed e-Nose. Proc. IEEE Sensors 2017;2016:7808805. Doi: 10.1109/ICSENS.2016.7808805
[200] Avhad KM, Ramgir NS, Bhusari R, Jishita R, Navneethan R, Avhad A, et al. Development of electronic nose based on ZnO nanowires for toxic gas detection. Proc. 2017 3rd IEEE Int. Conf. Sensing, Signal Process. Secur. ICSSS 2017;2017:275–278. Doi:10.1109/SSPS.2017.8071605.
[201] Adib M, Eckstein R, Hernandez-Sosa G, Sommer M, Lemmer U. SnO2 nanowire-based aerosol jet printed electronic nose as fire detector. IEEE Sens. J. 2018;18:494–500. Doi:10.1109/JSEN.2017.2777178.
[202] Suzuki M, Miyauchi T, Isaji S, Hirabayashi Y, Naganawa R. Decay detection of constructional softwoods using machine olfaction. J. Wood Sci. 2021;67:62. Doi: 10.1186/s10086-021-01995-3.
[203] Maccato C, Bigiani L, Carraro G, Gasparotto A, Sada C, Comini E, et al. Toward the detection of poisonous chemicals and warfare agents by functional Mn3O4 nanosystems. ACS Appl. Mater. Interfaces 2018;10:12305–12310. Doi: 10.1021/acsami.8b0183.
[204] Bigiani L, Zappa D, Barreca D, Gasparotto A, Sada C, Tabacchi G, et al. Sensing nitrogen mustard gas simulant at the ppbv scale via selective dual-site activation at Au/Mn3O4 interfaces. ACS Appl. Mater. Interfaces 2019;11:23692–23700. Doi: 10.1021/acsami.9b0487.
[205] Bigiani L, Zappa D, Maccato C, Gasparotto A, Sada C, Comini E, et al. Mn_3O_4 nanomaterials functionalized with Fe2O3 and ZnO: Fabrication, characterization, and Ammonia sensing properties. Adv. Mater. Interfaces 2019;6:1901239. Doi: 10.1002/admi.201901239.
[206] Bigiani L, Zappa D, Maccato C, Comini E, Barreca D, Gasparotto A. Quasi-1D MnO_2 nanocomposites as gas sensors for hazardous chemicals. Appl. Surf. Sci. 2020;215:145667. Doi: 10.1016/j.apsusc.2020.145667.
[207] Jiang, Y.; Xing, J.; Wang, S.; Chang, X.; Liu, S.; Shi, A.; Liu, B.; Sahu, S.K. Understand the local and regional contributions on air pollution from the view of human health impacts. Front. Environ. Sci. Eng. 2021, 15, 1–11. Doi: 10.1007/s11783-020-1382-2.
[208] Zhou, X.; Strezov, V.; Jiang, Y.; Kan, T.; Evans, T. Temporal and spatial variations of air pollution across China from 2015 to 2018. J. Environ. Sci. 2022, 112, 161–169. Doi: 10.1016/j.jes.2021.04.025.
[209] Manisalidis, I.; Stavropoulou, E.; Stavropoulos, A.; Bezirtzoglou, E. Environmental and health impacts of air pollution: A review. Front. Public Health 2020, 8, 14. Doi: 10.3389/fpubh.2020.00014.
[210] Noh, Y.; Boor, B.E.; Shannahan, J.H.; Troy, C.D.; Jafvert, C.T.; Whelton, A.J. Emergency responder and public health considerations for plastic sewer lining chemical waste exposures in indoor environments. J. Hazard. Mater. 2022, 422, 126832. Doi: 10.1016/j.jhazmat.2021.126832.
[211] Ghelli, F.; Bellisario, V.; Squillacioti, G.; Grignani, E.; Garzaro, G.; Buglisi, M.; Bergamaschi, E.; Bono, R. Oxidative stress induction in woodworkers occupationally exposed to wood dust and formaldehyde. J. Occup. Med. Toxicol. 2021, 16, 1–9. Doi: 10.1186/s12995-021-00293-4.
[212] Huang, L.; Wei, Y.; Zhang, L.; Ma, Z.; Zhao, W. Estimates of emission strengths of 43 VOCs in wintertime residential indoor environments, Beijing. Sci. Total Environ. 2021, 793, 148623. Doi: 10.1016/j.scitotenv.2021.148623.

[213] Barreca, D.; Gasparotto, A.; Gri, F.; Comini, E.; Maccato, C. Plasma-assisted growth of β-MnO_2 nanosystems as gas sensors for safety and food industry applications. Adv. Mater. Interfaces 2018, 5, 1800792. Doi: 10.1002/admi.201800792.
[214 Al Makky, A.; Alaswad, A.; Gibson, D.; Olabi, A.G. Renewable energy scenario and environmental aspects of soil emission measurements. Renew. Sustain. Energy Rev. 2017, 68, 1157–1173. Doi: 10.1016/j.rser.2016.05.088.
[215] Ge, Y.; Wei, Z.; Li, Y.; Qu, J.; Zu, B.; Dou, X. Highly sensitive and rapid chemiresistive sensor towards trace nitro-explosive vapors based on oxygen vacancy-rich and defective crystallized In-doped ZnO. Sens. Actuators B Chem. 2017, 244, 983–991. Doi: 10.1016/j.snb.2017.01.092.
[216] Righettoni, M.; Amann, A.; Pratsinis, S.E. Breath analysis by nanostructured metal oxides as chemo-resistive gas sensors. Mater. Today 2015, 18, 163–171. Doi: 10.1016/j.mattod.2014.08.017.
[217] Mirzaei, A.; Lee, J.-H.; Majhi, S.M.; Weber, M.; Bechelany, M.; Kim, H.W.; Kim, S.S. Resistive gas sensors based on metal-oxide nanowires. J. Appl. Phys. 2019, 126, 241102. Doi: 10.1063/1.5118805.
[218] Tonezzer, M. Detection of mackerel fish spoilage with a gas sensor based on one single SnO_2 nanowire. Chemosensors 2021, 9, 2. Doi: 10.3390/chemosensors9010002.
[219] Bigiani, L.; Zappa, D.; Maccato, C.; Gasparotto, A.; Sada, C.; Comini, E.; Barreca, D. Hydrogen gas sensing performances of p-type Mn_3O_4 nanosystems: The role of built-in Mn_3O_4/Ag and Mn_3O_4/SnO_2 junctions. Nanomaterials 2020, 10, 511. Doi: 10.3390/nano10030511.
[220] Wang, B.-Y.; Lim, D.-S.; Oh, Y.-J. CO gas detection of Al-doped ZnO nanostructures with various shapes. Jpn. J. Appl. Phys. 2013, 52, 101103. Doi: 10.7567/jjap.52.101103
[221] Tonezzer, M.; Van Hieu, N. Size-dependent response of single-nanowire gas sensors. Sens. Actuators B Chem. 2012, 163, 146–152. Doi: 10.1016/j.snb.2012.01.022.
[222] Nikolic, M.V.; Milovanovic, V.; Vasiljevic, Z.Z.; Stamenkovic, Z. Semiconductor gas sensors: materials, technology, design, and application. Sensors 2020, 20, 6694. Doi: 10.3390/s20226694.
[223] Simion, C.E.; Tomescu-Stănoiu, A. Differences in the gas sensing properties readout with n and p-type MOX materials. In Proceedings of the International Semiconductor Conference (CAS 2010), Sinaia, Romania, 11–13 October 2010; pp. 201–204; https://doi.org/10.1109/SMICND.2010.5649077.
[224] Marzorati, D.; Mainardi, L.; Sedda, G.; Gasparri, R.; Spaggiari, L.; Cerveri, P. MOS sensors array for the discrimination of lung cancer and at-risk subjects with exhaled breath analysis. Chemosensors 2021, 9, 209. Doi: 10.3390/chemosensors9080209.
[225] Moon, H.G.; Jung, Y.; Han, S.D.; Shim, Y.-S.; Shin, B.; Lee, T.; Kim, J.-S.; Lee, S.; Jun, S.C.; Park, H.-H.; et al. Chemiresistive electronic nose toward detection of biomarkers in exhaled breath. ACS Appl. Mater. Interfaces 2016, 8, 20969–20976. Doi: 10.1021/acsami.6b03256.
[226] Rodríguez-Aguilar, M.; de León-Martínez, L.D.; Gorocica-Rosete, P.; Pérez-Padilla, R.; Domínguez-Reyes, C.A.; Teno-rio-Torres, J.A.; Ornelas-Rebolledo, O.; Mehta, G.; Zamora-Mendoza, B.N.; Flores-Ramírez, R. Application of chemoresistive gas sensors and chemometric analysis to differentiate the fingerprints of global volatile organic compounds from diseases. Preliminary results of COPD, lung cancer and breast cancer. Clin. Chim. Acta 2021, 518, 83–92. Doi: 10.1016/j.cca.2021.03.016.
[227] Sysoev, V.V.; Kiselev, I.; Frietsch, M.; Goschnick, J. Temperature gradient effect on gas discrimination power of a metal-oxide thin-film sensor microarray. Sensors 2004, 4, 37–46. Doi: 10.3390/s40400037.
[228] Sysoev, V.V.; Goschnick, J.; Schneider, T.; Strelcov, A.E.; Kolmakov, A. A gradient microarray electronic nose based on percolating SnO_2 nanowire sensing elements. Nano Lett. 2007, 7, 3182–3188. Doi: 10.1021/nl071815+.
[229] Thai, N.X.; Tonezzer, M.; Masera, L.; Nguyen, H.; Van Duy, N.; Hoa, N.D. Multi gas sensors using one nanomaterial, temperature gradient, and machine learning algorithms for discrimination of gases and their concentration. Anal. Chim. Acta 2020, 1124, 85–93. Doi: 10.1016/j.aca.2020.05.015.
[230] Thai, N.X.; Van Duy, N.; Hung, C.M.; Nguyen, H.; Tonezzer, M.; Van Hieu, N.; Hoa, N.D. Prototype edge-grown nanowire sensor array for the real-time monitoring and classification of multiple gases. J. Sci. Adv. Mater. Devices 2020, 5, 409–416. Doi: 10.1016/j.jsamd.2020.05.005.
[231] Kim, J.-Y.; Kim, S.S.; Tonezzer, M. Selective gas detection and quantification using a resistive sensor based on Pd-decorated soda-lime glass. Sens. Actuators B Chem. 2021, 335, 129714. Doi: 10.1016/j.snb.2021.129714.
[232] Tischner, A.; Maier, T.; Stepper, C.; Köck, A. Ultrathin SnO2 gas sensors fabricated by spray pyrolysis for the detection of humidity and carbon monoxide. Sens. Actuators B: Chem. 2008, 134, 796–802. Doi: 10.1016/j.snb.2008.06.032.
[233] Acetone. Available online: https://www.osha.gov/chemicaldata/476, accessed on 21 September 2021.
[234] Ammonia. Available online: https://www.osha.gov/chemicaldata/623, accessed on 21 September 2021.
[235] Ethanol. Available online: https://www.osha.gov/chemicaldata/1034, accessed on 21 September 2021.

[236] Hydrogen. Available online: https://www.osha.gov/laws-regs/regulations/standardnumber/1910/1910.103, accessed on 21 September 2021.
[237] Nitrogen dioxide. Available online: https://www.osha.gov/chemicaldata/21, accessed on 21 September 2021.
[238] Khan, A.H.; Thomson, B.; Debnath, R.; Motayed, A.; Rao, M.V. Nanowire-Based Sensor Array for Detection of Cross-Sensitive Gases Using PCA and Machine Learning Algorithms. IEEE Sens. J. 2020, 20, 6020–6028. Doi: 10.1109/jsen.2020.2972542.
[239] Huang, Y.; Doh, I.-J.; Bae, E. Design and Validation of a Portable Machine Learning-Based Electronic Nose. Sensors 2021, 21, 3923. Doi: 10.3390/s21113923.
[240] M. Tonezzer, N. Bazzanella, F. Gasperi, F. Biasioli, Nanosensor Based on Thermal Gradient and Machine Learning for the Detection of Methanol Adulteration in Alcoholic Beverages and Methanol Poisoning, Sensors, 22 (2022) 5554. Doi: 10.3390/s22155554
[241] L. Quercia, I. Khomenko, R. Capuano, M. Tonezzer, R. Paolesse, E. Martinelli, A. Catini, F. Biasioli, C. Di Natale, Optimization of gas sensors measurements by dynamic headspace analysis supported by simultaneous direct injection mass spectrometry, Sensors and Actuators B: Chemical, 347 (2021) 130580. Doi: 10.1016/j.snb.2021.130580
[242] K. Burlachenko, J.; Kruglenko, I.; Snopok, B.; Persaud, Sample handling for electronic nose technology: State of the art and future trends, TrAC - Trends Anal. Chem. 82 (2016) 222–236.
[243] N.H. Snow, G.C. Slack, Head-space analysis in modern gas chromatography, TrAC - Trends Anal. Chem. 21 (2002) 608–617. https://doi.org/10.1016/S0165-9936(02)00802-6.
[244] B. Kolb, L.S. Ettre, Static Headspace-Gas Chromatography: Theory and Practice, Second Edition, 2006. https://doi.org/10.1002/0471914584.
[245] D.A. Storace, L.B. Cohen, Measuring the olfactory bulb input-output transformation reveals a contribution to the perception of odorant concentration invariance, Nat. Commun. 8 (2017). https://doi.org/10.1038/s41467-017-00036-2.
[246] B. Salehi, A.P. Mishra, I. Shukla, M. Sharifi-Rad, M.D.M. Contreras, A. Segura-Carretero, H. Fathi, N.N. Nasrabadi, F. Kobarfard, J. Sharifi-Rad, Thymol, thyme, and other plant sources: Health and potential uses, Phyther. Res. 32 (2018) 1688–1706. https://doi.org/10.1002/ptr.6109.
[247] F.D. Gonelimali, J. Lin, W. Miao, J. Xuan, F. Charles, M. Chen, S.R. Hatab, Antimicrobial properties and mechanism of action of some plant extracts against food pathogens and spoilage microorganisms, Front. Microbiol. 9 (2018). https://doi.org/10.3389/fmicb.2018.01639.
[248] R. Paolesse, S. Nardis, D. Monti, M. Stefanelli, C. Di Natale, Porphyrinoids for chemical sensor applications, Chem. Rev. 117 (2017). https://doi.org/10.1021/acs.chemrev.6b00361.
[249] R.S. Blake, P.S. Monks, A.M. Ellis, Proton-transfer reaction mass spectrometry, Chem. Rev. 109 (2009) 861–896. https://doi.org/10.1021/cr800364q.
[250] R. Capuano, I. Khomenko, F. Grasso, V. Messina, A. Olivieri, L. Cappellin, R. Paolesse, A. Catini, M. Ponzi, F. Biasioli, F. Biasioli, C. Di Natale, Simultaneous proton transfer reaction-mass spectrometry and electronic nose study of the volatile compounds released by Plasmodium falciparum infected red blood cells in vitro, Sci. Rep. 9 (2019). https://doi.org/10.1038/s41598-019-48732-x.
[251] A. D'Amico, C. Di Natale, C. Falconi, G. Pennazza, M. Santonico, I. Lundstrom, Equivalent electric circuits for chemical sensors in the Langmuir regime, Sensors Actuators, B Chem. 238 (2017) 214–220. https://doi.org/10.1016/j.snb.2016.07.011.
[252] P.A. Brown, S.M. Cristescu, S.J. Mullock, D.F. Reich, C.S. Lamont-Smith, F.J.M. Harren, Implementation and characterization of an RF ion funnel ion guide as a proton transfer reaction chamber, Int. J. Mass Spectrom. 414 (2017) 31–38. https://doi.org/10.1016/j.ijms.2017.01.001.
[253] U. Oprea, A.; Weimar, Gas sensors based on mass-sensitive transducers part 1: transducers and receptors-basic understanding, Anal. Bioanal. Chem. 411 (2019) 1761–1787.
[254] J.W. Buchler, Synthesis and properties of metalloporphyrins, in: D. Dolphin (Ed.), Porphyrins Vol. 1, Academic Press, 1978.
[255] L. Cappellin, F. Biasioli, A. Fabris, E. Schuhfried, C. Soukoulis, T.D. Märk, F. Gasperi, Improved mass accuracy in PTR-TOF-MS: Another step towards better compound identification in PTR-MS, Int. J. Mass Spectrom. 290 (2010) 60–63. https://doi.org/10.1016/j.ijms.2009.11.007.
[256] L. Cappellin, F. Biasioli, E. Schuhfried, C. Soukoulis, T.D. Mark, F. Gasperi, Extending the dynamic range of proton transfer reaction time-of-flight mass spectrometers by a novel dead time correction, Rapid Commun. Mass Spectrom. 25 (2011) 179–183. https://doi.org/10.1002/rcm.4819.

[257] W. Lindinger, A. Hansel, A. Jordan, On-line monitoring of volatile organic compounds at pptv levels by means of Proton-Transfer-Reaction Mass Spectrometry (PTR-MS) Medical applications, food control and environmental research, Int. J. Mass Spectrom. Ion Process. 173 (1998) 191–241. https://doi.org/10.1016/s0168-1176(97)00281-4.
[258] S. Pyo, K. Lee, T. Noh, E. Jo, J. Kim, Sensitivity enhancement in photoionization detector using microelectrodes with integrated 1D nanostructures, Sensors Actuators, B Chem. 288 (2019) 618–624. https://doi.org/10.1016/j.snb.2019.03.045.
[259] Scharff, R.L. Economic burden from health losses due to foodborne illness in the United States. J. Food Prot. 2012, 75, 123–131, doi:10.4315/0362-028X.JFP-11-058.
[260] Sundström, K. Cost of Illness for Five Major Foodborne Illnesses and Sequelae in Sweden. Appl. Health Econ. Health Policy 2018, 16, 243–257, doi:10.1007/s40258-017-0369-z.
[261] Boyer, D.; Ramaswami, A. Comparing urban food system characteristics and actions in US and Indian cities from a multi-environmental impact perspective: Toward a streamlined approach. J. Ind. Ecol. 2020, 24, 841–854, doi:10.1111/jiec.12985.
[262] The State of World Fisheries and Aquaculture 2020. Sustainability in Action; FAO: Rome, Italy, 2020. ISBN 978-92-5-132692-3. ISSN 1020–5902. doi:10.4060/ca9229en.
[263] Olafsdóttir, G.; Martinsdóttir, E.; Oehlenschläger, J.; Dalgaard, P.; Jensen, B.; Undeland, I.; Mackie, I.M.; Henehan, G.; Nielsen, J.; Nilseng, H. Methods to evaluate fish freshness in research and industry. Trends Food Sci. Technol. 1997, 8, 258–265, doi:10.1016/S0924-2244(97)01049-2.
[264] Wojnowski, W.; Majchrzak, T.; Dymerski, T.; Gębicki, J.; Namieśnik, J. Electronic noses: Powerful tools in meat quality assessment. Meat Sci. 2017, 131, 119–131, doi:10.1016/j.meatsci.2017.04.240.
[265] Deisingh, A.K.; Stone, D.C.; Thompson, M. Applications of electronic noses and tongues in food analysis, Int. J. Food Sci. Technol. 2004, 39, 587–604, doi:10.1111/j.1365-2621.2004.00821.x.
[266] Wojnowski, W.; Majchrzak, T.; Dymerski, T.; Gębicki, J.; Namieśnik, J. Portable Electronic Nose Based on Electrochemical Sensors for Food Quality Assessment. Sensors 2017, 17, 2715, doi:10.3390/s17122715.
[267] Loutfi, A.; Coradeschi, S.; Mani, G.K.; Shankar, P.; Rayappan, J.B.B. Electronic noses for food quality: A review. J. Food Eng. 2015, 144, 103–111, doi:10.1016/j.jfoodeng.2014.07.019.
[268] Macías, M.M.; Agudo, J.; Manso, A.G.; Orellana, C.J.G.; Velasco, H.M.G.; Caballero, R.G. A compact and low cost electronic nose for aroma detection. Sensors 2013, 13, 5528–5541, doi:10.3390/s130505528.
[269] Silva, F.; Duarte, A.M.; Mender, S.; Pinto, F.R.; Barroso, S.; Ganhão, R.; Gil, M.M. CATA vs. FCP for a rapid descriptive analysis in sensory characterization of fish. J. Sens. Stud. 2020, e12605, doi:10.1111/joss.12605.
[270] Jia, S.; Li, Y.; Zhuang, S.; Sun, X.; Zhang, L.; Shi, J.; Hong, H.; Luo, Y. Biochemical changes induced by dominant bacteria in chill-stored silver carp (*Hypophthalmichthys molitrix*) and GC-IMS identification of volatile organic compounds. Food Microbiol. 2019, 84, 103248, doi:10.1016/j.fm.2019.103248.
[271] Gram, L.; Huss, H.H. Microbiological spoilage of fish and fish products. Int. J. Food Microbiol. 1996, 33, 121–137, doi:10.1016/0168-1605(96)01134-8.
[272] Mustafa, F.; Andreescu, S. Chemical and Biological Sensors for Food-Quality Monitoring and Smart Packaging. Foods 2018, 7, 168, doi:10.3390/foods7100168.
[273] Dikeman, M.; Devine, C. Encyclopedia of Meat Sciences, 2nd ed.; Academic Press: Amsterdam, The Netherlands, 2004. ISBN 978-0124649705.
[274] Seyama, T.; Kato, A.; Fujishi, K.; Nagatani, M. A New Detector for Gasous Components Using Semiconductive Thin Films. Anal. Chem. 1962, 34, 1502, doi:10.1021/ac60191a001.
[275] Tonezzer, M.; Le, D.T.T.; Iannotta, S.; Hieu, N.V. Selective discrimination of hazardous gases using one single metal oxide resistive sensor. Sensor Actuat. B Chem. 2018, 277, 121–128, doi:10.1016/j.snb.2018.08.103.
[276] Ngoc, T.M.; Duy, N.V.; Hung, C.M.; Hoa, N.D.; Nguyen, H.; Tonezzer, M.; Hieu, N.V. Self-heated Ag-decorated SnO_2 nanowires with low power consumption used as a predictive virtual multisensor for H_2S-selective sensing. Anal. Chim. Acta 2019, 1069, 108–116, doi:10.1016/j.aca.2019.04.020.
[277] Tonezzer, M. Selective gas sensor based on one single SnO_2 nanowire, Sensor Actuat. B Chem. 2019, 288, 53–59, doi:10.1016/j.snb.2019.02.096.
[278] Tischner, A.; Maier, T.; Stepper, C.; Köck, A. Ultrathin SnO_2 gas sensors fabricated by spray pyrolysis for the detection of humidity and carbon monoxide. Sensor Actuat. B Chem. 2008, 134, 796–802, doi:10.1016/j.snb.2008.06.032.
[279] López, A.; Baguer, B.; Goñi, P.; Rubio, E.; Gómez, J.; Mosteo, R.; Ormad, M.P. Assessment of the methodologies used in microbiological control of sewage sludge. Waste Manag. 2019, 96, 168–174, doi:10.1016/j.wasman.2019.07.024.
[280] Tsuda, N.; Nasu, K.; Fujimori, A.; Siratori, K. Electronic Conduction in Oxides, 2nd ed.; Springer-Verlag: Berlin, Germany, 2000.

[281] Marikutsa, A.; Rumyantseva, M.; Gaskov, A. Selectivity of catalytically modified tin dioxide to CO and NH_3 gas mixtures. Chemosensors 2015, 3, 241–252, doi:10.3390/chemosensors3040241.
[282] Koutsoumanis, K. Predictive Modeling of the Shelf Life of Fish under Nonisothermal Conditions. Appl. ENviron. Microbiol. 2001, 67, 1821–1829, doi:10.1128/AEM.67.4.1821-1829.2001.
[283] Sciortino, J.A.; Ravikumar, R. Chapter 5: Fish Quality Assurance. In Fishery Harbour Manual on the Prevention of Pollution, Bay of Bengal Programme; Bay of Bengal Programme: Madras, India, 1999.
[284] Scharff, R.L. Economic burden from health losses due to foodborne illness in the United States. J. Food Prot. 2012, 75, 123–131, doi:10.4315/0362-028X.JFP-11-058.
[285] Sundström, K. Cost of illness for five major foodborne illnesses and sequelae in Sweden. Appl. Health Econ. Health Policy 2018, 16, 243–257, doi:10.1007/s40258-017-0369-z.
[286] Boyer, D.; Ramaswami, A. Comparing urban food system characteristics and actions in US and Indian cities from a multi-environmental impact perspective: Toward a streamlined approach. J. Ind. Ecol. 2020, 24, 841–854, doi:10.1111/jiec.12985.
[287] The State of World Fisheries and Aquaculture 2020. Sustainability in Action; FAO: Rome, Italy, 2020; ISBN: 978-92-5-132692-3, ISSN 1020-5902, doi:10.4060/ca9229en.
[288] Skilbrei, O.T. The importance of escaped farmed rainbow trout (*Oncorhynchus mykiss*) as a vector for the salmon louse (Lepeophtheirus salmonis) depends on the hydrological conditions in the fjord. Hydrobiologia 2012, 686, 287–297, doi:10.1007/s10750-012-1028-x.
[289] FAO Cultured Aquatic Species Information Programme. Oncorhynchus Mykiss. Available online: http://www.fao.org/fishery/culturedspecies/Oncorhynchus_mykiss/en (accessed on 28 April 2021).
[290] Chytiri, S.; Chouliara, I.; Savvaidis, I.N.; Kontominas, M.G. Microbiological, chemical and sensory assessment of iced whole and filleted aquacultured rainbow trout. Food Microbiol. 2004, 21, 157–165, doi:10.1016/S0740-0020(03)00059-5.
[291] Olafsdóttir, G.; Martinsdóttir, E.; Oehlenschläger, J.; Dalgaard, P.; Jensen, B.; Undeland, I.; Mackie, I.M.; Henehan, G.; Nielsen, J.; Nilseng, H. Methods to evaluate fish freshness in research and industry. Trends Food Sci. Technol. 1997, 8, 258–265, doi:10.1016/S0924-2244(97)01049-2.
[292] Silva, F.; Duarte, A.M.; Mender, S.; Pinto, F.R.; Barroso, S.; Ganhão, R.; Gil, M.M. CATA vs. FCP for a rapid descriptive analysis in sensory characterization of fish. J. Sens. Stud. 2020, 35, e12605, doi:10.1111/joss.12605.
[293] Mustafa, F.; Andreescu, S. Chemical and Biological Sensors for Food-Quality Monitoring and Smart Packaging. Foods 2018, 7, 168, doi:10.3390/foods7100168.
[294] Gram, L.; Huss, H.H. Microbiological spoilage of fish and fish products. Int. J. Food Microbiol. 1996, 33, 121–137, doi:10.1016/0168-1605(96)01134-8.
[295] Jia, S.; Li, Y.; Zhuang, S.; Sun, X.; Zhang, L.; Shi, J.; Hong, H.; Luo, Y. Biochemical changes induced by dominant bacteria in chill-stored silver carp (*Hypophthalmichthys molitrix*) and GC-IMS identification of volatile organic compounds. Food Microbiol. 2019, 84, 103248, doi:10.1016/j.fm.2019.103248.
[296] Ghaly, A.E.; Dave, D.; Budge, S.; Brooks, M. Fish spoilage mechanisms and preservation techniques: Review. Am. J. Appl. Sci. 2010, 7, 859–877, doi:10.3844/ajassp.2010.859.877.
[297] Dikeman, M.; Devine, C. Encyclopedia of Meat Sciences, 2nd ed.; Academic Press: Amsterdam, The Netherlands, 2004; ISBN 978-0124649705.
[298] Pacquit, A.; Frisby, J.; Diamond, D.; Lau, K.T.; Farrell, A.; Quilty, B.; Diamond, D. Development of a smart packaging for the monitoring of fish spoilage. Food Chem. 2007, 102, 466–470, doi:10.1016/j.foodchem.2006.05.052.
[299] Seyama, T.; Kato, A.; Fujishi, K.; Nagatani, M. A new detector for gasous components using semiconductive thin films. Anal. Chem. 1962, 34, 1502, doi:10.1021/ac60191a001.
[300] Korotcenkov, G. Current trends in nanomaterials for metal oxide-based conductometric gas sensors: advantages and limitations. Part 1: 1D and 2D nanostructures. Nanomaterials 2020, 10, 1392, doi:10.3390/nano10071392.
[301] Akbari-Saatlu, M.; Procek, M.; Mattsson, C.; Thungström, G.; Nilsson, H.-E.; Xiong, W.; Xu, B.; Li, Y.; Radamson, H.H. Silicon nanowires for gas sensing: a review. Nanomaterials 2020, 10, 2215, doi:10.3390/nano10112215.
[302] Kim, D.; Park, C.; Choi, W.; Shin, S.-H.; Jin, B.; Baek, R.-H.; Lee, J.-S. Improved long-term responses of Au-decorated Si nanowire FET sensor for NH_3 detection. IEEE Sens. J. 2020, 20, 2270, doi:10.1109/JSEN.2019.2952582.
[303] Pichon, L.; Rogel, R.; Jacques, E.; Salaun, A.C. N-type in-situ doping effect on vapour-liquid-solid silicon nanowire properties for gas sensing applications. Phys. Status Solidi C 2014, 11, 344, doi:10.1002/pssc.201300206.
[304] Pichon, L.; Salaün, A.-C.; Wenga, G.; Rogel, R.; Jacques, E. Ammonia sensors based on suspended silicon nanowires. Proc. Eng. 2014, 87, 1003, doi:10.1016/j.proeng.2014.11.329.

[305] Jacques, E.; Ni, L.; Salaün, A.C.; Rogel, R.; Pichon, L. Polysilicon Nanowires for chemical sensing applications. Mater. Res. Soc. Symp. Proc. 2012, 1429, 133, doi:10.1557/opl.2012.1217.
[306] Selvaraj, B.; Balaguru Rayappan, J.B.; Jayanth Babu, K. Influence of calcination temperature on the growth of electrospun multi-junction ZnO nanowires: A room temperature ammonia sensor. Mater. Sci. Semicon. Proc. 2020, 112, 105006, doi:10.1016/j.mssp.2020.105006.
[307] Srinivasan, P.; Rayappan, J.B.B. Growth of Eshelby twisted ZnO nanowires through nanoflakes & nanoflowers: A room temperature ammonia sensor. Sens. Actuat. B Chem 2018, 277, 129, doi:10.1016/j.snb.2018.09.003.
[308] Tonezzer, M.; Le, D.T.T.; Iannotta, S.; Hieu, N.V. Selective discrimination of hazardous gases using one single metal oxide resistive sensor. Sensor Actuat. B Chem. 2018, 277, 121–128, doi:10.1016/j.snb.2018.08.103.
[309] Krawczyk, M.; Suchorska-Woźniak, P.; Szukiewicz, R.; Kuchowicz, M.; Korbutowicz, R.; Teterycz, H. Morphology of Ga_2O_3 Nanowires and Their Sensitivity to Volatile Organic Compounds. Nanomaterials 2021, 11, 456, doi:10.3390/nano11020456.
[310] Ngoc, T.M.; Duy, N.V.; Hung, C.M.; Hoa, N.D.; Nguyen, H.; Tonezzer, M.; Hieu, N.V. Self-heated Ag-decorated SnO_2 nanowires with low power consumption used as a predictive virtual multisensor for H_2S-selective sensing. Anal. Chim. Acta 2019, 1069, 108–116, doi:10.1016/j.aca.2019.04.020.
[311] Thai, N.X.; Van Duy, N.; Hung, C.M.; Nguyen, H.; Tonezzer, M.; Van Hieu, N.; Hoa, N.D. Prototype edge-grown nanowire sensor array for the real-time monitoring and classification of multiple gases. J. Sci. Adv. Mater. Dev. 2020, 5, 409–416, doi:10.1016/j.jsamd.2020.05.005.
[312] Tonezzer, M. Selective gas sensor based on one single SnO_2 nanowire, Sensor Actuat. B Chem. 2019, 288, 53–59, doi:10.1016/j.snb.2019.02.096.
[313] D'Amico, A.; Di Natale, C. A contribution on some basic definitions of sensors properties. IEEE Sens. J. 2001, 1, 183–190, doi:10.1109/JSEN.2001.954831.
[314] Thai, N.X.; Tonezzer, M.; Masera, L.; Nguyen, H.; Duy, N.V.; Hoa, N.D. Multi gas sensors using one nanomaterial, temperature gradient, and machine learning algorithms for discrimination of gases and their concentration. Anal. Chim. Acta 2020, 1124, 85–93, doi:10.1016/j.aca.2020.05.015.
[315] Koutsoumanis, K. Predictive Modeling of the Shelf Life of Fish under Nonisothermal Conditions. Appl. Environ. Microbiol. 2001, 67, 1821–1829, doi:10.1128/AEM.67.4.1821-1829.2001.
[316] Khoshnoudi-Nia, S.; Moosavi-Nasab, M. Nondestructive Determination of Microbial, Biochemical, and Chemical Changes in Rainbow Trout (Oncorhynchus mykiss) During Refrigerated Storage Using Hyperspectral Imaging Technique. Food Anal. Methods 2019, 12, 1635–1647, doi:10.1007/s12161-019-01494-8.
[317] Sciortino, J.A.; Ravikumar, R. Chapter 5: Fish Quality Assurance. In Fishery Harbour Manual on the Prevention of Pollution; Bay of Bengal Programme; Bay of Bengal Programme: Madras, India, 1999.
[318] Poli, B.M. Total quality in the fisheries chain, Chapter 19.2. In The State of Italian Marine Fisheries and Aquaculture; Cautadella, S., Spagnolo, M., Eds.; Ministero delle Politiche Agricole, Alimentari e Forestali (MiPAAF): Rome, Italy, 2011.
[319] Gui, M.; Song, J.; Zhang, Z.; Hui, P.; Li, P. Biogenic amines formation, nucleotide degradation and TVB-N accumulation of vacuum-packed minced sturgeon (Acipenser schrencki) stored at 4°C and their relation to microbiological attributes. J. Sci. Food Agric. 2014, 94, 2057–2063, doi:10.1002/jsfa.6524.
[320] Bekhit, A.E.-D.; Holman, B.W.B.; Giteru, S.G.; Hopkins, D.L. Total volatile basic nitrogen (TVB-N) and its role in meat spoilage: A review. Trends Food Sci. Technol. 2021, 109, 280–302, doi:10.1016/j.tifs.2021.01.006.
[321] Kim, J.-Y.; Kim, S.S.; Tonezzer, M. Selective gas detection and quantification using a resistive sensor based on Pd-decorated soda-lime glass. Sensor Actuat. B Chem. 2021, 335, 129714, doi:10.1016/j.snb.2021.129714.
[322] Jolliffe, I.T.; Cadima, J. Principal component analysis: A review and recent developments. Phil. Trans. R. Soc. A 2016, 374, 20150202, doi:10.1098/rsta
[323] Scharff, R.L. Economic burden from health losses due to foodborne illness in the United States. *J. Food Prot.* **2012**, *75*, 123–131. Doi: 10.4315/0362-028X.JFP-11-058.
[324] Sundström, K. Cost of illness for five major foodborne illnesses and sequelae in Sweden. *Appl. Health Econ. Health Policy* **2018**, *16*, 243–257. Doi: 10.1007/s40258-017-0369-z.
[325] Boyer, D.; Ramaswami, A. Comparing urban food system characteristics and actions in US and Indian cities from a multi-environmental impact perspective: Toward a streamlined approach. Journal of Industrial Ecology 2020, 24, 841-854. Doi: 10.1111/jiec.12985.
[326] Comi G. Spoilage of Meat and Fish. In The Microbiological Quality of Food; Comi G. Ed.; Woodhead Publishing Series, 2017. Doi: 10.1016/B978-0-08-100502-6.00011-X.
[327] Wojnowski, W.; Majchrzak, T.; Dymerski, T.; Gębicki, J.; Namieśnik, J. Portable electronic nose based on electrochemical sensors for food quality assessment, Sensors 2017, 17, 2715. Doi: 10.3390/s17122715.

[328] Deisingh, A.K.: Stone, D.C.; Thompson, M. Applications of electronic noses and tongues in food analysis. International Journal of Food Science and Technology 2004, 39, 587-604. Doi: 10.1111/j.1365-2621.2004.00821.x
[329] Chang L-Y.; Chuang M-Y.; Zan H-W.; Meng H-F.; Lu C-J.; Yeh P-H.; Chen J-N. One-minute fish freshness evaluation by testing the volatile amine gas with an ultrasensitive porous-electrode-capped organic gas sensor system. ACS Sens. 2017, 2, 4, 531–539. Doi: 10.1021/acssensors.6b00829
[330] Perez de Vargas-Sansalvador I.M.; Erenas M.M.; Martinez-Olmos A.; Mirza-Montoro F.; Diamond D.; Capitan-Vallvey L.F. Smartphone based meat freshness detection. Talanta 2020, 216, 120985. Doi: 10.1016/j.talanta.2020.120985
[331] Leng, T.; Li, F.; Chen, Y.; Tang, L.; Xie, J.;Yu, Q. Fast quantification of total volatile basic nitrogen (TVB-N) content in beef and pork by near-infrared spectroscopy: Comparison of SVR and PLS model. Meat Sci. 2021, 180, 108559. Doi: 10.1016/j.meatsci.2021.108559
[332] Olafsdóttir, G.; Martinsdóttir, E.; Oehlenschläger, J.; Dalgaard, P.; Jensen, B.; Undeland, I.; Mackie, I.M.; Henehan, G.; Nielsen, J.; Nilseng, H. Methods to evaluate fish freshness in research and industry. Trends in Food Science & Technology 1997, 8, 258-265. Doi: 10.1016/S0924-2244(97)01049-2
[333] Thai, N.X.; Van Duy, N.; Hung, C.M.; Nguyen, H.; Tonezzer, M.; Van Hieu, N.; Hoa N.D. Prototype edge-grown nanowire sensor array for the real-time monitoring and classification of multiple gases. J. Sci.: Adv. Mater. Devices 2021, 5, 409-416. Doi: 10.1016/j.jsamd.2020.05.005
[334] Zeng, H.; Zhang, G.; Nagashima, K.; Takahashi, T.; Hosomi, T.; Yanagida T. Metal-oxide nanowire molecular sensors and their promises. Chemosensors 2021, 9, 41. Doi: 10.3390/chemosensors9020041
[335] Thai, N.X.; Tonezzer, M.; Masera, L.; Nguyen H.; Duy, N.V.; Hoa, N.D. Multi gas sensors using one nanomaterial, temperature gradient, and machine learning algorithms for discrimination of gases and their concentration. Anal. Chim. Acta 2020, 1124, 85-93. Doi: 10.1016/j.aca.2020.05.015
[336] Redwing, J.M.; Miao, X; Li, X. Vapor-Liquid-Solid Growth of Semiconductor Nanowires. In Handbook of Crystal Growth, 2nd ed.; Thomas F. Kuec, Ed.; Publisher: Elsevier North-Holland, Amsterdam, The Netherlands, 2015; Volume 3, pp. 399–439.Seyama, T.; Kato, A.; Fujishi, K.; Nagatani, M. A New Detector for Gasous Components Using Semiconductive Thin Films. Anal. Chem. 1962, 34, 1502. Doi: 10.1021/ac60191a001
[337] Lin, Y-F.; Jian, W-B. The impact of nanocontact on nanowire based nanoelectronics, Nano Lett. 2008, 8, 3146-3150. Doi: 10.1021/nl801347x
[338] Todeschini, M.; Bastos da Silva Fanta, A.; Jensen, F.; Birkedal Wagner, J.; Han, A. Influence of Ti and Cr Adhesion Layers on Ultrathin Au Films, ACS Appl. Mater. Interfaces 2017, 9, 37374-37385. Doi: 10.1021/acsami.7b10136
[339] Zeng, H.; Takahashi, T.; Kanai, M.; Zhang, G.; He, Y.; Nagashima, K.; Yanagida, T. Long-term stability of oxide nanowire sensors via heavily doped oxide contact, ACS Sens. 2017, 8, 1854-1859. Doi: 10.1021/acssensors.7b00716
[340] Tischner, A.; Maier, T.; Stepper, C.; Köck, A. Ultrathin SnO_2 gas sensors fabricated by spray pyrolysis for the detection of humidity and carbon monoxide. Sensor Actuat. B-Chem. 2008, 134, 796-802. Doi: 10.1016/j.snb.2008.06.032
[341 López, A.; Baguer, B.; Goñi, P.; Rubio, E.; Gómez, J.; Mosteo, R.; Ormad, M.P. Assessment of the methodologies used in microbiological control of sewage sludge. Waste Manag. 2019, 96, 168-174. Doi: 10.1016/j.wasman.2019.07.024
[342] Tonezzer, M.; Izidoro, S.C.; Moraes, J.P.A.; Dang, L.T.T. Improved gas selectivity based on carbon modified SnO_2 nanowires. Front. Mater. Sci. 2019, 6, 277. Doi: 10.3389/fmats.2019.00277
[343] Bekhit, A.E.A.; Holman, B.W.B.; Giteru, S.G.; Hopkins, D.L. Total volatile basic nitrogen (TVB-N) and its role in meat spoilage: A review. Trends Food Sci. Technol. 2021, 109, 280-302. Doi: 10.1016/j.tifs.2021.01.006
[344] Tsuda, N.; Nasu, K.; Fujimori, A.; Siratori, K. Electronic Conduction in Oxides, 2nd ed.; Publisher: Springer-Verlag, Berlin, 2000.
[345] Marikutsa, A.; Rumyantseva, M.; Gaskov, A. Selectivity of catalytically modified tin dioxide to CO and NH_3 gas mixtures. Chemosensors 2015, 3, 241-252. Doi: 10.3390/chemosensors3040241
[346] Wagh, M.S.; Jain, G.H.; Patil, D.R.; Patil, S.A.; Patil, L.A. Modified zinc oxide thick film resistors as NH_3 gas sensor. Sensor Actuat. B-Chem. 2005, 115, 128-133. Doi: 10.1016/j.snb.2005.08.030
[347] Wu, H.; Ma, Z.; Lin, Z.; Song, H.; Yan, S.; Shi, Y. High-sensitive ammonia sensors based on tin monoxide nanoshells. Nanomaterials 2019, 9, 388. Doi: 10.3390/nano9030388
[348] Koutsoumanis, K. Predictive modeling of the shelf life of fish under nonisothermal conditions. Appl. Environ. Microbiol. 2001, 67, 1821-1829. Doi: 10.1128/AEM.67.4.1821-1829.2001

[349] Sciortino, J.A.; Ravikumar, R. Chapter 5: Fish Quality Assurance. In Fishery Harbour Manual on the Prevention of Pollution, Bay of Bengal Programme. Publisher: Bay of Bengal Programme, Madras, India, 1999.